



Hatton, Daniel (2020) *High precision quark mass determinations and studies of meson properties using lattice QCD*. PhD thesis.

<https://theses.gla.ac.uk/81428/>

Copyright and moral rights for this work are retained by the author

A copy can be downloaded for personal non-commercial research or study, without prior permission or charge

This work cannot be reproduced or quoted extensively from without first obtaining permission in writing from the author

The content must not be changed in any way or sold commercially in any format or medium without the formal permission of the author

When referring to this work, full bibliographic details including the author, title, awarding institution and date of the thesis must be given

Enlighten: Theses

<https://theses.gla.ac.uk/>
research-enlighten@glasgow.ac.uk

High precision quark mass determinations and studies of meson properties using lattice QCD

Daniel Hatton

Supervised by Prof. Christine Davies



Submitted in fulfillment of the requirements for the degree of
Doctor of Philosophy

School of Physics and Astronomy
College of Science and Engineering
University of Glasgow

Abstract

Strongly interacting systems such as the internal dynamics of the myriad bound states seen in particle physics experiments are notoriously difficult to obtain a precise quantitative theoretical description of. Without systematically improvable methods of analysis of such system a vast region of particle physics phenomenology is left without proper confrontation with theory and systematic uncertainties arising from knowledge of fundamental particle physics parameters in the strong sector are difficult to control. Lattice quantum chromodynamics (QCD) has arisen as a methodological solution to the calculational difficulties raised by the theory of the strong interaction.

The main testing ground for high precision calculations utilised here is the properties of the two lowest lying states of the charmonium spectrum, the η_c and the J/ψ . Certain properties of these mesons are experimentally determined to high precision which makes them good targets for high precision lattice QCD calculations. At this level of precision it becomes necessary to include at least leading order electromagnetic corrections. This is addressed in this thesis with the inclusion of quenched QED in the study of charmonium properties.

In various calculations renormalisation factors need to be computed to high precision. The technique of nonperturbatively computing renormalisation factors in a momentum subtraction scheme on the lattice provides a computationally cheap method for the determination of these factors and is examined using the Highly Improved Staggered Quark (HISQ) action.

The charmonium calculations are then extended to higher masses leading up to the b quark mass allowing for comparisons with experimental results. It is demonstrated that this method offers a way to improve on the precision of previous lattice calculations that used nonrelativistic quark actions. Finally, sub-percent determinations of the strange and charm quark masses are presented, making use of nonperturbatively determined mass renormalisation factors. These are shown to agree, at this high level of precision, with other lattice calculations that use different methodologies, indicating that the systematic uncertainties are appropriately controlled.

Acknowledgements

There are obviously a lot of people to thank. Primarily I thank Christine Davies for her supervision and support; this document would not and could not exist without it. I also thank the numerous collaborators with whom I have had the pleasure of working, particularly Andrew Lytle who has greatly influenced much in the coming chapters.

I am grateful to the remarkable foundational support provided so willingly by my family.

A great many others are owed acknowledgement but as the full list would be obnoxiously long and through fear of inevitable omissions I only explicitly thank those in some sense most proximate: Dan, Donatas, Dwayne, Euan, Lauren, Stephen, Will, Esther and Panos.

To everyone who has been willing to help, thank you.

Declaration of originality

Apart from the background material in Chapters 1 and 2 and Sections 3.1, 4.1, 5.1 and 6.1 the work presented here is my own, working in collaboration with others members of the HPQCD collaboration. This includes work published in [1] , [2] and [3]. All figures are mine with the exception of Figs. 2.1 and 2.2 which are courtesy of Andrew Lytle and Figs. 4.20, 4.25 and 6.5 which are courtesy of Christine Davies.

Contents

Abstract	i
Acknowledgements	iii
Declaration of originality	iv
1 Theoretical Foundations	1
1.1 Quantum fields	2
1.1.1 Gauge fields	6
1.1.2 Vectors and spinors	7
1.1.3 Spontaneous symmetry breaking	10
1.2 Quantisation through the path integral	10
1.3 Renormalisation	12
1.3.1 The renormalisation group	13
1.4 The Standard Model	14
1.5 Perturbative approaches to QCD	18
1.5.1 Correlator time moments	19
1.5.2 Chiral symmetry	22

1.5.3	The Operator Product Expansion	24
1.5.4	Structure of the quark propagator	25
2	Lattice Formulations of Quantum Field Theories	27
2.1	Fields on the Lattice	27
2.2	Fermions on the Lattice	29
2.2.1	The staggered transformation	30
2.3	Symanzik effective theory	32
2.4	Computational challenge	33
2.4.1	The conjugate gradient solver	33
2.4.2	Gauge field generation	35
2.4.3	HISQ ensembles	36
2.5	Construction of staggered correlation functions	37
2.5.1	Arbitrary momentum with twisted boundary conditions	39
2.6	Parallelisation	39
2.7	Fitting 2-point functions	41
2.8	Principles of Bayesian fitting	42
2.9	QED on the lattice	45
2.10	Scale setting	47
3	Nonperturbative Renormalisation in Momentum Subtraction Schemes with Staggered Quarks	49
3.1	MOM schemes and their lattice implementation	49
3.1.1	Momentum space quark fields with staggered quarks	53
3.1.2	Staggered quark bilinears	54

3.2	Z_m : mass renormalisation	55
3.2.1	Landau gauge fixing	56
3.2.2	Z_m in the RI-SMOM scheme	57
3.2.3	Data and statistics	59
3.2.4	Valence mass extrapolation	60
3.2.5	Systematic uncertainties	61
3.2.6	Electromagnetic corrections to Z_m	68
3.3	Z_V : lattice vector current renormalisation	71
3.3.1	The vector Ward-Takahashi identity on the lattice	72
3.3.2	Tree level vertex functions	77
3.3.3	Lattice calculation	79
3.3.4	Conserved vector current renormalisation	84
3.3.5	Local vector current renormalisation	86
3.3.6	1-link vector current renormalisation	92
3.3.7	QED corrections	94
3.3.8	Calculating Z_V on finer lattices	102
3.3.9	Conclusions: Z_V	102
3.4	Z_T : tensor current renormalisation	104
3.4.1	Z_T in the RI-SMOM scheme	105
3.4.2	Valence mass extrapolation	106
3.4.3	Conversion to $\overline{\text{MS}}$	108
3.4.4	Strategy for condensate corrections	110
3.5	Conclusions	112

4	Properties of Ground State Charmonium	113
4.1	The charmonium spectrum	113
4.2	Charmonium on the lattice	115
4.3	Lattice setup	117
4.3.1	Two-point correlator fitting	119
4.3.2	Including quenched QED	120
4.3.3	Fitting strategy for inclusion of QED effects	123
4.4	Hyperfine splitting	124
4.4.1	Discussion	128
4.5	J/ψ and η_c decay constants	133
4.5.1	J/ψ decay constant	133
4.5.2	f_{η_c}	136
4.5.3	Discussion	139
4.6	J/ψ tensor decay constant	142
4.6.1	Final Z_T values	147
4.7	a_μ^c and vector time moments	151
4.7.1	a_μ^c lattice spacing dependence	156
4.8	Conclusions	161
5	Bottomonium Ground State Properties with a Fully Relativistic Action	163
5.1	Heavyonium physics	163
5.2	Lattice calculation	164
5.3	Hyperfine splitting	166
5.4	Vector and pseudoscalar decay constants	171

5.5	Bottomonium vector time moments and a_μ^b	176
5.6	Conclusions	180
6	Quark Mass Determinations	182
6.1	Tuning to the physical point	183
6.2	\bar{m}_c and \bar{m}_s using the RI-SMOM intermediate scheme	185
6.2.1	Conversion to $\overline{\text{MS}}$ scheme	186
6.2.2	Mass results	186
6.3	Charm tuning with the J/ψ	191
6.4	QED impact on the determination of m_c in the $\overline{\text{MS}}$ scheme	192
6.5	Cross-check with determination from time moments	196
6.6	Summary	197
7	Conclusions	199

List of Figures

1.1	The running of the strong coupling in the $\overline{\text{MS}}$ scheme with the scale μ . The four-loop QCD β function is used for the calculation. This clearly shows the sharp growth at low μ values.	20
1.2	Feynman diagram of the quark loop contribution to the vacuum polarisation of the photon.	20
2.1	Performance of MILC code conjugate gradient routine on Skylake systems for various lattice volumes. Peta4 provides 32 CPUs per node (2 sockets). [Figure courtesy of A. T. Lytle.]	40
2.2	Performance of MILC code (calling QUDA) conjugate gradient routine on Wilkes2 for various lattice volumes. Wilkes2 provides 4 Nvidia P100 GPUs per node. [Figure courtesy of A. T. Lytle.]	41
3.1	Depiction of the kinematic setup of the vertex functions used in momentum subtraction scheme. The circle represents the insertion of an operator.	50
3.2	$P_{\Lambda_P} - P_{\Lambda_S}$ in the RI-SMOM scheme for sets 14 and 7 indicating the decrease in chirality violating effects with increasing μ . The line shown has the form B/μ^6 and is drawn to indicate the speed of this decrease.	58
3.3	Plot of the chiral extrapolation of set 16 with $\mu = 3$ GeV. The highest mass point is not included in the fit but is shown to indicate that the fit operates well far from the point being extrapolated to.	61

- 3.4 The linear and quadratic slopes of the valence mass dependence of Z_m^{SMOM} as a function of μ . These are d_1 and d_2 from Eq. 3.19. The curve is a fit of the form C/μ^4 to the d_2 data. 62
- 3.5 Upper: Z_m against μ for sets 6, 7 and 8. Lower: The three points at $\mu = 1.80$ GeV (upper left of upper plot) against the spatial extent of the lattice in lattice units. This indicates that the volume dependence of Z_m is negligible. 63
- 3.6 Plots indicating the charm and strange sea quark mass dependence of Z_m , which is clearly small. However, the final continuum extrapolation still allows for some sea mass dependence. The charm mass variation is shown on sets 4, 5 and 6 and the strange mass variation on sets 7, 9, 10 and 11. 65
- 3.7 Z_m^{SMOM} against the charm (upper) and strange (lower) sea masses on the same ensembles as in Fig. 3.6. Here a μ value close to 2 GeV is chosen in each case. A clearer indication of the variation of the values in Fig. 3.6 is given with no variation beyond a few σ 66
- 3.8 Gauge fixing difference as a function of μ on set 5. There is a clear decrease in this residual systematic as μ is increased. 67
- 3.9 Scatter plot of bootstrapped Z_m against the trace link on set 7. Dashed horizontal lines indicate the mean value. 67
- 3.10 The difference between the (amputated, projected local) vector and axial vector vertex functions as a function of μ in the RI'-MOM and RI-SMOM schemes. The improvement obtained by using the RI-SMOM scheme is clear. These values have been extrapolated to zero valence quark mass and are shown for the finest lattice we use (set 16 in Table 3.5.) 73

- 3.11 Demonstration of the vector Ward-Takahashi identity in momentum space on the lattice. The solid line is the values of $-\frac{2i}{a}\sin\left(\frac{aq\mu}{2}\right)$ as a function of q represented by the quantity $x+\theta/2$ which is the momentum divided by $2\pi/L$ with L the extent of the lattice in the relevant direction. The points correspond to lattice results for the ratio $\Lambda_V/(S^{-1}(p_2)-S^{-1}(p_1))$ (averaging over all matrix components) on a single configuration with crosses representing Coulomb gauge fixing and the circles Landau gauge fixing. Orange points correspond to a valence mass of $am_{\text{val}} = 0.0306$ while purple points correspond to 0.0102. The Ward-Takahashi identity requires these points to lie on the line. 77
- 3.12 Test of the identity in Eq. 3.30. The squares are for set 5, the hexagons are set 14 and the circles are set 16. 78
- 3.13 Valence mass dependence of local Z_V values in the RI-SMOM and RI'-MOM schemes. Upper: Local Z_V in the RI-SMOM scheme at $\mu = 3$ GeV. Lower: Local Z_V in the RI'-MOM scheme at $\mu = 3$ GeV. The strongest valence mass dependence we observe is in the local vector current renormalisation in the RI'-MOM scheme, which can be seen to be very small. The label $Z_V^{\text{loc,MOM,raw}}$ indicates that these are local MOM Z_V values before they are multiplied by a conversion factor to the $\overline{\text{MS}}$ scheme. 83
- 3.14 $Z_V^{\text{con}}(\text{MOM})$ for μ values 2, 2.5, 3 and 4 GeV. The fit shown accounts for discretisation errors and condensate contributions, which prove to be necessary for a good fit. Discretisation errors proportional to α_s are also allowed. The $\alpha_s(a\mu)^2$ coefficient is very small, consistent with the suppression of one-loop taste changing interactions when using the HISQ action [39]. The disagreement between the different μ values after the continuum extrapolation is performed is the result of condensate contributions. 86
- 3.15 The difference between the MOM local Z_V and Z_V determined from form factor methods. The situation for this case is clearly different to that when the SMOM scheme is used shown in Fig. 3.17. The MOM case shows a clear μ dependent effect as can be expected from the lack of Ward-Takahashi identity protection in the MOM scheme. 88

- 3.16 The same as Fig. 3.15 but using the ratio of the MOM local and conserved vector current renormalisation. These results are consistent with a lack of nonperturbative contamination, unlike when just using the MOM local vector current (Fig. 3.15). 89
- 3.17 The difference between the SMOM local vector current renormalisation factor and the local vector renormalisation determined through a form factor at zero momentum. In the absence of nonperturbative contamination this is expected to be consistent with pure discretisation effects. Values as low as $\mu = 1$ GeV are included and no sign of μ dependent nonperturbative effects is seen. 90
- 3.18 The difference between the local to conserved vector current renormalisation in the $\text{SMOM}_{\gamma\mu}$ scheme and the local renormalisation determined from form factor methods. Similarly to Fig. 3.17 there is no indication of nonperturbative contamination. 90
- 3.19 Plot showing the difference between the local Z_V determined using form factors and an SMOM local Z_V derived from results at μ values of 2 and 3 GeV in order to reduce discretisation effects. This uses Eq. 3.44 91
- 3.20 $Z_V^{\text{loc}}(\text{SMOM})$ data with the fit given by Eq. 3.45. The grey band shows the lattice perturbation theory component of the fit and the black diamonds are form factor renormalisations from [75]. The blue band is the lattice perturbation theory component of the fit to the form factor data. 92
- 3.21 $Z_V^{\text{link}}(\text{SMOM})$ subtracted from the Z_V at the corresponding lattice spacing, determined from the vector form factor at zero momentum transfer. The range of μ values from 1 to 4 GeV indicates that there is not a visible nonperturbative effect growing at small μ . The fit lines shown are the fit of Eq. 3.48 which consists of only discretisation effects. 95
- 3.22 Local SMOM Z_V at electromagnetic charges of 0 and 2/3 the proton charge. The fit shown is linear in the charge squared. This fit could be used to extract Z_V values at different values of the electromagnetic charge. 96
- 3.23 Z_V for the SMOM conserved current with the inclusion of quenched QED. The quark charge used is 2/3 the charge of the proton. As expected all values are consistent with 1. The squares are for set 5, the hexagons are set 14 and the circles are set 16. 97

3.24	Ratio of Z_V^{loc} values for QCD+QED and QCD in the RI-SMOM scheme. Results are given on sets 14 and 16 for μ values of 2, 3 and 4 GeV and on set 6 values of 2, 2.5 and 3 GeV. The dashed lines give the results of the fit of Eq. 3.51 which indicates that the results are described well by a perturbative series up to discretisation effects.	100
3.25	Upper: Volume dependence of the ratio of Z_V^{loc} (SMOM) calculated with QCD and quenched QED to the same quantity calculated with pure QCD at $\mu = 2$ GeV. There is no observable dependence. Lower: Volume dependence of the same ratio for Z_q at $\mu = 2$ GeV. In this case there is some visible volume dependence which is largely cancelled by the volume dependence of P_{Λ_V}	101
3.26	Local vector current renormalisation in the RI-SMOM scheme. This fit is given by Eq. 3.52 and includes discretisation effects and an expansion in the strong coupling (in the $\overline{\text{MS}}$ scheme) evaluated at $1/a$. All the data points shown are included in the fit but only the 2 and 3 GeV fit lines are drawn.	103
3.27	Example of a penguin diagram for the rare decay $B \rightarrow K\ell^+\ell^-$	104
3.28	Valence mass dependence of tensor current renormalisation factors in the RI-SMOM (upper) and RI'-MOM (lower) schemes. The values shown are for $\mu = 2$ GeV on Set 16. Both show reasonably mild dependence on the valence mass but the dependence is clearly less for RI-SMOM.	107
4.1	The charmonium spectrum below the open charm threshold. Moving from left to right the first five columns are pseudoscalars, vectors, axialvectors, scalars and spin 2. The bars to the right indicate the relative widths of the particles.	114

- 4.2 Top panel: Pure QCD J/ψ masses on all 15 sets from Table 4.1 using the valence masses in that Table. Two error bars are shown. The error can be broken into parts that are uncorrelated between different sets and the contribution from w_0 which is correlated. The outer error bar shows the full uncertainty and the inner bar the uncertainty without the contribution from w_0 . Bottom panel: The J/ψ masses on sets 2, 7, 10 and 14 with and without the inclusion of quenched QED. On each set the same valence mass was used for both pure QCD and QCD+QED but the points have been separated on the x -axis for clarity. The error bars are the same as for the top panel, but note that here there is a correlation of the uncertainty from w_0/a for the QCD and QCD+QED results on each set. 122
- 4.3 The hyperfine splitting against $(am_c)^2$ with the fit of Eq. 4.6. The top plot shows the pure QCD part of the fit while the bottom gives the full fit as well as showing the QCD+QED data points in violet. The two points at purposefully mistuned valence mass are not shown. The black cross is the experimental average and the orange cross is the continuum extrapolation. There is a clear difference between the continuum lattice value and the experimental value which could be explained by the annihilation of the η_c to two gluons. 126
- 4.4 Fit results for the hyperfine splitting in QCD+QED (excluding the contribution from the J/ψ annihilation to a photon) with various pieces of data removed. By mistuned masses it is meant the data on sets 7 and 18 that have deliberately mistuned valence masses. 127
- 4.5 The QED effect on the hyperfine splitting against $(am_c)^2$. This shows the smallness of discretisation effects as well as the precision that can be obtained by capitalising on the correlations between QCD+QED and pure QCD correlators. The dashed line shows the average of the points. 129
- 4.6 The J/ψ and η_c mass shifts from the inclusion of quenched QED presented as the ratio of the QCD+QED value to the pure QCD value. These lines are flat indicating an absence of visible finite volume effects. 129

- 4.7 Comparison of different experimental results for the charmonium hyperfine splitting as well as the PDG average. The PDG average is obtained from taking the differences of the PDG J/ψ and η_c masses rather than from experiments that directly measure the splitting. The η_c results represent a recent subset of those used in the PDG average. The most recent result is from BELLE [115]. There are three different determinations from LHCb [113, 114, 116], two of which also measured the hyperfine splitting. We include a KEDR measurement [112], two from different BaBar analyses [117] and two from BESIII [118, 119]. 130
- 4.8 Comparison of different lattice results for the charmonium hyperfine splitting and separate experimental results as well as the PDG average. The squares represent 2+1 lattice results and the hexagon this 2+1+1 result. All lattice results have had uncertainties from neglecting η_c annihilation results removed so that we expect some difference between them and experiment. The Fermilab/MILC result using asqtad ensembles and Fermilab charm quarks was presented in [120]. The χ QCD result is from [121] and Briceño et al. is from [122]. 131
- 4.9 The electromagnetic correction to the J/ψ decay constant on lattices with different lattice spacings. 136
- 4.10 The J/ψ decay constant calculated on the ensembles of Table 4.1. The upper plot only gives the pure QCD data points and fit, while the lower plot includes the QCD+QED points in blue which are also included in the fit shown there. There is quite a significant lattice spacing dependence but the sea quark mass dependence is less visible than for the hyperfine splitting. The vector current renormalisation factors determined in the RI-SMOM scheme contribute little to the uncertainties. They also contribute relatively little to the discretisation effects. 137
- 4.11 The volume dependence of the electromagnetic effect on the J/ψ and η_c decay constants measured on sets 6-8. All results are perfectly consistent with each other indicating that there is no observable finite volume effect. 138
- 4.12 The continuum extrapolation of $f_{J/\psi}$ using Z_V at reference scales of 2 and 3 GeV. The points at am_c values of ~ 0.8 are not present for the 3 GeV case as the discretisation errors in Z_V become too large. There is a clear agreement between the two continuum results. 138

- 4.13 The decay constant of the η_c in pure QCD (upper) and QCD+QED (lower). The fit form is the same as was used for $f_{J/\psi}$. The discretisation effects are noticeably smaller than in the J/ψ case. 140
- 4.14 Ratio of the vector and pseudoscalar decay constants with continuum extrapolation fit. 141
- 4.15 Continuum extrapolation of the J/ψ tensor decay constant in the $\overline{\text{MS}}$ scheme at a scale of 2 GeV using tensor current renormalisation in the RI-SMOM scheme. Three different values of the renormalisation scale μ , all converted to $\overline{\text{MS}}$ and run to a reference scale of 2 GeV, are used to allow nonperturbative μ dependence to be fit. These three different μ values are shown as different coloured lines. The purple line is 2 GeV, the blue 3 GeV and the red 4 GeV. The black hexagon at $am_c = 0$ is the physical result for $f_{J/\psi}^T(2 \text{ GeV})$ obtained from the fit (with the condensate pieces removed). The square shows the ETMC result [128] for the J/ψ tensor decay constant. 144
- 4.16 The “correction” to the tensor current renormalisation designed to account for nonperturbative effects that must be removed defined in terms of a subset of the fit posteriors of the fit shown in Fig. 4.15. This is the absolute correction. If the corrected value of Z_T is denoted Z_T^{true} and the uncorrected value Z_T^{raw} then $Z_T^{\text{true}} = Z_T^{\text{raw}} - \text{“correction”}$ 145
- 4.17 Continuum extrapolation of the J/ψ decay constant using a nonperturbative renormalisation of the tensor current in the RI'-MOM scheme. Multiple values of the renormalisation scale μ have been used so that μ dependent nonperturbative effects can be removed in the fit. The result is in agreement with that using RI-SMOM renormalisation (see Fig. 4.15). The colours and shapes denote the same things as in Fig. 4.15. 146
- 4.18 The same as Fig. 4.16 but using a tensor current renormalisation in the RI'-MOM scheme. 147

- 4.19 Continuum extrapolation of the ratio of the tensor and vector J/ψ decay constants using renormalisation factors in the RI-SMOM scheme. Again, purple points and lines show $\mu = 2$ GeV data and fit lines, blue are 3 GeV and red 4 GeV. The bold dashed lines are continuum extrapolations at each μ value with the condensate terms left in. The black hexagon is the continuum extrapolation with condensates removed. 148
- 4.20 Nonperturbative “correction” calculated from a fit to the ratio of the J/ψ vector and tensor decay constants using renormalisation factors from the RI-SMOM scheme. This agrees with Fig. 4.16 as expected from the lack of condensate contributions to the RI-SMOM vector current renormalisation. 148
- 4.21 The four lowest time moments multiplied by the J/ψ mass and their extrapolation to $a = 0$. The values of the moments increase as the moment number is increased. The extrapolations of the moments shown are performed simultaneously. 154
- 4.22 Comparisons of various determinations of the first two vector charm moments. Lattice QCD results are shown in blue and phenomenological determinations using $e^+e^- \rightarrow$ hadrons cross-section data are shown in red. The previous HPQCD result is from [76] and the JLQCD result is from [132]. For the latter only the second of the two moments is available due to discretisation effects. The phenomenological results are from [129] and [133]. [Figure courtesy of C. T. H. Davies.] 155
- 4.23 Extrapolation of the charm connected HVP contribution to the anomalous magnetic moment of the muon to the continuum. The continuum result is compared to the result obtained by calculating a_μ^c from the individually continuum extrapolated time moments. Agreement is seen, as expected. The result also agrees well with, with a significantly decreased uncertainty, the previous HPQCD result. There is also agreement with the BMW result of [134] and the ETMC result of [135, 136] where we have used the QED correction of [136]. The upper plot displays only pure QCD data with a fit line excluding the QED part of the fit. The lower plot includes the QCD+QED data and the full fit. 157
- 4.24 Comparison of the discretisation effects in the data of Table 4.17 (red open symbols) and the data from BMW [134] (green circles). The BMW data points are estimates and do not include an uncertainty. 159

4.25	Volume dependence of the electromagnetic correction to a_μ^c and the first four vector current correlator time moments on sets 6-8. There is no observable dependence as expected from previous analyses of QED finite volume effects in the hadronic vacuum polarisation.	159
4.26	Comparison of the charm connected hadronic vacuum polarisation contribution to the anomalous magnetic moment of the muon from different lattice QCD calculations. The BMWc result is from [134]. The ETMC result is from [135]. [Figure courtesy of C. T. H. Davies.]	161
5.1	Summary of the current status of experimental measurements of the bottomonium hyperfine splitting. The BELLE12 result is from [143], the CLEO12 result is from [144], the BABAR09 result is from [145] and BABAR08 is from [140]. The red band is the PDG average.	168
5.2	Hyperfine splitting of heavyonium including a simultaneous continuum extrapolation and mass interpolation to the b mass, using the vector meson mass as a proxy. The black cross marks the PDG average of the bottomonium hyperfine splitting. The labels in the legend correspond to ensembles according to Table 5.1.	169
5.3	Heavy mass dependence of the light sea quark mass mistuning dependence of the hyperfine splitting as calculated from the output of a fit to the form given in Eq. 5.1. The two lines shown are for the δ_ℓ values on sets 16 (purple) and 17 (blue). For the hyperfine splitting this shows little heavy mass dependence with a slight decrease at higher masses.	170
5.4	Comparison of lattice results for the bottomonium hyperfine splitting. The red band shows the PDG average. The green squares show results that use either NRQCD (HPQCD13 [146] and Meinel10 [147]), Fermilab heavy quarks (FNAL/MILC09 [142]) or the RHQ action (RBC/UKQCD12) [148].	170
5.5	Fit of the vector decay constant of heavyonium to Eq. 5.1. The PDG experimental average of the Υ decay constant is shown as a black cross and a previous HPQCD result [150], shown as a red star, using NRQCD b quarks which is set at a point higher than the Υ mass on the x -axis for clarity.	173

5.6	Same as Fig. 5.3 but for the vector decay constant. The heavy mass dependence in this case is more significant than for the hyperfine splitting.	173
5.7	The heavyonium pseudoscalar decay constant with the fit of Eq. 5.1. There is no experimental observable that corresponds to this so we compare to a previous HPQCD result [94] (also using the heavy HISQ method) which is shown as a black cross.	174
5.8	Same as Fig. 5.3 but for the heavyonium pseudoscalar decay constant. This is very similar to the vector decay constant case shown in Fig. 5.6.	175
5.9	Ratio of the heavyonium vector and pseudoscalar decay constants with a fit of the form Eq. 5.1. It is clear that the ratio is above 1 at the charm mass but moves to be below 1 at the b mass.	176
5.10	Continuum extrapolation and heavy mass interpolation of the 4 th vector time moment. The value extracted from experimental data in [151] is shown as the black circle.	178
5.11	Continuum extrapolation and heavy mass interpolation of the 6 th vector time moment. The value extracted from experimental data in [151] is shown as the black circle.	178
5.12	Continuum extrapolation and heavy mass interpolation of the 8 th vector time moment. The value extracted from experimental data in [151] is shown as the black circle.	179
5.13	Continuum extrapolation and heavy mass interpolation of the 10 th vector time moment. The value extracted from experimental data in [151] is shown as the black circle.	179
6.1	Final mass continuum extrapolations. The dashed lines have the sea quark mass mistunings set to 0. The shaded point on the left gives the final value at $a = 0$ with the condensate contributions removed. The empty black circle is the value from the current-current correlator method of [27].	189

- 6.2 Robustness checks of the final mass fits. The 5 $a\mu$ points mark only uses 5 different powers of $a\mu$ in the fit as opposed to 10, which was used in the fit presented in Figure 6.1. 190
- 6.3 $\bar{m}_c(3 \text{ GeV})$ extrapolated to the continuum with a fit form that allows for condensate terms that behave like inverse powers of the renormalisation scale μ . This plot is the same as the upper section of Fig. 6.1 but with added data at a finer lattice spacing (ultrafine). The ultrafine points deviate from the μ values of the corresponding lines by 1-2% because the μ values on these points are slightly mistuned. We are also here using tuning to the J/ψ mass rather than the η_c mass as was done in [1]. 192
- 6.4 Electromagnetic correction to the charm quark mass in the $\overline{\text{MS}}$ scheme at a scale of 3 GeV. The final, continuum extrapolated, result is shown as the red circle to the left. The different μ values, shown as different colours and shapes, have all been run to 3 GeV and only differ by discretisation and condensate effects. In fact, there is no visible difference. The vast majority of the discretisation effect here is due to discretisation effects in the ratio of the charm bare mass tuned to give the experimental J/ψ mass with and without the inclusion of QED effects. These appear as even powers of am_c 195
- 6.5 Comparison plot of lattice determinations of the charm quark running mass in the $\overline{\text{MS}}$ scheme with four flavours in the sea. The grey band corresponds to the PDG average. [Figure courtesy of C. T. H. Davies.] 198

List of Tables

1.1	Hypercharges of the Standard Model fermion fields.	15
1.2	Masses and electromagnetic charges of the Standard Model particles as measured by experiment [23].	17
1.3	Coefficients in the perturbative expansion of pseudoscalar and vector time moments from [28] and [29].	22
1.4	Coefficients of logarithmic terms in the perturbative expansion of pseudoscalar and vector time moments from [28].	23
2.1	Important parameters for the lattice ensembles used generated by the MILC collaboration [42]. The value of w_0 is 0.1715(9) fm [46]. The lattice spacings approximately range from 0.15 to 0.03 fm. Sets 1-3 are referred to as very coarse, 4-12 as coarse, 13-15 as fine, 16-17 as superfine, 18 as ultrafine and 19 as exafine.	37
3.1	Details of the range of lattice ensembles used in the RI-SMOM quark mass determination calculation. Those with $\beta = 6.0$ are referred to as coarse, $\beta = 6.3$ as fine and $\beta = 6.72$ as superfine.	60
3.2	Data used in final fits including the correlation matrices across the μ values on a given set, coming from the simultaneous chiral extrapolation.	69
3.3	The electromagnetic correction to Z_m for different values of μ and different lattice spacings are shown in the third column.	70

3.4	Tree-level matrix elements of the various operators in the different schemes that we consider. We also give the projectors that we use in the construction of each Z_V . For definitions of \not{q} in each case we refer to the main text. S and T are the vectors describing the spin and taste of the operator (see [64]). The first column labels both the scheme (SMOM for RI-SMOM and MOM for RI'-MOM) and the operator. The local operator is labelled "loc", the conserved current operator "con" and the 1-link operators of Eqs. 3.46 and 3.47 "1link-fwd" and "1link-cov" respectively.	79
3.5	Simulation parameters for the MILC gluon field ensembles that we use, labelled by set number in the first column. $\beta = 10/g^2$ is the bare QCD coupling and L_s and L_t give the lattice dimensions. am_l^{sea} , am_s^{sea} and am_c^{sea} give the sea quark masses in lattice units. Set 1 will be referred to in the text as 'very coarse', sets 5–8 'coarse', sets 14 as 'fine' and set 16 as 'superfine'.	81
3.6	Conversion factors from the momentum subtraction schemes we consider to $\overline{\text{MS}}$ at the μ values used in this calculation, calculated with $n_f = 4$ using the results of [62]. Z_V values in momentum subtraction schemes are multiplied by these factors to obtain Z_V in the $\overline{\text{MS}}$ scheme. These factors are multiplied into any RI'-MOM results that are not a ratio of Z_V for different currents.	85
3.7	Local vector current renormalisation factors at the values of μ used in our calculations for different schemes at the lattice spacings we use. R_c denotes that we take the ratio with the conserved current renormalisation in that scheme. The values for $Z_V^{\text{loc}}(\text{MOM})$ given here are the raw RI'-MOM number that we obtain multiplied by the $\overline{\text{MS}}$ conversion factors of Table 3.6.	87
3.8	1-link vector current renormalisation factors at all μ values considered for different schemes at the lattice spacings we use. R_c denotes that we take the ratio with the conserved current renormalisation in that scheme.	94
3.9	The ratio of renormalisation factors Z_V for the QCD + quenched QED case to the pure QCD case. These are for the local HISQ vector current calculated in the RI-SMOM scheme on gluon field configuration sets listed in column 1 and at μ values listed in column 2 (and at a valence quark mass of m_l).	99

- 3.10 The parameters of the ensembles used in the calculation of the tensor current renormalisation factors in the RI-SMOM and RI'-MOM schemes. On each ensemble we calculate the renormalisation factor at three masses: the sea light quark mass and two and three times that mass. The values are then extrapolated to zero valence mass. The lattice spacings quoted here are sea mass independent and are the spacings for an ensemble with the same β but physical sea quark masses. Note that this definition of the lattice spacing differs from that used for the calculation of the mesonic properties we study here. To distinguish the two definitions we denote the sea mass independent lattice spacing \tilde{a} while the sea mass dependent spacing is denoted a 108
- 3.11 Values for the conversion factor between RI-SMOM and $\overline{\text{MS}}$ and the $\overline{\text{MS}}$ running to a scale of 2 GeV for different values of μ . The three-loop tensor anomalous dimension can be found in [100]. All of these values are correlated through their use of a common determination of α_s [27]. 110
- 3.12 RI-SMOM Z_T value on the ensembles in Table 3.10 at different μ values along with the correlation matrices for these different μ values on a given Set. In most cases it can be seen that these correlations are reasonably strong. 111
- 3.13 RI'-MOM equivalents of the RI-SMOM values in Table 3.12. The correlations are not as strong in this case, perhaps because of the slightly larger valence mass dependence of the RI'-MOM results. 111
- 4.1 Details of the lattice ensembles and calculation parameters used. Each lattice spacing can be determined in fm by using $w_0 = 0.1715(9)$ fm. L_s and L_t are the lattice spatial and temporal extents in lattice units. The column headed $N_{\text{cfg}} \times N_t$ shows both the number of configurations used in pure QCD and the number of time sources. $N_{\text{cfg,QED}}$ refers to the number of configurations (and time sources) used in QCD+QED calculations. 118
- 4.2 The η_c and J/ψ masses and their difference ($a\Delta M_{\text{hyp}}$) in pure QCD on each set in lattice units. The pseudoscalar and vector correlator fits have been performed separately and the correlations between aM_{η_c} and $aM_{J/\psi}$ have therefore been ignored because they have little impact. 125

4.3	QCD+QED η_c and J/ψ masses in lattice units and the QED correction to the hyperfine splitting, presented as the ratio of the QCD+QED result to the pure QCD one. Here only the configurations used in the QCD+QED calculation are used for the pure QCD result in the ratio so that correlations in the data can be used.	128
4.4	Error budget for our final result for the charmonium hyperfine splitting including quenched QED corrections. The uncertainties shown are given as a percentage of the final result. The largest uncertainties are clearly due to the determination of the lattice spacing.	132
4.5	Lattice data and electromagnetic corrections for the J/ψ and η_c decay constants. The electromagnetic corrections for $f_{J/\psi}$ do not include the corrections to Z_V . We take these from [2], using the $\mu = 2$ GeV values except on sets 1-3 which we have calculated for this work as 0.999544(14).	135
4.6	Vector renormalisation constants in the RI-SMOM scheme at both 2 and 3 GeV along with the QED correction at 2 GeV. Most of these values are taken from [2].	135
4.7	Error budget of the J/ψ and η_c decay constants. In both cases the largest uncertainty is contributed by the uncertainty on the value of w_0 , as has also been seen to be the case for the hyperfine splitting. The contributions from different sources are very similar between the two decay constants. The most significant difference between the error budgets is the presence of Z_V in the J/ψ case. This uncertainty has been greatly reduced from the work of [76] by using the RI-SMOM results of [2].	141
4.8	Parameters of the ensembles on which we calculate the J/ψ tensor decay constant. Some of these ensembles are the same as those in Table 3.10, but here we use a different definition of the lattice spacing that depends on the sea quark masses. .	143
4.9	Data for the J/ψ tensor decay constant on each of the ensembles in Table 4.8 in lattice units before multiplication by the tensor renormalisation factor and the ratio of the tensor and vector J/ψ decay constants (again, before renormalisation). The vector decay constant numbers can be found in Table 4.5 in Section 4.5. . .	143

4.10	Error budget for the ratio of the J/ψ vector and tensor decay constants. The “Missing α_s^3 ” and “Condensates” error contributions come from the terms in the fit that the Z_T “correction” discussed in the text. Combined, these give the largest contribution to the total uncertainty.	149
4.11	Z_T values in the RI-SMOM scheme run to a renormalisation scale of the b quark running mass in the $\overline{\text{MS}}$ scheme. The notation $Z_T(\mu_1 \mu_2)$ indicates that Z_T has been calculated in the RI-SMOM scheme at a scale of μ_1 and then converted to the $\overline{\text{MS}}$ scheme and run to a scale of μ_2 . The first set of results are given without any correction for nonperturbative effects. The second set have a correction applied calculated from continuum fits to the J/ψ vector to tensor decay constant ratio. The superscript c indicates that these are corrected values, i.e. the correction to remove condensate contamination has been applied.	150
4.12	Correlation matrix of the corrected Z_T values from Table 4.11. These correlations are large in part due to the correlation of the perturbative matching and running calculations that have been applied.	150
4.13	Vector current time moment data on the ensembles in Table 4.1. The values given are $(G_n/Z_V^2)^{1/(n-2)}$ in lattice units.	152
4.14	(QCD+QED)/QCD values for the time moments on a subset of the ensembles in Table 4.1. The values given are $(G_n/Z_V^2)^{1/(n-2)} [(QCD+QED)/QCD]$	152
4.15	The first four time moments calculated from our lattice data in the continuum limit compared with the results extracted from experiment in [129]. Agreement at the level of a single standard deviation is seen for all time moments.	152
4.16	Error budget for various time moments as calculated from an extrapolation in the (rooted) moment multiplied by the J/ψ mass.	156
4.17	Values of a_μ^c and the electromagnetic correction $R_{\text{QED}}^{(0)} [a_\mu^c]$ used in the fit shown in Fig. 4.23. The uncertainties quoted are correlated through w_0 across all ensembles and, to a lesser extent, Z_V across those sharing the same β	158

4.18	Error budget for the direct determination of the charm quark connected HVP contribution to the anomalous magnetic moment of the muon. Factors of the lattice spacing cancel in the raw data we use in the extrapolation but w_0 and w_0/a still contribute to the uncertainty through their use in the calculation of mistuning parameters.	160
5.1	Parameters of the ensembles used in this analysis and the heavy valence masses used on each of the ensembles in lattice units. 165	
5.2	Vector and pseudoscalar heavyonium ground state masses and hyperfine splitting on the ensembles detailed in Table 5.1 with the valence masses given there. . . .	167
5.3	Error budget for the bottomonium hyperfine splitting. The contributions from the continuum extrapolation are separated into pieces that are independent of the heavy mass and dependent on it (c_{0j} and c_{ij} and $i \neq 0$). There is also an uncertainty contribution from the physical M dependence terms which are not multiplied by a power of am_h	171
5.4	Vector and pseudoscalar heavyonium ground state decay constants on the ensembles detailed in Table 5.1 with the valence masses given there.	172
5.5	Error budgets for the Υ and η_b decay constants.	175
5.6	Time moments on the ensembles and valence masses given in Table 5.1. These are $G_n^{1/(n-2)}$ as in Table 4.15.	177
5.7	Comparison of time moments extracted from our fits and those extracted from experiment in [151] for the first four moments.	180
6.1	RI-SMOM to $\overline{\text{MS}}$ matching factor coefficients and shifts in the α_s^2 coefficient due to the presence of physical charm quarks in the sea and the appropriate $\alpha_s^{\overline{\text{MS}}}$. The penultimate column contains the $\overline{\text{MS}}$ mass running to 3 GeV. The value given for c_3 was not used in the initial mass calculations presented in [1] and Section 6.2.2 which is indicated by the asterisk. These values were computed recently in [97, 154].	186

6.2	Error budget, giving a breakdown of the uncertainties in the c and s quark masses in the $\overline{\text{MS}}$ scheme at a scale of 3 GeV obtained from the fits described in the text. All the uncertainties are given as a percentage of the final answer. The condensate uncertainties include all the uncertainties from that term in the fit function, which also allows for discretisation and m_{sea} effects.	190
6.3	The electromagnetic correction to Z_m for different values of μ and different lattice spacings are shown in the third column, The fourth column is the QED component of the RI-SMOM to $\overline{\text{MS}}$ matching for each μ and the fifth is the QED mass running to a reference scale of 3 GeV.	193
6.4	Error budget for the calculation of the charm quark mass in the $\overline{\text{MS}}$ scheme at a scale of 3 GeV using RI-SMOM as an intermediate scheme. The listed contributions have the same meaning as those in [1] except for the “QED effect” which comes from the continuum extrapolation shown in Fig. 6.4.	195
6.5	The charm quark mass determined from various vector time moments at scales of the charm mass itself and 3 GeV.	196

Chapter 1

Theoretical Foundations

The Standard Model of particle physics is a specific example of a quantum field theory, obeying the constraints of unitarity and Lorentz invariance. It comprises possibly the most verified theoretical construction in physics and has withstood decades of rigorous testing across a huge range of observable processes. While this success has validated the theoretical tools and paradigms developed and utilised during the compositional phases of the Standard Model there are still unanswered questions that may seem to lie within the purview of particle physics arising both from a lack of explanation of certain experimental observations on the macroscopic scales of astronomy (dark matter) and technical concerns about the soundness of the structure from a theoretical perspective. In addition there are a few more recent tensions with experimental results that have not yet reached the level of statistical incompatibility. The Standard Model does provide a candidate particle to explain the amount of dark matter detected in astronomical observations. In addition, from the point of view established following the work of Wilson the presence of a scalar field introduces difficulties due to presumed higher dimensional operators from new physics giving uncontrolled large contributions to the Higgs mass (known as the hierarchy problem). There also a few tensions between experimental measurements of flavour physics observables and their theoretical predictions from the Standard Model. In particular, these are LHCb measurements of the ratio of semileptonic B meson decay rates with differing final state leptons [4, 5, 6, 7, 8] and the high precision measurement of the anomalous magnetic moment of the muon [9].

With the discovery of the Higgs boson by the ATLAS [10] and CMS [11] experiments the experi-

mental validation of all components of the Standard Model is now complete and a major focus of experimental effort is the discovery of beyond the Standard Model (BSM) physics. This proceeds in, broadly, two ways. One is known as the energy frontier and involves extending the energy reach of experiments to directly search for new physics appearing beyond some threshold. The other is the precision frontier. In this case physics at high energies are probed through quantum vacuum effects. As there can be substantial suppression of high energy effects this involves the comparison of experiment and Standard Model theory to high precision to search for deviations. Where experiment can provide high precision it is therefore essential for theoretical calculations to push for the same level of precision. Perturbative calculations can systematically reach high precision through the inclusion of higher order terms. While this is technically challenging these calculational programmes have been a huge success. A problem arises when, often inevitably, nonperturbative effects from the strong force arise in calculations. It is therefore vital to have a method of calculation in this regime with fully controlled and quantifiable uncertainties that offers the possibility of systematic improvement. Lattice QCD is this method.

Lattice QCD simplifies the exact calculations necessary through the approximation of spacetime as a lattice, rendering the number of degrees of freedom finite and making the problems numerically tractable. In many cases the limiting factor on the precision of the calculation becomes computational power; a resource that continues to undergo rapid expansion. This is not to say that lattice QCD calculations are simple and active work in the development and application of new techniques and strategies is critical for further advances in the field.

With lattice calculations reaching and surpassing the 1% landmark efforts are being made in several directions to fully control such high precision and this work represents some contribution to that goal. This opening chapter outlines some of the foundational theory of the Standard Model largely following the treatments of [12, 13, 14, 15]. This is followed by an introductory chapter on lattice QCD with the remaining chapters providing details of research in the use of momentum subtraction renormalisation schemes and properties of heavyonium mesons using the highly improved staggered quark (HISQ) action.

1.1 Quantum fields

A relativistic theory must be invariant under the actions of the group of Lorentz transformations. In order to ensure Lorentz invariance the Lagrangian of the Standard Model is constructed from fields lying in unitary irreducible representations of the Poincaré group (Lorentz group plus

translations). These representations can be classified by their mass and spin.

A simple enumeration of the irreducible representations (irreps) that classify particle states can be obtained through a study of the Lorentz group, and more specifically an infinitesimal Lorentz transformation. If such a Lorentz transformation is denoted $\Lambda^{\mu\nu}$ then it may be written as $\delta^{\mu\nu} + \delta\omega^{\mu\nu}$. A unitary operator implementing a Lorentz transformation on a state in a Hilbert space $U(\Lambda)$ may then be written $U(\Lambda) = I + (i/2)\delta\omega_{\mu\nu}M^{\mu\nu}$ where the generators $M^{\mu\nu}$ can be decomposed into more familiar operators $J_i = \frac{1}{2}\epsilon_{ijk}M^{jk}$ (angular momentum) and $K_i = M^{i0}$ (boosts). In terms of these operators the Lie algebra of the Lorentz group is

$$\begin{aligned} [J_i, J_j] &= i\epsilon_{ijk}J_k, \\ [J_i, K_j] &= i\epsilon_{ijk}K_k, \\ [K_i, K_j] &= -i\epsilon_{ijk}J_k. \end{aligned} \tag{1.1}$$

(The exponentiation of the generators of the Lorentz algebra only generates the elements of the group connected to the identity. Time reversal and parity transformations are also needed to generate the full group.) By constructing the operators $J_i^+ = \frac{1}{2}(J_i + iK_i)$ and $J_i^- = \frac{1}{2}(J_i - iK_i)$ this can be written as

$$\begin{aligned} [J_i^-, J_j^-] &= i\epsilon_{ijk}J_k^-, \\ [J_i^+, J_j^+] &= i\epsilon_{ijk}J_k^+, \\ [J_i^-, J_j^+] &= 0, \end{aligned} \tag{1.2}$$

which reveals two commuting $\mathfrak{su}(2)$ subalgebras. Representations of $SU(2)$ are labelled by the highest eigenvalue of one of the three group generators, typically chosen to be J_3 . The eigenvalues of J_3 must be of the form $j = \ell/2$ where ℓ is an integer. The representations are therefore labelled by an integer or half-integer n . It follows that the irreps of the Lorentz group may be labelled by a pair of such values (n, n') . Hermitian conjugation will swap this labelling $(J^+)^\dagger = J^-$. $SO(3)$ is a subgroup of the Lorentz group and any representation of the latter therefore gives a representation of the former which provides a definition of the spin of the representation. The number of components of a representation is $(2n+1)(2n'+1)$. For example, $(0,0)$ corresponds

to a state of spin 0 (scalar) and both (1/2,0) and (0,1/2) correspond to spin 1/2 states, which have two components (\pm spin). The (1/2,1/2) representation corresponds to a spin 1 (vector) state.

A general field $\phi_a(x)$ will transform under a Lorentz transformation according to

$$U(\Lambda)^{-1}\phi_a(x)U(\Lambda) = L_a^b(\Lambda)\phi_b(\Lambda^{-1}x), \quad (1.3)$$

with $L_a^b(\Lambda)$ a matrix in the appropriate representation of the Lorentz group.

A spin 1/2 spinor field in the (1/2,0) representation is a two-component object known as a left-handed Weyl field. It is related to the right-handed (0,1/2) field via Hermitian conjugation. Writing right-handed Weyl fermions with a dot over the index ($\psi_{\dot{a}}$) we can examine the difference between these two representations through their Lorentz transformation properties. An element of the Lorentz group can be obtained through the exponentiation of the generators $\Lambda = \exp(i\theta_j J_j + i\beta_j K_j)$ which, upon expansion about the identity, gives $\Lambda = 1 + i\theta_j J_j + i\beta_j K_j$. The matrices J_j and K_j in the (1/2,0) representation must be 2×2 . The Pauli matrices are 2×2 matrices that satisfy the $\mathfrak{su}(2)$ Lie algebra. We may therefore identify $J_i^- = \frac{1}{2}\sigma_i$ and take $J^+ = 0$. We can take these to be the other way around for the (0,1/2) representation. This gives the following:

$$\begin{aligned} \left(\frac{1}{2}, 0\right) : J_i &= \frac{1}{2}\sigma_i, K_i = \frac{i}{2}\sigma_i \\ \left(0, \frac{1}{2}\right) : J_i &= \frac{1}{2}\sigma_i, K_i = -\frac{i}{2}\sigma_i. \end{aligned} \quad (1.4)$$

The left and right handed spinors therefore act in the same way under rotations but in the opposite sense under boosts. As they are both spin 1/2 particles they are expected to behave the same under rotations and the behaviour under boosts suggests that in some sense their spins are aligned in opposite directions.

If a mass term is to be included in a Lagrangian then a Lorentz invariant quadratic of the fields must be created. Terms such as $\psi_{\dot{a}}^\dagger \psi^{\dot{a}}$ are not Lorentz invariant¹; a term compensating for the

¹The indices on ψ are raised using the antisymmetric tensor: $\psi^{\dot{a}} = \epsilon^{\dot{a}\dot{b}}\psi_{\dot{b}}$.

boost part of the transformation is needed. This is achieved with the construction $\psi_a^\dagger \psi_{\dot{a}}$ and its Hermitian conjugate $\psi_{\dot{a}}^\dagger \psi_a$. This leads to the Dirac mass term $m(\psi_a^\dagger \psi_{\dot{a}} + \psi_{\dot{a}}^\dagger \psi_a)$ which can be written in terms of a single object: the Dirac spinor

$$\Psi = \begin{pmatrix} \psi^a \\ \xi_b \end{pmatrix}. \quad (1.5)$$

Defining the Dirac adjoint as $\bar{\Psi} \equiv (\xi_b^\dagger \psi_a^\dagger)$ the Dirac mass term is $m\bar{\Psi}\Psi$.

A kinetic term may be written with a single derivative as $\bar{\Psi}i\gamma^\mu\partial_\mu\Psi$. This comes from the Lorentz invariant term

$$i\xi_b^\dagger\sigma^\mu\partial_\mu\xi_b + i\psi_a^\dagger\bar{\sigma}^\mu\partial_\mu\psi_a, \quad (1.6)$$

with $\sigma^\mu = (1, \sigma)$ and $\bar{\sigma}^\mu = (1, -\sigma)$. Defining

$$\gamma^\mu = \begin{pmatrix} 0 & \sigma^\mu \\ \bar{\sigma}^\mu & 0 \end{pmatrix} \quad (1.7)$$

gives the kinetic term in terms of the Dirac field.

The Dirac γ matrices can be used to construct operators that project out the left or right handed components of the Dirac spinor. Starting with $\gamma^5 \equiv i\gamma^0\gamma^1\gamma^2\gamma^3$ we can define $P_R = \frac{1+\gamma^5}{2}$ and $P_L = \frac{1-\gamma^5}{2}$ which give

$$\begin{aligned} P_R \begin{pmatrix} \psi_a \\ \xi_b \end{pmatrix} &= \begin{pmatrix} 0 \\ \xi_b \end{pmatrix}, \\ P_L \begin{pmatrix} \psi_a \\ \xi_b \end{pmatrix} &= \begin{pmatrix} \psi_a \\ 0 \end{pmatrix}. \end{aligned} \quad (1.8)$$

The projection of the spin on to the direction of the momentum, the helicity, is given by the operator $\frac{\boldsymbol{\sigma}\cdot\mathbf{p}}{|\mathbf{p}|}$. If there is no mass term then left and right handed states are eigenstates of the helicity operator with eigenvalues of opposite sign. This can be seen from the massless Dirac

equation:

$$\begin{aligned}\sigma_\mu p^\mu \xi_{\dot{a}} &= 0, \\ \bar{\sigma}_\mu p^\mu \psi_a &= 0.\end{aligned}\tag{1.9}$$

1.1.1 Gauge fields

A spin 1 state will be embedded in a vector field in order to have the correct behaviour under $SO(3)$ but a massless spin 1 particle only has two degrees of freedom, and a massive one three, while a Lorentz vector has four. There must therefore be some redundancy in this embedding described through some relationship between the different components. This redundancy manifests itself through gauge invariance. The Lagrangian of a massless vector field is

$$\mathcal{L} = -\frac{1}{4}G_{\mu\nu}G^{\mu\nu},\tag{1.10}$$

for an antisymmetrised function of the vector field A_μ . Assume that there is a local symmetry transformation that leaves this Lagrangian invariant. A scalar or spinor field will transform according to

$$\phi^a(x) \rightarrow U^{ab}(x)\phi_b(x).\tag{1.11}$$

If U can be connected directly to the identity then an infinitesimal transformation may be written

$$U_{ab}(x) = \delta_{ab} - ig\theta^i(x)(T_i)_{ab} + \mathcal{O}(\theta^2).\tag{1.12}$$

We take the generators T (which are exponentiated to obtain group elements) to satisfy the commutation relations

$$[T^i, T^j] = if^{ijk}T_k,\tag{1.13}$$

which defines a Lie algebra with structure constants f^{ijk} . Choosing a Lie group is natural because

they correspond to differentiable manifolds and as such provide a positive real symmetric metric which gives a notion of an inner product required for unitarity. (Here, a gauge theory built on a Lie gauge group will be termed a Yang-Mills theory.) A gauge field $A_\mu^a(x)$ transforms as (suppressing the a index)

$$A_\mu(x) \rightarrow U(x)A_\mu(x)U^\dagger(x) + \frac{i}{g}U(x)\partial_\mu U^\dagger(x). \quad (1.14)$$

The covariant derivative is defined as $D_\mu = \partial_\mu - igA_\mu(x)$ which can be used to construct a field strength tensor (in analogy with the definition of the Riemann curvature tensor)

$$G_{\mu\nu}(x) \equiv \frac{i}{g}[D_\mu, D_\nu] = \partial_\mu A_\nu - \partial_\nu A_\mu - ig[A_\mu, A_\nu]. \quad (1.15)$$

The Lagrangian Eq. 1.10 is then invariant under gauge transformations. The invariance under the transformation of Eq. 1.14 indicates the redundancy in the embedding of a spin 1 state into a vector field as choosing a specific gauge amongst the orbit described by Eq. 1.14 will lead to a reduction in the number of degrees of freedom.

When a classical field is Fourier transformed the momentum space is written in terms of basis vectors $\epsilon_\mu^i(p)$, known as polarisation vectors. The equation of motion $\partial_\mu A^\mu = 0$ forces $p^\mu \epsilon_\mu^i(p) = 0$. With $p^2 = 0$ there are two independent polarisation vectors (with the appropriate gauge choice) while for $p^2 = m^2$ there are three. These polarisation vectors furnish infinite dimensional representations of the Poincaré group.

1.1.2 Vectors and spinors

The fact that a Lorentz vector lies in the $(1/2, 1/2)$ indicates that vectors can be written as bispinors. Defining Lorentz invariant spinor inner products with the totally antisymmetric ϵ tensors we have

$$\langle \lambda \xi \rangle = \epsilon^{ab} \lambda_a \xi_b, \quad [\lambda \xi] = \epsilon_{\dot{a}\dot{b}} \lambda^{\dot{a}} \xi^{\dot{b}}. \quad (1.16)$$

Momenta can be written as bispinors by using σ : $p^{a\dot{a}} \equiv \sigma_\mu^{a\dot{a}} p^\mu$. The determinant of $p^{a\dot{a}}$ is equal to the mass squared and is therefore 0 when p is lightlike. Such a matrix can be written as an outer product $p^{a\dot{a}} = \lambda^a \xi^{\dot{a}} = \lambda \rangle \xi$.

Polarisation bispinors are given in terms of some reference momentum q (with $q \cdot p \neq 0$) as $\epsilon_p^-(q) = \sqrt{2}p\rangle[q/[pq]$ and $\epsilon_p^+(q) = \sqrt{2}q[p/\langle qp]$.

Consider a 3-point amplitude between massless vector bosons. Labelling the legs 1, 2 and 3 momentum conservation gives $1\rangle[1+2][2+3]3 = 0$. Contracting with $\langle 1$ and $\langle 2$ leads to either $\langle 12\rangle = \langle 13\rangle = \langle 23\rangle = 0$ or $[12] = [13] = [23] = 0$ meaning that the 3-point amplitude can only depend on $\langle ij\rangle$ or $[ij]$.

The set of transformations that preserve the bispinor momentum $p^{a\dot{a}}$ (the little group transformations) are simple rescalings of the spinors ²

$$p\rangle \rightarrow zp\rangle, \quad [p \rightarrow \frac{1}{z}[p. \quad (1.17)$$

The consequence of this is that negative polarisations transform as z^2 and positive polarisations as z^{-2} . Therefore, for each vector boson entering an amplitude the number of angle brackets minus square brackets appearing in the amplitude must be 2 for a negative helicity boson and -2 for a positive helicity boson. The 3-point function is then determined up to a factor carrying a group index (a colour factor) C^{abc} by the helicities of the bosons entering the vertex.

Next, consider a 4-point amplitude. If the helicities are taken as $--++$, with all momenta directed towards the vertex so that this corresponds to two negative helicity bosons annihilating to two negative helicity bosons, then the little group scaling requires this amplitude to take the form

$$\mathcal{M}^{--++} = \langle 12\rangle^2[34]^2\mathcal{G}^{abcd}(s, t, u). \quad (1.18)$$

$\mathcal{G}^{abcd}(s, t, u)$ has been written as a function of the Mandelstam kinematic variables: $s = \langle 12\rangle[21]$, $t = \langle 14\rangle[41]$ and $u = \langle 13\rangle[31]$ ³. Dimensional analysis shows that \mathcal{G} has mass dimension -4. This inverse power scaling implies that \mathcal{G} has a pole as a function of the momenta. Unitarity requires poles to correspond to the exchange of an on-shell intermediate state $[12, 13]$. This intermediate state can be taken to be in the s, t or u channel and splits the 4-point function into two 3-points

²The little group is the subgroup of the Lorentz group that leaves a chosen momentum invariant. For a massless boson this momentum must be lightlike and the corresponding little group is ISO(2) which is the group of 2-dimensional Euclidean rotations and translations. This corresponds to rescaling by a complex number (the phase gives a rotation and the magnitude a translation).

³These are not independent variables; they satisfy $s + t + u = 0$.

with an internal on-shell propagator. The massless vector propagator is i/P^2 . Decomposing into the two 3-point amplitudes near the s pole

$$\lim_{s \rightarrow 0} s \mathcal{M}^{--++} = -C^{abe} C^{cde} \frac{\langle 12 \rangle^3}{\langle 2P \rangle \langle P1 \rangle} \frac{[34]^3}{[3P][P4]} = -C^{abe} C^{cde} \frac{\langle 12 \rangle^2}{\langle 41 \rangle} \frac{[34]^2}{[14]}, \quad (1.19)$$

where e is the group index for the intermediate boson. Eq. 1.19 implies $\lim_{s \rightarrow 0} st \mathcal{G}^{abcd} = -C^{abe} C^{cde}$. A similar analysis for the t and u channels (where there are two possible polarisation constructions) give

$$\begin{aligned} \lim_{t \rightarrow 0} ts \mathcal{G}^{abcd} &= C^{ade} C^{bce}, \\ \lim_{u \rightarrow 0} us \mathcal{G}^{abcd} &= C^{ace} C^{bde}. \end{aligned} \quad (1.20)$$

As s , t and u are not independent we can write

$$\mathcal{G}^{abcd} = \frac{1}{st} g^{abcd}(s/t) + \frac{1}{tu} g^{abcd}(u/t), \quad (1.21)$$

and Taylor expand

$$\mathcal{G}^{abcd} = \frac{1}{st} \sum_{n=0}^{\infty} a_n^{abcd} (s/t^n) + \frac{1}{tu} \sum_{n=0}^{\infty} b_n^{abcd} (u/t^n). \quad (1.22)$$

The limits from the analysis of \mathcal{G} imply $a_0^{abcd} = -C^{abe} C^{cde}$ and $b_0^{abcd} = -C^{ace} C^{bde}$ along with

$$C^{ade} C^{bce} = \lim_{t \rightarrow 0} \sum_{n=0}^{\infty} (a_n^{abcd} - (-1)^n b_n^{abcd}) (s/t)^n. \quad (1.23)$$

To avoid singularities $a_n^{abcd} = (-1)^n b_n^{abcd}$ and therefore

$$C^{ade} C^{bce} = a_0^{abcd} - b_0^{abcd} = -C^{abe} C^{cde} + C^{ace} C^{bde}. \quad (1.24)$$

That is, the C factors satisfy the Jacobi identity and are the structure constants of a Lie algebra. This analysis is somewhat lengthy but shows that if you wish to construct a field theory of self-interacting massless vector bosons then gauge theories based on Lie groups must be what you produce. The confinement seen in the strong force presumably comes from strong self-interactions implying that it can be described by a Yang-Mills theory, i.e. QCD. This conclusion, and QCD in particular, are supported by a wealth of phenomenological evidence at both high and low energies.

1.1.3 Spontaneous symmetry breaking

If only gauge invariant terms are allowed in the Lagrangian of a field theory then there can be no mass term for the gauge bosons. However, a term coupling a charged scalar field to a gauge field looks somewhat like a mass term. Through minimal coupling this term is (schematically)

$$(\partial_\mu \phi^* - ieA_\mu \phi^*)(\partial_\mu \phi + ieA_\mu \phi), \quad (1.25)$$

one part of which is $e^2 \phi^2 A_\mu^2$. If ϕ can dynamically acquire a vacuum expectation value (vev) of $v/\sqrt{2}$ then this is $(1/2)e^2 v^2 A_\mu^2$ and a mass term is achieved with only gauge invariant terms. The development of this expectation value is done through a potential term

$$m^2 \phi^2 - \frac{\lambda}{4} \phi^4. \quad (1.26)$$

If $m^2 > 0$ then the potential has a minimum at $2m^2/\lambda$ which provides a vev for the scalar at that value. This is the essence of the Higgs mechanism to be discussed in the context of the Standard Model in Section 1.4.

1.2 Quantisation through the path integral

Given a Lagrangian for a field theory the theory may be quantised by defining the path integral or, in analogy with statistical mechanics, partition function. The partition function is given by

$$Z[\phi] = \int \mathcal{D}\phi e^{iS[\phi]}, \quad (1.27)$$

where ϕ is used to generically denote all field content. The measure $\mathcal{D}\phi$ indicates a functional integral over all configurations of the fields (which depend on x). Matrix elements are then calculated as

$$\langle T\{\phi(x_1)\dots\phi(x_n)\} \rangle = \frac{\int \mathcal{D}\phi e^{iS[\phi]} \phi(x_1)\dots\phi(x_n)}{\int \mathcal{D}\phi e^{iS[\phi]}}. \quad (1.28)$$

These are the calculable quantities of the theory and observables should be extracted from them for comparison with experiment. When the fields involved are fermionic the integration is over Grassmann (anticommuting) numbers. Integration rules for such numbers may be written down by exploiting the fact that $\theta^2 = 0$ for a Grassmann θ . This allows the fairly simple expansion of functions such as exponentials. A very important class of integrals which can be evaluated analytically are Gaussian Grassmann integrals such as

$$\int d\bar{\theta}_1\dots d\bar{\theta}_n d\theta_1\dots d\theta_n e^{-\bar{\theta}_i A_{ij} \theta_j} = \det(A). \quad (1.29)$$

This is recognisable as the fermionic part of the partition function of a Yang-Mills theory coupled to fermions with $A = \not{D} - m$. Also of interest is the fermionic 2-point function, which can also be evaluated,

$$\int d\bar{\theta}_1 d\bar{\theta}_2 d\theta_1 d\theta_2 \bar{\theta}_1 \theta_2 e^{-\bar{\theta}_i A_{ij} \theta_j} = \det(A) A_{ij}^{-1}. \quad (1.30)$$

These evaluations becomes important when the path integral is tackled numerically and the fermionic variables have to be removed.

The term e^{iS} can be expanded and then, if the couplings entering the action are small, higher order terms in the couplings can be dropped. It is typical, for calculational purposes, to write this expansion in terms of Feynman diagrams where different terms are represented by the edges and vertices of a graph with rules to map between the two (an example is given in Section 1.5). This perturbation theory breaks down if the coupling becomes too large.

Often it is convenient to perform a Wick rotation $t \rightarrow it$ which renders the weight term in the path integral e^{-S} . This does not oscillate and has a damping effect away from the minimum (classical solution) of the action.

1.3 Renormalisation

The perturbative evaluation of the path integral generically leads to divergent integrals over internal momenta. While this seems fundamentally problematic the problem can actually be dealt with through a systematic procedure.

First the divergent integral is regulated in some manner in order to make it finite. The simplest method is to apply a cutoff to the momenta included in the integral. The integral can then be split into a finite part and a divergent part that depends on the regulator. A physically measurable quantity may then be chosen to absorb this divergence. These quantities are typically the masses and couplings of the theory.

Take for example a mass appearing in the Lagrangian. If we call this mass the bare mass and denote it m_0 then we can take it to be infinite and proportional to the experimentally measured renormalised mass m ; $m_0 = Z_m m$. Writing this factor as $Z_m = 1 + \delta_m$ gives $m_0 = m + \delta_m m$ with the divergent part contained in the counterterm δ_m . In so-called renormalisable theories, which include the Standard Model, the divergences at all orders can be absorbed into a finite number of parameters. A finite set of conditions are then required to determine the renormalisation factors. In momentum subtraction schemes these take the fairly natural form that certain correlation functions evaluated with renormalised parameters are equal to their tree-level (non-interacting) values. These schemes do not directly rely on perturbation theory and are therefore well suited to nonperturbative calculations.

The most common regularisation used in perturbative calculations is dimensional regularisation. This involves shifting the dimensionality of spacetime from 4 to $4 - \epsilon$ where ϵ need not be an integer. As the divergence of a momentum integral is dependent on the number of spacetime dimension minus the number of momentum powers in the denominator of the integrand, changing the dimension appropriately renders the integral finite. The momentum integrals are then performed and the result is given as a function of ϵ where the poles can clearly be identified as the divergent parts as $\epsilon \rightarrow 0$. These poles must then be absorbed into theory parameters. In perturbation theory this can be done by adding counter-terms to the Lagrangian which subtract away the divergence. These then generate extra Feynman diagrams.

There is not a unique way to do this; a specific choice defines a renormalisation scheme. The most commonly used scheme is modified minimal subtraction or $\overline{\text{MS}}$. This is a scheme defined within the perturbative calculational framework. The minimal subtraction scheme is defined so

that counterterms have no finite part. The $\overline{\text{MS}}$ scheme is a modification of this prescription for use with dimensional regularisation in which the $\ln(4\pi)$ and γ_E (the Euler-Mascheroni constant) factors that arise from the expansion of Γ functions from spherical integrals in arbitrary dimension are also removed.

Given that the action is dimensionless the mass dimension of a coupling such as that appearing in Eq. 1.15 is $(4-d)/2$ which is 0 for $d = 4$. In order to maintain this while varying the dimension an arbitrary parameter with dimensions of mass, μ , is introduced and the coupling rescaled:

$$g \rightarrow \mu^{\frac{4-d}{2}} g. \quad (1.31)$$

Both ϵ and μ are unphysical and physical results must not depend on them. The regulator is removed by taking the limit $\epsilon \rightarrow 0$ and μ is left as a choice in the final result. The requirement of μ independence leads to the renormalisation group equations.

1.3.1 The renormalisation group

As the results for physical observables must be independent of the renormalisation scale, given that it is an arbitrary choice, it must be that the bare parameters of the theory are also independent of μ . Taking the coupling of a theory g , renormalised in the $\overline{\text{MS}}$ scheme, as an example:

$$\mu \frac{d}{d\mu} g_0 = 0 = \mu \frac{d}{d\mu} (Z_g g). \quad (1.32)$$

Z_g is calculated in perturbation theory and is generally μ dependent. This means that the renormalised coupling g must also be μ dependent in such a way as to cancel that of Z_g . The function $\mu(d/d\mu)g$ is known as the β function and gives the running of g with μ . The same relation holds for other parameters such as the mass, and for any operator written in terms of bare fields and parameters. This defines the anomalous dimension of an operator

$$\mu \frac{d}{d\mu} \mathcal{O} = \gamma_{\mathcal{O}} \mathcal{O}. \quad (1.33)$$

These are known as anomalous dimensions as they quantify the deviation of the scaling behaviour of an operator from that in the classical theory. A classical correlation function can only depend

on powers of the quantities in the Lagrangian with the sum of the powers multiplied by the scaling dimension of the quantity giving the mass dimension of the correlation function. In the quantum theory the correlation function may also depend on the renormalisation scale μ to some power γ . If the correlation function G_n has mass dimension n then it now scales as

$$G_n \rightarrow \mu^{n-\gamma} G_n, \quad (1.34)$$

where γ is the anomalous dimension.

1.4 The Standard Model

The Standard Model consists of the union of the theory of the electroweak interaction as an $SU(2) \times U(1)$ gauge theory [16, 17, 18] with the gauge group being broken through the Higgs mechanism to give the weak bosons masses [19, 20, 21] and the strong force described by an $SU(3)$ gauge theory.

The gauge group of the Standard Model (SM) is $SU(3) \times SU(2) \times U(1)$. The fermion content is broadly classified into quarks and leptons (colour charged and uncharged). All these fermions are in the $(1/2, 0) \oplus (0, 1/2)$ representation of the Lorentz group (Dirac). The left handed leptons and quarks sit in doublets in the fundamental representation of $SU(2)$. The lepton pairs consist of an electron like particle and a corresponding neutrino and the quark doublets are formed by pairs of quarks with differing electromagnetic charge:

$$\begin{pmatrix} \nu_L^e \\ e_L \end{pmatrix} \quad \begin{pmatrix} \nu_L^\mu \\ \mu_L \end{pmatrix} \quad \begin{pmatrix} \nu_L^\tau \\ \tau_L \end{pmatrix} \quad \diamond \quad \begin{pmatrix} u_L \\ d_L \end{pmatrix} \quad \begin{pmatrix} c_L \\ s_L \end{pmatrix} \quad \begin{pmatrix} t_L \\ b_L \end{pmatrix} \quad (1.35)$$

The right handed fermions are all singlets of $SU(2)$ (the right handed neutrino has not been observed and its existence depends on whether the neutrino mass is Majorana or Dirac). It is this asymmetry between the left and right handed particles that leads to the observed parity violation in the weak interaction [22]. All the quarks also lie in the fundamental of $SU(3)$ giving them one of three charges: red, green or blue. The hypercharges (charges under $U(1)$) of the fermions are collected in Table 1.1. The hypercharges repeat across the generations.

Table 1.1: Hypercharges of the Standard Model fermion fields.

	$\begin{pmatrix} \nu_L \\ e_L \end{pmatrix}$	e_R	ν_R	$\begin{pmatrix} u_L \\ d_L \end{pmatrix}$	u_R	d_R
hypercharge	$-\frac{1}{2}$	-1	0	$\frac{1}{6}$	$\frac{2}{3}$	$-\frac{1}{3}$

A scalar doublet with hypercharge $1/2$ and transforming in the fundamental of $SU(2)$ is included in the theory. Denoting this field H , quadratic and quartic terms are included in the Lagrangian:

$$\mathcal{L}_{V_H} = m^2 H^\dagger H - \lambda (H^\dagger H)^2, \lambda > 0. \quad (1.36)$$

Due to the shape of this potential (resulting from the different signs of the two terms) the H field spontaneously acquires a vacuum expectation value (vev) and breaks the $SU(2) \times U(1)$ symmetry to just $U(1)$. This is the Higgs field.

Due to the coupling of this Higgs field to the $SU(2) \times U(1)$ gauge bosons the Higgs vev gives rise to mass terms for what are now the W and Z bosons without breaking the gauge invariance of the Lagrangian. The fermions are given masses through Yukawa couplings ($\bar{\psi}_L H \psi_R$ ⁴) to the Higgs field.

The gauge field content before symmetry breaking consists of the eight gluons in the adjoint representation of $SU(3)$ which are not charged under $U(1)$. The $U(1)$ gauge field is denoted B_μ . The three $SU(2)$ gauge bosons are charged differently under $U(1)$: $+1$, -1 and 0 for the W^1 , W^2 and W^3 respectively. Symmetry breaking mixes the $W^{1,2,3}$ and the B_μ to leave the W^\pm and Z bosons and the photon.

When the SM Lagrangian is written in a basis in which the quark masses are diagonal then a matrix in flavour space is introduced in interaction terms between the W bosons and quarks. For example:

$$\frac{e}{\sqrt{2} \sin(\theta_w)} W_\mu^+ \bar{u}_L^i \gamma_\mu V^{ij} d_L^j. \quad (1.37)$$

⁴This term is gauge invariant due to the $SU(2)$ doublet natures of the left handed fermion field and the Higgs field.

V is the Cabibbo-Kobayashi-Maskawa (CKM) matrix. The moduli of the elements are measured from various processes and display a clear structure. The diagonal elements are largest with values decreasing away from the diagonal. This means that transitions between quarks of different generations are suppressed. The CKM matrix in the Standard Model is unitary by construction and studies of the unitarity of the experimentally measured matrix are therefore an avenue for BSM searches. Lattice QCD provides important contributions to these efforts by calculating the form factors that enter the theoretical determinations of weak meson decays.

To summarise the particles of the Standard Model along with their masses and electromagnetic charges (in units of the proton charge) are given in Table 1.2. The masses are taken from the PDG [23]. For the quark masses the $\overline{\text{MS}}$ masses at the chosen scale of the PDG are given, except for the top quark for which the pole mass⁵ is given. Lattice determinations, which are included in the PDG average, can provide considerably more precise results than those given in Table 1.2 as shown in Chapter 6. (The PDG average weights different determinations differently.)

⁵The mass that gives rise to a pole in the fermion propagator. This can be measured for the top quark as it is so heavy that it decays before binding into a hadron.

Table 1.2: Masses and electromagnetic charges of the Standard Model particles as measured by experiment [23].

Particle	Mass [GeV]	Charge
W^\pm	80.379(12)	\pm
Z	91.1876(21)	0
Photon (γ)	0	0
Gluon	0	0
Higgs boson (H)	125.10(14)	0
Electron (e)	$0.5109989461(31) \times 10^{-3}$	-1
Muon (μ)	$105.6583745(24) \times 10^{-3}$	-1
Tau (τ)	1.77686(12)	-1
Electron neutrino (ν_e)	< 2 eV	0
Muon neutrino (ν_μ)	$\lesssim 1$ eV	0
Tau neutrino (ν_τ)	< 0.19 MeV	0
Up (u)	$2.16^{+0.49}_{-0.26} \times 10^{-3}$	+2/3
Down (d)	$4.67^{+0.48}_{-0.17} \times 10^{-3}$	-1/3
Strange (s)	$93^{+11}_{-5} \times 10^{-3}$	-1/3
Charm (c)	1.27(2)	+2/3
Bottom (b)	$4.18^{+0.03}_{-0.02}$	-1/3
Top (t)	172.9(4)	+2/3

1.5 Perturbative approaches to QCD

The SU(3) part of the Standard Model, QCD, has a history of great success in describing the varied phenomena of the strong interaction. As a stand alone SU(3) gauge theory, as it will be treated for the majority of this work, it is described by the simple Lagrangian

$$\mathcal{L}_{\text{QCD}} = \sum_f \bar{\psi}_f (i\not{D} - m)\psi_f - \frac{1}{4}G^{\mu\nu}G_{\mu\nu}, \quad (1.38)$$

where the fermion fields are in the fundamental representation of SU(3), as already stated.

The following vertices and Feynman rules can be extracted from the Lagrangian Eq. 1.38:

The image shows three Feynman diagrams with their corresponding mathematical expressions:

- Top diagram:** A vertex where two fermion lines (solid lines with arrows) meet at a point, and a gluon line (wavy line) extends from the vertex. The expression is $-ig\gamma_\mu t^a$.
- Middle diagram:** A three-gluon vertex where three gluon lines (wavy lines) meet at a central point. The momenta are labeled k_1 , k_2 , and k_3 . The expression is $-gf^{abc}[g^{\mu\nu}(k_1 - k_2)^\rho + g^{\nu\rho}(k_2 - k_3)^\mu + g^{\rho\mu}(k_3 - k_1)^\nu]$.
- Bottom diagram:** A four-gluon vertex where four gluon lines (wavy lines) meet at a central point. The momenta are labeled k_1 , k_2 , k_3 , and k_4 . The expression is $-ig^2[f^{abc}f^{cde}(g^{\mu\rho}g^{\nu\sigma} - g^{\mu\sigma}g^{\nu\rho}) + f^{ace}f^{bde}(g^{\mu\nu}g^{\rho\sigma} - g^{\mu\sigma}g^{\rho\nu}) + f^{ade}f^{bce}(g^{\mu\nu}g^{\sigma\rho} - g^{\mu\rho}g^{\sigma\nu})]$.
- Bottom-most diagram:** A fermion propagator consisting of a solid line with an arrow pointing to the right, labeled with momentum k . The expression is $\frac{i}{\not{k} - m}$.

$$\frac{\text{wavy line}}{k} = \frac{-g^{\mu\nu}}{k^2} - \frac{(\xi - 1)k^\mu k^\nu}{k^4}$$

The t^a are elements of the SU(3) Lie algebra. These rules are given in the so-called R_ξ gauge which parameterises the gauge with ξ . A choice of $\xi = 1$ corresponds to Feynman gauge and $\xi = 0$ to Landau gauge. A calculation of the 1-loop gluon vacuum polarisation, quark self-energy and quark-gluon vertex leads to an expression for the QCD β function that depends on the number of fermions in the theory n_f (and the number of colours N_c) [24, 25]

$$\frac{\partial g}{\partial \log(\mu)} \equiv \beta_{\text{QCD}}(g) = \frac{g^3}{16\pi^2} \left(-\frac{11}{3}N_c + \frac{2}{3}n_f \right). \quad (1.39)$$

Clearly the sign is of great importance and for QCD within the standard model ($N_f = 6$ and $N_c = 3$) it is negative. (This is just the 1-loop expression but it is known through five loops with no change in the qualitative picture [26].) This means that the strength of the QCD coupling will decrease with increasing energy, or increase with decreasing energy. This is shown in Fig. 1.1 using the four-loop β function and the value of α_s in the $\overline{\text{MS}}$ scheme at 5 GeV from [27]. The consequences of this are profound for both the phenomenology of QCD and the tools needed for the extraction of that phenomenology. The growth of the QCD coupling at low energies means that QCD perturbation theory will break down in an energy regime relevant to hadronic physics. Indeed, it means that the degrees of freedom at low energy appear different to the quark degrees of freedom present in Eq. 1.38. One method of dealing with this is to separate the high and low energy regimes in the effective field theory sense and work with a theory that explicitly works with the observed degrees of freedom. In the case of QCD this can be done with chiral perturbation theory.

1.5.1 Correlator time moments

The quark loop contribution to the vacuum polarisation (hadronic vacuum polarisation or HVP) will be of some interest in this work. Fig. 1.5.1 gives a depiction of this contribution. The vacuum polarisation function

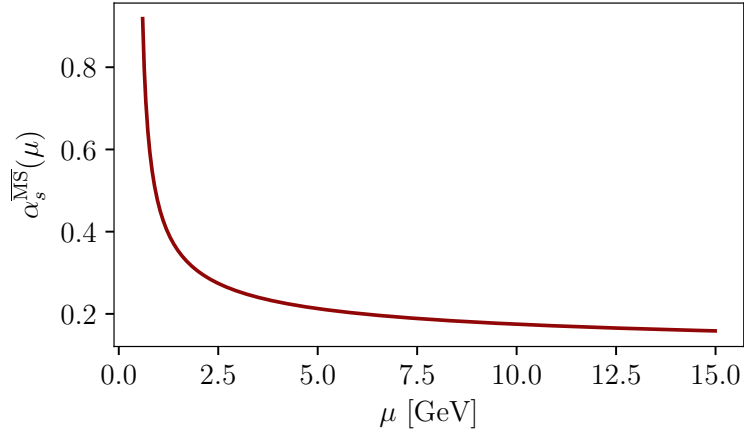


Figure 1.1: The running of the strong coupling in the $\overline{\text{MS}}$ scheme with the scale μ . The four-loop QCD β function is used for the calculation. This clearly shows the sharp growth at low μ values.

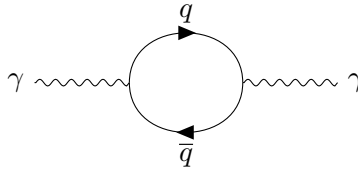


Figure 1.2: Feynman diagram of the quark loop contribution to the vacuum polarisation of the photon.

$$\begin{aligned}\Pi^{\mu\nu}(q^2) &\equiv Q^2 \int d^4x e^{iq \cdot x} \langle T \{ J^\mu(x) J^\nu(0) \} \rangle, \\ J^\mu(x) &= \bar{\psi}(x) \gamma^\mu \psi(x),\end{aligned}\tag{1.40}$$

can be tackled perturbatively if q^2 is large enough. The hadronic vacuum polarisation tensor in Eq. 1.40 can be Lorentz decomposed into $\Pi^{\mu\nu}(q^2) = (q^2 g^{\mu\nu} - q^\mu q^\nu) \Pi(q^2)$.

Time moments, labelled by a nonzero integer k , can be defined in terms of integrals over a normalised cross-section R :

$$\mathcal{M}_k = \int \frac{ds}{s^{k+1}} R(s), \quad (1.41)$$

with $R(s) = \sigma(e^+e^- \rightarrow \text{hadrons})/\sigma_{\text{pt}}$ and $\sigma_{\text{pt}} = 4\pi\alpha^2/3s$. An application of the optical theorem relates this cross-section to the imaginary part of the vacuum polarisation function Π : $12\pi\text{Im}[\Pi(q^2 = s)]$.

The reason these are referred to as time moments here is that they can be related to a sum over the current-current correlation function at zero spatial momentum weighted by a corresponding power of the time. This is because

$$\mathcal{M}_k = \frac{12\pi^2}{k!} \left(\frac{d}{dq^2} \right)^k \Pi(q^2)|_{q^2=0}. \quad (1.42)$$

The perturbative results for these moments (which can only be used for heavy quarks) depend on the quark mass, and in this way the experimental data for e^+e^- to various hadrons can be used, in conjunction with high order perturbative calculations, to extract the values of quark masses to high precision.

For future use a summary of the current status of the perturbative calculation of QCD time moments is given here. The pseudoscalar time-moments (in which $J(x) = \bar{\psi}(x)\gamma_5\psi(x)$ in Eq. 1.40) are known analytically through $\mathcal{O}(\alpha_s^3)$ up to $k = 4$ [28]. However, for the vector time-moments the $\mathcal{O}(\alpha_s^3)$ term for $k = 4$ is only known numerically [29]. The precision is good enough that this is not a concern. Writing the perturbative and kinematic threshold expansions of the vacuum polarisation function as

$$\Pi_S(q^2) = \frac{3}{16\pi^2} \sum_{k=1}^{\infty} C_{k,S} \left(\frac{q^2}{4m^2} \right)^k, \quad (1.43)$$

where S labels whether the pseudoscalar p or vector v vacuum polarisation is being considered and

$$C_{k,S} = C_{k,S}^{(0)} + \frac{\alpha_s(\mu)}{\pi} C_{k,S}^{(1)} + \left(\frac{\alpha_s(\mu)}{\pi} \right)^2 C_{k,S}^{(2)} + \dots \quad (1.44)$$

Table 1.3: Coefficients in the perturbative expansion of pseudoscalar and vector time moments from [28] and [29].

k	$C_{k,p}^{(0)}$	$C_{k,p}^{(1)}$	$C_{k,p}^{(2)}$	$C_{k,p}^{(4)}$	$C_{k,v}^{(0)}$	$C_{k,v}^{(1)}$	$C_{k,v}^{(2)}$	$C_{k,v}^{(4)}$
1	1.3333	3.1111	0.1154	-1.2224	1.0667	2.5547	2.4967	-5.6404
2	0.5333	2.0642	7.2362	7.0659	0.4571	1.1096	2.7770	-3.4937
3	0.3048	1.2117	5.9992	14.5789	0.2709	0.5194	1.6388	-2.8395
4	0.2032	0.7128	4.2670	11.3419	0.1847	0.3021	0.7956	-3.349(11)

Due to the derivative and evaluation at $q^2 = 0$ in the definition of the time moments it is the k^{th} coefficient C_k that is important for the k^{th} moment. The numerical values of these coefficients are given in Table 1.3.

This is the perturbative expansion if the scale is chosen to be the quark mass in which case logarithmic terms vanish. Given that the charm quark mass is quite low it is sometimes desirable to evaluate the perturbative expansion at a scale higher than the quark mass in which case the logarithmic terms are required. We expand Eq. 1.44 to include logarithmic terms with $l_m \equiv \log(m^2(\mu)/\mu^2)$:

$$C_{k,S} = C_{k,S}^{(0)} + \frac{\alpha_s(\mu)}{\pi} \left(C_{k,S}^{(1)} + C_{k,S}^{(1,1)} l_m \right) + \left(\frac{\alpha_s(\mu)}{\pi} \right)^2 \left(C_{k,S}^{(2)} + C_{k,S}^{(2,1)} l_m + C_{k,S}^{(2,2)} l_m^2 \right) + \dots \quad (1.45)$$

The necessary coefficients are given in Table 1.4.

1.5.2 Chiral symmetry

Massless QCD exhibits two global SU(2) symmetries: the left and right handed up and down quarks may be rotated inside the doublet by an SU(2) matrix. (If they are massive but have the same mass then there remains a single SU(2) symmetry.) This symmetry is denoted $SU(2)_L \times SU(2)_R$ and is known as chiral symmetry.

Due to the confining nature of QCD it is reasonable to expect that the quark bilinears $\langle \bar{u}u \rangle$ and $\langle \bar{d}d \rangle$ may have non-zero expectation values in the ground state. As these operators are not invariant under $SU(2)_L \times SU(2)_R$ this indicates a spontaneous breaking of the global symmetry. A single SU(2) symmetry survives. A theory of scalar fields with this symmetry breaking pattern can be written on general grounds.

Table 1.4: Coefficients of logarithmic terms in the perturbative expansion of pseudoscalar and vector time moments from [28].

k	$C_{k,p}^{(1,1)}$	$C_{k,p}^{(2,1)}$	$C_{k,p}^{(2,2)}$	$C_{k,p}^{(3,1)}$	$C_{k,p}^{(3,2)}$	$C_{k,p}^{(3,3)}$
1	0.0000	-6.4815	0.0000	2.5008	13.5031	0.0000
2	1.0667	1.5909	-0.0444	-7.5852	0.5505	0.0321
3	1.2190	4.3373	1.1683	7.3626	4.2523	-0.0649
4	1.2190	4.8064	2.3873	14.7645	11.0345	1.4589
k	$C_{k,v}^{(1,1)}$	$C_{k,v}^{(2,1)}$	$C_{k,v}^{(2,2)}$	$C_{k,v}^{(3,1)}$	$C_{k,v}^{(3,2)}$	$C_{k,v}^{(3,3)}$
1	2.1333	3.3130	-0.0889	4.0669	0.9590	0.0642
2	1.8286	5.1489	1.7524	6.7216	6.4916	-0.0974
3	1.6254	4.7207	3.1831	7.5736	13.1654	1.9452
4	1.4776	3.6440	4.3713	4.9487	17.4612	5.5856

Take a set of scalar fields $\Sigma_{ij}(x)$ that transform under $SU(2)_L \times SU(2)_R$ as (g denoting an $SU(2)$ element, i.e. $g_L = \exp(i\theta_L^a \tau_a)$):

$$\Sigma \rightarrow g_L \Sigma g_R^\dagger, \Sigma^\dagger \rightarrow g_R \Sigma^\dagger g_L^\dagger. \quad (1.46)$$

A Lagrangian can be simply constructed using traces of $\Sigma^2 = \Sigma \Sigma^\dagger$. If we imagine that the symmetry is broken by Σ relaxing into a minima, then Σ can be expanded about that minima v in terms of two real fields

$$\Sigma(x) = \frac{v + \sigma(x)}{\sqrt{2}} \exp\left(\frac{2i\pi^a(x)\tau_a}{F_\pi}\right). \quad (1.47)$$

which will exhibit spontaneous symmetry breaking. The σ field is invariant under $SU(2)$ and can be decoupled from the system leaving

$$U(x) = \exp\left(\frac{2i\pi^a \tau_a}{F_\pi}\right), \quad (1.48)$$

from which an $SU(2)_L \times SU(2)_R$ invariant Lagrangian can be constructed:

$$\mathcal{L}_\chi = \frac{F_\pi^2}{4} \text{Tr}[(D_\mu U)(D_\mu U)^\dagger] + L_1 \text{Tr}[(D_\mu U)(D_\mu U)^\dagger]^2 + \dots \quad (1.49)$$

This is the Lagrangian of chiral perturbation theory which is frequently used to aid calculations in lattice QCD by guiding light quark mass extrapolations or estimating finite volume effects.

1.5.3 The Operator Product Expansion

The operator product expansion (OPE) as developed by Wilson [30] writes a product of operators at points x and y as a sum over local operators as the distance between x and y goes to 0

$$A(x)B(y) \rightarrow \sum_n C_n(x-y)\mathcal{O}_n((x+y)/2). \quad (1.50)$$

This separates the short and long distance contributions where the coefficients contain the short distance effects and are therefore perturbatively calculable. For short distances $x-y$, corresponding to high momenta, Eq. 1.50 can be shown to hold through perturbation theory. As the operators of which the basis of Eq. 1.50 is constructed may contain large nonperturbative corrections at low energies it is interesting to think of the OPE in an environment where the external momenta are low.

We wish to use the OPE to determine the allowed long-distance operators that may contaminate short-distance matrix elements that will be used to determine momentum subtraction renormalisation constants and their dependence on the momentum. To see how such nonperturbative contributions can be separated out, consider the Lagrangian of a theory of interest. If a Lagrangian is constructed from local operators $\mathcal{O}_i(x)$ as $\mathcal{L} = \sum_i \eta_i(x)\mathcal{O}_i(x)$ then the theory can be treated perturbatively in some region between the ultraviolet cutoff Λ_{UV} and some other scale μ . After integration of these momenta there remains an effective Lagrangian

$$\mathcal{L}_{\text{eff}} = \tilde{\mathcal{L}}(x, \Lambda_{UV}, \mu) + \sum_i \eta_i(x)C_i(\Lambda_{UV}, \mu)\mathcal{O}_i(x, \mu). \quad (1.51)$$

All these operators are now renormalised at a scale μ . If μ is sufficiently large that $\alpha_s(\mu) \ll 1$ then the coefficients C can be perturbatively calculated and the long range interactions are contained in the operators \mathcal{O} . Even if C cannot be perturbatively calculated operators of various dimension should still be present, suppressed by the appropriate power of μ to keep the Lagrangian dimensionless. The operators of lower dimension will therefore have a larger impact. This kind of analysis allows for the construction of fit functions including nonperturbative effects

that should capture the behaviour of nonperturbative data.

1.5.4 Structure of the quark propagator

For the nonperturbative renormalisation discussion below it is useful to have a functional understanding of the form of the quark propagator in QCD (particularly in Landau gauge). The quark propagator can be written in terms of scalar and vector dressing functions ($B(q^2)$ and $V(q^2)$) as [31]

$$S(q^2) \equiv i \int dx e^{iqx} \langle T \{ \psi(x) \bar{\psi}(0) \} \rangle = \frac{\not{q}}{-q^2} V(q^2) + \frac{B(q^2)}{-q^2}. \quad (1.52)$$

These dressing functions may be expanded in terms of both perturbative and nonperturbative pieces which are proportional to various condensates. The nonperturbative pieces are written using the OPE, and are suppressed by appropriate powers of q . The perturbative expansion has been performed to three loops. Certain Wilson coefficients in the OPE are also perturbatively expanded to three loops. The dressing functions can be written as

$$\begin{aligned} V(q^2) &= V_0(\mu/q, \alpha_s) + \frac{C_{m^2}(\mu/q, \alpha_s)}{-q^2} m^2 + \frac{C_{A^2}(\mu/q, \alpha_s)}{-q^2} \langle A^2 \rangle \\ S(q^2) &= S_0(\mu/q, \alpha_s) m + \frac{C_{m^3}(\mu/q, \alpha_s)}{-q^2} m^3 + \frac{C_{A^2}(\mu/q, \alpha_s)}{-q^2} \langle mA^2 \rangle + \frac{C_{\bar{\psi}\psi}(\mu/q, \alpha_s)}{-q^2} \langle \bar{\psi}\psi \rangle, \end{aligned} \quad (1.53)$$

to lowest order in powers of q . The values of the condensate (in a given renormalisation scheme) can then in principle be extracted from fits to lattice propagator data. $\langle \bar{\psi}\psi \rangle$ is the chiral condensate familiar from chiral perturbation theory. $\langle A^2 \rangle$ is a gauge-noninvariant gluonic condensate which can appear as the quark propagator is gauge dependent. The perturbative expansion of Wilson coefficients has not been done for higher mass dimension condensates which makes a quantitative measurement of those condensates impossible (the number of such condensates seriously complicates the problem).

The calculation of the coefficients can be performed by considering the scattering of low energy gluons from the operators.

The importance of this expansion is that it shows that quantities constructed from gauge fixed

quark propagators will have nonperturbative contributions suppressed by only two powers of the scale μ , even in the massless limit. These effects have to be considered when dealing with nonperturbative data of gauge-noninvariant quantities.

Chapter 2

Lattice Formulations of Quantum Field Theories

We now move to a discussion of QCD as formulated on a discrete spacetime lattice [32]. As discussed in Sections 1.2 and 1.5 the evaluation of correlation functions can often not be performed in the well developed framework of perturbation theory due to the large values that the coupling takes. A different approximation is therefore required. Wilson proposed, and originally formulated [33], QCD on a spacetime lattice, reducing the number of degrees of freedom in the path integral to a finite, and computationally manageable, number. A large number of techniques have been developed to extract observables from the discretised theory the most relevant of which to this work are summarised in this chapter.

2.1 Fields on the Lattice

In order to calculate field theory on the lattice the fields must be given appropriate discretised definitions. The simplest such interpretation would be to fix field values at each lattice site. This is what is done for the fermion fields, which will be discussed in more detail in Section 2.2. However, it turns out to be necessary to deal with the gluons with a different approach: rather than placing the field at the lattice sites the field is effectively distributed among the links between the lattice sites. (These links are typically denoted $U_\mu(x)$ for a site x and direction μ .) This allows for a gauge invariant formulation of the lattice QCD action.

The link nature of these fields can be understood in terms of Wilson loops. A Wilson line is defined as

$$W(x, y) = e^{ig \int_y^x A_\mu(z) dz}, \quad (2.1)$$

with a Wilson loop being the case in which the end point x and start point y coincide. Wilson loops are gauge invariant as can be seen from the transformation of a Wilson line under a gauge transformation ($A_\mu(x) \rightarrow A_\mu(x) + \frac{1}{g} \partial_\mu \alpha(x)$):

$$W(x, y) \rightarrow e^{ig \left[\int_y^x A_\mu(z) dz + \frac{1}{g} \int_y^x \partial_\mu \alpha(z) dz \right]} = e^{i\alpha(x)} W(x, y) e^{-i\alpha(y)}, \quad (2.2)$$

where the phase factors will cancel when $x = y$. The discretised formulation of the Wilson loop is natural. Each link on the lattice is associated with a factor of $e^{iagA_\mu(n)}$ where n is the starting lattice site of the link and μ is the vector pointing in the direction of travel and a is the lattice spacing. (A_μ itself is the product of the gluon fields with the corresponding SU(3) generators $A_\mu^a \lambda_a$.) The Wilson loop is then formed by multiplying the factors associated with a chain of links that form a loop together. The simplest Wilson loop has dimensions of $a \times a$, with a the lattice spacing, and is known as a plaquette. Each of these link factors is an SU(3) matrix due to the exponentiation of the generators. The question of how to construct a lattice QCD action from the gauge invariant Wilson loops that matches the QCD action in the continuum limit can be elucidated by expanding the Wilson loop.

Stokes' theorem can be applied to the definition of the Wilson loop to give

$$W = \exp \left(i \frac{ag}{2} \int_\Sigma F_{\mu\nu} d\sigma^{\mu\nu} \right), \quad (2.3)$$

which is an integration over the full spacetime volume. Expanding the exponential gives $1 + i(ag/2)F_{\mu\nu} - (a^2g^2/4)F_{\mu\nu}^2 + \dots$ where $F_{\mu\nu}^2$ makes an appearance. As $F_{\mu\nu}$ is antisymmetric its trace vanishes. The function, denoting the colour trace tr ,

$$\frac{1}{(ag)^2} \sum_{\mu\nu, n} \text{Re}(\text{tr}(1 - W_{\mu\nu}(n))), \quad (2.4)$$

is then $(1/4)F_{\mu\nu}^2$ plus terms that contain factors of a^2 and higher. Eq. 2.4 is then an appropriate gauge invariant discretisation of the pure gauge action known as the Wilson action.

2.2 Fermions on the Lattice

Fermions present a particular challenge for lattice field theories. The problem encountered on the lattice is fundamentally related to the approximate chiral symmetry of massive QCD. This is the invariance of the Lagrangian under the fermion field transformation $\psi \rightarrow e^{i\alpha\gamma_5}\psi$ with $\gamma_5 = i\gamma_0\gamma_1\gamma_2\gamma_3$. In QCD this symmetry is not only explicitly broken by the quark masses but is also spontaneously broken when $\langle\bar{\psi}\psi\rangle$ becomes non-zero due to strong QCD dynamics as discussed in Section 1.5.2.

A simple discretisation of the Dirac action $\int d^4x\bar{\psi}(\gamma^\mu\partial_\mu + m)\psi$ replaces the derivative with a finite difference across lattice sites. The resulting action can be written as

$$a^4 \sum_{x,\mu} \frac{1}{2a} (\bar{\psi}_x \gamma_\mu \psi_{x+\mu} - \bar{\psi}_{x+\mu} \gamma_\mu \psi_x) + a^4 \sum_x m \bar{\psi}_x \psi_x, \quad (2.5)$$

where μ is a unit vector in one of the four directions. This can be thought of in terms of a Dirac operator inserted in between ψ and $\bar{\psi}$: $D_{x,y} = \sum_\mu \frac{1}{2a} (\gamma_\mu \delta_{x+\mu,y} - \gamma_\mu \delta_{x-\mu,y}) + m \delta_{x,y}$. The quark propagator is found by inverting this operator as per the discussion of Section 1.2. When performing the inversion in momentum space the boundary conditions induced by the spacetime discretisation have to be accounted for. The momentum space is a 4-dimensional Brillouin zone with momenta lying in the interval $[0, \frac{\pi}{a}]$. Due to the periodicity of the allowed momenta the quark propagator takes the form $\left(i \sum_\mu \gamma_\mu \frac{1}{a} \sin(ap_\mu) + m\right)^{-1}$ as compared to the continuum form $(p^2 - m^2 + i\epsilon)^{-1}$. There are then propagator poles at all 16 corners of the Brillouin zone indicating that the theory has 16 fermions rather than the desired 1.

This so-called doubling problem can be seen as a symmetry of the action. The action is invariant under $\psi(x) \rightarrow \mathcal{B}_\rho(x)\psi(x)$ and $\bar{\psi}(x) \rightarrow \mathcal{B}_\rho^\dagger(x)\bar{\psi}(x)$ with

$$\mathcal{B}_\rho(x) \equiv \gamma_5 \gamma_\rho (-1)^{x_\rho/a} = \gamma_5 \gamma_\rho e^{ix_\rho \pi/a}. \quad (2.6)$$

In momentum space this transformation shifts $\tilde{\psi}(p)$ to $\tilde{\psi}(p - (\pi/a)\hat{\mu})$. This transformation can be applied multiple times in different directions leading to a total of 16 transformations and

therefore 16 poles in the propagator.

The original solution of this problem proposed by Wilson was to add terms that decouple the extra fermions from the theory by giving them masses inversely proportional to the lattice spacing [33]. This involves adding a term to the action that breaks chiral symmetry in the massless limit. Nielsen and Ninomiya proved that this doubling will always occur in a theory with the following properties [34, 35]:

- ▶ Formulated on a lattice with periodic boundary conditions
- ▶ Locality, hermiticity and translation invariance of the Hamiltonian
- ▶ Even number of dimensions
- ▶ Chiral invariance

2.2.1 The staggered transformation

The simplest discretisation of the Dirac action which simply replaces the covariant derivative by a finite difference operator

$$\Delta_\mu \psi(x) = \frac{1}{2a} (U_\mu(x) \psi(x + a\hat{\mu}) - U_\mu^\dagger(x - \hat{\mu}) \psi(x - a\hat{\mu}))$$

allows a transformation that diagonalises the spin space structure [32, 36]. Consider the operator

$$\Omega(x) \equiv \prod_{\mu=0}^3 (\gamma_\mu)^{x_\mu}$$

acting on quark fields as

$$\psi(x) \rightarrow \Omega(x) \chi(x), \quad \bar{\psi}(x) \rightarrow \bar{\chi}(x) \Omega^\dagger(x).$$

The Dirac action (naive)

$$\sum_x \bar{\psi}(x) (\gamma^\mu \Delta_\mu + m) \psi(x)$$

can be written as

$$\sum_x \bar{\chi}(x) (\Omega^\dagger(x) \gamma_\mu \Omega(x \pm \hat{\mu}) \Delta_\mu + m) \chi(x). \quad (2.7)$$

The factor $\Omega^\dagger(x) \gamma_\mu \Omega(x \pm \hat{\mu})$ reduces to $(-1)^{x_\mu^<}$ where $x_\mu^< = \sum_{\nu < \mu} x_\nu \pmod 2$ and the action is diagonal in spin space with every component of χ being equal to all the others. The computational cost can therefore be reduced by a factor of four by only using one component, with the added benefit that the number of doublers is reduced from 16 to 4. The staggered action Eq. 2.7 is the basis on which the Highly Improved Staggered Quark (HISQ) action is built, as detailed below. There are three remaining doublers. These different quarks, which become degenerate in the continuum are called different tastes of quark, in analogy with flavour.

Improvement

Discretised actions should map to the desired continuum action in the limit of vanishing lattice spacing, but the speed of that convergence is variable. An action with faster falling discretisation errors will allow for reduced extrapolation errors and a generally better control when taking the continuum limit. One source of discretisation error is the use of a finite difference to approximate a derivative. The leading error resulting from this can be removed by the replacement

$$\Delta_\mu \rightarrow \Delta_\mu - \frac{a^2}{6} \Delta_\mu^2. \quad (2.8)$$

This is known as the Naik term [37]. The staggered formalism also suffers from another source of discretisation artefact in the form of taste changing interactions. If a low energy quark absorbs momentum near π/a in some direction then the quark becomes a low energy quark of another taste. The suppression of these interactions is then important for high precision applications of staggered quarks. A relatively simple way to do this is to effectively introduce a form factor at the quark gluon vertex which vanishes as $q \rightarrow \pi/a$. This is done through a smearing procedure. In the asqtad (a^2 and tadpole improved) action [38] this was replacing the gauge links $U_\mu(x)$ with $\mathcal{F}_\mu U_\mu(x)$ where \mathcal{F}_μ is defined as

$$\mathcal{F}_\mu \equiv \prod_{\rho \neq \mu} \left(1 + \frac{a^2 \delta_\rho^{(2)}}{4} \right), \quad (2.9)$$

with

$$\begin{aligned} \delta_\rho^{(2)} U_\mu(x) \equiv & \frac{1}{a^2} (U_\rho(x) U_\mu(x + a\hat{\rho}) U_\rho^\dagger(x + a\hat{\mu})) \\ & - 2U_\mu(x) + U_\rho^\dagger(x - a\hat{\rho}) U_\mu(x - a\hat{\rho}) U_\rho(x - a\hat{\rho} + a\hat{\mu}), \end{aligned} \quad (2.10)$$

and then the further replacement

$$\mathcal{F}_\mu \rightarrow \mathcal{F}_\mu - \sum_{\rho \neq \mu} \frac{a^2 (\delta_\rho)^2}{4}, \quad (2.11)$$

with

$$\begin{aligned} \delta_\rho U_\mu(x) \equiv & \frac{1}{a} (U_\rho(x) U_\mu(x + a\hat{\rho}) U_\rho^\dagger(x + a\hat{\mu})) \\ & - U_\rho^\dagger(x - a\hat{\rho}) U_\mu(x - a\hat{\rho}) U_\rho(x - a\hat{\rho} + a\hat{\mu}). \end{aligned} \quad (2.12)$$

In this case the Naik term uses the unsmeared links.

The HISQ action adds another layer of smearing to this by applying the smearing operator \mathcal{F}_μ with a unitarisation operation in between $\mathcal{F}_\mu \rightarrow \mathcal{F}_\mu \mathcal{U} \mathcal{F}_\mu$. This extra smearing further reduces taste splitting effects. In the HISQ case the Naik term uses links after one level of smearing.

The HISQ action has been demonstrated to have greatly reduced discretisation effects, particularly in the case of heavy quarks such as the charm for which calculations can be performed directly, even on coarse lattices [39].

2.3 Symanzik effective theory

Discretisation explicitly introduces an energy scale into the theory, given by the inverse of the lattice spacing a . The effects of discretisation can therefore be captured by a Wilson style effective theory in which higher dimension operators are added to the desired continuum Lagrangian suppressed by powers of a . (This assumes that the only operators appearing are irrelevant which

will be the case if the lattice theory has been correctly constructed to be within the universality class of the continuum theory under consideration.) This effective theory is known as Symanzik effective theory, or the Symanzik expansion.

If the expansion of an action in terms of higher order operators can be performed such that the coefficients are known then these terms can be removed by simply adding these operators to the action with a negative coefficient. These operator contributions will vanish with a and are therefore harmless. This process is known as Symanzik improvement. More discussion can be found in [32, 40].

2.4 Computational challenge

Following the discussion around Eq. 1.30 the calculation of fermionic correlation functions requires the evaluation of the determinant and the inverse of the Dirac matrix (here denoted M). Given the size of the Dirac matrix for commonly used lattice volumes both of these tasks can become computationally expensive. The computational problems worsen with decreasing lattice spacing (as the lattice volume has to be increased to maintain physical volume) and decreasing quark mass. We first discuss the numerical method employed here to perform matrix inversions (or, more accurately, solves) on given gauge configurations. Then we briefly discuss the generation of dynamical gauge configurations which involves calculating the determinant.

2.4.1 The conjugate gradient solver

The fundamental objects in a vast number of lattice calculations are quark propagators. These take the form of SU(3) vectors and are the solutions of the Dirac equation

$$(\not{D} - m)\psi \equiv M\psi = \psi_0, \quad (2.13)$$

for a source vector ψ_0 , which could, for example, be a δ function at a single spacetime point. (This source vector also carries colour and possibly spin indices.) In the case of a point source ψ would give the propagator from that point to every site on the lattice.

Given the typical size of M which carries colour and spacetime indices (and spin if staggered fermions are not used) Eq. 2.13 is solved numerically. All solves for the data presented here used the conjugate gradient algorithm [41] which is an adaptation of the principle of gradient

descent algorithms that displays faster convergence. The key is to define conjugate directions. For a symmetric matrix A a set of vectors d_i are A -orthogonal if $d_i^T A d_j = 0$. If A is positive definite then these vectors are linearly independent (as the name suggests). It turns out that when solving $Ax = b$ for x , the solution x^* can be written as $\sum_i \alpha_i d_i$ with

$$\alpha_i = -\frac{d_i^T g_i}{d_i^T A d_i}, \quad (2.14)$$

where g_i is the i^{th} gradient $Ax_i - b$. The conjugate gradient algorithm constructs the vectors d_i iteratively from the gradients starting from an initial solution vector x_0 :

$$\begin{aligned} d_0 &= b - Ax_0 \\ g_0 &= -d_0 \\ \alpha_i &= -\frac{g_i^T d_i}{d_i^T A d_i} \\ x_{i+1} &= x_i + \alpha_i d_i \\ g_i &= Ax_i - b \\ \beta_i &= \frac{g_{i+1}^T A d_i}{d_i^T A d_i} \\ d_{i+1} &= -g_{i+1} + \beta_i d_i \end{aligned} \quad (2.15)$$

We use the implementation of this algorithm in the MILC code¹ to calculate our propagators.

There is freedom in the choice of source vector. Constructing the all-to-all propagator matrix by solving Eq. 2.13 for every point source extracts a maximum amount of information from a given configuration. However, for any modern lattice size the computational expense of this is prohibitive. There are therefore several techniques used to increase the statistics gained from each configuration with only a small number of solves. One way to do this is to use a source vector, $\eta(x)$, that is nonzero across a time slice, with a random number on every spatial point of that time slice. The values are random numbers with the statistical property $\langle \eta(x) \eta^\dagger(y) \rangle = \delta_{x,y}$.

¹https://github.com/milc-qcd/milc_qcd

We call such a source a random wall source.

2.4.2 Gauge field generation

Gauge fields need to be drawn from a distribution determined by the action which is peaked at the minima of the action. (If the calculation is performed with dynamical fermions, now common practice, the Dirac determinant is also part of the distribution.) Markov chain Monte Carlo (MCMC) methods are used for this purpose. All the ensembles used here were generated by the MILC collaboration [42] using some variant of the hybrid Monte Carlo (or Hamiltonian Monte Carlo) algorithm.

In such algorithms a momentum P is associated with each link U . The evolution of the link in so-called molecular dynamics time is given by

$$\dot{U}_\mu(x) = iP_\mu(x)U_\mu(x). \quad (2.16)$$

In order to keep U within $SU(3)$ P is Hermitian and traceless. The determinant of the Dirac matrix is written in terms of an integral over a scalar field known as a pseudofermion ϕ :

$$\det(M) = \int d\phi d\phi^\dagger e^{-\phi^\dagger M^{-1} \phi}. \quad (2.17)$$

Writing an effective action S_{eff} as the sum of the gauge action and $-\phi^\dagger M^{-1} \phi$ a Hamiltonian is defined as

$$\mathcal{H} = \frac{1}{2}P^2 + S_{\text{eff}}, \quad (2.18)$$

and the evolution of the gauge field is determined by the equations of motion of \mathcal{H} . The so-called RHMC algorithm proceeds according to:

- ▶ Refresh the momentum from a Gaussian noise distribution $\exp(-P^2/2)$
- ▶ Refresh the pseudofermion field using an intermediate η drawn from $\exp(-\eta^\dagger \eta)$ according to $(\not{D} + m)^\dagger \eta^\dagger$
- ▶ Use the Hamiltonian equations of motion to update U

- Introduce a Metropolis style accept/reject step with probability of acceptance $\min(1, e^{-\delta\mathcal{H}})$ where $\delta\mathcal{H}$ is the change in the Hamiltonian between this step and the last

The use of the Hamiltonian and the Hamilton equations guides the Markov chain [43] through the neighbourhood of high contributions. The logarithm of the determinant is calculated as this is what is needed in the statistical distribution. This logarithm is divided by 4 corresponding to taking the fourth root of the determinant. This is to eliminate the effects of having fermion doublers in the sea. While this leads to nonlocalities in the lattice theory studies of the eigenvalue spectrum for the staggered Dirac matrix support the assumption that these problems vanish in the continuum [44].

2.4.3 HISQ ensembles

All the ensembles used here were generated using an $\alpha_s a^2$ improved gauge action [45] and HISQ fermions. Some important parameters of these ensembles are given in Table 2.1. The β value is related to the inverse of the coupling and corresponds (approximately or precisely based on the definition of the continuum limit, see Section 6.1) to the lattice spacing. L_s and L_t are the spatial and temporal extents in lattice units respectively. The masses of the (degenerate) light quarks, strange quark and charm quark in the sea (that is, those that are included in the fermion determinant) are also given in lattice units. Finally two values from which lattice spacings can be calculated are given in terms of the constant w_0 discussed in Section 2.10. When considering ensembles with the same β value but different sea quark masses a choice must be made about the approach to the continuum limit (i.e. the definition of the lattice spacing). We can choose to vary the lattice spacing as the sea quark masses are changed at fixed β (a) or we can hold the lattice spacing fixed as these masses are varied (\tilde{a}). Both definitions of the lattice spacing are used in the following chapters and so both are given here for reference (where available). The w_0/\tilde{a} values are calculated from w_0/a values using the results of [27].

Table 2.1: Important parameters for the lattice ensembles used generated by the MILC collaboration [42]. The value of w_0 is 0.1715(9) fm [46]. The lattice spacings approximately range from 0.15 to 0.03 fm. Sets 1-3 are referred to as very coarse, 4-12 as coarse, 13-15 as fine, 16-17 as superfine, 18 as ultrafine and 19 as exafine.

Set	β	L_s	L_t	am_l^{sea}	am_s^{sea}	am_c^{sea}	w_0/a	w_0/\bar{a}
1	5.8	16	48	0.013	0.065	0.838	1.1119(10)	1.1322(14)
2	5.8	24	48	0.0064	0.064	0.828	1.1272(7)	1.1322(14)
3	5.8	36	48	0.00235	0.0647	0.831	1.1367(5)	1.1322(14)
4	6.0	20	64	0.008	0.040	0.480	-	1.4075(18)
5	6.0	24	64	0.0102	0.0509	0.635	1.3826(11)	1.4075(18)
6	6.0	24	64	0.00507	0.0507	0.628	1.4029(9)	1.4075(18)
7	6.0	32	64	0.00507	0.0507	0.628	1.4029(9)	1.4075(18)
8	6.0	40	64	0.00507	0.0507	0.628	1.4029(9)	1.4075(18)
9	6.0	32	64	0.00507	0.00507	0.628	-	1.4075(18)
10	6.0	32	64	0.00507	0.012675	0.628	-	1.4075(18)
11	6.0	32	64	0.00507	0.022815	0.628	-	1.4075(18)
12	6.0	48	64	0.00184	0.0507	0.628	1.4149(6)	1.4075(18)
13	6.30	32	96	0.0074	0.037	0.440	1.9006(20)	1.9500(21)
14	6.30	48	96	0.00363	0.0363	0.430	1.9330(20)	1.9500(21)
15	6.30	64	96	0.00120	0.0363	0.432	1.9518(7)	1.9500(21)
16	6.72	48	144	0.0048	0.024	0.286	2.8960(60)	2.994(10)
17	6.72	96	192	0.0008	0.022	0.260	3.0170(23)	2.994(10)
18	7.0	64	192	0.00316	0.0158	0.188	3.892(12)	3.970(15)
19	7.28	96	288	0.00223	0.01115	0.1316	5.243(16)	-

2.5 Construction of staggered correlation functions

Once quark propagators have been computed they can be used to calculate various correlators as a function of time. Here we will focus on 2-point correlators as they are most relevant to the work presented here. The 2-point correlator is given by

$$C(t) = \sum_x \langle J(x, t) J(0, 0) \rangle, \quad (2.19)$$

$$J(x, t) = \bar{\psi}(x, t) \Gamma \psi(x, t).$$

The sum over x projects onto the zero momentum state. For 2-point functions we take the Γ

structure in the two currents to be the same. Following the discussion of Section 1.2 this may be constructed by summing over propagators P :

$$C(t) = \frac{1}{4} \sum_x \text{Tr}(\Gamma P_a(0, x) \Gamma \gamma_5 P_b^\dagger(0, x) \gamma_5), \quad (2.20)$$

where the trace is over colour (the a and b indices) and spin indices and the factors of γ_5 come from exchanging a $P(x, 0)$ for $P^\dagger(0, x)$ (γ_5 Hermiticity). The factor of $1/4$ comes from the taste degree of freedom. With staggered quarks the Γ reduces to a phase arising from the trace over staggering operations and γ matrices. The propagators in Eq. 2.20 are replaced with the staggering transformation Ω multiplied by a staggered propagator. With the pseudoscalar this works as follows:

$$\begin{aligned} & \text{Tr}(\gamma_5 \Omega(0) \Omega^\dagger(x) \gamma_5 \gamma_5 \Omega(x) \Omega^\dagger(0) \gamma_5) \\ &= \text{Tr}(\gamma_0^{x_0} \gamma_1^{x_1} \gamma_2^{x_2} \gamma_3^{x_3} (\gamma_3^{x_3})^\dagger (\gamma_2^{x_2})^\dagger (\gamma_1^{x_1})^\dagger (\gamma_0^{x_0})^\dagger) \\ &= \text{Tr}(\mathbf{1}). \end{aligned} \quad (2.21)$$

There is therefore no phase needed for the pseudoscalar current. A similar procedure can be followed for other Γ structures and for point-split operators where the two currents are not placed at the same point. In that way it is seen that the operators point split within a hypercube but with the same Γ structure produce different phases. This indicates that they have different taste structures.

The construction of staggered meson interpolating operators on a single time slice often leads to contamination of correlators by states of the opposite parity. Due to the fact that there is no projection onto low energy modes (there is only a sum over spatial \mathbf{x} to project onto zero momentum) a staggered two-point function couples to a state of a different taste “in the temporal direction”; that is ρ in Eq. 2.6 is in the t direction. An application of Eq. 2.6 then gives

$$\psi(x) \rightarrow \gamma_5 \gamma_0 (-1)^t \psi(x). \quad (2.22)$$

When this substitution is inserted into the current it produces a state of the opposite parity which oscillates in time (with alternating sign). It is therefore necessary to include terms to

account for this when fitting correlator data.

2.5.1 Arbitrary momentum with twisted boundary conditions

Momentum can be given to a correlation function by multiplying by $e^{ip \cdot x}$ in the sum over x . Due to the discretisation of the momentum insertion (discrete Fourier transform) here can only be an integer multiple of $2\pi/L_x$. To access arbitrary momenta fermion fields with twist can be defined as

$$\psi(x, t) \rightarrow \psi(x, t)e^{-ip \cdot x}, \quad (2.23)$$

with $p_\mu = \theta_\mu(2\pi/L_\mu)$. These fields then satisfy the boundary conditions $\psi(x + \hat{\mu}L_\mu) = \exp(2i\pi\theta_\mu)\psi(x)$ [47, 48, 49]. This can be achieved by multiplying the links by e^{iap_μ} :

$$\bar{\psi}(x)e^{iap_\mu}U_\mu(x)\psi(x + a\hat{\mu}) = \bar{\psi}(x)e^{-ip \cdot x}U_\mu(x)e^{ip \cdot (x+a\hat{\mu})}\psi(x + a\hat{\mu}). \quad (2.24)$$

If these phases are included in the gauge links then the propagators produced with our standard inversion techniques from a random wall source have momentum p .

2.6 Parallelisation

Calculations in lattice QCD are obviously amenable to parallel computing techniques due to the locality of the lattice action (although this locality is in some sense decreased by smearing in the action utilised throughout). If the calculation of the Wilson gluon action is taken as an example then it is clear that the evaluation of the action over the whole lattice can be split into the evaluation of the action at each point individually, and that only the link variables connecting nearest neighbours are required. This suggests splitting the lattice into sublattices and performing the evaluation of the action on every sublattice in parallel, with the necessary communications at the boundaries, in order to increase the speed of the computation.

The level of parallelisation possible makes the use of GPUs for some tasks desirable due to the vastly increased number of cores. When the MILC code² is built for GPUs, inversions are performed through calls to the QUDA [50] conjugate gradient inverter (a multimass option is

²https://github.com/milc-qcd/milc_qcd

also available). The performance difference between CPUs and GPUs can be seen in Figures 2.1 and 2.2 which show the performance (in Gflop/s per CPU or GPU respectively) of the MILC code conjugate gradient on the Peta4 (and Cosma7) Skylake and Wilkes2 facilities. The other important aspect of these performance numbers is the poor scaling with the number of nodes for the GPUs relative to CPUs.

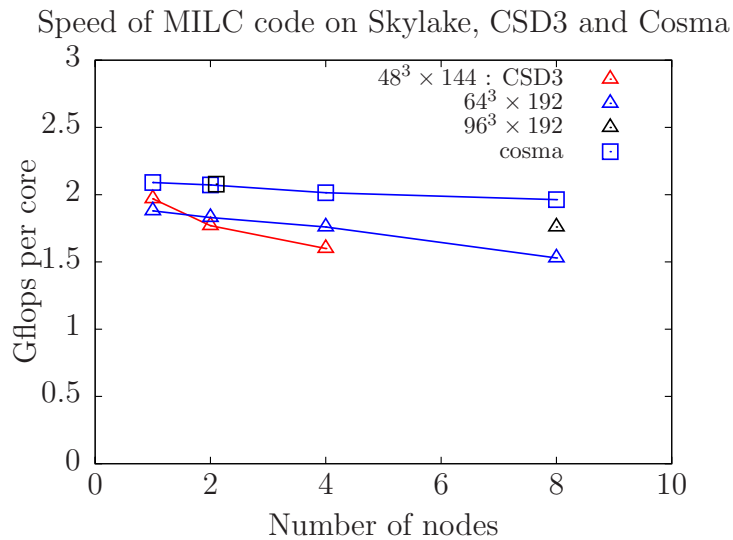


Figure 2.1: Performance of MILC code conjugate gradient routine on Skylake systems for various lattice volumes. Peta4 provides 32 CPUs per node (2 sockets). [Figure courtesy of A. T. Lytle.]

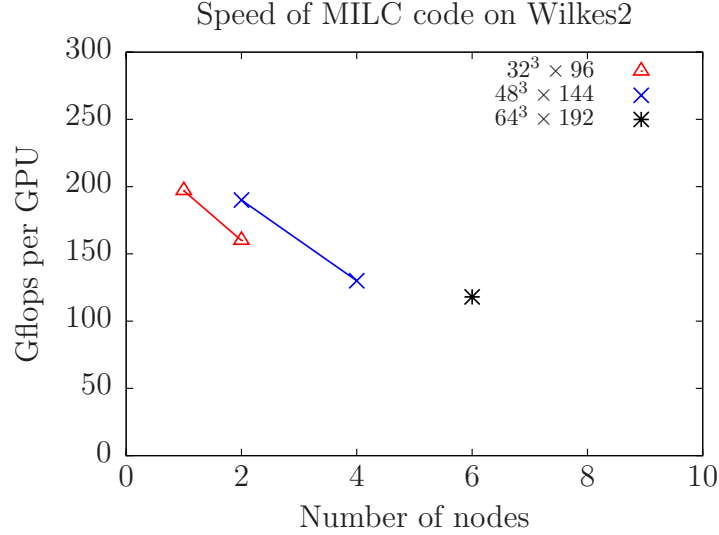


Figure 2.2: Performance of MILC code (calling QUDA) conjugate gradient routine on Wilkes2 for various lattice volumes. Wilkes2 provides 4 Nvidia P100 GPUs per node. [Figure courtesy of A. T. Lytle.]

2.7 Fitting 2-point functions

Correlators are formed from the tie-together of propagators with the choice of γ structure (phase for staggered quarks) that gives the required spin. Physical observables must then be extracted which is done through a fit. Consider the 2-point pseudoscalar correlator. The correlator $C(t)$ as a function of time is written as an expansion in the energy levels E_i via an insertion of the complete energy basis into the correlation function (assuming large temporal extent T):

$$C(t) = \sum_{i=0}^{\infty} a_i^2 e^{-E_i t}. \quad (2.25)$$

The lowest energy level E_0 corresponds to the mass of the lightest particle with the quantum numbers of the correlator. The amplitudes a_i give the overlap of the E_i energy state with the vacuum. The higher energy states will contribute less at large values of t as their exponentials fall faster. The ground state therefore dominates the high t behaviour of the correlator. On a periodic lattice the backward propagating states also have to be included which gives a fit function of

$$C(t) = \sum_{i=0}^{\infty} a_i^2 \left(e^{-E_i t} + e^{-E_i(T-t)} \right), \quad (2.26)$$

with T the extent of the lattice. For certain staggered correlators it is also necessary to include states of the opposite parity which oscillate in time (see Section 2.5):

$$C(t) = \sum_{i=0}^{\infty} a_i^2 \left(e^{-E_i t} + e^{-E_i(T-t)} \right) + (-1)^t (a_i^o)^2 \left(e^{-E_i^o t} + e^{-E_i^o(T-t)} \right). \quad (2.27)$$

In order to make the problem numerically tractable the series in Eq. 2.25 is truncated at some value of i , typically ~ 5 . To perform these and other fits we use the Bayesian fitting techniques discussed in Section 2.8.

2.8 Principles of Bayesian fitting

Throughout this work a Bayesian fitting procedure based on [51] as implemented in the `gvar`³, `lsqfit`⁴ and `corrfit`⁵ packages is used. The discussion here follows [51] and the Appendices of [52, 53].

The χ^2 of a fit is typically defined in terms of the difference between a fit function evaluated with fit parameters p_i and some set of input data. Denoting this difference Δ_a and the covariance matrix of the data C_{ab} the χ^2 is given by

$$\chi^2(p) = \sum_{ab} \Delta(p)_a C_{ab}^{-1} \Delta(p)_b. \quad (2.28)$$

The standard χ^2 is augmented in order to penalise a fit that drifts far from the chosen prior values. This is done simply by

³<https://github.com/gplepage/gvar>

⁴<https://github.com/gplepage/lsqfit>

⁵<https://github.com/gplepage/corrfit>

$$\begin{aligned}\chi^2 &\rightarrow \chi^2 + \chi_{\text{prior}}^2, \\ \chi_{\text{prior}}^2 &\equiv \sum_n \frac{(\eta_n - \tilde{\eta}_n)^2}{\tilde{\sigma}_{\tilde{\eta}_n}^2},\end{aligned}\tag{2.29}$$

where a quantity with a tilde denotes a prior.

Best fit parameters are those that minimise the χ^2 . An approximation for the covariance matrix of these best fit parameters can be obtained by considering the derivative of the χ^2 w.r.t the parameters (denoted ∂_i for $\partial/\partial p_i$). We have (at the best fit point)

$$\begin{aligned}\partial_i \chi^2(p) = 0 &= 2 \sum_{ab} \partial_i f_a(p) C_{ab}^{-1} \Delta(p)_b \\ \Rightarrow (C_p^{-1})_{ij} &= \sum_{ab} \partial_i f_a(p) C_{ab}^{-1} \partial_j f_b(p) + \mathcal{O}(\Delta).\end{aligned}\tag{2.30}$$

This allows the covariance matrix of the fit output parameters to be calculated in terms of derivatives of the fit function. All of this is calculated automatically in the `gvar` and `lsqfit` packages.

If the first part of Eq. 2.30 is differentiated w.r.t the input data y_a and then solved for $\partial p_i / \partial y_a$ the result is

$$\frac{\partial p_j}{\partial y_b} = \sum_{ai} (C_p)_{ji} \partial_a f_i(p) C_{ab}^{-1}.\tag{2.31}$$

In the high statistics limit the parameter covariances are related to those of the data via

$$(C_p)_{ij} = \sum_{ab} \frac{\partial p_i}{\partial y_a} C_{ab} \frac{\partial p_j}{\partial y_b}.\tag{2.32}$$

From these relations the variance of a function of the fit parameters $g(p)$ can be calculated:

$$\begin{aligned}\sigma_g^2 &\equiv \sum_{ij} \partial_i g(p) (C_p)_{ij} \partial_j g(p) = \sum_{ab} c_{ab} C_{ab} \\ c_{ab} &= \sum_{ij} \partial_i g(p) \frac{\partial p_i}{\partial y_a} \frac{\partial p_j}{\partial y_b} \partial_j g(p).\end{aligned}\tag{2.33}$$

This allows the error budget (the breakdown of various contributions to the uncertainty of a quantity derived from the fit outputs) to be constructed through the calculation of the coefficients c_{ab} .

Working with covariance matrices, specifically their inverses, can be numerically problematic unless there are a very large number of statistical samples. Defining the correlation matrix through the relationship

$$\mathbf{C} = \mathbf{D} \mathbf{C}_{\text{corr}} \mathbf{D},\tag{2.34}$$

where \mathbf{D} is the diagonal matrix of standard deviations. The inverse of the covariance matrix is then given by

$$\mathbf{C}^{-1} = \sum_i \frac{\mathbf{D}^{-1} \mathbf{v}_i \mathbf{v}_i^T \mathbf{D}^{-1}}{\lambda_i},\tag{2.35}$$

where \mathbf{v}_i and λ_i are the eigenvectors and eigenvalues of \mathbf{C}_{corr} . This form highlights the possibility of numerical instability when considering small eigenvalues. If the size of the covariance matrix is N_{corr} then there are N_{corr} eigenvalues and a sample size N_s much larger than N_{corr} is needed to reliably estimate all of those eigenvalues. If $N_s < N_{\text{corr}}$ then the low eigenvalues will be zero. Therefore, if the statistics are not high enough then the small eigenvalues are underestimated, incorrectly exaggerating their impact.

In order to deal with this we introduce an svd cut. This is a value, λ_{svd} , between 0 and 1. This is a fraction of the largest eigenvalue, λ_{max} , below which we wish to alter the eigenvalues. All eigenvalues below this fraction are replaced by $\lambda_{\text{svd}} \lambda_{\text{max}}$; *no eigenvalues are removed in this procedure*. This procedure has the effect of increasing uncertainties on fit outputs as the svd cut is raised (hence it is a conservative move). This can be seen by representing the input data as a

vector of Gaussian random variables

$$\mathbf{G} = \overline{\mathbf{G}} + \delta\mathbf{G}, \quad (2.36)$$

with $\delta\mathbf{G} = \sum_i z_i \sqrt{\lambda_i} \mathbf{D}\mathbf{v}_i$ with the uncorrelated random numbers z_i satisfying $\langle z_i \rangle = 0$ and $\langle z_i z_j \rangle = \delta_{ij}$. The svd cut adds an extra term

$$\delta\mathbf{G}_{\text{svd}} = \sum_{\lambda_i < \lambda_{\text{svd}} \lambda_{\text{max}}} \bar{z}_i \sqrt{\lambda_{\text{svd}} \lambda_{\text{max}} - \lambda_i} \mathbf{D}\mathbf{v}_i, \quad (2.37)$$

where the random variables \bar{z}_i again have zero mean. This is an additional source of uncertainty which increases the overall uncertainty.

With a relatively high svd cut it is often found that lower χ^2/dof values than expected are produced. This smallness is due to the fact that random fluctuations in $\overline{\mathbf{G}}$ are not characteristic of the fluctuations in $\delta\mathbf{G}_{\text{svd}}$. You therefore expect to obtain χ^2/dof closer to the expectation of ~ 1 if noise drawn from the distribution given by $\delta\mathbf{G}_{\text{svd}}$ is added to Eq. 2.36. This is indeed what is seen [53].

2.9 QED on the lattice

As lattice determinations of various quantities approach or push past 1% precision there is an increased focus on the effects of electromagnetic interactions on hadronic systems. If calculations of these effects are to be done on lattices of finite volume then there are certain theoretical difficulties that need to be addressed. The simplest way to see that there is a problem is to consider Gauss' law in a finite volume with periodic boundary conditions. The integral of the divergence of the electric field across the volume vanishes due to the periodicity from which it follows that charged states cannot propagate through the volume. How to tackle the problem can be illuminated by observing that the QED action on a torus is invariant under a shift symmetry:

$$A_\mu(x) \rightarrow A_\mu(x) + b_\mu. \quad (2.38)$$

In a space with no boundary conditions this can be written as a gauge transformation $b_\mu = \partial_\mu \omega(x)$

and is therefore removed by gauge fixing. With periodic boundary conditions the requirement that the associated U(1) transformation $e^{i\omega}$ also be periodic leads to

$$\begin{aligned}\omega(x) &= \omega(x + L), \\ \implies b_\mu x^\mu + c &= b_\mu x^\mu + b_\mu L + c, \\ \implies b_\mu L &= 0.\end{aligned}\tag{2.39}$$

The triviality of this condition indicates that the shift symmetry can no longer be written as a local gauge transformation. It must therefore be removed manually. In momentum space the shift transformation modifies the zero mode of the field. A common way to deal with it is therefore to remove the zero modes.

The prescription for removing the zero modes used here is known as QED_L. This requires that $A_\mu(k_0, \mathbf{k} = 0) = 0$. This can be done simply if the field is generated in momentum space. In Feynman gauge the (discretised) QED action takes the form

$$S[A_\mu(x)] = -\frac{1}{2} \sum_{x,\mu} A_\mu(x) \Delta^2 A^\mu(x),\tag{2.40}$$

with a discretised Laplacian Δ^2 . In momentum space this is

$$S[A] = \frac{1}{2} \sum_{k,\mu} \hat{k}^2 |\tilde{A}_\mu(k)|^2,\tag{2.41}$$

with \hat{k}_μ the discretised momentum $2 \sin(k_\mu/2)$. A momentum space field can therefore be drawn from a Gaussian distribution with variance $2/\hat{k}^2$ and then Fourier transformed. Fields in other gauges can be produced by first generating the field in Feynman gauge and then applying a projection operation. A U(1) field is then constructed from $A_\mu(x)$ by multiplying by the quark charge eQ and exponentiating $\exp(i e Q A_\mu)$. The U(1) field is then multiplied into the SU(3) links which we do before HISQ smearing is applied.

Once generated the fields can be directly tested against perturbative results for the average link and plaquette. Due to the smallness of the QED coupling these perturbative results at order α_{QED} are expected to hold to a high degree of precision. The perturbation theory prediction for

the average plaquette is given in [54] and is independent of the gauge choice. The α_{QED} coefficient of the average value of the U(1) links can be extracted from the $\mathcal{O}(\alpha_s)$ QCD coefficient in [55] by multiplying by Q^2/C_F . The results are:

$$\begin{aligned} \text{Landau gauge : } & 1 - \alpha_{\text{QED}} Q^2 0.0581 \\ \text{Feynman gauge : } & 1 - \alpha_{\text{QED}} Q^2 0.0775 \end{aligned} \tag{2.42}$$

We have checked that the U(1) fields used in the analyses that follow have mean values that agree with these perturbative results.

2.10 Scale setting

The lattice spacing, or equivalently the strong coupling, have to be set using an experimental measurement, similar to how the masses are set. Clearly, for good precision, this requires a quantity that can be calculated to high precision and is well known experimentally. For example, the $\Upsilon(2S-1S)$ splitting has historically been used to set the scale [56]. Throughout this work the lattice spacing is determined ultimately via f_π through the intermediate quantity w_0 . The benefit of this is that w_0/a is determined on each ensemble with a computationally cheap calculation and it then suffices to have a single calculation of the physical value of w_0 tied to f_π to obtain a .

w_0 is a gluonic property of the gauge field that is determined in terms of the gradient (or Wilson) flow of the field. This is a flow dependent on a flow time variable t that drives the fields closer to the values that minimise the action. It is defined by the flow equations [57]:

$$\begin{aligned} B_\mu|_{t=0} &= A_\mu, \\ \partial_t B_\mu &= D_\nu G_{\nu\mu} + \alpha_0 D_\mu \partial_\nu B_\nu, \\ G_{\mu\nu} &= \partial_\mu B_\nu - \partial_\nu B_\mu + [B_\mu, B_\nu], \\ D_\mu &= \partial_\mu + [B_\mu, \cdot]. \end{aligned} \tag{2.43}$$

This flow is applied numerically to the gauge field and the dimensionless variable $t^2 \langle E(t) \rangle$ where

E is the contraction of $G_{\mu\nu}$ with itself $(1/4)G_{\mu\nu}G^{\mu\nu}$ is computed. Originally a scale t_0 was defined as the flow time at which $t^2\langle E(t)\rangle$ reaches the (somewhat arbitrary) value of 0.3. In [58] the alternative scale w_0 was proposed:

$$t\frac{d}{dt}(t^2\langle E(t)\rangle)|_{t=w_0^2} = 0.3. \quad (2.44)$$

w_0 was shown to have smaller discretisation effects than t_0 .

The discretised version of these flow equations, which are integrated numerically, offer a few options. The unimproved Wilson action can be used in the flow (which is referred to as Wilson flow) or the Symanzik improved definition may be used (referred to as Symanzik flow) [58, 59]. These definitions only differ by discretisation effects so as long as one is consistently used the continuum limits will agree. Here the Wilson flow is used.

The physical value of w_0 was determined in [46] from a fit to w_0f_π , w_0f_K , $w_0f_{\eta_s}$ and $w_0^2M_{\eta_s}^2$ with the experimental value of the leptonic width of the π^\pm and the value of V_{ud} from nuclear β -decay used as inputs.

Chapter 3

Nonperturbative Renormalisation in Momentum Subtraction Schemes with Staggered Quarks

3.1 MOM schemes and their lattice implementation

In a quantum field theoretic calculation performed on a discretised space-time the lattice spacing acts as an ultraviolet regulator. As the regulator is removed, i.e. the continuum limit is taken, divergences will appear in some operator matrix elements unless a renormalisation of the operators involved in the calculation is performed. In a lattice calculation this amounts to multiplying a matrix element $X(a)$ at a lattice spacing a by a renormalisation constant $Z_X(a, \mu)$ which, in addition to depending on the cutoff a , may also have a renormalisation scale μ dependence. The renormalisation constant accounts for the differences in the UV of the lattice and continuum theories arising from the exclusion of higher modes in the former.

Clearly the commonly used $\overline{\text{MS}}$ scheme is not viable for lattice renormalisation as it relies on dimensional regularisation (see Section 1.3). However, due to its prominence in perturbative computations, scheme dependent quantities, such as quark masses, are conventionally quoted at a given scale μ in the $\overline{\text{MS}}$ scheme. Lattice computations therefore often employ an intermediate scheme which is perturbatively matched to $\overline{\text{MS}}$ in the continuum. It is clear that using a scheme that can be defined independently of the regularisation directly on the lattice can be

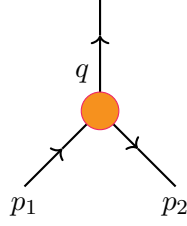


Figure 3.1: Depiction of the kinematic setup of the vertex functions used in momentum subtraction scheme. The circle represents the insertion of an operator.

advantageous. Momentum subtraction schemes offer this possibility [60].

Momentum subtraction schemes are defined such that certain renormalised matrix elements are equal to their tree-level values. In the momentum subtraction schemes discussed here the quantities of interest are quark propagators and vertex functions. In this context a vertex function is an operator inserted between two external off-shell quark states. A generic kinematic setup for this is shown in Fig. 3.1. As quantities such as quark propagators are not gauge invariant the scheme is defined in a fixed gauge, typically Landau gauge.

The wavefunction renormalisation factor, Z_q , is defined in terms of the inverse propagator $S^{-1}(p)$. At tree-level $S^{-1}(p) = \not{p} - m$. Due to the separation of γ structures, the p dependent part can be isolated by tracing over the inverse propagator multiplied by γ_μ . We can define a projector to multiply S^{-1} by, and then take the trace over colour and spin, which will give 1 at tree-level:

$$\frac{1}{12p^2} \text{Tr}[\not{p}S^{-1}(p)]. \quad (3.1)$$

The wavefunction renormalisation may then be defined according to

$$\frac{1}{12p^2 Z_q} \text{Tr}[\not{p}S^{-1}(p)] = 1. \quad (3.2)$$

We use two such schemes in this Chapter. These are the RI-SMOM [61] and RI'-MOM [62] schemes. (We find the former to be a better choice for the reasons discussed below.) These two schemes differ in the relationship between p_1 , p_2 and q in Fig. 3.1. The RI'-MOM scheme is simpler and takes $p_1 = p_2$ with $q = 0$. The RI-SMOM scheme uses the more symmetric setup $p_1 - p_2 = q$ with $p_1^2 = p_2^2 = q^2 \equiv \mu^2$. Both these schemes use the definition of Z_q already

discussed. However, certain definitions of the renormalisation factors of different currents $\bar{\psi}\Gamma\psi$ differ between the schemes.

Currents are renormalised using amputated vertex functions traced over a projector, similar to the case of wavefunction renormalisation. Here, a vertex function is an operator inserted between external quark states: e.g. schematically $\langle\psi(p_1)\overline{psi}\Gamma\psi\overline{psi}(p_2)\rangle$ for some Dirac structure Γ . An amputated vertex function is a vertex function that has been divided on either side by the relevant quark propagators. Denoting a vertex function for operator \mathcal{O} $G_{\mathcal{O}}(p_1, p_2)$, the amputated vertex function is

$$\Lambda_{\mathcal{O}}(p_1, p_2) = S^{-1}(p_1)G_{\mathcal{O}}(p_1, p_2)S^{-1}(p_2). \quad (3.3)$$

In the RI'-MOM scheme [61]

$$\begin{aligned} \frac{Z_V}{Z_q} &\equiv \lim_{m \rightarrow 0} \frac{1}{12} \text{Tr}\{\Lambda_V^\mu(p)\gamma_\mu\} \\ \frac{Z_A}{Z_q} &\equiv \lim_{m \rightarrow 0} \frac{1}{12} \text{Tr}\{\Lambda_A^\mu(p)\gamma_\mu\gamma_5\} \\ \frac{Z_S}{Z_q} &\equiv \lim_{m \rightarrow 0} \frac{1}{12} \text{Tr}\{\Lambda_S(p)\mathbf{1}\} \\ \frac{Z_P}{Z_q} &\equiv \lim_{m \rightarrow 0} \frac{1}{12i} \text{Tr}\{\Lambda_P(p)\gamma_5\} \\ \frac{Z_T}{Z_q} &\equiv \lim_{m \rightarrow 0} \frac{1}{32} \text{Tr}\{\Lambda_T^{\mu\nu}(p)\sigma_{\mu\nu}\}. \end{aligned} \quad (3.4)$$

All of these conditions are expressed as a ratio of a current renormalisation factor to the wavefunction renormalisation being equal to an amputated vertex function traced over a γ structure which we refer to as a projector. For the trace of an amputated vertex function $\Lambda_{\mathcal{O}}$ over a projector we use the notation $P_{\Lambda_{\mathcal{O}}}$. For example, $Z_V/Z_q = P_{\Lambda_V}$. These conditions are defined in the massless limit¹. This is not necessary but leads to some simplifications discussed briefly below.

In the RI-SMOM scheme [61]:

¹On the lattice the sea quarks cannot be set to zero mass. This is compensated for in the perturbative matching to $\overline{\text{MS}}$ in the mass calculations of Chapter 6.

$$\begin{aligned}
\frac{Z_V}{Z_q} &\equiv \lim_{m \rightarrow 0} \frac{1}{12q^2} \text{Tr}\{q_\mu \Lambda_V^\mu(p_1, p_2) \not{q}\} \\
\frac{Z_A}{Z_q} &\equiv \lim_{m \rightarrow 0} \frac{1}{12q^2} \text{Tr}\{q_\mu \Lambda_A^\mu(p_1, p_2) \gamma_5 \not{q}\} \\
\frac{Z_S}{Z_q} &\equiv \lim_{m \rightarrow 0} \frac{1}{12} \text{Tr}\{\Lambda_S(p_1, p_2) \mathbb{1}\} \\
\frac{Z_P}{Z_q} &\equiv \lim_{m \rightarrow 0} \frac{1}{12i} \text{Tr}\{\Lambda_P(p_1, p_2) \gamma_5\} \\
\frac{Z_T}{Z_q} &\equiv \lim_{m \rightarrow 0} \frac{1}{32} \text{Tr}\{\Lambda_T^{\mu\nu}(p_1, p_2) \sigma_{\mu\nu}\}.
\end{aligned} \tag{3.5}$$

The largest difference between the two schemes is in the definition of the vector current renormalisation. This will be discussed in terms of the Ward-Takahashi identity in Section 3.3 following the presentation of results for the mass renormalisation in the RI-SMOM scheme. This is presented first as in some senses it is the simplest calculation (as it uses the scalar current) and reveals some of the potential concerns about using momentum subtraction schemes implemented in a fully nonperturbative manner. The renormalisation of the tensor current will then be discussed in Section 3.4.

In a lattice computation the vertex functions needed are computed from a tie together of propagators. The steps of such a calculation are outlined here. We consider local functions; point split operators are complicated by the need to insert gauge links.

1. Numerically fix gluon fields to Landau gauge
2. Compute a quark propagator for each momentum (incoming and outgoing) using a momentum source $e^{ip \cdot x}$: $S(p_1, x)$ and $S(p_2, x)$
3. For each vertex function being considered construct it according to
$$G_{\mathcal{O}}(q) = \sum_x S(p_1, x) e^{iq \cdot x} \mathcal{O} S(p_2, x)$$
4. Fourier transform the x index on the quark propagator to give the momentum space propagator
5. The vertex functions and propagator in momentum space are 48×48 matrices.² These

²It is 48×48 matrices for staggered quarks due to taste degrees of freedom (16 tastes times 3 colours). With colour and spin degrees of freedom they are just 12×12 (4 spins times 3 colours).

can be manipulated easily. For example, the propagator can be numerically inverted very quickly. These inverted propagators are used to amputate the vertex functions $G_{(\mathcal{O})}$ according to Eq. 3.3

6. $Z_{\mathcal{O}}$ is calculated from S^{-1} and $\Lambda_{\mathcal{O}}$ using the definitions given in Eqs. 3.4 or Eqs. 3.5
7. A perturbative matching calculation can be used to convert between the momentum subtraction scheme and, for example, the $\overline{\text{MS}}$ scheme

Step 2 is of importance in being able to achieve good statistical precision with relatively few configurations. These momentum sources are spread out over the whole lattice and we find that this allows us to achieve the desired precision with only 20 configurations.

Throughout we use twisted boundary conditions to access arbitrary momenta [63].

3.1.1 Momentum space quark fields with staggered quarks

The use of staggered quarks adds some slight complications to the technical details of the lattice calculation which are detailed in [64]. The construction of momentum space quark fields must appropriately handle the taste degrees of freedom. These taste degrees of freedom are, in some sense, distributed over a hypercube (rather than a single site).

The full Brillouin zone (after the Fourier transform is performed) may be split into subzones which are labelled with a hypercube vector B . Any momentum may then be written

$$p_{\mu} = \hat{p}_{\mu} + \pi B_{\mu}, \quad (3.6)$$

with \hat{p} lying in the reduced Brillouin zone $\{-\pi/2, \pi/2\}$. The momentum space field is then taken to be

$$\tilde{\psi}_B(\hat{p}) = \sum_n e^{-ip \cdot n} \chi(n). \quad (3.7)$$

Here n denotes sites on the lattice and χ is the standard staggered quark field.

In the free theory this gives the inverse propagator (defined through $\langle \tilde{\psi}_A \tilde{\psi}_B \rangle$)

$$S^{-1}(\hat{p}) = m \overline{(\mathbf{1} \otimes \mathbf{1})}_{AB} + i \sum_{\mu} \sin(\hat{p}_{\mu}) \overline{(\gamma_{\mu} \otimes \mathbf{1})}_{AB}, \quad (3.8)$$

with appropriately defined transformations of the γ -structures $\overline{(\gamma_S \otimes \xi_T)}$, which resembles the continuum form³. In this notation the first γ matrix (γ_S) gives the spin structure and the second (ξ_T) the taste. This shows that the propagator is a taste singlet ($\xi_T = \mathbf{1}$). The notation used here is the same as in [64] and is defined through

$$\begin{aligned} \overline{(\gamma_S \otimes \xi_T)}_{AB} &\equiv \frac{1}{4} \text{Tr}(\gamma_A^{\dagger} \gamma_S \gamma_B \gamma_T^{\dagger}), \\ \overline{(\gamma_S \otimes \xi_T)} &\equiv \sum_{CD} \frac{(-1)^{A \cdot C}}{4} \overline{(\gamma_S \otimes \xi_T)}_{CD} \frac{(-1)^{D \cdot B}}{4}. \end{aligned} \quad (3.9)$$

A shorthand for products of γ matrices has been used here with

$$\gamma_S = \gamma_0^{S_0} \gamma_1^{S_1} \gamma_2^{S_2} \gamma_3^{S_3}, \quad (3.10)$$

with capital letters denoting 4-dimensional hypercube vectors consisting of 1s and 0s.

3.1.2 Staggered quark bilinears

The calculation of quark bilinears, and therefore vertex functions, also has complications due to the presence of taste. These bilinears are written (in the notation of [64])

$$\mathcal{O}_{S \otimes T} = \frac{1}{16N} \sum_n \sum_{A,B} \bar{\chi}(n) \overline{(\gamma_S \otimes \xi_T)}_{n, n+B-A} U_{n, n+B-A} \chi(n+B-A), \quad (3.11)$$

where the gauge link connecting the sites n and $n+B-A$, U is inserted in order to maintain gauge invariance. This defines the so-called covariant form of the operator. (The operator can also be defined in a ‘‘hypercubic’’ sense with a sum over a partitioning of the lattice into hypercubes. The covariant form is simpler to implement numerically and avoids bilinear mixing as discussed in [64].) This can be rewritten for a local operator as

³This is discussed in detail in [64].

$$\mathcal{O}_{S \otimes T} = \frac{1}{N} \sum_n \bar{\chi}(n) \overline{(\gamma_S \otimes \xi_T)} \chi(n). \quad (3.12)$$

(For the generalisation to the point-split case see [64].) This is just a sum over sites n with a staggered phase $\overline{(\gamma_S \otimes \xi_T)}$ inserted between quark fields.

As there are multiple tastes of each operator given in Eq. 3.1 the staggered versions of those conditions must use the appropriate taste structures in the projectors. This can be illustrated for Z_q . In the free theory $S^{-1}(p)$ can be written in terms of $\overline{(\mathbf{1} \otimes \mathbf{1})}$ and $\overline{(\gamma_\mu \otimes \mathbf{1})}$ which indicates that the correct form of Z_q is

$$Z_q(\hat{p}) = -i \frac{1}{48} \sum_\mu \frac{\tilde{p}_\mu}{\tilde{p}^2} \text{Tr} \left[\overline{(\gamma_\mu \otimes \mathbf{1})} S^{-1}(\hat{p}) \right], \quad (3.13)$$

with $\tilde{p} = \sin(\hat{p}) + \sin^3(\hat{p})/6$ to ensure that $Z_q = 1$ in the free theory. The $\sin^3(\hat{p})/6$ term comes from the contribution of the Naik term (see Section 2.2.1). For the various vertex functions the taste structures required are chosen to match the phases used in the calculation of the vertex functions. Examples of this are seen throughout this Chapter.

3.2 Z_m : mass renormalisation

A major area in which the precision obtainable through lattice calculations is difficult to match by other means is the determination of the fundamental parameters of QCD. These include the quark masses. Due to the origin of these masses in the SM through the interaction with the Higgs field, precise quark masses are needed for precision Higgs studies [65], a region of great interest to the particle physics community. Part of obtaining precise and robust results is to compare different methodologies with different sources of systematic uncertainty. The HPQCD collaboration performed a calculation of the charm mass using fits to heavy quark current-current correlator moments and then determined the strange mass using a determination of m_c/m_s [27]. In Chapter 6 we use some of the same gluon field configurations to perform the calculation of charm and strange quark masses using the bare quark masses on a range of lattices in conjunction with the mass renormalisation factor in the RI-SMOM scheme, calculated nonperturbatively on those lattices, to be able to perform a continuum extrapolation of the renormalised mass. (A published account of his work can be found in [1].) This Section details the calculation of the

renormalisation factors in the RI-SMOM scheme.

The renormalisation of quark masses must be performed within the framework of a renormalisation scheme and then matching calculations may be used to convert between any two schemes. For nonperturbative lattice calculations it is convenient to use the RI-SMOM scheme from which results may be converted to the $\overline{\text{MS}}$ scheme, which is the standard for quoting quark masses. The matching calculation is done perturbatively in the continuum so it is necessary to perform the lattice calculation in a momentum region where such a perturbative calculation is valid, and also to consider nonperturbative effects that are not present in the perturbative calculation. The lowest momentum value used in this calculation was therefore chosen to be 2 GeV. The range of μ values we use has been chosen so that discretisation effects of the form $a\mu$ are not too large.

3.2.1 Landau gauge fixing

Momentum subtraction schemes must be performed in a specific gauge as they make use of non-gaugeinvariant quantities such as quark propagators. Here Landau gauge was chosen, which in the continuum corresponds to the choice of A_μ fields satisfying $\partial_\mu A_\mu(x) = 0$. On the lattice this condition becomes the maximisation of the functional of the gauge links $\sum_\mu \text{Re}(\text{Tr}(U_\mu(x)))$, which must obviously be performed numerically. This is done by applying gauge group transformations to the link variables, typically in some form of gradient descent, normally accelerated by overrelaxation [66], Fourier acceleration [67] or both. The tolerance of the resulting gauge fixing can be measured as the magnitude of the gradient of the gauge field. In cases where a very stringent tolerance is required, particularly on larger lattices, both overrelaxation and Fourier acceleration are needed. Here, by a stringent gauge fixing tolerance we mean 10^{-14} . This is discussed in more detail in Section 3.2.5.

Working in a fixed gauge raises the possibility of effects from Gribov copies. These copies are the results obtained at different maxima of the gauge fixing functional $\sum_\mu \text{Re}(\text{Tr}(U_\mu(x)))$. These arise as the gauge fixing condition is not uniquely satisfied [68]. Here we do not address this issue and assume that such effects are negligible following the findings of [69], which found no observable effects at a precision below 1%.

3.2.2 Z_m in the RI-SMOM scheme

The definition of the RI-SMOM scheme is given in Section 3.1. Here the following explicit kinematic setup was chosen:

$$\begin{aligned} ap_1 &= \frac{2\pi}{L_s} \left(x + \frac{\theta}{2}, 0, x + \frac{\theta}{2}, 0 \right) \\ ap_2 &= \frac{2\pi}{L_s} \left(x + \frac{\theta}{2}, -x - \frac{\theta}{2}, 0, 0 \right) \quad , \end{aligned} \quad (3.14)$$

where x is an integer and θ is the momentum twist. This makes aq equal to

$$\frac{2\pi}{L_s} \left(0, x + \frac{\theta}{2}, x + \frac{\theta}{2}, 0 \right), \quad (3.15)$$

and so the symmetric RI-SMOM condition is satisfied. The conditions of Eq. 3.5 give expressions for the relevant renormalisation constants. For mass renormalisation only the values of Z_q and P_{Λ_S} are required as $Z_m = 1/Z_S$ where $Z_S = Z_q/P_{\Lambda_S}$. Z_q is given by $\frac{1}{12p^2} \text{Tr}\{S^{-1}(p)\not{p}\}$ in our choice of scheme.

The kinematic setup of the quark bilinears is symmetric with a momentum insertion at the vertex of q_μ such that $p_1^2 = p_2^2 = q^2$. This was originally chosen in order to suppress chiral symmetry breaking effects present in the RI'-MOM scheme. By studying $\Lambda_P - \Lambda_S$ (P here denotes the pseudoscalar operator γ_5) it was shown that the RI'-MOM scheme could have chiral symmetry breaking effects disappearing as μ^{-2} . In [70] it was argued that these effects in RI-SMOM fall as μ^{-6} . A similar analysis may be performed with the data generated here: this is shown in Fig. 3.2. These results are shown in the $m_{\text{val}} \rightarrow 0$ limit, the limit being taken with a polynomial fit to $(am_{\text{val}})^2$ (discussed further below). The line in Fig. 3.2 is of the form B/μ^6 and is included to indicate that the chiral symmetry breaking μ suppression seen is approximately as fast as suggested in [70]. The difference of the scalar and pseudoscalar vertex functions shows a $1/\mu^6$ dependence but the individual vertex functions have a μ dependence which falls more slowly.

Rather than using simple point sources in the Dirac operator inversions necessary, momentum sources are instead used in order to improve the statistical precision of the results. (They also

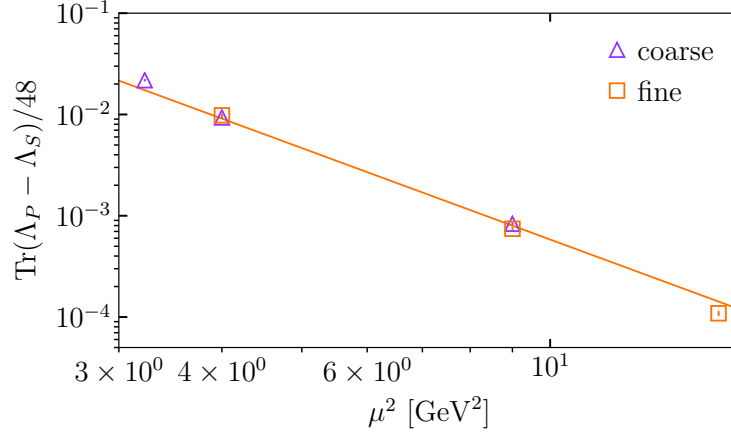


Figure 3.2: $P_{\Lambda_P} - P_{\Lambda_S}$ in the RI-SMOM scheme for sets 14 and 7 indicating the decrease in chirality violating effects with increasing μ . The line shown has the form B/μ^6 and is drawn to indicate the speed of this decrease.

allow for a neat construction of the required momentum space functions.) These sources have the form e^{ipx} where $p = \hat{p} + \pi A$ with A a hypercubic 4-vector as discussed in Section 3.1.1. These propagators are then Fourier transformed with momentum $-\hat{p} + \pi B$ where B is another hypercubic 4-vector and are combined into a 48×48 propagator matrix. This procedure gives very precise results on only a small number of configurations (typically 20 are used here) which makes calculations relatively inexpensive, despite the large number of inversions performed on each configuration: 32 when using the RI-SMOM scheme with staggered quarks there being 16 for both p_1 and p_2 as there are 16 hypercubic vectors (see Eq. 3.6).

The scalar vertex function is constructed as

$$G_{S,AB}(p_1, p_2) \equiv \left\langle \chi(\hat{p}_1 + \pi A) \left(\sum_x \bar{\chi}(x) \chi(x) e^{i(\hat{p}_1 - \hat{p}_2)x} \right) \bar{\chi}(\hat{p}_2 + \pi B) \right\rangle. \quad (3.16)$$

The quark fields can be contracted into propagators $S(\hat{p}_1 + \pi A, x)$ which are the solutions of the relevant momentum source ($MS = e^{-ip \cdot x}$ where M is the Dirac matrix) and the arguments of the propagator switched using γ_5 hermiticity ($(-1)^n M^\dagger (-1)^n = M$):

$$S(\hat{p} + \pi A, x) = (-1)^n S^\dagger(x, \hat{p} + \pi \tilde{A}), \quad \tilde{A} = A +_2 (1, 1, 1, 1), \quad (3.17)$$

with $n = x_0 + x_1 + x_2 + x_3$ and $+_2$ denoting summation modulo 2. $G_{S,AB}$ then becomes

$$\sum_x S(\hat{p}_1 + \pi A, x) e^{i(\hat{p}_1 - \hat{p}_2)x} (-1)^n S^\dagger(\hat{p}_2 + \pi \tilde{B}, x). \quad (3.18)$$

(In the case of the pseudoscalar there is an extra factor of $(-1)^n$ which cancels the one coming from γ_5 hermiticity. There is therefore no phase included in that case.) For other operators the staggered phase factors are more complicated; some are discussed in later Sections.

3.2.3 Data and statistics

The propagator and scalar vertex function were calculated on the range of lattices in Table 3.1. (This is a subset of those in Table 2.1 collected here for ease of reference.) The correct statistical procedure is to average propagators and vertex functions over configurations and then form the elements required for the calculation of Z factors from these averages. However, it is difficult to propagate the errors through procedures such as matrix inversion which are applied to the propagators and a bootstrap procedure on the values of Z_q and P_{Λ_S} on each configuration was therefore performed as an alternative method to the direct one. Bootstrap samples are formed by randomly choosing n values from the data on the n configurations, allowing for repeat choices, and then taking the mean of that selection. This is done N times to produce a dataset of N samples from which uncertainties and correlations are calculated. The same bootstrap sampling was used for both the Z_q and P_{Λ_S} so that correlations between the two could be included when the bootstrap samples were averaged and the ratio taken. In each case 1000 bootstrap samples were used, although there was no significant variation when 100 samples were used.

Different μ values were used to allow an examination of nonperturbative contributions which will vanish as μ is increased as discussed in Section 1.5.3. Ensembles with different sea quark masses were used at the coarse and fine lattice spacings in order to assess possible effects further. The results obtained for Z_m are given in Table 3.2, where the correlation matrices resulting from the simultaneous chiral extrapolations (discussed in 3.2.4) are also given. [Note that throughout this Chapter lattice spacings independent of the sea quark masses, chosen to coincide with the physical point, are used as they reduce sea quark mass dependence in this case. This is discussed

Table 3.1: Details of the range of lattice ensembles used in the RI-SMOM quark mass determination calculation. Those with $\beta = 6.0$ are referred to as coarse, $\beta = 6.3$ as fine and $\beta = 6.72$ as superfine.

Set	β	L_s	L_t	am_l^{sea}	am_s^{sea}	am_c^{sea}
4	6.0	20	64	0.008	0.040	0.480
5	6.0	24	64	0.0102	0.0509	0.635
6	6.0	24	64	0.00507	0.0507	0.628
7	6.0	32	64	0.00507	0.0507	0.628
8	6.0	40	64	0.00507	0.0507	0.628
9	6.0	32	64	0.00507	0.00507	0.628
10	6.0	32	64	0.00507	0.012675	0.628
11	6.0	32	64	0.00507	0.022815	0.628
12	6.0	48	64	0.00184	0.0507	0.628
14	6.30	48	96	0.00363	0.0363	0.430
15	6.30	64	96	0.00120	0.0363	0.432
16	6.72	48	144	0.0048	0.024	0.286

further in Section 6.1.] (There is a complication being ignored for simplicity here that on all ensembles except set 16 there was a slight mistuning of some of the μ values. This amounts to shifting 2, 3 and 4 GeV to 2.004, 3.005 and 4.007 GeV, which is accounted for when all values are run to the same reference scale of 3 GeV.)

3.2.4 Valence mass extrapolation

As the RI-SMOM scheme being used is defined at zero valence mass and the lattice calculation cannot be performed at $am_{\text{val}} = 0$ this limit must be taken using data at different valence masses. This will have the benefit of removing condensate contributions proportional to the quark mass. The precise form of the quark mass dependence of Z_m is not known, although the data displays very little variation with am_{val} and polynomial fits produce good χ^2 for all cases. These fits are performed simultaneously for each μ on a given lattice in order to correctly propagate the correlations between these variables.

A third order polynomial was used although this resulted in no significant difference from using second order:

$$Z_m(am_{\text{val}}) = Z_m + d_1 \frac{am_{\text{val}}}{am_s} + d_2 \left(\frac{am_{\text{val}}}{am_s} \right)^2 + d_3 \left(\frac{am_{\text{val}}}{am_s} \right)^3. \quad (3.19)$$

Priors decreasing with both m and μ were used to account for the expected decrease in the relevant condensate terms. The priors used for the m coefficients at 2 GeV were $\{0 \pm 0.1, 0 \pm 0.01, 0 \pm 0.001\}$ which were decreased by a factor of 2 for 3 GeV and a factor of 4 for 4 GeV. The Z_m prior was 1.0 ± 0.5 .

The fits all produced χ^2 values lower than 1 and Fig. 3.3 shows that the results of the superfine 3 GeV fit can be extended to the strange quark mass, which is not included in the fit, indicating the reliability of the procedure.

In principle the slope of the chiral extrapolations should be related to chiral condensate terms in the OPE (see Section 1.5.4), but the size of the observed slopes is too large to be consistent with this picture given that the value of $\langle \bar{\psi}\psi \rangle$ is ~ 0.0081 (GeV)⁴ and the observed effect is ~ -0.1 (GeV)⁴. This is shown in Fig. 3.4 where d_1 and d_2 can be seen as a function of μ . An alternative condensate explanation arises when considering terms proportional to the nongaugeinvariant condensate $\langle A^2 \rangle$, which are expected to be considerably larger.

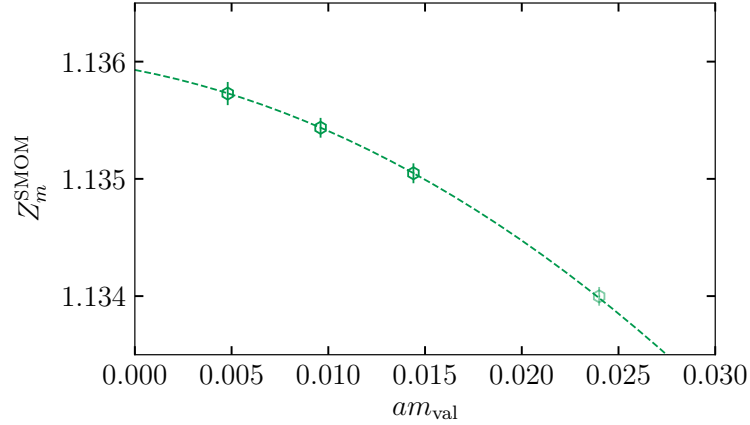


Figure 3.3: Plot of the chiral extrapolation of set 16 with $\mu = 3$ GeV. The highest mass point is not included in the fit but is shown to indicate that the fit operates well far from the point being extrapolated to.

3.2.5 Systematic uncertainties

Several sources of systematic uncertainty have been examined and appropriately addressed where necessary. The different lattices used differ by the values of the quark masses in the sea and the

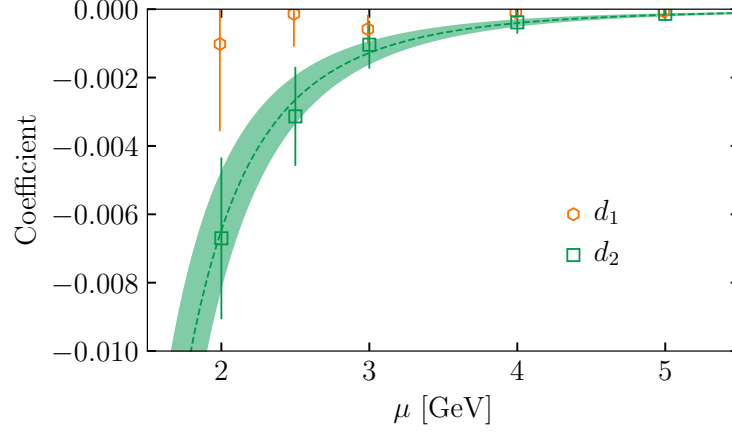


Figure 3.4: The linear and quadratic slopes of the valence mass dependence of Z_m^{SMOM} as a function of μ . These are d_1 and d_2 from Eq. 3.19. The curve is a fit of the form C/μ^4 to the d_2 data.

spatial and temporal extents. While terms allowing for sea quark mass effects were used in the continuum extrapolation it is still useful to check that no large effects are present and the lack of modelling of finite volume effects makes some level of direct study essential.

In addition to these systematics in the lattice setup there are also potential numerical systematics at this level of precision resulting from the use of various stopping conditions; specifically the Dirac matrix solver and gauge fixing tolerances. No significant effect is observed in the first case. Gauge fixing effects will be discussed in more detail in Section 3.2.5.

Volume dependence

Finite volume effects are associated with long wavelength (IR) modes. Matching factors are expected to be UV dominated and therefore no significant finite volume effects should be observed. In order to test this three lattices with the same parameters except for their spatial extent were used to calculate Z_m across a range of μ values, extending below 2 GeV. No significant variation was observed as shown in Fig. 3.5.

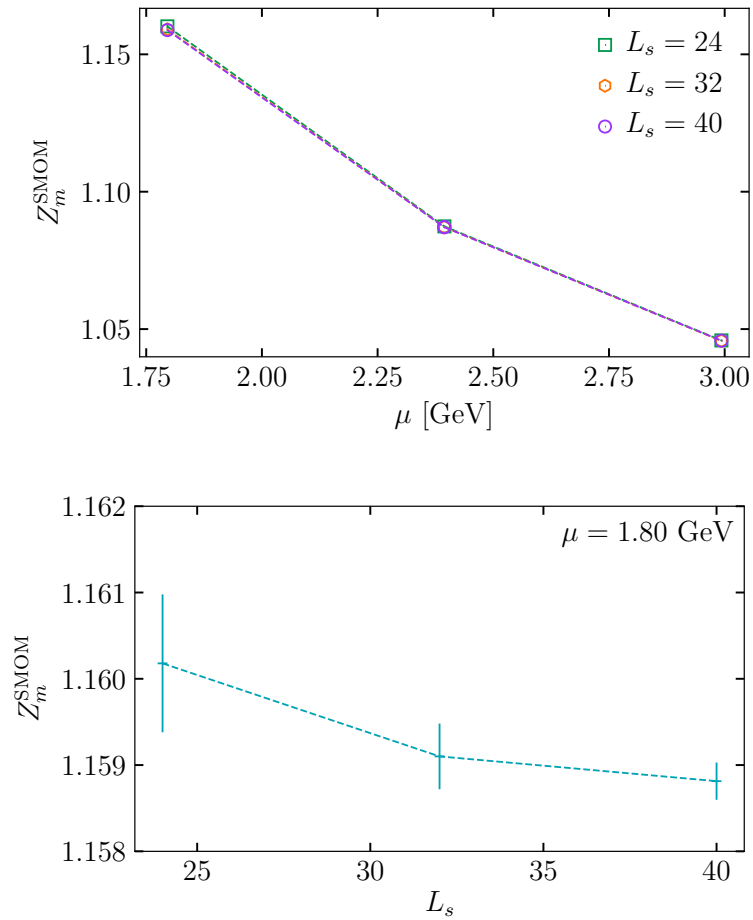


Figure 3.5: Upper: Z_m against μ for sets 6, 7 and 8. Lower: The three points at $\mu = 1.80$ GeV (upper left of upper plot) against the spatial extent of the lattice in lattice units. This indicates that the volume dependence of Z_m is negligible.

Sea quark mass dependence

The lattices detailed in Table 3.1 (crucially including those used in the final analysis) have a range of nonphysical sea quark masses and it is therefore necessary to address the issue of sea quark mass dependence of Z_m . This was done directly with lattices with a range of m_c^{sea} and m_s^{sea} on coarse lattices with a single valence mass. These comparisons for a range of μ values and a very large range of m_s^{sea} and m_c^{sea} are shown in Figure 3.6. There it can be seen that any effects are not visible, despite which we allow for terms to account for these effects in the continuum limit fit. This is the sea quark mass dependence we see using a lattice spacing defined to be fixed as the sea quark masses are varied. This definition of the lattice spacing has been chosen, partially, to make this variation small.

Gauge fixing tolerance dependence

Due to computational expense a full study of the dependence of Z_m on gauge fixing tolerance across the various lattices used was not conducted, but a limited study on mostly coarse lattices indicates some essential features. For example, there is a clear decrease in the difference between two Z_m values calculated with different gauge fixing tolerances with increasing μ . This is shown in Figure 3.8. This μ dependence can be explained in terms of decreasing gauge-noninvariant condensate contributions as discussed in Sections 1.5.3 and 1.5.4.

It is instructive to observe the convergence of the gauge fixing employed. In Figure 3.9 this is depicted as a scatter plot of the gauge trace link (which is minimised by the Landau gauge fixing procedure) against Z_m^{SMOM} at $\mu = 2$ GeV. There it can be seen that there is a significant residual effect from using the relatively high ϵ value of 10^{-7} which must be accounted for in the calculation as this was the tolerance used on Sets 5 , 7 , 12 , 14 and 15. In order to account for this, uncorrelated (as the possible correlations are not known) errors are added to all Z_m^{SMOM} values which are chosen to be the same on all lattices but to decrease with μ , as justified above. The values for 2, 3 and 4 GeV were respectively 0.0004, 0.0001 and 0.00002. This is of the order of the statistical errors. On Set 16 a gauge fixing tolerance of 10^{-14} was used in order to remove these problems from consideration⁴.

The RI-SMOM Z_m values we obtain are given in Table 3.2 along with their correlations. The factors for different μ values are correlated on each ensemble as correlations have been propagated through the valence mass extrapolation procedure.

⁴I thank Eduardo Follana and Eduardo Royo-Amondarain for performing this gauge fixing.

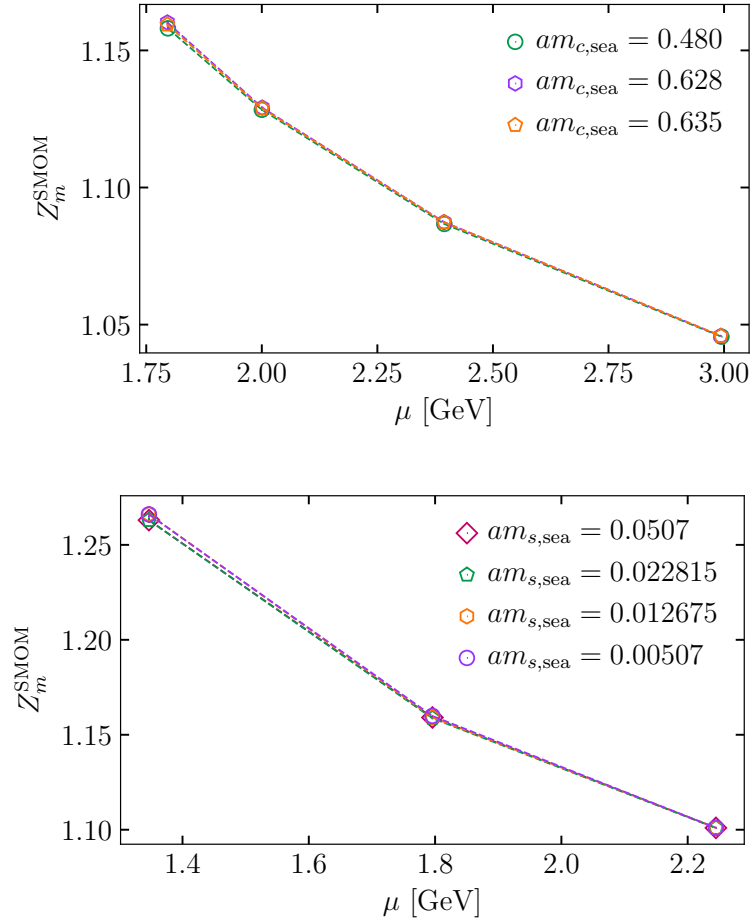


Figure 3.6: Plots indicating the charm and strange sea quark mass dependence of Z_m , which is clearly small. However, the final continuum extrapolation still allows for some sea mass dependence. The charm mass variation is shown on sets 4, 5 and 6 and the strange mass variation on sets 7, 9, 10 and 11.

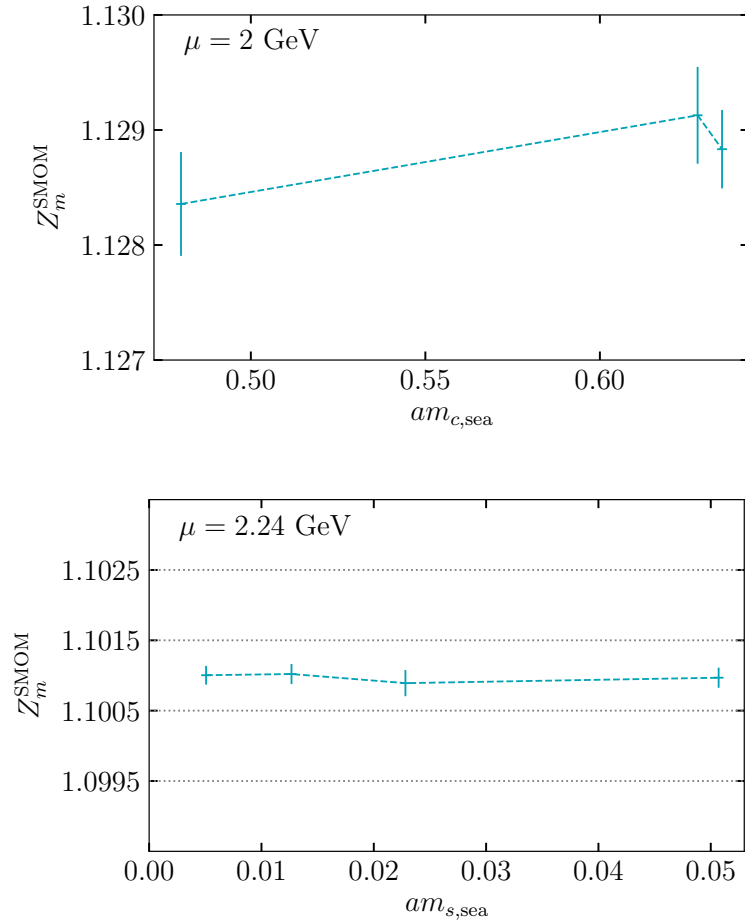


Figure 3.7: Z_m^{SMOM} against the charm (upper) and strange (lower) sea masses on the same ensembles as in Fig. 3.6. Here a μ value close to 2 GeV is chosen in each case. A clearer indication of the variation of the values in Fig. 3.6 is given with no variation beyond a few σ .

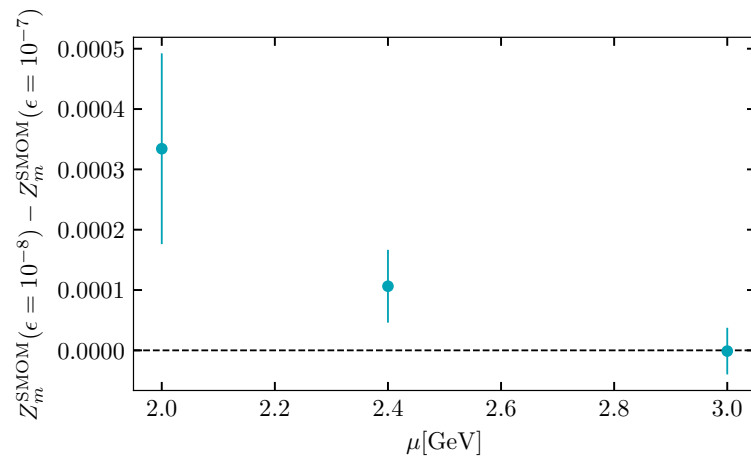


Figure 3.8: Gauge fixing difference as a function of μ on set 5. There is a clear decrease in this residual systematic as μ is increased.

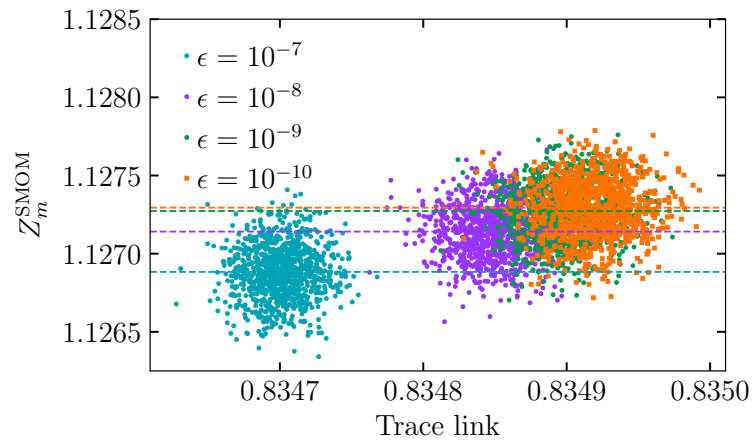


Figure 3.9: Scatter plot of bootstrapped Z_m against the trace link on set 7. Dashed horizontal lines indicate the mean value.

3.2.6 Electromagnetic corrections to Z_m

Given the level of precision achieved in Chapter 6 it becomes necessary to consider the impact of electromagnetic corrections on the determination of quark masses. Part of this is to calculate QED corrections to the mass renormalisation which we can do relatively easily in RI-SMOM.

Here we include quenched QED in our lattice calculations using the QED_L formulation of compact QED [71] (also see Section 2.9), in which all zero modes are set to zero, $A_\mu(k_0, \mathbf{k} = 0) = 0$ with A_μ the U(1) gauge field and k the momentum, in Landau gauge. Here, in our lattice calculation, we use $k = 2\sin(ap/2)$, with ap from Eq. 3.14. Our calculations are performed with a quark charge of $2e/3$ with $-e$ the charge of the electron (i.e. the up or charm quark charge).

We compute the QED correction to Z_m in the RI-SMOM scheme on a range of lattice spacings and at different μ values. These are presented in Table 3.3 as a ratio of the QCD+QED value to the pure QCD result. These are calculated including the correlations between the results.

Table 3.2: Data used in final fits including the correlation matrices across the μ values on a given set, coming from the simultaneous chiral extrapolation.

Set	$Z_m^{\text{SMOM}}(\mu), \mu$ in GeV :				correlation	
	2.004	2.500	3.005	4.007		
4	1.12967(40)	1.07935(20)	1.045628(90)	-	$\begin{pmatrix} 1 & 0.41 & 0.12 \\ 0.41 & 1 & 0.45 \\ 0.12 & 0.45 & 1 \end{pmatrix}$	
7	1.12990(42)	-	1.045434(61)	-	$\begin{pmatrix} 1 & -0.17 \\ -0.17 & 1 \end{pmatrix}$	
12	1.13061(22)	-	1.045518(53)	-	$\begin{pmatrix} 1 & 0.33 \\ 0.33 & 1 \end{pmatrix}$	
14	1.17726(45)	1.11954(15)	1.083082(77)	1.040445(25)	$\begin{pmatrix} 1 & -0.19 & 0.41 & 0.52 \\ -0.19 & 1 & -0.21 & -0.13 \\ 0.41 & -0.21 & 1 & 0.42 \\ 0.52 & -0.13 & 0.42 & 1 \end{pmatrix}$	
15	1.17748(35)	-	1.082955(55)	1.040350(23)	$\begin{pmatrix} 1 & 0.16 & 0.36 \\ 0.16 & 1 & 0.72 \\ 0.36 & 0.72 & 1 \end{pmatrix}$	
	2.000	2.500	3.000	4.000	5.000	correlation
16	1.24884(93)	1.18100(31)	1.13662(12)	1.083481(54)	1.053782(32)	$\begin{pmatrix} 1 & 0.35 & 0.26 & 0.19 & 0.22 \\ 0.35 & 1 & 0.32 & 0.45 & 0.22 \\ 0.26 & 0.32 & 1 & 0.26 & 0.10 \\ 0.19 & 0.45 & 0.26 & 1 & 0.59 \\ 0.22 & 0.22 & 0.10 & 0.59 & 1 \end{pmatrix}$

Table 3.3: The electromagnetic correction to Z_m for different values of μ and different lattice spacings are shown in the third column.

Set	μ [GeV]	$Z_m^{\text{SMOM}}(\mu)[(\text{QCD}+\text{QED})/\text{QCD}]$
6	2	1.001200(83)
14	2	1.001516(35)
16	2	1.001853(83)
6	2.5	1.000827(31)
6	3	1.000540(15)
14	3	1.000851(11)
16	3	1.001308(18)
14	4	1.0005001(21)
16	4	1.0009331(34)

3.3 Z_V : lattice vector current renormalisation

We now move to a discussion of the renormalisation of lattice vector currents. This largely follows the work presented in [2].

QCD matrix elements that cannot be evaluated within perturbation theory are of importance to many experimental programmes such as the overdetermination of the Cabibbo-Kobayashi-Maskawa matrix [72, 73] or the precision study of the anomalous magnetic moment of the muon [74] where the level of experimental precision requires a good understanding of hadronic contributions.

While the QCD vector current is conserved, and does not suffer renormalisation in the continuum, certain lattice definitions of the vector current are not and must be renormalised. A conserved vector current does exist on the lattice which is absolutely normalised. However, the conserved vector current construction for improved actions is considerably more complex than, for example, that of the local vector current. It is therefore typical to make use of the local vector current and perform a renormalisation calculation. There is the added benefit that local currents tend to be less noisy.

In the past the HPQCD collaboration have performed vector current renormalisation calculations by requiring that the vector form factor be 1 between two identical hadron states at zero momentum transfer [75].⁵ The form factor methods have been very successful in providing high precision renormalisation factors on MILC lattice ensembles with lattice spacings ranging from ~ 0.15 fm to ~ 0.09 fm with the value at a lattice spacing of ~ 0.06 fm extracted from a fit to the a^2 dependence of the lattice data. These Z_V s have been used in calculations such as the leading order hadronic vacuum polarisation (HVP) contribution to the anomalous magnetic moment of the muon presented in [77, 78]. However, they require high statistics 3-point correlators so for future calculations that require new evaluations of Z_V it is desirable to have a computationally cheaper methodology that is still capable of high precision. The use of momentum sources in conjunction with a momentum subtraction scheme offers this possibility as only a small number of configurations are required for good statistical precision. Momentum subtraction schemes also provide an, in principal, simple method for obtaining the renormalisation constants for a variety of currents.

⁵Vector current renormalisations have also been calculated from matching lattice QCD time moments to high order continuum QCD perturbation theory determinations of the same quantities [76].

In order to improve the results of [78] it will be necessary to include the effects of the electromagnetic interaction and the local vector renormalisation done in pure QCD will have to be appropriately corrected. If this were to be done using the form factor method it would require a large further computational effort. The use of momentum subtraction schemes on the lattice with the HISQ action has shown promise in providing a methodology that avoids the computation of large numbers of 3-point correlation functions required for good precision in the form factor calculation. There are, however, several systematic effects present in momentum subtraction scheme calculations, as already discussed. It is therefore desirable to perform a comparison of the Z_V values obtained from schemes such as RI-SMOM and the previous HPQCD results. We perform this comparison in both the RI-SMOM and the earlier developed RI'-MOM schemes and assess the viability for future calculations in both. This includes implementing the HISQ conserved current and checking the Ward-Takahashi identity used in the construction of the RI-SMOM scheme on the lattice, discussed further in Section 3.3.1.

Furthermore, the HISQ 1-link vector current renormalisation is required by ongoing calculations of the quark-line disconnected contribution to a_μ^{HVP} [79].

As mentioned in Section 3.2.2 (in the context of scalar and pseudoscalar currents) the RI-SMOM scheme was originally introduced with the motivation of improving the μ suppression of the difference between Λ_V and Λ_A (the axial vector current vertex function) relative to that observed in RI'-MOM. In Fig. 3.10 we demonstrate the improved performance of the RI-SMOM scheme in this respect with $(P_{\Lambda_V} - P_{\Lambda_A})$. The data points here have been extrapolated to zero valence mass using a similar procedure to that discussed in Sec. 3.3.3 (there is significant valence mass dependence of P_{Λ_A}) and are shown for lattice set 6 (see Table 3.5). We again note that the RI-SMOM data approximately demonstrates the expected μ^{-6} suppression [70].

3.3.1 The vector Ward-Takahashi identity on the lattice

Following the discussion in [2, 80, 81] the Ward-Takahashi identity (WTI) can be derived from the observation that the path integral is invariant under a local change of the fermion fields with unit Jacobian. The relevant transformation here is multiplication of the field $\psi(x)$ at the point x by the phase $e^{i\epsilon(x)}$ and $\bar{\psi}(x)$ by $e^{-i\epsilon(x)}$. Denoting the transformed field ψ^ϵ we have

$$\langle f(\psi, \bar{\psi}) \rangle = \langle f(\psi^\epsilon, \bar{\psi}^\epsilon) \rangle = \int \mathcal{D}\psi \mathcal{D}\bar{\psi} e^{-S[\psi^\epsilon, \bar{\psi}^\epsilon]} f(\psi^\epsilon, \bar{\psi}^\epsilon) \quad (3.20)$$

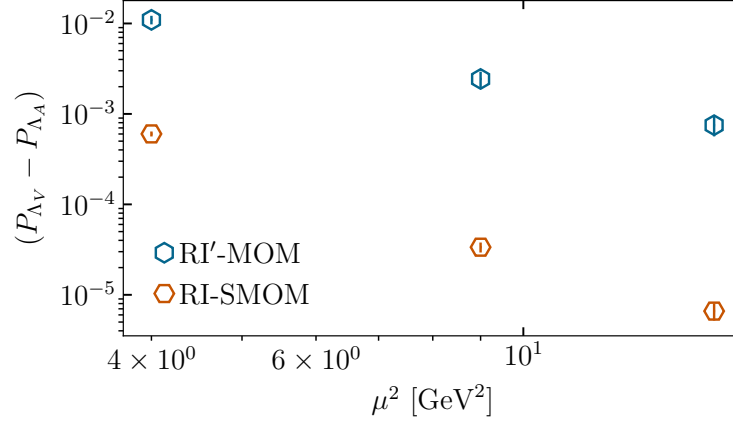


Figure 3.10: The difference between the (amputated, projected local) vector and axial vector vertex functions as a function of μ in the RI'-MOM and RI-SMOM schemes. The improvement obtained by using the RI-SMOM scheme is clear. These values have been extrapolated to zero valence quark mass and are shown for the finest lattice we use (set 16 in Table 3.5.)

and expanding to first order in ϵ

$$\langle -\Delta S \cdot f + \Delta f \rangle = 0, \quad (3.21)$$

where $\Delta S = S^\epsilon - S$ and $\Delta f = f^\epsilon - f$. Using $f = \bar{\psi}(y_1)\psi(y_2)$, Δf is the difference of propagators from y_1 and y_2 to x . ΔS is simply the derivative of the vector current $\partial_\mu J^\mu$. The same logic holds on the lattice but the derivative is replaced with a finite difference and J^μ becomes the, action dependent, lattice conserved vector current (to be discussed further below). Performing the Fourier transform of Eq. 3.21 gives a relationship between the vector vertex function G_V^μ and a difference of propagators

$$iq_\mu G_V^\mu(p_1, p_2) = S(p_1) - S(p_2) \quad (3.22)$$

with

$$G_V^\mu = \langle \psi(p_1) \left(\sum_x \bar{\psi}(x) \gamma^\mu \psi(x) e^{i(p_1 - p_2) \cdot x} \right) \bar{\psi}(p_2) \rangle \quad (3.23)$$

and $q_\mu = (p_1)_\mu - (p_2)_\mu$.

The existence of the vector WTI and the conservation of the vector current (in the continuum) mean that the vector current operator has no anomalous dimension and does not require renormalisation. This amounts to the fact that the WTI can be used in the construction of a renormalisation scheme to protect the lattice conserved vector current from renormalisation.

With RI'-MOM kinematics Eq. 3.22 becomes trivial, but another WTI can be derived in this limit by first taking the derivative w.r.t. the momentum. Note that, with the RI'-MOM definitions, Z_V and Z_q will not satisfy this WTI. The vector current in this scheme therefore suffers a μ dependent matching to the $\overline{\text{MS}}$ scheme which obscures the fact that the vector current is conserved and therefore absolutely normalised. The matching to $\overline{\text{MS}}$ was calculated in [82] and found to start at $\mathcal{O}(\alpha_s^2)$.

Consideration of the two point correlator $\langle \bar{\psi}(y_1) \psi(y_2) \rangle$ then leads to a relation between the derivative (or finite difference) of the vector vertex function and the difference between the propagators from the points y_1 and y_2 to the vector current insertion point x (this is a form of Eq. 3.21) [80]:

$$\begin{aligned} \langle \Delta_\mu J^\mu(x) \bar{\psi}(y_1) \psi(y_2) \rangle &= \delta_{y_2, x} \langle \bar{\psi}(y_1) \psi(x) \rangle \\ &\quad - \delta_{y_1, x} \langle \bar{\psi}(x) \psi(y_2) \rangle. \end{aligned} \quad (3.24)$$

For the case of the HISQ lattice action Δ_μ may be chosen to be either the forward or backward finite difference with the appropriate conserved currents being the backward and forward 3-link currents respectively. The forward HISQ conserved current is given by

$$\begin{aligned}
J^\mu = & \frac{1}{2}[\bar{\psi}(x)\gamma_\mu W_\mu(x)\psi(x + \hat{\mu}) + h.c.] \\
& + \frac{1}{16}[\bar{\psi}(x)\gamma_\mu X_\mu(x)\psi(x + \hat{\mu}) + h.c.] \\
& - \frac{1}{48}[\bar{\psi}(x - 2\hat{\mu})\gamma_\mu X_\mu(x - 2\hat{\mu})X_\mu(x - \hat{\mu})X_\mu(x)\psi(x + \hat{\mu}) \\
& + \bar{\psi}(x - \hat{\mu})\gamma_\mu X_\mu(x - \hat{\mu})X_\mu(x)X_\mu(x + \hat{\mu})\psi(x + 2\hat{\mu}) \\
& + \bar{\psi}(x)\gamma_\mu X_\mu(x)X_\mu(x + \hat{\mu})X_\mu(x + 2\hat{\mu})\psi(x + 3\hat{\mu}) + h.c.]
\end{aligned} \tag{3.25}$$

where W are HISQ links and X are the links after the first level of HISQ smearing in the notation of [39]. The backward conserved current is the same but with $x \rightarrow x - \hat{\mu}$ and $x + \hat{\mu} \rightarrow x$.

The Fourier transform of Eq. 3.24 can be performed, giving

$$(1 - e^{iaq_\mu}) \int d^4x d^4y_1 d^4y_2 e^{iqx} e^{-ip_1 y_1} e^{ip_2 y_2} \langle J^\mu(\tilde{x}) \bar{\psi}(y_1) \psi(y_1) \rangle, \tag{3.26}$$

on the left handside where \tilde{x} is the midpoint of x and $x + \hat{\mu}$, which is where the current sits. The right handside is simply

$$\int d^4x d^4y_1 e^{ip_1 x} e^{-ip_1 y_1} \langle \bar{\psi}(y_1) \psi(x) \rangle - \int d^4x d^4y_2 e^{-ip_2 x} e^{ip_2 y_2} \langle \bar{\psi}(x) \psi(y_2) \rangle = S(p_1) - S(p_2). \tag{3.27}$$

Multiplying both sides of Eq. 3.24 by the two inverse propagators gives

$$-\frac{2i}{a} \sin\left(\frac{aq_\mu}{2}\right) \Lambda_V^\mu(p_1, p_2) = -S^{-1}(p_1) + S^{-1}(p_2). \tag{3.28}$$

We have tested both Eq. 3.24 and Eq. 3.28 using the forward conserved current in numerical calculations. This is illustrated in Fig. 3.11 for the momentum space case. There the solid line is the momentum factor $-\frac{2i}{a} \sin\left(\frac{aq_\mu}{2}\right)$ and the points are numerical results on a single configuration for the ratio $\Lambda_V / (S^{-1}(p_2) - S^{-1}(p_1))$ averaged over all matrix components. We also checked that the real part is zero. The different points demonstrate the fulfillment of the Ward-Takahashi momentum space identity on the lattice for different values of the quark mass, momentum scale

and for different gauges.

It is important to understand this identity on the lattice as it is used to construct the vector vertex projector used in the RI-SMOM scheme. The fact that there is an exact lattice Ward-Takahashi identity allows the construction of a Z_V which is always 1, independent of the momenta or lattice spacing. Following the continuum derivation of the vector vertex projector in [61], we take the spin colour trace of Eq. 3.28 (with appropriate normalisation) multiplied by \not{q} to obtain

$$\begin{aligned} & -\frac{1}{48\tilde{q}^2} \frac{2i}{a} \sin\left(\frac{aq_\mu}{2}\right) \text{Tr}(\Lambda_V^\mu \not{q}) \\ & = \frac{1}{48\tilde{q}^2} [\text{Tr}(\not{q}S^{-1}(p_2)) - \text{Tr}(\not{q}S^{-1}(p_1))]. \end{aligned} \quad (3.29)$$

(Note that the correct gamma matrix in \not{q} is $\overline{(\gamma_\mu \otimes \mathbf{1})}$ due to the taste singlet nature of the inverse propagator.) Here we have started using the momentum discretisation relevant to the calculation of Z_q , i.e. $\tilde{q} = \sin(p) + \sin^3(p)/6$ (see Eq. 3.13). If the r.h.s of Eq. 3.29 is equal to $(1/48q^2)\text{Tr}(\not{q}S^{-1}(q))$, as it is in continuum perturbation theory, then the r.h.s is Z_q and the l.h.s may be identified as the required denominator (with Z_q the numerator) in the definition of $Z_V \equiv Z_q/P_{\Lambda_V}$ such that $Z_V = 1$ for the conserved current. The requirement is

$$\text{Tr}(\not{q}S^{-1}(p_2)) - \text{Tr}(\not{q}S^{-1}(p_1)) = \text{Tr}(\not{q}S^{-1}(q)). \quad (3.30)$$

This equality would have to hold including discretisation effects and non-perturbative condensate contributions. Assuming that the inverse propagator takes the form $i\not{p}\Sigma_V(p^2) + \Sigma_S(p^2)$ then this is true. We observe this to be the case, at least once the configuration average has been taken, to better than 0.05%, as demonstrated in Fig. 3.12.

The general form of the staggered quark propagator is derived in [64] from symmetry constraints. We can use this form to analyse the discretisation errors that we expect to appear in the lattice propagator and whether we expect the equality Eq. 3.30 to hold. Considering the massless case the leading terms are

$$S^{-1}(\hat{p}) = c_1 \hat{p}_\mu \overline{(\gamma_\mu \otimes \mathbf{1})} + c_2 \sum_{\mu\nu\rho} \hat{p}_\mu (\hat{p}_\nu)^3 (\hat{p}_\rho)^5 \overline{(\gamma_{\mu\nu\rho} \otimes \mathbf{1})} \quad (3.31)$$

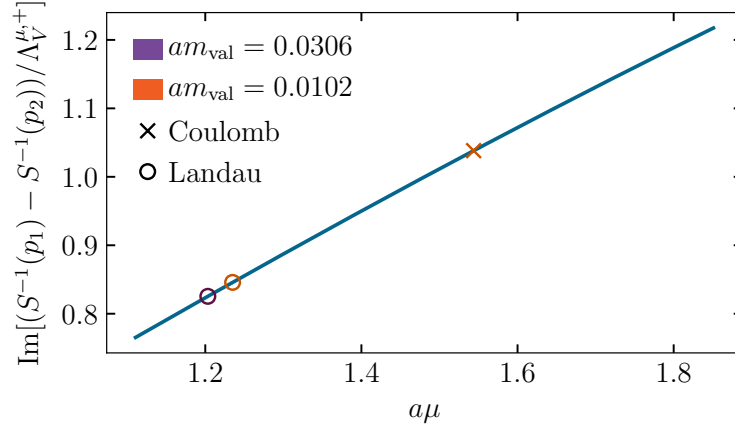


Figure 3.11: Demonstration of the vector Ward-Takahashi identity in momentum space on the lattice. The solid line is the values of $-\frac{2i}{a} \sin\left(\frac{aq\mu}{2}\right)$ as a function of q represented by the quantity $x + \theta/2$ which is the momentum divided by $2\pi/L$ with L the extent of the lattice in the relevant direction. The points correspond to lattice results for the ratio $\Lambda_V/(S^{-1}(p_2) - S^{-1}(p_1))$ (averaging over all matrix components) on a single configuration with crosses representing Coulomb gauge fixing and the circles Landau gauge fixing. Orange points correspond to a valence mass of $am_{\text{val}} = 0.0306$ while purple points correspond to 0.0102. The Ward-Takahashi identity requires these points to lie on the line.

with $\gamma_{\mu\nu\rho} = \gamma_\mu\gamma_\nu\gamma_\rho$. It is clear from this that the first term will not affect Eq. 3.30. The second term also presents no problem when RI-SMOM kinematics are used as various factors of μ^2 can be factored out of the terms with momentum to the third and fifth powers. There is therefore nothing here to suggest Eq. 3.30 will not hold.

The leading order condensates that might appear as corrections to Eq. 3.30 can be analysed using the techniques explained in the Appendix of [1]. As the leading $\langle A^2 \rangle$ contribution goes like $\sim r \cdot s$ for $\text{Tr}(\not{r}S^{-1}(s))$ this term is the same on both the l.h.s and r.h.s of Eq. 3.30. This must be the case for the WTI to hold fully nonperturbatively as it should. It means that the RI-SMOM Z_V will not contain condensate contamination.

3.3.2 Tree level vertex functions

It is necessary to pause to discuss a technical element relating to some of the vector currents we will be using. In cases where the spin and taste of the operator insertion differ it is necessary to

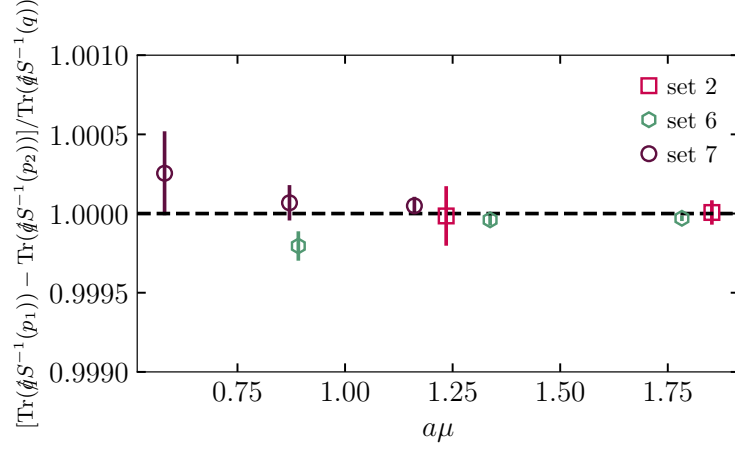


Figure 3.12: Test of the identity in Eq. 3.30. The squares are for set 5, the hexagons are set 14 and the circles are set 16.

divide out the tree level discretisation effects that are introduced. This will then give Z values of 1 for the free theory as well as reducing the discretisation effects.

Matrix elements of the covariant operator defined in Eq. 3.11 (with appropriate gauge links multiplied in) can be easily computed at tree level. For the 1-link vector case $\Delta = \pm 1$ in the μ direction. For RI'-MOM this gives the tree level matrix element of the operator $M_{ST}^{(0),\text{cov}}$ as

$$\mathcal{M}_{ST}^{(0),\text{cov}} = \sum_n \sum_{\Delta} e^{i\hat{p}\cdot n} e^{-i\hat{p}\cdot(n+\Delta)} \overline{(\gamma_S \otimes \xi_T)_{n,n+S-T}} \quad (3.32)$$

$$= \sum_{\Delta} e^{-i\hat{p}\cdot\Delta} \overline{(\gamma_S \otimes \xi_T)_{A,B}} = \prod_{\mu} \cos(\hat{p}_{\mu}(S-T)_{\mu}) \overline{(\gamma_S \otimes \xi_T)_{A,B}}, \quad (3.33)$$

leading to a division by $\prod_{\mu} \cos(\hat{p}_{\mu}(S-T)_{\mu})$ or in this case just $\cos(\hat{p}_{\mu}(S-T)_{\mu})$ for the vector current in direction μ . RI-SMOM differs in that the quark fields carry different momenta, giving the result

Table 3.4: Tree-level matrix elements of the various operators in the different schemes that we consider. We also give the projectors that we use in the construction of each Z_V . For definitions of \tilde{q} in each case we refer to the main text. S and T are the vectors describing the spin and taste of the operator (see [64]). The first column labels both the scheme (SMOM for RI-SMOM and MOM for RI'-MOM) and the operator. The local operator is labelled "loc", the conserved current operator "con" and the 1-link operators of Eqs. 3.46 and 3.47 "1link-fwd" and "1link-cov" respectively.

Operator/scheme	Projector	$\mathcal{M}^{(0)}$
loc/SMOM	$\frac{1}{48(\hat{q})^2} \tilde{q} \tilde{q}'$	1
con/SMOM	$\frac{1}{48(\hat{q})^2} (1 - e^{iq_\mu}) \tilde{q}'$	1
1link-fwd/SMOM	$\frac{1}{48(\hat{q})^2} \tilde{q} \tilde{q}'$	$\frac{1}{2}(e^{ip_2} + e^{-ip_1})$
1link-cov/SMOM	$\frac{1}{48(\hat{q})^2} \tilde{q} \tilde{q}'$	$\prod_\mu \cos(p_2^\mu)$
loc/MOM	$\overline{(\gamma_\mu \otimes \xi_\mu)}$	1
con/MOM	$\overline{(\gamma_\mu \otimes \mathbf{1})}$	$\prod_\mu \left(\frac{9}{8} \cos(p_1^\mu (S - T)^\mu) + \frac{1}{8} \cos(3p_1^\mu (S - T)^\mu) \right)$
1link-fwd/MOM	$\overline{(\gamma_\mu \otimes \mathbf{1})}$	$\prod_\mu \cos(p_1^\mu (S - T)^\mu)$
1link-cov/MOM	$\overline{(\gamma_\mu \otimes \mathbf{1})}$	$\prod_\mu \cos(p_1^\mu (S - T)^\mu)$

$$\mathcal{M}_{ST}^{(0),\text{cov}} = \sum_n \sum_\Delta e^{i\hat{q}\cdot n} e^{i\hat{p}_1\cdot n} e^{-i\hat{p}_2\cdot(n+\Delta)} \overline{(\gamma_S \otimes \xi_T)_{n,n+S-T}} \quad (3.34)$$

$$= \sum_\Delta e^{-i\hat{p}_1\cdot\Delta} \overline{(\gamma_S \otimes \xi_T)_{A,B}} = \prod_\mu \cos(\hat{p}_{1,\mu}(S - T)_\mu) \overline{(\gamma_S \otimes \xi_T)_{A,B}}. \quad (3.35)$$

The matrix elements for the various operators we consider are collected in Table 3.4. These are obtained through purely kinematic calculations. Further details can be found in [64] App. D, [83] and [84].

3.3.3 Lattice calculation

We perform calculations on the MILC 2+1+1 HISQ ensembles [42, 85] listed in Table 3.5. We use broadly the same calculational set up as in [1] and Section 3.2 but here we are considering vector vertex functions as opposed to scalar. The local vector vertex function is constructed in much the same way as the scalar case but with a different staggered phase corresponding to a different gamma structure, which differs between different currents. For the RI-SMOM scheme

the local current is given by

$$G_{V,AB}(p_1, p_2) = \frac{1}{n_{\text{cfg}}} \sum_{x, \text{cfg}} S(\hat{p}_1 + \pi A, x) e^{-(\hat{p}_1 - \hat{p}_2)x} (-1)^{x+x_\mu} S^\dagger(\hat{p}_2 + \pi \tilde{B}, x). \quad (3.36)$$

Here $(-1)^x = (-1)^{x_1+x_2+x_3+x_4}$ and arises from γ_5 -hermiticity of the Dirac matrix, as before. We follow the notation of [1] where p' denotes the momentum in a reduced Brillouin zone used to separate momentum and taste information. As explained in Section 3.1.2 we need to perform 32 inversions on each configuration to construct the propagators and vertex functions when using staggered quarks. From these 32 inversions we can construct all vertex functions for both the RI-SMOM and RI'-MOM schemes. For RI'-MOM \hat{p}_2 is replaced by \hat{p}_1 so that there is no exponential factor in the equivalent of Eq. 3.36. The point-split operators are similarly constructed although these operators are taste singlets which changes the required phase and the propagators have different spatial locations. This separation slightly complicates the factor coming from γ_5 -hermiticity. Twisted boundary conditions are utilised to give the incoming and outgoing quarks arbitrary momenta. The use of momentum twists for point-split operators is slightly complicated.

The twisted propagator is defined as

$$\tilde{S}(x, p) = e^{-i(\theta/2)x} S(x, p + (\theta/2)). \quad (3.37)$$

Not writing the links for brevity, for a point-split operator we want (using a 1-link operator as an example)

$$\begin{aligned} & \sum_x \gamma_5 e^{i(p_1 + \frac{\theta_1}{2})x} S^\dagger(x, p_1 + \frac{\theta_1}{2}) \\ & \times \gamma_5 \Gamma e^{-i(p_2 + \frac{\theta_2}{2})x} S(x + \hat{\mu}, p_2 + \frac{\theta_2}{2}) \\ & = \sum_x \gamma_5 e^{ip_1 x} \tilde{S}^\dagger(x, p_1) \gamma_5 \Gamma e^{-ip_2 x} e^{i(\theta_2/2)\hat{\mu}} \tilde{S}(x + \hat{\mu}, p_2). \end{aligned} \quad (3.38)$$

There is a factor of $\exp(i(\theta_2/2)\hat{\mu})$ here that does not arise in the local case. Similar factors arise for the RI'-MOM setup.

Table 3.5: Simulation parameters for the MILC gluon field ensembles that we use, labelled by set number in the first column. $\beta = 10/g^2$ is the bare QCD coupling and L_s and L_t give the lattice dimensions. am_l^{sea} , am_s^{sea} and am_c^{sea} give the sea quark masses in lattice units. Set 1 will be referred to in the text as ‘very coarse’, sets 5–8 ‘coarse’, sets 14 as ‘fine’ and set 16 as ‘superfine’.

Set	β	L_s	L_t	am_l^{sea}	am_s^{sea}	am_c^{sea}	u_0	w_0/\tilde{a}
2	5.80	24	48	0.00640	0.0640	0.828	0.820192(14)	1.1322(14)
5	6.0	24	64	0.0102	0.0509	0.635	0.834613(14)	1.4075(18)
6	6.0	24	64	0.00507	0.0507	0.628	-	1.4075(18)
7	6.0	32	64	0.00507	0.0507	0.628	-	1.4075(18)
8	6.0	40	64	0.00507	0.0507	0.628	-	1.4075(18)
14	6.30	48	96	0.00363	0.0363	0.430	0.852477(9)	1.9500(21)
16	6.72	48	144	0.0048	0.024	0.286	0.870935(5)	2.994(10)

All gauge field configurations used are numerically fixed to Landau gauge by maximising the trace over the gluon field link with a gauge fixing tolerance of $\epsilon = 10^{-14}$. This is enough to remove the difficulties related to loose gauge fixing discussed in Section 3.2.5 and [1]. A bootstrap method is again used to estimate all uncertainties with correlations. Bootstrap samples are formed for each Z_q and each P_{Λ_V} before the bootstrap average is taken.

The anomalous dimension of the vector current operator is zero (ignoring the issue with RI'-MOM) which leads to the expectation that there should be no μ dependence. However, discretisation artefacts appearing as even powers of $a\mu$ will give lattice data some, hopefully small, μ dependence which will be removed when taking the continuum limit. In order to determine the size of these effects, and any possible power corrections, we again perform calculations at multiple values of μ and a . The same kinematic setup as for the mass renormalisation calculation [1] is used here, given in Eq. 3.14. We also use the same μ values of 2, 2.5 and 3 GeV on coarse lattices and 2, 3 and 4 GeV on fine and superfine ensembles. It is generally important to choose momenta such that $\Lambda_{\text{QCD}} \ll \mu \ll \pi/a$ in order to avoid both large discretisation effects and nonperturbative power corrections. However, in some cases we also make use of data at the low μ value of 1 GeV, discussed further in Section 3.3.5. This data is included to further demonstrate the lack of condensate contributions in some cases. If the current is not the conserved current, for example the local vector current, then the value of Z_V will have lattice spacing dependence which can be expressed, using lattice perturbation theory, as a power series in $\alpha_s(\Lambda_{\text{UV}})$ with Λ_{UV} an appropriately chosen scale near the cutoff provided by the finite lattice spacing. The

coefficients of this expansion should not depend on the details of the scheme employed (although they will depend on the details of the lattice action) as long as $Z_V = 1$ in the continuum and can therefore be used as a useful check on the agreement of different methodologies.

Valence mass dependence

As already discussed, all of our results are determined at small but non-zero quark mass. This has no impact on the calculation. Again, it is necessary to calculate each Z_V at different masses and then extrapolate to the $am_{\text{val}} = 0$ point, as in Section 3.2.4. To do this we perform all calculations at three masses corresponding to the light quark sea mass on a given ensemble, am_l , and at $2am_l$ and $3am_l$.

We follow the procedure used in [1] for the mass renormalisation in the RI-SMOM scheme and extrapolate Z_V results using a polynomial in am_{val}/am_s :

$$Z_V(am_{\text{val}}, \mu) = Z_V(\mu) + d_1(\mu) \frac{am_{\text{val}}}{am_s} + d_2(\mu) \left(\frac{am_{\text{val}}}{am_s} \right)^2. \quad (3.39)$$

We find no need for higher powers of am_{val}/am_s here as the valence mass dependence of Z_V is observed to be very mild in all cases.

For the conserved current there should be no valence mass dependence as the vector WTI holds irrespective of the mass as long as the masses are degenerate. This will protect all RI-SMOM vector currents from nonperturbative contributions in the continuum that are proportional to the mass. This will not be the case for the RI'-MOM scheme. However, we still observe a near negligible valence mass dependence in the RI'-MOM scheme. This is shown in Fig. 3.13.

For the prior on $Z_V(\mu)$ in Eq. 3.39 we use 1.0 ± 0.2 with different priors for the coefficients d_i of $\{0 \pm 0.1, 0 \pm 0.01\}$ at $\mu = 2$ GeV with the widths decreased according to μ^{-2} .

Any sea quark mass dependence should be suppressed relative to the valence mass dependence by powers of α_s . As the valence mass dependence is already negligible the sea mass dependence should be tiny. Above and in [1] it was shown that the sea quark mass dependence of Z_m (a quantity with larger, although still small, valence mass dependence) was unobservable at this level of precision and we therefore expect the same to be true of Z_V .

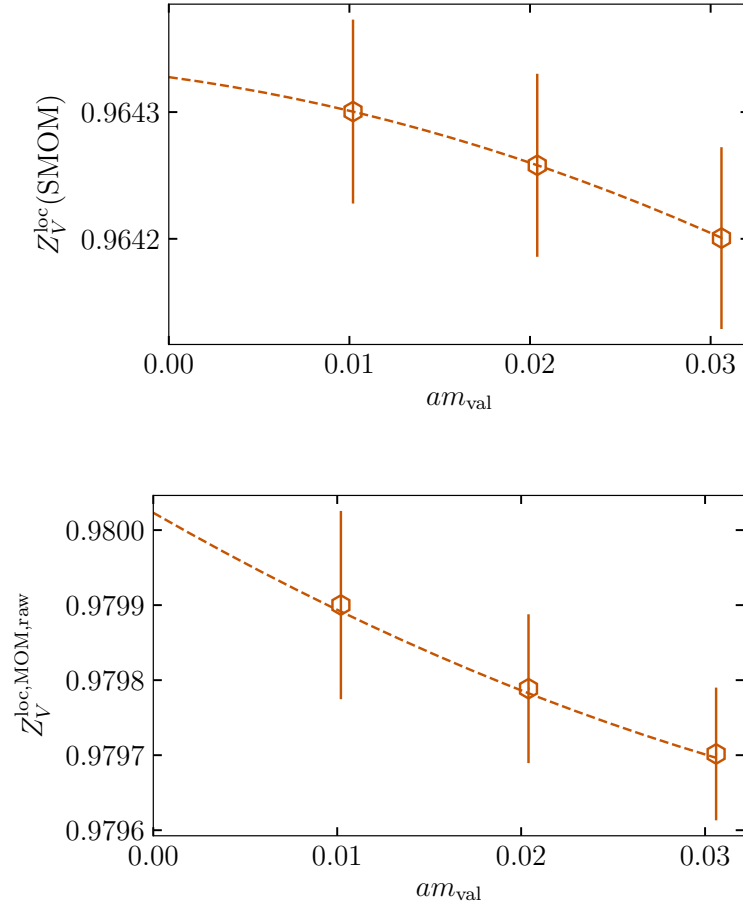


Figure 3.13: Valence mass dependence of local Z_V values in the RI-SMOM and RI'-MOM schemes. Upper: Local Z_V in the RI-SMOM scheme at $\mu = 3$ GeV. Lower: Local Z_V in the RI'-MOM scheme at $\mu = 3$ GeV. The strongest valence mass dependence we observe is in the local vector current renormalisation in the RI'-MOM scheme, which can be seen to be very small. The label $Z_V^{\text{loc, MOM, raw}}$ indicates that these are local MOM Z_V values before they are multiplied by a conversion factor to the $\overline{\text{MS}}$ scheme.

We divide vertex functions by the tree-level values given in Table 3.4. These are trivial when the current is local.

3.3.4 Conserved vector current renormalisation

Throughout we consider both the RI-SMOM and RI'-MOM schemes which will henceforth be denoted SMOM and MOM. We will also consider the variation of the SMOM scheme that uses the same vector vertex projector as the MOM scheme, which then obviously requires different conditions to obtain a wavefunction renormalisation such that $Z_V = 1$ in the continuum. We refer to this scheme as SMOM γ_μ . The conserved vector current renormalisation in the SMOM scheme, as discussed in Section 3.3.1, is 1 to high precision, independent of μ and the lattice spacing, as well as the mass of the quark.

However, in the MOM scheme the vector WTI for renormalised quantities has to be abandoned due to the constraints of numerical implementation of derivatives and the vector current suffers a renormalisation even in the continuum. The matching to $\overline{\text{MS}}$ begins at order α_s^2 and is given in [62] through order α_s^3 . We therefore multiply all our MOM results by this factor. These conversion factors for $n_f = 4$ are collected for the various μ values we use in Table 3.6. The lack of protection from the Ward-Takahashi identity means that $Z_V^{\text{con}}(\text{MOM})$ is expected to contain discretisation errors and condensate contributions. In order to remove the leading discretisation effects and ensure that $Z_V^{\text{con}}(\text{MOM}) = 1$ in the noninteracting theory we divide P_{Λ_V} by the tree-level matrix element of the MOM conserved vector operator given in Table 3.4. This is a procedure common to all point-split operators we use and more detail is provided above in Section 3.3.2. We then fit the $\overline{\text{MS}}$ converted $Z_V^{\text{con}}(\text{MOM})$ values to the form

$$\begin{aligned}
Z_V^{\text{con}}(\text{MOM})(a, \mu) &= 1 + \sum_i c_{a^2\mu^2}^{(i)} (a\mu/\pi)^{2i} \\
&+ \sum_i c_{\alpha a^2\mu^2}^{(i)} (a\mu/\pi)^{2i} \alpha_{\overline{\text{MS}}}(1/a) \\
&+ \sum_j c_{\text{cond}}^{(j)} \alpha_{\overline{\text{MS}}}(\mu) \frac{(1 \text{ GeV})^{2j}}{\mu^{2j}} \\
&\times [1 + c_{\text{cond},a^2}^{(j)} (a\Lambda/\pi)^2] + c_\alpha \alpha_{\overline{\text{MS}}}^4(\mu),
\end{aligned} \tag{3.40}$$

which constrains $Z_V^{\text{con}}(\text{MOM})$ to be 1 in the continuum once condensates are removed. Here

Table 3.6: Conversion factors from the momentum subtraction schemes we consider to $\overline{\text{MS}}$ at the μ values used in this calculation, calculated with $n_f = 4$ using the results of [62]. Z_V values in momentum subtraction schemes are multiplied by these factors to obtain Z_V in the $\overline{\text{MS}}$ scheme. These factors are multiplied into any RI'-MOM results that are not a ratio of Z_V for different currents.

μ [GeV]	$Z_V^{\overline{\text{MS}}/\text{RI}'\text{-MOM}}$	$Z_V^{\overline{\text{MS}}/\text{RI-SMOM}}$
2	0.99118(38)	1
2.5	0.99308(26)	1
3	0.99420(20)	1
4	0.99549(14)	1

$\alpha_{\overline{\text{MS}}}(\mu)$ is the value of the strong coupling in the $\overline{\text{MS}}$ scheme at the scale μ calculated from running the value obtained in [27] using the four-loop QCD β function. The fit allows for discretisation errors of the generic form $(a\mu)^{2i}$ and terms $\mathcal{O}(\alpha_s(a\mu)^{2i})$. These further suppressed terms are included as the very small uncertainties on the data mean that these terms may have non-negligible effects. The final term allows for systematic uncertainty from the missing α_s^4 term in the $\overline{\text{MS}}$ conversion factor. All coefficients are given a prior of 0 ± 1 , except c_α which is given a prior of 0 ± 5 based on the lower order coefficients. The condensate terms start at $1/\mu^2$ to allow for the gauge-noninvariant $\langle A^2 \rangle$ condensate present in the operator product expansion (OPE) of the inverse propagator. For the MOM kinematic setup it is not possible to perform an OPE for vertex functions as they are not short-distance quantities. However, the OPE is still valid for Z_q and as this is a component of Z_V we still allow for terms of this form. The results of this fit are shown in Fig. 3.14. The fit has a χ^2/dof of 0.6 and gives a sizeable condensate contribution of

$$c_{\text{cond}}^{(1)} = 0.154(54). \quad (3.41)$$

If the condensate terms are not included then the quality of the fit is very poor with a χ^2/dof of 7.7, further indicating their necessity. This shows that features of the data are well understood and that similar fits should be viable for other quantities. The fit also indicates the importance of the condensate contribution to Z_V in schemes not protected by the Ward-Takahashi identity, which appear at a 1% level for $\mu = 2$ GeV.

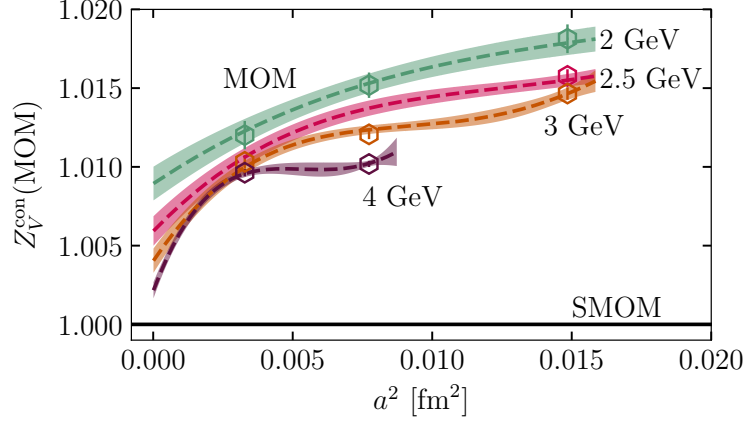


Figure 3.14: $Z_V^{\text{con}}(\text{MOM})$ for μ values 2, 2.5, 3 and 4 GeV. The fit shown accounts for discretisation errors and condensate contributions, which prove to be necessary for a good fit. Discretisation errors proportional to α_s are also allowed. The $\alpha_s(a\mu)^2$ coefficient is very small, consistent with the suppression of one-loop taste changing interactions when using the HISQ action [39]. The disagreement between the different μ values after the continuum extrapolation is performed is the result of condensate contributions.

3.3.5 Local vector current renormalisation

Here we examine the local vector current renormalisation factor in the various schemes we have discussed. Our aim is to compare the results we obtain with those found in [75]. The two cases should only differ by discretisation effects in the SMOM scheme, since both approaches respect the WTI, and may have nonperturbative μ dependent effects in the MOM scheme. We should therefore find that the difference of the SMOM renormalisation factors and the Z_V factors obtained from form factor methods in [75] can be fit to a form that is pure discretisation effects. While we do not expect to see nonperturbative effects in the SMOM scheme we allow for such effects in our fit function. The MOM case is expected to require such terms suppressed by even powers of μ as well as a term allowing for the next-order missing term in the perturbative matching calculation between the MOM and $\overline{\text{MS}}$ schemes. All of the momentum subtraction results obtained and analysed in this Section are given in Table 3.7.

Table 3.7: Local vector current renormalisation factors at the values of μ used in our calculations for different schemes at the lattice spacings we use. R_c denotes that we take the ratio with the conserved current renormalisation in that scheme. The values for $Z_V^{\text{loc}}(\text{MOM})$ given here are the raw RI'-MOM number that we obtain multiplied by the $\overline{\text{MS}}$ conversion factors of Table 3.6.

Set	μ [GeV]	$Z_V^{\text{loc}}(\text{MOM})$	$Z_V^{\text{loc}}(\text{MOM}_{R_c})$	$Z_V^{\text{loc}}(\text{SMOM})$	$Z_V^{\text{loc}}(\text{SMOM}_{\gamma\mu, R_c})$
2	1	-	-	0.9743(11)	-
5	1	-	-	0.9837(20)	-
2	2	0.97359(64)	0.95426(40)	0.95932(18)	0.87610(26)
5	2	0.98771(85)	0.97012(25)	0.97255(22)	0.91864(25)
14	2	0.99784(79)	0.98292(44)	0.98445(11)	0.959434(58)
16	2	1.00202(89)	0.99012(19)	0.99090(36)	0.982435(21)
5	2.5	0.97968(34)	0.96447(17)	0.96768(12)	0.89506(19)
5	3	0.97434(26)	0.96027(23)	0.964328(75)	0.87733(21)
14	3	0.98785(28)	0.97608(14)	0.977214(35)	0.930025(40)
16	3	0.99651(43)	0.98633(11)	0.98702(11)	0.969563(42)
14	4	0.98090(16)	0.971009(90)	0.972415(18)	0.905823(40)
16	4	0.99241(21)	0.982942(40)	0.983270(54)	0.954992(30)

MOM

The difference of the local vector current renormalisation results from form factor methods $Z_V^{\text{loc}}(\text{F}(0))$ and the renormalisation factor in the MOM scheme $Z_V^{\text{loc}}(\text{MOM})$ are shown in Fig. 3.15. We denote the difference ΔZ_V^{loc} . The data have been fit to the form

$$\begin{aligned}
\Delta Z_V^{\text{loc}}(\tilde{a}, \mu) = & \sum_{i=1}^3 [c_{a^2\mu^2}^{(i)} (\tilde{a}\mu/\pi)^{2i} + c_{\alpha a^2\mu^2} (\tilde{a}\mu/\pi)^{2i} \alpha_{\overline{\text{MS}}}(1/\tilde{a})] \\
& + \sum_{j=1}^3 c_{\text{cond}}^{(j)} \alpha_{\overline{\text{MS}}}(1/\tilde{a}) \frac{(1 \text{ GeV})^{2j}}{\mu^{2j}} \times [1 + c_{\text{cond}, a^2}^{(j)} (\tilde{a}\Lambda/\pi)^2] \\
& + c_\alpha (\alpha_{\overline{\text{MS}}}(\mu)/\pi)^4.
\end{aligned} \tag{3.42}$$

The fit gives a χ^2/dof of 0.14 and returns a significant coefficient for the $(1/\mu^2)$ condensate of -0.209(63). This is consistent with the value obtained from the fit to the conserved current in the RI'-MOM scheme Eq. 3.41. If the condensate terms are dropped from the fit then the χ^2 degrades to an unacceptable value. The fit is unable to account for the movement towards 1 as

μ is increased as $a\mu$ discretisation effects would push the values away from 1 at higher μ values. This reinforces the conclusion that if a RI'-MOM Z_V at 2 GeV is used then there is a $\mathcal{O}(1\%)$ nonperturbative effect that either has to be dealt with through some sort of fit or has to be taken as a systematic uncertainty.

We can consider the ratio of the MOM local and conserved currents in this setting, which we would expect to cancel the condensate contribution that survives the continuum in both cases. We denote this ratio $Z_V^{\text{loc}}(\text{MOM}_{R_c})$. Calculating ΔZ_V^{loc} with $Z_V^{\text{loc}}(\text{MOM}_{R_c})$ and using the fit of Eq. 3.42 gives a χ^2/dof of 0.32 while placing a constraint on the lowest order condensate contribution coefficient of -0.01(5). This data and fit are shown in Fig. 3.16. The conclusion here is that $Z_V^{\text{loc}}(\text{MOM}_{R_c})$ does not suffer the condensate contamination of $Z_V^{\text{loc}}(\text{MOM})$.

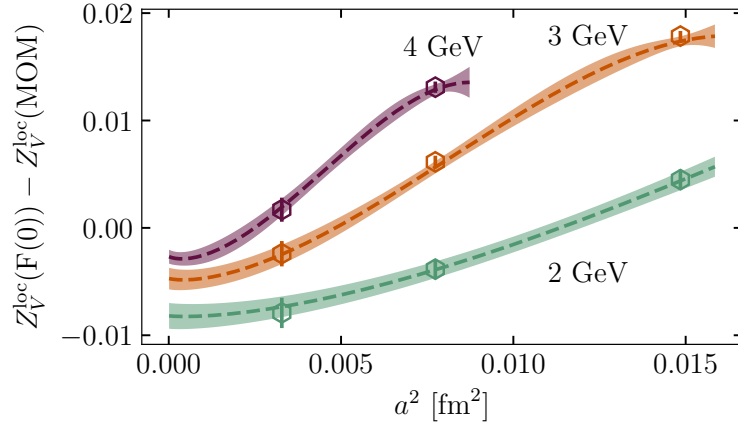


Figure 3.15: The difference between the MOM local Z_V and Z_V determined from form factor methods. The situation for this case is clearly different to that when the SMOM scheme is used shown in Fig. 3.17. The MOM case shows a clear μ dependent effect as can be expected from the lack of Ward-Takahashi identity protection in the MOM scheme.

SMOM

A little care is required in the construction of the SMOM projector using staggered quarks. The operator $\not{q}q_\mu\Lambda_V^\mu$ must be constructed to be a taste singlet. The gamma matrices entering the \not{q} must therefore have different taste for different Λ_V^μ . The correct construction is

$$\sum_{\mu,\nu} q_\nu \overline{(\gamma_\nu \otimes \xi_\mu)} q_\mu \Lambda_V^\mu. \quad (3.43)$$

We again use the fit form Eq. 3.42 but we drop the $\alpha_{\overline{\text{MS}}}^4$ term (as there is no matching to $\overline{\text{MS}}$ required here). The data and fit are shown in Fig. 3.17.

The coefficients were given priors of 0 ± 1 . The fit has a χ^2/dof value of 0.18 and no significant condensate term is seen: the $(1/\mu^2)$ condensate coefficient returned is $-0.020(44)$. ΔZ_V^{loc} is therefore compatible with pure discretisation effects, as we expect.

We can also examine the local to conserved ratio in the SMOM_{γ_μ} scheme which is shown in Fig. 3.18. Again, there is no evidence of condensate contamination with a leading order coefficient of $-0.03(5)$ and a χ^2/dof of 0.56.

The lack of nonperturbative effects in principle has an impact on the idea of a window bounded from below of acceptable μ values. The fact that 1 GeV SMOM data can be fit is an indication that low μ values can be used. As the value of μ is lowered the discretisation effects decrease. It may therefore be advantageous to use as low a μ as possible. However, the expense of the calculation increases with decreasing μ as does the uncertainty on the Z_V values. We can

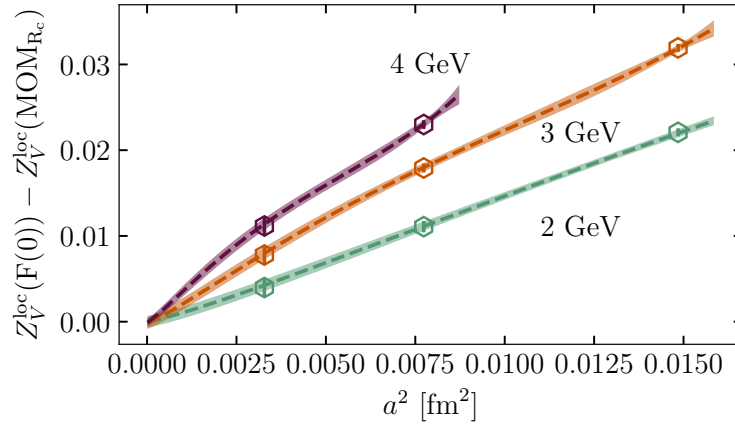


Figure 3.16: The same as Fig. 3.15 but using the ratio of the MOM local and conserved vector current renormalisation. These results are consistent with a lack of nonperturbative contamination, unlike when just using the MOM local vector current (Fig. 3.15).

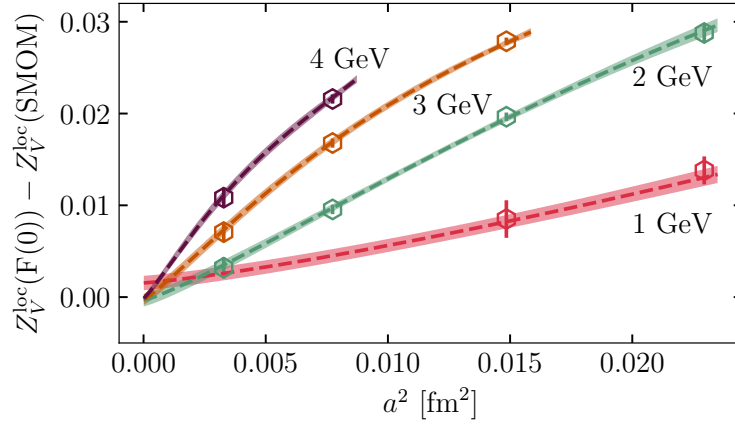


Figure 3.17: The difference between the SMOM local vector current renormalisation factor and the local vector renormalisation determined through a form factor at zero momentum. In the absence of nonperturbative contamination this is expected to be consistent with pure discretisation effects. Values as low as $\mu = 1$ GeV are included and no sign of μ dependent nonperturbative effects is seen.

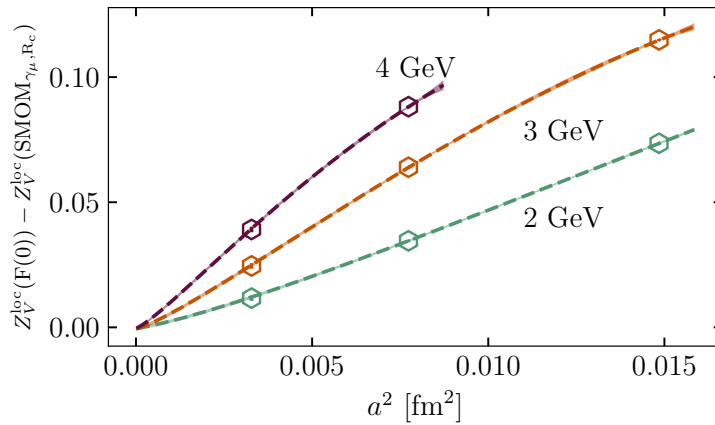


Figure 3.18: The difference between the local to conserved vector current renormalisation in the SMOM_{γ_μ} scheme and the local renormalisation determined from form factor methods. Similarly to Fig. 3.17 there is no indication of nonperturbative contamination.

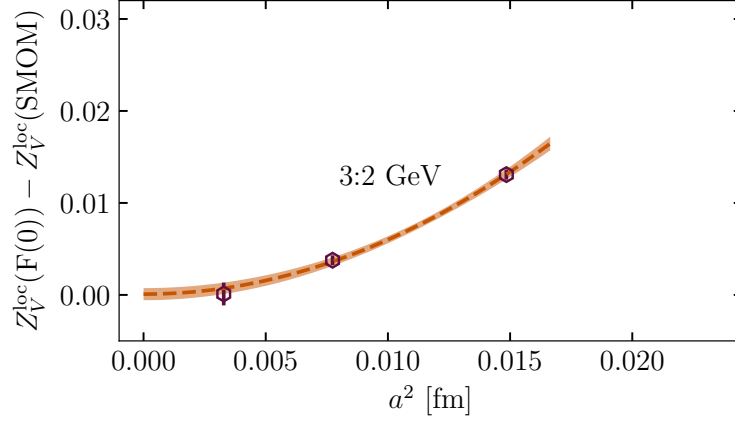


Figure 3.19: Plot showing the difference between the local Z_V determined using form factors and an SMOM local Z_V derived from results at μ values of 2 and 3 GeV in order to reduce discretisation effects. This uses Eq. 3.44

construct a Z_V value with decreased discretisation effects from results at two different μ values. We define

$$Z_V^{\text{loc}}(\mu_1, \mu_2) = \frac{\mu_1^2 Z_V^{\text{loc}}(\text{SMOM})(\mu_2) - \mu_2^2 Z_V^{\text{loc}}(\text{SMOM})(\mu_1)}{\mu_1^2 - \mu_2^2}, \quad (3.44)$$

which can be done if the only μ dependence in Z_V is through discretisation effects, and we choose $\mu_1 = 3$ GeV and $\mu_2 = 2$ GeV. We again take the difference with $Z_V^{\text{loc}}(F(0))$ and plot this difference in Fig. 3.19. The fit is of the very simple form $C + D(a \times 1 \text{ GeV})^4$. The fit returns $C = 0.00008(36)$. This indicates that the construction of Eq. 3.44 has effectively removed a^2 effects.

It is possible to fit the SMOM data on its own, without the subtraction of the form factor data. The local operator is not conserved on the lattice and therefore Z_V has the form of a power series in α_s in lattice perturbation theory with the scale set by the lattice spacing. Here we choose to use $\alpha_{\overline{\text{MS}}}(1/a)$. This is slightly different to the scale used in [75], although there it was checked that this choice of scale did not affect the $\beta = 6.72$ Z_V extracted from that fit. We therefore allow for this expansion in a fit form for the SMOM local current. The fit form used incorporates this lattice perturbation theory component and discretisation errors

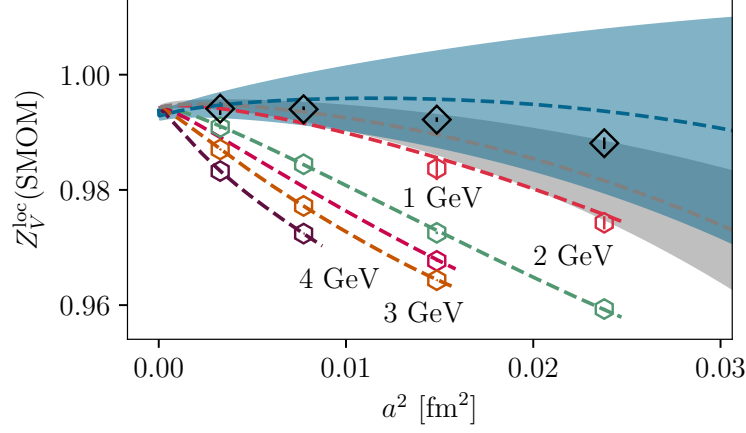


Figure 3.20: $Z_V^{\text{loc}}(\text{SMOM})$ data with the fit given by Eq. 3.45. The grey band shows the lattice perturbation theory component of the fit and the black diamonds are form factor renormalisations from [75]. The blue band is the lattice perturbation theory component of the fit to the form factor data.

$$Z_V^{\text{loc}}(\text{SMOM})(a, \mu) = \sum_k (c_k + \sum_i c_{a^2\mu^2}^{(i,k)} (\tilde{a}\mu/\pi)^{2i}) \alpha_{\overline{\text{MS}}}^k(1/a). \quad (3.45)$$

For the local current the α_s coefficient of the lattice perturbation theory is known and so we fix the leading coefficient to that value: $-0.1164(3)$ [75]. As explained earlier Z_V in the SMOM scheme has no condensate contributions and so we do not include any in the fit form. The fit gives a χ^2/dof below 1 showing that they are not required. This is shown in Fig. 3.20. The grey band is the result of removing the discretisation effects of the form $(a\mu)^{2i}$ from the fit. It is therefore the result the fit gives for the lattice perturbation theory expansion. The blue band is the same thing but using the Z_V data of [75], the individual data points of which are shown as black diamonds. The two bands overlap, indicating an agreement between the lattice perturbation expansions in the two cases. We obtain an α_s^2 coefficient of $0.725(65)$.

3.3.6 1-link vector current renormalisation

Next we consider the 1-link point-split vector operator with spin-taste $\overline{(\gamma_\mu \otimes \mathbf{1})}$. The operators we use insert thin (unsmeared) links between the point-split quark fields to maintain gauge invariance. Tadpole effects in lattice QCD lead to a renormalisation of the link operator which

enlarges the coefficients of lattice perturbation theory by approximately the inverse of the vacuum expectation value of the link operator [86]. We have therefore used a current definition that divides by the average trace link in Landau gauge on each ensemble we use, u_0 . We do not have the value on set 6 but we do know the values on ensembles with the same β but physical light quarks and light quarks such that $m_s/m_l = 5$. As the variation of u_0 with the light quark mass in the sea is small we take the result on the $m_s/m_l = 5$ ensemble.

We considered two possible constructions of these operators. One, which we denote the forward 1-link operator, is the conserved current with all 3-link terms removed and a thin link

$$j_\mu^{\text{1link-fwd}} \equiv \frac{1}{2u_0} \bar{\psi}(x) \overline{(\gamma_\mu \otimes \mathbf{1})} U_\mu(x) \psi(x + \hat{\mu}) + h.c. \quad (3.46)$$

The other 1-link operator we consider is the covariant operator of [64]

$$\begin{aligned} j_\mu^{\text{1link-cov}} &\equiv \frac{1}{2u_0} \bar{\psi}(x) \overline{(\gamma_\mu \otimes \mathbf{1})} U_\mu(x) \psi(x + \hat{\mu}) \\ &+ \frac{1}{2u_0} \bar{\psi}(x) \overline{(\gamma_\mu \otimes \mathbf{1})} U_\mu^\dagger(x - \hat{\mu}) \psi(x - \hat{\mu}). \end{aligned} \quad (3.47)$$

The two definitions coincide with MOM kinematics. In the SMOM case, while the values produced from the two different definitions are not identical they agree within errors and we only present results for the forward 1-link current. The results of the various tree-level matrix elements of these operators in the MOM and SMOM schemes are gathered in Table 3.4. We now consider the MOM and SMOM schemes in turn.

We collect results for various schemes in Table 3.8. Given the discussion regarding the local current we only study the SMOM results here but the findings in the case of the local current apply here as well.

The HISQ 1-link current renormalisation has been calculated for some of the lattice spacings used here using form factor methods in [87] and some more recent calculations using pion form factors⁶. We use the pion results, denoting them $Z_V^{\text{1link}}(F(0))$. Table V in Appendix B of [2]

⁶I thank J. Koponen and A. C. Zimmerane-Santos for providing these values.

Table 3.8: 1-link vector current renormalisation factors at all μ values considered for different schemes at the lattice spacings we use. R_c denotes that we take the ratio with the conserved current renormalisation in that scheme.

Set	μ [GeV]	$Z_V^{\text{link}}(\text{MOM})$	$Z_V^{\text{link}}(\text{MOM}_{R_c})$	$Z_V^{\text{link}}(\text{SMOM})$	$Z_V^{\text{link}}(\text{SMOM}_{\gamma\mu, R_c})$
2	1	-	-	0.9617(11)	-
5	1	-	-	0.9713(19)	-
2	2	0.93754(58)	0.90850(50)	0.93516(16)	0.89407(16)
5	2	0.95732(88)	0.93197(21)	0.94966(20)	0.92184(13)
14	2	0.97918(68)	0.95602(46)	0.96695(11)	0.952406(40)
16	2	0.99511(79)	0.97462(20)	0.97996(34)	0.974162(41)
5	2.5	0.94154(36)	0.92050(13)	0.94236(11)	0.905919(88)
5	3	0.93219(39)	0.91340(14)	0.939193(87)	0.895805(67)
14	3	0.95545(23)	0.93859(16)	0.954643(37)	0.929364(26)
16	3	0.97939(40)	0.96376(13)	0.97225(12)	0.961377(20)
14	4	0.94159(15)	0.927888(99)	0.948641(20)	0.914207(23)
16	4	0.96756(20)	0.954010(52)	0.965353(56)	0.948977(19)

gives these values. If we form the difference of $Z_V^{\text{link}}(F(0))$ and $Z_V^{\text{link}}(\text{SMOM})$, ΔZ_V^{link} , then the lattice perturbative expansion common to both should cancel, as in the local case, and a fit consisting of purely discretisation effects

$$\Delta Z_V^{\text{link}}(a, \mu) = \sum_{i=0, j=1}^{2,3} c_{ij} \alpha_s^i (a\mu/\pi)^{2j} + \sum_{i=0, j=1}^{2,3} d_{ij} \alpha_s^i (a\Lambda/\pi)^{2j}, \quad (3.48)$$

can be considered. The result of this fit is shown in Fig. 3.21. The fit includes discretisation effect terms for both the SMOM results ($a\mu$) and the form factor values ($a\Lambda$). The priors on the coefficients of the fit are taken to be 0 ± 3 . The fit gives a χ^2/dof of 0.9 confirming that the ΔZ_V^{link} data are consistent with pure discretisation effects indicating that there is no visible condensate contribution and that there is no visible remnant of a perturbative expansion in $\alpha_s(1/a)$. In this case we have made use of data at 1 GeV to further constrain possible condensate terms which are still not needed by the fit.

3.3.7 QED corrections

As lattice QCD calculations reach percent (or sub-percent) precision it will become necessary to evaluate the QED corrections expected at this level. If QED effects are included in calcula-

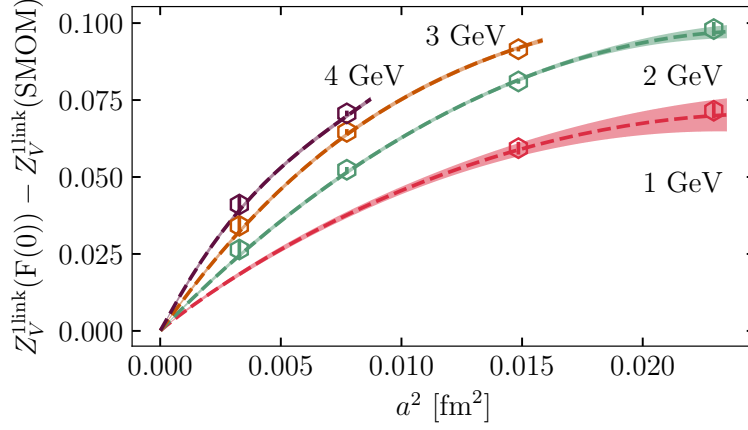


Figure 3.21: $Z_V^{\text{link}}(\text{SMOM})$ subtracted from the Z_V at the corresponding lattice spacing, determined from the vector form factor at zero momentum transfer. The range of μ values from 1 to 4 GeV indicates that there is not a visible nonperturbative effect growing at small μ . The fit lines shown are the fit of Eq. 3.48 which consists of only discretisation effects.

tions involving vector currents, such as the ongoing anomalous magnetic moment of the muon calculations, then consistency requires that QED effects are also included in the vector current renormalisation. We again included quenched QED in the QED_L formulation as we did in Section 3.2. These calculations are performed with a quark charge of $2e/3$ with $-e$ the charge of the electron (i.e. the up or charm quark charge). The value of Z_V at other charges can be obtained from a linear fit in Q^2 to the $Q = 0$ and $Q = 2e/3$ results, an example of which is shown in Fig. 3.22.

The QED effects are included in the lattice calculation by multiplying the QCD gauge field configurations by a U(1) field such that each link variable is simply multiplied by a phase. This does not change the derivation of the lattice vector WTI Eq. 3.28 so the conserved vector current renormalisation (in the SMOM scheme) will still be 1. This is explicitly demonstrated in Fig. 3.23. It is necessary to use the gauge links multiplied by the U(1) field in the conserved current for this to be true. The local and 1-link currents will be effected by this QED inclusion in two ways; one will be an actual change in the renormalisation constant while the other will be a change in discretisation errors. Including QED will change the coefficients of the lattice perturbation theory expansion. The leading order correction can be estimated by replacing α_s with $(4/3)q^2\alpha_{\text{QED}}$ where q is the quark charge and the $4/3$ is a group theory factor. This leads

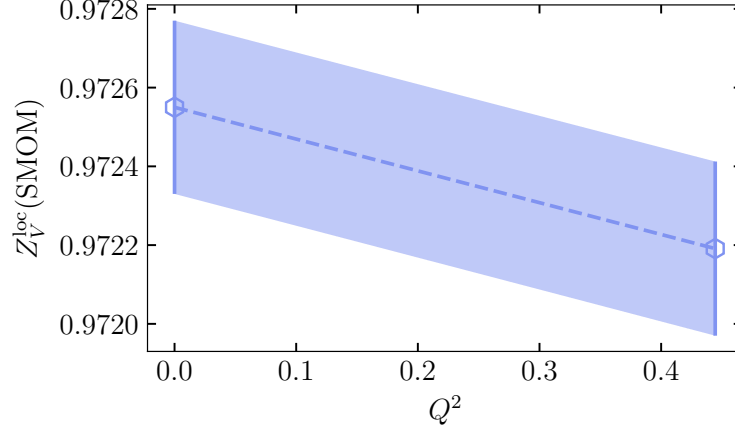


Figure 3.22: Local SMOM Z_V at electromagnetic charges of 0 and $2/3$ the proton charge. The fit shown is linear in the charge squared. This fit could be used to extract Z_V values at different values of the electromagnetic charge.

to a multiplicative correction factor of ~ 0.9997 using the HISQ one-loop lattice perturbation theory result. (This is not quite correct as the U(1) gauge links are not improved but the HISQ calculation was performed with improved links. However, this analysis may still provide an approximate expectation.) The change in the gauge fields will lead to different discretisation errors that are potentially larger than the difference in the lattice perturbation theory coefficients. We ignore the effects of QED on the determination of the lattice spacing. This will slightly shift the physical momentum of our QCD+QED simulations relative to pure QCD. However, any momentum dependence is a discretisation artefact of the form $(a\mu)^{2n}$ and therefore of no relevance here. This will not be the case for, for example, the mass renormalisation.

The quantities we choose to study are ratios of renormalisation constants calculated with both QCD and QED (QCD+QED) to those calculated within pure QCD. This gives a multiplicative correction factor to apply to pure QCD values. Although the QED effects are small the precision of our data and the high correlation between the QCD+QED and pure QCD data (a typical correlation being ~ 0.99) mean that we can obtain statistically significant results. We will denote a quantity X calculated in pure QCD as $X[\text{QCD}]$ and the same quantity calculated with the inclusion of quenched QED $X[\text{QCD}+\text{QED}]$. The notation $X[(\text{QCD} + \text{QED})/\text{QCD}] \equiv X[\text{QCD} + \text{QED}]/X[\text{QCD}]$ will also be employed.

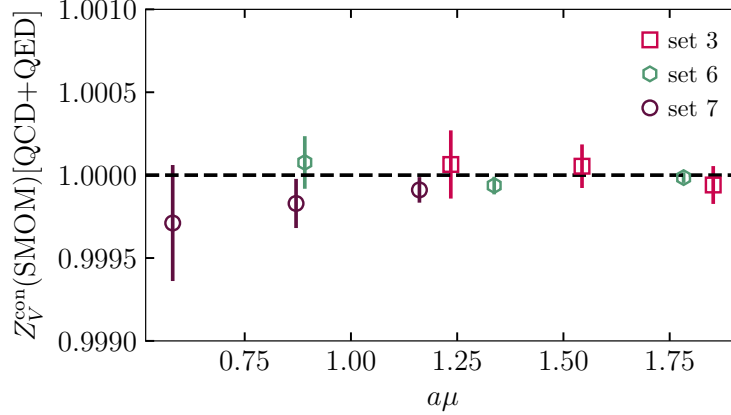


Figure 3.23: Z_V for the SMOM conserved current with the inclusion of quenched QED. The quark charge used is $2/3$ the charge of the proton. As expected all values are consistent with 1. The squares are for set 5, the hexagons are set 14 and the circles are set 16.

Given the long-distance nature of the electromagnetic interaction there are reasonably large finite volume effects expected in various quantities. For an example relevant here, the finite volume corrections of the quark self-energy function were discussed in [88]. These should be effects that are seen in the wavefunction renormalisation. The finite volume effects on the off-shell self energy function can be expanded in inverse powers of the spatial extent of the lattice. In [88] these finite volume effects are divided into components arising from the two poles in the ‘electromagnetic kernel’ that defines the self energy function. One of these poles only arises in the case of a massive quark and may therefore be dropped for our application. We can therefore take the leading finite volume correction to the self energy function to be

$$\Delta_V \Sigma = \frac{2iQ^2 \not{p} c_1}{4\pi p^2 L_x^2}, \quad (3.49)$$

where $c_1 = -2.83729748$ and Q is the electromagnetic charge of the quark in units of the electron charge [88]. Taking the dominant quark propagator finite volume effects to come from the electromagnetic self energy function we can use Eq. 3.49 to estimate the size of finite volume corrections to Z_q in the RI-SMOM scheme. The finite volume correction to the inverse propagator is simply $\Delta_V S^{-1} = -i\Delta_V \Sigma$. This translates to a finite volume correction to Z_q of

$$\Delta_V Z_q = \frac{2Q^2 c_1}{4\pi L_x^2} \simeq -\frac{0.2}{L_x^2}. \quad (3.50)$$

This calculation was performed in Feynman gauge and as we work in Landau gauge the coefficient of the finite volume effect may be different. The leading term behaves as $1/L_x^2$ leading to large reductions in the effect at large volume.

We perform a numerical study of finite volume effects on sets 6, 7 and 8 at a single valence mass corresponding to the light sea mass. The vector WTI holds in finite volume so we may expect that the finite volume effects from continuum QED on a torus vanish for Z_V . There is still then the possibility of finite volume effects in the lattice perturbation theory coefficients although these are likely to be small given that the QED correction will already be small. Indeed, we see in the upper panel of Fig. 3.25 that the volume dependence of $Z_V^{\text{loc}}(\text{SMOM})$ is negligible. There is also no significant volume dependence in Z_q (lower panel of Fig. 3.25).

Our full set of $Z_V^{\text{loc}}(\text{SMOM})[(\text{QCD}+\text{QED})/\text{QCD}]$ results across 3 lattice spacings and a range of μ values are given in Table 3.9. The results are plotted in Fig. 3.24. We fit this data to a form allowing for discretisation effects and a perturbative expansion for the ratio of renormalisation constants. The leading QCD effect cancels between the numerator and denominator so that the expansion starts at $\mathcal{O}(\alpha_{\text{QED}})$. The coefficient of this leading term can be fixed as the HISQ pure QCD α_s coefficient is known to be $-0.1164(3)$. We therefore take the $\alpha_{\text{QED}}Q^2$ coefficient to be $-0.1164 \times 3/4 = -0.0873$. For $Q = 2e/3$ this gives a coefficient of -0.0388 corresponding to a leading order result for $Z_V^{\text{loc}}(\text{SMOM})[(\text{QCD}+\text{QED})/\text{QCD}]$ of 0.9997 , as previously stated. The largest corrections to this will come from $\mathcal{O}(\alpha_{\text{QED}}\alpha_s)$ terms. We use a fit form of

$$Z_V^{\text{loc}}(\text{SMOM})[(\text{QCD} + \text{QED})/\text{QCD}] = 1 + \alpha_{\text{QED}} \left[\sum_i c_i \alpha_s^i \left(1 + \sum_j d_{ij} (a\mu)^{2j} \right) \right], \quad (3.51)$$

fixing the value of c_0 . We use $i = 0, 1, 2, 3$ and $j = 1, 2, 3$. The χ^2/dof is 0.25 . As Fig. 3.24 shows the impact of quenched QED is very small and negligible at an accuracy of 0.1% . This smallness is due to the improvement in the HISQ action leading to a local vector current renormalisation with HISQ that is very close to 1.

Additive corrections to the pure QCD local vector current renormalisation from QED for do-

Table 3.9: The ratio of renormalisation factors Z_V for the QCD + quenched QED case to the pure QCD case. These are for the local HISQ vector current calculated in the RI-SMOM scheme on gluon field configuration sets listed in column 1 and at μ values listed in column 2 (and at a valence quark mass of m_l).

Set	μ [GeV]	$Z_V^{\text{loc}}(\text{SMOM})[(\text{QED} + \text{QCD})/\text{QCD}]$
6	2	0.999631(24)
14	2	0.999756(32)
16	2	0.999831(43)
6	2.5	0.999615(12)
6	3	0.999622(13)
14	3	0.9997043(39)
16	3	0.9997797(92)
14	4	0.9996754(26)
16	4	0.9997425(24)

main wall fermions using a two-point function ratio method are given in [89]. Those values are comparable, although a little larger, to ours and they also observe a decrease with the inclusion of QED. The Z_V values without QED reported in [89] are significantly further than 1 from those presented here so the larger effect seen there may be due to more substantial discretisation effects in the calculations of [89].

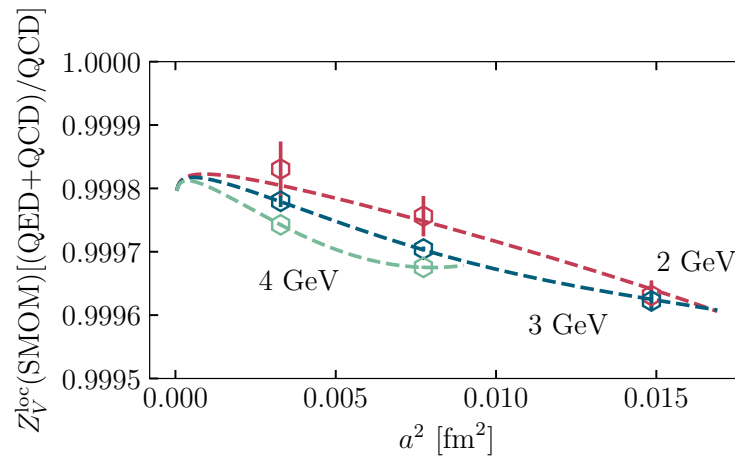


Figure 3.24: Ratio of Z_V^{loc} values for QCD+QED and QCD in the RI-SMOM scheme. Results are given on sets 14 and 16 for μ values of 2, 3 and 4 GeV and on set 6 values of 2, 2.5 and 3 GeV. The dashed lines give the results of the fit of Eq. 3.51 which indicates that the results are described well by a perturbative series up to discretisation effects.

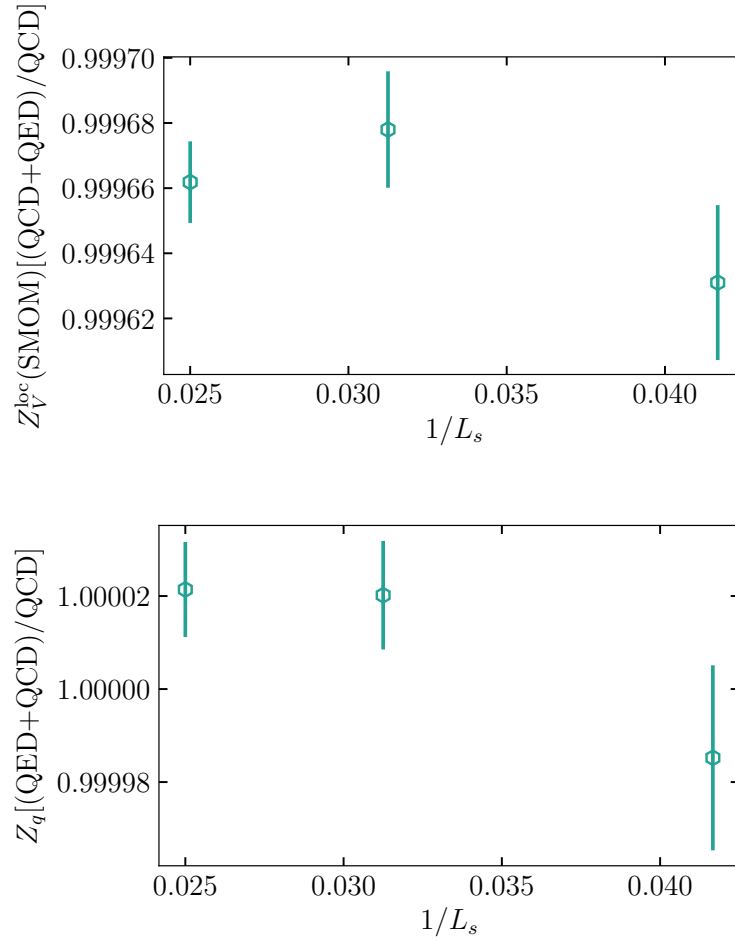


Figure 3.25: Upper: Volume dependence of the ratio of $Z_V^{\text{loc}}(\text{SMOM})$ calculated with QCD and quenched QED to the same quantity calculated with pure QCD at $\mu = 2$ GeV. There is no observable dependence. Lower: Volume dependence of the same ratio for Z_q at $\mu = 2$ GeV. In this case there is some visible volume dependence which is largely cancelled by the volume dependence of P_{Λ_V} .

3.3.8 Calculating Z_V on finer lattices

The need for stringent Landau gauge fixing makes even these relatively cheap RI-SMOM calculations expensive for large lattices. We can follow [75] and use a fit to extract Z_V values at very small lattice spacings. We fit the SMOM local data in Table III of [2] to a form allowing for $a\mu$ discretisation effects and a power series in α_s evaluated in the $\overline{\text{MS}}$ scheme at a scale of $1/a$:

$$Z_V^{\text{loc}}(\text{SMOM})(a, \mu) = \sum_{i=0, j=1} \left[c_i + d_{ij} \left(\frac{a\mu}{\pi} \right)^{2j} \right] \alpha_s^i \quad (3.52)$$

This is very similar to the approach adopted in Appendix B of [75] using form factor data. Data on Set 18 are included: 0.99203(108) at 2 GeV and 0.99023(56) at 3 GeV. As there, we fix the α_s coefficient to its known perturbative value of -0.11640(30). Fig. 3.26 shows the Z_V data and fit as well as a vertical line at $a \sim 0.03$ fm. The fit lines for 2 and 3 GeV are also shown. This fit has a χ^2/dof of 0.93.

There is a mistuning of μ on Set 18; the true values are 2.04 and 2.98 GeV rather than 2 and 3. Particularly at this small lattice spacing the variation in Z_V with μ is small enough that this small mistuning can be neglected. In this case it is only a discretisation effect and should not greatly affect the continuum limit trajectory.

The MILC collaboration have generated an ensemble with a lattice spacing of approximately 0.03 fm [90] (set 19). The value the fit obtains for this ensemble at 2 GeV is 0.99297(21) and at 3 GeV is 0.99188(18). As these have been determined from this fit, they now do not have to be directly calculated on set 19.

3.3.9 Conclusions: Z_V

We have examined vector current renormalisation with staggered quarks in various momentum subtraction schemes and compared the results to determinations from form factor methods which have different sources of systematic uncertainty. We have explicitly demonstrated the vector Ward-Takahashi identity with the HISQ action and used this to construct the correct lattice definition of the conserved vector current renormalisation in the RI-SMOM scheme. We have also calculated Z_V for the local vector and 1-link vector currents in the RI-SMOM, RI-SMOM γ_μ and RI'-MOM schemes and demonstrated that nonperturbative contributions are necessary to understand the behaviour of the RI'-MOM conserved current renormalisation. We have demonstrated

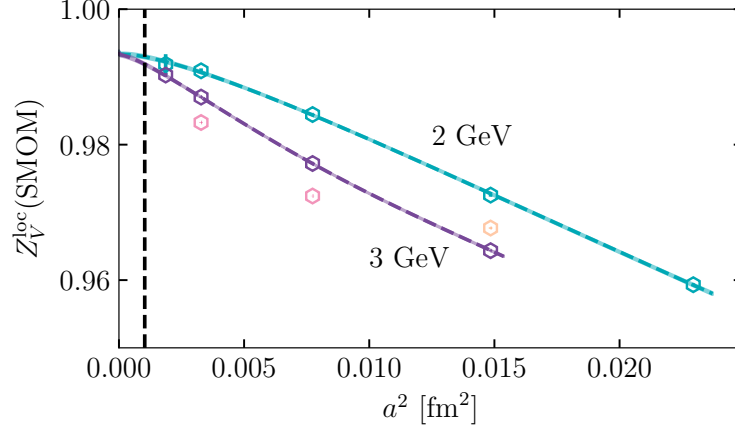


Figure 3.26: Local vector current renormalisation in the RI-SMOM scheme. This fit is given by Eq. 3.52 and includes discretisation effects and an expansion in the strong coupling (in the $\overline{\text{MS}}$ scheme) evaluated at $1/a$. All the data points shown are included in the fit but only the 2 and 3 GeV fit lines are drawn.

the consistency of the results in these momentum subtraction schemes with those obtained, at much greater computational cost, through form factor methods.

We have also performed a preliminary study of QED corrections to Z_V the results of which indicate that using momentum subtraction schemes for this purpose is viable, and finite volume effects are not an issue even at the very high precision that we have here.

The important points of this Section are:

1. The RI-SMOM scheme obeys the Ward-Takahashi identity which results in $Z_V = 1$ for the conserved current. This is not the case for the RI'-MOM scheme.
2. The local and 1-link vector currents in the RI-SMOM scheme can be determined fully nonperturbatively without any unwanted nonperturbative artefacts. This has been demonstrated by comparison to renormalisation factors from form factor methods.
3. Again, this is not true of the RI'-MOM scheme. The use of Z_V results from the RI'-MOM scheme will therefore result in a systematic error in the continuum. Considering ratios of a RI'-MOM vector current to the RI'-MOM conserved current removes these problems.

Several uses of the Z_V values calculated here will be used in later Chapters in the context of

heavyonium physics. This is a high precision area of lattice QCD application and allows for very precise further tests.

3.4 Z_T : tensor current renormalisation

Rare standard model processes, for example those that first appear at 1-loop order through so-called “penguin” diagrams (one example of which is shown in Fig. 3.4), are objects of great interest in searches for new physics. They are well placed at the precision frontier as the suppression of the Standard Model contribution opens the possibility of significant contributions from beyond the Standard Model physics. Clearly, precise theoretical results for such processes are also desirable. For hadronic quantities this requires the application of lattice QCD. These processes, as well as those of several BSM scenarios, require the calculation of tensor current form factors.

An example of such a calculation is the rare semileptonic $B \rightarrow K$ decay. A first unquenched lattice QCD calculation of this decay was performed in [91] by members of the HPQCD collaboration and another was given in [92] by the Fermilab lattice and MILC collaborations. The former used HISQ light and strange quarks and NRQCD b quarks and the latter using asqtad light and strange quarks and Fermilab b quarks. In the HPQCD calculation the tensor current was renormalised using one-loop perturbation theory for the NRQCD-HISQ current. A 4% systematic uncertainty on the tensor form factor was then taken to account for higher order terms. The Fermilab/MILC calculation also uses one-loop lattice perturbation theory and estimates an $\mathcal{O}(\alpha_s^2)$ uncertainty.

The HPQCD collaboration has recently performed a series of B physics calculations using only HISQ fermions by extrapolating to the physical b quark mass from lighter masses [93, 94, 95, 96]. The success of this methodology indicates the possibility of improvement on previous $B \rightarrow K$

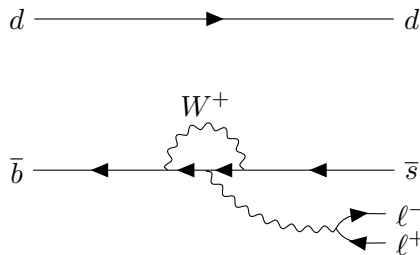


Figure 3.27: Example of a penguin diagram for the rare decay $B \rightarrow K \ell^+ \ell^-$.

calculations for which it would be important to reduce the uncertainty arising from the tensor current renormalisation.

Here we use a partially nonperturbative procedure using the RI-SMOM scheme implemented on the lattice as an intermediate scheme as we do for mass renormalisation in Section 6. This produces tensor current renormalisation factors to a greater level of precision than those used in the calculations mentioned above as the perturbative part of the calculation, the matching to the $\overline{\text{MS}}$ scheme, is known beyond 1-loop. In order to investigate systematic effects in these renormalisation factors we require a matrix element to multiply by Z_T to give a quantity that we can study in the continuum limit (where the regulator is removed). For this purpose we use the J/ψ tensor decay constant $f_{J/\psi}^T$ as discussed in Section 4.6.

3.4.1 Z_T in the RI-SMOM scheme

The tensor current renormalisation is defined in terms of Z_q and the tensor vertex function Λ_T :

$$\int d^4x d^4y_1 d^4y_2 e^{iqx} e^{-ip_1 y_1} e^{ip_2 y_2} \langle T^{\mu\nu}(x) \bar{\psi}(y_1) \psi(y_2) \rangle. \quad (3.53)$$

Here $T^{\mu\nu}(x)$ is the tensor current $\bar{\psi}(x) \sigma^{\mu\nu} \psi(x)$. The wavefunction renormalisation may be calculated using either the incoming (p_1) or outgoing (p_2) quarks propagators. The tensor current renormalisation may then be defined as

$$\frac{Z_q}{Z_T} = \frac{1}{144} \text{Tr}(\Lambda_T^{\mu\nu} \sigma_{\mu\nu}). \quad (3.54)$$

Renormalisation factors obtained in the RI-SMOM scheme can be matched to the more conventional choice of the $\overline{\text{MS}}$ scheme through a perturbative calculation in the continuum. For the tensor renormalisation this has been performed to two loop order⁷.

We also make use of some results in the RI'-MOM scheme which has a simpler kinematic setup than the RI-SMOM scheme, with no momentum inserted at the vertex and therefore only one quark momentum, but uses the same definitions of Z_q and Z_T . The RI'-MOM to $\overline{\text{MS}}$ conversion is known through $\mathcal{O}(\alpha_s^3)$ for the tensor current renormalisation factor.

⁷A recent result [97] extends this to three loop order but is not used in this analysis.

With the staggered quark fields χ the local tensor vertex function is

$$\begin{aligned}
& \left\langle \chi(p'_1 + \pi A) \right. \\
& \left. \left(\sum_x \bar{\chi}(x) (-1)^{(x_\mu + x_\nu)} \chi(x) e^{i(p'_1 - p'_2)x} \right) \right. \\
& \left. \bar{\chi}(p'_2 + \pi B) \right\rangle \\
& = \frac{1}{n_{\text{cfg}}} \sum_{x, \text{cfg}} S(p'_1 + \pi A, x) e^{i(p'_1 - p'_2)x} (-1)^{x_0 + x_1 + x_2 + x_3 - x_\mu - x_\nu} \times \\
& S^\dagger(p'_2 + \pi \tilde{B}, x),
\end{aligned} \tag{3.55}$$

making use of γ_5 -hermiticity in the last line. The elements of \tilde{B} are permuted compared to those of B via $\tilde{B} = B +_2 (1, 1, 1, 1)$.

On each ensemble we use 20 configurations apart from on Set 18 where only 6 configurations with stringent gauge fixing were available. In order to compensate for a potential underestimation of the uncertainty due to the low statistics we double the uncertainty on the Z_T values on Set 18. This small number of configurations is sufficient to achieve high precision given our use of momentum sources.

We again use the kinematic setup of Eq. 3.14 for RI-SMOM and for RI'-MOM we take the outgoing momentum to be the same as the ingoing momentum.

3.4.2 Valence mass extrapolation

In order to obtain values at zero valence mass we yet again calculate Z_T at three different quark masses and extrapolate to 0 using a polynomial fit in am . (This is the same procedure we used in Sections 6 and 3.3.) Fig. 3.28 shows an example of the mass dependence of Z_T which is reasonably benign.

The renormalisation of the tensor current in QCD does not depend on the masses of the fermions in the current; the renormalisation scheme may be defined at any mass as already noted. Here we take the bilinears in the renormalisation procedure to be non-diagonal in flavour. For staggered (and Wilson) fermions the renormalisation factors for flavour singlet and non-singlet bilinears

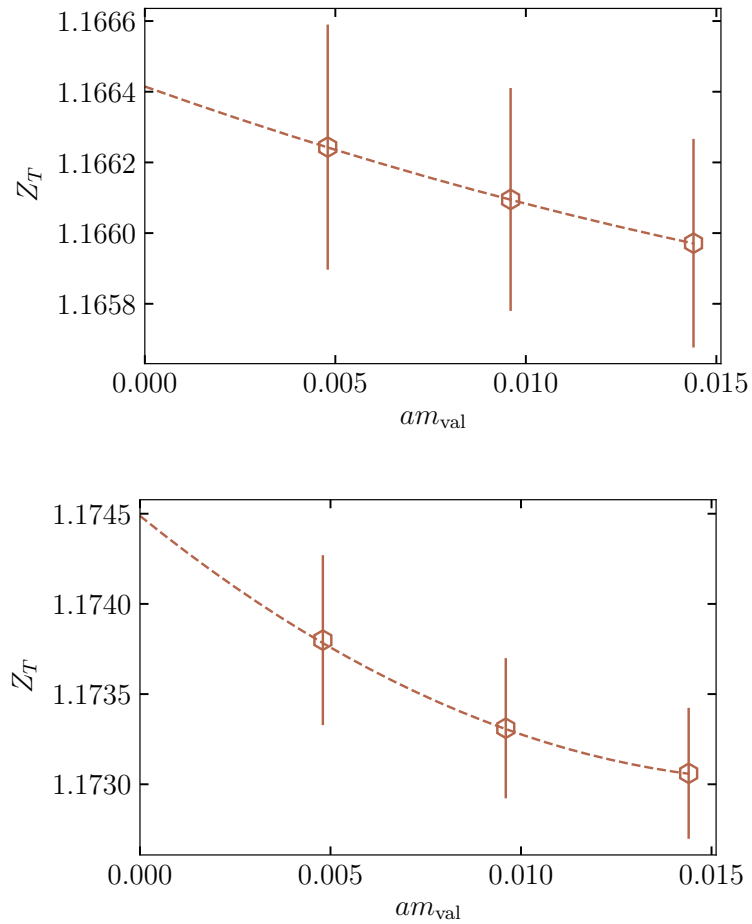


Figure 3.28: Valence mass dependence of tensor current renormalisation factors in the RI-SMOM (upper) and RI'-MOM (lower) schemes. The values shown are for $\mu = 2$ GeV on Set 16. Both show reasonably mild dependence on the valence mass but the dependence is clearly less for RI-SMOM.

Table 3.10: The parameters of the ensembles used in the calculation of the tensor current renormalisation factors in the RI-SMOM and RI'-MOM schemes. On each ensemble we calculate the renormalisation factor at three masses: the sea light quark mass and two and three times that mass. The values are then extrapolated to zero valence mass. The lattice spacings quoted here are sea mass independent and are the spacings for an ensemble with the same β but physical sea quark masses. Note that this definition of the lattice spacing differs from that used for the calculation of the mesonic properties we study here. To distinguish the two definitions we denote the sea mass independent lattice spacing \tilde{a} while the sea mass dependent spacing is denoted a .

Set	β	w_0/\tilde{a}	L_s	L_t	am_l^{sea}	am_s^{sea}	am_c^{sea}
2	5.80	1.1322(14)	24	48	0.00640	0.0640	0.828
7	6.00	1.4075(18)	32	64	0.00507	0.0507	0.628
14	6.30	1.9500(21)	48	96	0.00363	0.0363	0.430
16	6.72	2.994(10)	48	144	0.0048	0.024	0.286
18	7.00	3.970(15)	64	192	0.00316	0.0158	0.188

differ for the axial current at the two-loop level [98]. However, this is not the case for the tensor current (as well as the pseudoscalar and vector currents) and we may therefore safely use the Z_T calculated here for any flavour setup of the tensor current.

3.4.3 Conversion to $\overline{\text{MS}}$

We calculate Z_T in the RI-SMOM and RI'-MOM schemes at various values of the scale μ . We use multiple μ values in order to investigate μ dependence in Z_T arising from nonperturbative artefacts that will be suppressed by an even power of μ . In the final result these artefacts need to be removed. An Operator Product Expansion analysis, as outlined for the scalar current in [1], indicates that, at least through $\mathcal{O}(\alpha_s)$, the leading condensate contribution is the same as that for the scalar current renormalisation.

However, there will also be μ dependence due to the tensor anomalous dimension. In order to deal with this and present results in the conventionally used $\overline{\text{MS}}$ scheme we use the two loop matching of [99] which gives:

$$Z_T^{\overline{\text{MS}}/\text{SMOM}}(\mu) = 1 - 0.21517295 \frac{\alpha_{\overline{\text{MS}}}(\mu)}{4\pi} - (43.38395007 - 4.10327859n_f) \left(\frac{\alpha_{\overline{\text{MS}}}(\mu)}{4\pi} \right)^2. \quad (3.56)$$

This expression is multiplied by the Z_T^{SMOM} numbers calculated on the lattice to give $Z_T^{\overline{\text{MS}}}$: $Z_T^{\overline{\text{MS}}} = Z_T^{\overline{\text{MS}}/\text{SMOM}} Z_T^{\text{SMOM}}$. Here we will examine this series a little further with a comparison to the corresponding matching factor for the mass renormalisation factor in RI-SMOM. The perturbatively calculated mass renormalisation matching factor between RI-SMOM and $\overline{\text{MS}}$ converges rapidly to the order to which it is known, with the α_s^2 coefficient being significantly smaller than the leading $\mathcal{O}(\alpha_s)$. This is compared to the less convergent RI'-MOM to $\overline{\text{MS}}$ conversion factor in [99]. The situation is not the same for the tensor current renormalisation conversion. Evaluating Eq. 3.56 for $n_f = 4$ we find

$$1 - 0.0171229\alpha_s - 0.170795\alpha_s^2. \quad (3.57)$$

This can be compared with the RI'-MOM calculation which is done through $\mathcal{O}(\alpha_s^3)$ [100]

$$1 - 0.1976305\alpha_s^2 - 0.4768793\alpha_s^3. \quad (3.58)$$

Note that in Landau gauge the α_s term vanishes here. This series is similar to Eq. 3.57 and so it might be expected that the α_s^3 coefficient in the SMOM conversion is similar in value. Taking $\alpha_s(2 \text{ GeV}) \simeq 0.3$ the order α_s^2 term in the RI-SMOM matching is approximately 3 times the order α_s term and for the RI'-MOM matching the α_s^3 term is of approximately the same size as the α_s^2 term. This may raise some concerns about the impact of the truncation of the RI-SMOM matching factor.

We allow for an α_s^3 term in our fit that can in principle account for the missing next term in the series, but we also perform an analysis using RI'-MOM Z_T values as more of the series is known. This provides a check on the control of the uncertainty arising from the matching to $\overline{\text{MS}}$.

We may then run the values of $Z_T^{\overline{\text{MS}}}$ obtained at different values of μ , using the $\overline{\text{MS}}$ running, to the same reference scale μ_{ref} . The only remaining μ dependence should then be purely from nonperturbative effects, predominantly condensates (and possibly some very slowly varying dependence from higher order terms in the running or matching). We choose a reference scale μ_{ref} of 2 GeV. We will also present results for Z_T with the renormalisation scale chosen to be the b quark running mass in the $\overline{\text{MS}}$ scheme, $\overline{m}_b(\mu = \overline{m}_b)$.

The values of the two-loop conversion from RI-SMOM to $\overline{\text{MS}}$ at the value of μ relevant for our analysis are given in the second column of Table 3.11. The values of the running to 3 GeV are

given in the third column. As all these values result from a perturbative expansion in α_s there is a 100% correlation between all the values in Table 3.11.

We collect all the RI-SMOM and RI'-MOM results in Tables 3.12 and 3.13 respectively along with the correlation matrix for the different μ values on each ensemble. These correlations are, in general, quite strong for the RI-SMOM case but less so for RI'-MOM, possibly due to the slightly stronger valence mass dependence which is fit away.

Table 3.11: Values for the conversion factor between RI-SMOM and $\overline{\text{MS}}$ and the $\overline{\text{MS}}$ running to a scale of 2 GeV for different values of μ . The three-loop tensor anomalous dimension can be found in [100]. All of these values are correlated through their use of a common determination of α_s [27].

μ [GeV]	$Z_T^{\overline{\text{MS}}/\text{SMOM}}(\mu)$	$R(3 \text{ GeV}, \mu)$
2	0.97913(65)	-
3	0.98458(38)	1.03974(94)
4	0.98711(28)	1.0636(14)

3.4.4 Strategy for condensate corrections

In order to use these tensor current renormalisation factors reliably the effects of condensates must be understood and accounted for. In order to properly assess this we need to be able to examine the continuum limit which requires a matrix element with which to multiply Z_T . We may then perform a fit similar to that done in Chapter 6 to determine quark masses that allows an estimate of the condensate contribution which can then be accounted for. This analysis is performed using the J/ψ tensor decay constant in Chapter 4.

Table 3.12: RI-SMOM Z_T value on the ensembles in Table 3.10 at different μ values along with the correlation matrices for these different μ values on a given Set. In most cases it can be seen that these correlations are reasonably strong.

Set	$\mu = 2$ GeV	$\mu = 3$ GeV	$\mu = 4$ GeV	correlation
2	1.07293(18)	-	-	-
7	1.10035(28)	1.036117(92)	-	$\begin{pmatrix} 1 & 0.824 \\ 0.824 & 1 \end{pmatrix}$
14	1.13250(14)	1.064991(56)	1.030967(30)	$\begin{pmatrix} 1 & 0.560 & 0.375 \\ 0.560 & 1 & 0.861 \\ 0.375 & 0.861 & 1 \end{pmatrix}$
16	1.16641(40)	1.09808(12)	1.061844(57)	$\begin{pmatrix} 1 & 0.828 & 0.866 \\ 0.828 & 1 & 0.896 \\ 0.866 & 0.896 & 1 \end{pmatrix}$
	2.04	2.98	4	correlation
18	1.1791(17)	1.11629(64)	-	$\begin{pmatrix} 1 & 0.925 \\ 0.925 & 1 \end{pmatrix}$

Table 3.13: RI'-MOM equivalents of the RI-SMOM values in Table 3.12. The correlations are not as strong in this case, perhaps because of the slightly larger valence mass dependence of the RI'-MOM results.

Set	$\mu = 2$ GeV	$\mu = 3$ GeV	$\mu = 4$ GeV	correlation
2	1.08435(42)	-	-	-
7	1.10970(58)	1.04631(16)	-	$\begin{pmatrix} 1 & 0.637 \\ 0.637 & 1 \end{pmatrix}$
14	1.13949(47)	1.06979(13)	1.037388(39)	$\begin{pmatrix} 1 & 0.384 & 0.393 \\ 0.384 & 1 & 0.609 \\ 0.393 & 0.609 & 1 \end{pmatrix}$
16	1.17449(71)	1.10045(25)	1.063735(93)	$\begin{pmatrix} 1 & 0.103 & 0.155 \\ 0.103 & 1 & 0.337 \\ 0.155 & 0.337 & 1 \end{pmatrix}$
	2.04	2.98	4	correlation
18	1.1845(29)	1.1181(14)	-	$\begin{pmatrix} 1 & 0.234 \\ 0.234 & 1 \end{pmatrix}$

3.5 Conclusions

In this Chapter momentum subtraction schemes have been shown to offer computationally cheap and precise current renormalisation factors as long as unwanted nonperturbative effects are understood and controlled. This included the first applications of the RI-SMOM scheme to staggered quarks.

The mass renormalisation factors described in Section 3.2 will be used in Chapter 6 as a major component in high sub-percent determinations of the strange and charm quark masses. The effects of electromagnetism on that charm quark mass determination will also be calculated using the QED corrections to Z_m given in Section 3.2.6. The local vector current renormalisation factors given in Section 3.3 will be used for various calculations in Chapters 4 and 5: the decay constants of vector meson and connected contributions to the hadronic vacuum polarisation contribution to the anomalous magnetic moment of the muon.

The success of these programs indicates the potential future utility of nonperturbative renormalisation in momentum subtraction schemes for future calculations with the HISQ action.

Chapter 4

Properties of Ground State Charmonium

4.1 The charmonium spectrum

The spectrum of $c\bar{c}$ mesons is very well determined experimentally which makes it a promising landscape to perform precision lattice QCD studies. This is done below the open charm threshold at which decays to heavy-light mesons become kinematically allowed. Hadronic decays are often not allowed for in lattice calculations as they are typically restricted to connected correlation functions. This is controllable when only suppressed decays via annihilation are allowed, leading to particles with small widths which may be treated as stable.

A section of the low-lying charmonium spectrum is shown in Fig. 4.1. Pseudoscalar particles are given in the first column, vectors in the second and axialvectors in the third. One noticeable feature of this spectrum is that the splitting between different states is much smaller than the overall scale. This implies that dynamical scales (i.e. quark velocities) are considerably lower than the mass scales associated with the quarks implying that the quarks in the mesons are typically nonrelativistic [101].

The lines to the right of the η_c and J/ψ indicate the relative sizes of their widths. Both are dominated by decays to hadrons. The radiative η_c decay $\eta_c \rightarrow \gamma\gamma$ only constitutes $1.57(12) \times 10^{-4}$ times the total and the J/ψ decay to an e^+e^- pair partial width is $5.971(32)\%$ of the total width with a similar contribution from decays to $\mu^+\mu^-$. Clearly the J/ψ is much narrower. The larger

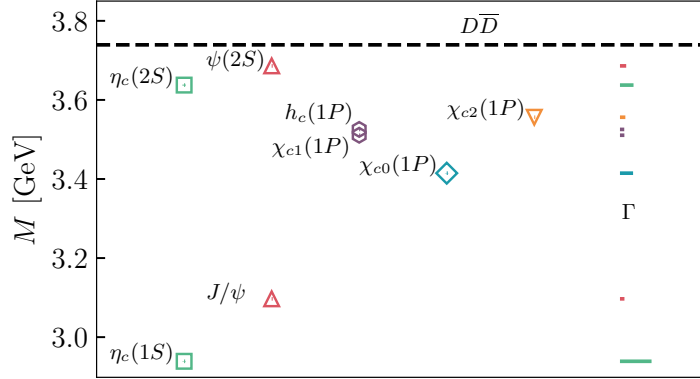


Figure 4.1: The charmonium spectrum below the open charm threshold. Moving from left to right the first five columns are pseudoscalars, vectors, axialvectors, scalars and spin 2. The bars to the right indicate the relative widths of the particles.

η_c width is due to the availability of a decay to two gluons. This decay is not allowed in the calculations presented here. In [39] a perturbative expression is used to relate the mass shift in the η_c due to annihilation to gluons to the hadronic width of the η_c :

$$\Delta E_{\eta_c} = \Gamma(\eta_c \rightarrow \text{hadrons}) \left(\frac{\ln(2) - 1}{\pi} + \mathcal{O}(\alpha_s) \right) \simeq -3.1 \text{ MeV}. \quad (4.1)$$

Lattice calculations of the η_c mass will be wrong if they are missing this effect, which ours, and most others, do. In order to be able to see the effect of missing this contribution the η_c mass needs to be determined to an accuracy of 1 MeV. Rather than look at the η_c mass directly, we examine the hyperfine splitting: the difference between the J/ψ and η_c masses. The only lattice computation of the disconnected correlation functions required to calculate this effect nonperturbatively have been done in the quenched approximation [102]. These gave an estimate of the effect of +1-4 MeV, which is of opposite sign but similar magnitude to Eq. 4.1. A calculation of the hyperfine splitting with enough precision to separate the lattice result from the experimental value may help to resolve this issue and we provide such a calculation here.

Heavy quarkonia ($q\bar{q}$) systems are challenging to tackle using perturbative means. Obviously any mesonic system cannot be studied directly through perturbative QCD due to the nonperturbative

nature of the confinement of the quarks within the meson but in some cases effective field theories may be used to provide some physical insight and predictions.

For pseudoscalar mesons composed of light quarks the approximate, spontaneously broken, chiral symmetry of QCD allows the construction of chiral perturbation theory. For heavy-light mesons the decomposition of the momentum of the meson according to

$$p^\mu = m_Q v^\mu + k^\mu, \quad (4.2)$$

where m_Q is the heavy quark mass, v^μ is the 4-velocity of the meson and $k^\mu \ll m_Q$ gives rise to heavy quark effective theory (HQET) which, among other things, gives the form of the heavy quark mass dependence of various mesonic properties. Both of these methods fail for heavyonium because they consist of two heavy valence quarks and no valence light quarks.

Some analysis can be performed within the NRQCD framework [103] which is able to make more precise (and field theoretic) statements than potential models, although for charmonium $v^2/c^2 \simeq 0.3$ and NRQCD is difficult to properly control. Given the discussion preceding this Chapter, it is clear that lattice QCD (with relativistic quarks) offers by far the most powerful method of studying the properties of heavyonium. This relies on overcoming the difficulties presented by the use of large bare masses which can render discretisation effects uncontrollable. The HISQ action was designed with such applications in mind [39]. The result is that the charm quark mass can be reached on the full range of MILC HISQ ensembles with visible but controllable discretisation effects. This Chapter presents the most precise theoretical study to date of charmonium ground state properties, including the hyperfine splitting and J/ψ decay constant (which is related to the partial width of the J/ψ to an e^+e^- pair). We will not study excited meson masses or their properties since these analyses need different techniques [104].

4.2 Charmonium on the lattice

The precision of lattice QCD calculations has been steadily improving for some time and is now approaching, or has surpassed, the 1% level for multiple quantities. In order to ensure reliability at such precision all percent level, and some subpercent level, systematics must be understood. An example calculation is provided by the lattice QCD effort to produce a competitive determination of the hadronic vacuum polarisation contribution to the anomalous magnetic moment

of the muon a_μ . New results are expected soon from the Muon $g - 2$ experiment at Fermilab [105] which aims to further examine the observed tension between experiment and theory seen by the Brookhaven E821 experiment [9]. Current lattice calculations have reached the precision of a few percent for a_μ and the issue of addressing electromagnetic corrections has become the focus of substantial efforts.

Using the highly improved staggered quark (HISQ) action [39] enables fully relativistic calculations with charm quarks that have controlled discretisation effects. Combined with the availability of precise experimental results for the properties of the lowest lying charmonium states, this makes the charmonium system a good place to study systematic effects of lattice calculations. Some of these effects, such as electromagnetism, are expected to be suppressed in a net neutral environment which allows for their controlled study. We can also make use of charmonium correlators to investigate the charm connected contribution to the anomalous magnetic moment of the muon a_μ^c . While this is a small component it allows for an initial study of electromagnetic effects, to be extended in the future.

By using the HISQ ensembles generated by the MILC collaboration we present the first charmonium calculations including the effects of light, strange and charm quarks in the sea. A further improvement on previous HPQCD calculations [76, 106] is that we include multiple ensembles with physical sea light quarks. This allows for excellent control over sea quark effects which is vital for the precise determination of certain quantities, for example, the charmonium hyperfine splitting. We also employ the renormalisation method explored with HISQ quarks in Section 3.3 and [2]. This leads to a vast improvement over the uncertainty coming from renormalisation in [76] for quantities involving the vector current. We also include the effects of electromagnetism on the valence quarks. We do this using “quenched QED” where only the QED effect on the valence quarks is included.

An issue that typically requires some consideration in lattice studies of QED is the presence of finite volume effects. These effects are suppressed by some power of the lattice extent rather than the exponential suppression typical in QCD quantities. While the power law suppression is expected to be greater in systems that are net neutral relative to those that carry some total charge we employ sets of lattices designed for dedicated finite volume studies to test for any visible effects.

Throughout we will refer to two types of calculation. Those referred to as “pure QCD” or just “QCD” are standard lattice QCD calculations. Those referred to as “QCD+QED” have

a U(1) field multiplied into the previously generated SU(3) configuration. The field multiplied in depends on the charge of the valence quark. In this setup the effect of electromagnetically charged sea quarks are neglected. To do this would require the SU(3) field to be freshly generated as well.

4.3 Lattice setup

We perform calculations on a total of 15 ensembles that include the effects of light, strange and charm quarks in the sea ($n_f = 2 + 1 + 1$) all using the HISQ action [39], generated by the MILC collaboration [42, 90]. These include lattices at 6 different β (the bare QCD coupling) values (approximately corresponding to lattice spacing) with the finest lattice reaching a spacing of ~ 0.03 fm. In addition we use ensembles with sea masses at the physical point on all but the two finest spacings. We also employ three ensembles with shared parameters except for their spatial extent in units of the lattice spacing L_s . These ensembles allow us to investigate finite volume effects in our QED analysis where they are only suppressed by powers of the spatial extent due to the long range nature of the electromagnetic interaction. The gluon action on these ensembles is improved so that discretisation errors through $\mathcal{O}(\alpha_s a^2)$ are removed [45]. Parameters for these ensembles are given in Table 4.1.

For our calculations in pure QCD we use 8 time sources (except on Set 19 where 4 were used), where the propagator is obtained from solving the Dirac equation for a source consisting of random U(1) numbers across a single time slice, to increase statistics and N_{cfg} configurations given in Table 4.1. For the valence charm quark we also use the HISQ action and use valence masses tuned in [27].

We calculate two types of connected two-point correlation functions: pseudoscalar and vector. The pseudoscalar ground state corresponds to the η_c meson and the vector ground state to the J/ψ . When using staggered quarks, as we are here, the different spin structures (γ matrices) reduce to position dependent phases that are inserted in the tie-together of the propagators and source. The two-point correlation functions are constructed from quark propagators $S(x, y)$ as

$$C(t) = \frac{1}{4} \sum_x \langle (-1)^{\eta(x)} \text{Tr}(S(x, 0)S^\dagger(x, 0)) \rangle. \quad (4.3)$$

Table 4.1: Details of the lattice ensembles and calculation parameters used. Each lattice spacing can be determined in fm by using $w_0 = 0.1715(9)$ fm. L_s and L_t are the lattice spatial and temporal extents in lattice units. The column headed $N_{\text{cfg}} \times N_t$ shows both the number of configurations used in pure QCD and the number of time sources. $N_{\text{cfg,QED}}$ refers to the number of configurations (and time sources) used in QCD+QED calculations.

Set	w_0/a	L_s	L_t	am_s^{sea}	am_s^{sea}	am_c^{sea}	am_c^{val}	ϵ_{Naik}	$N_{\text{cfg}} \times N_t$	$N_{\text{cfg,QED}} \times N_t$
1	1.1119(10)	16	48	0.013	0.065	0.838	0.888	-0.3820	1020×8	-
2	1.1272(7)	24	48	0.0064	0.064	0.828	0.873	-0.3730	1000×8	340×16
3	1.1367(5)	36	48	0.00235	0.0647	0.831	0.863	-0.3670	1000×8	-
5	1.3826(11)	24	64	0.0102	0.0509	0.635	0.664	-0.2460	1053×8	-
6	1.4029(9)	24	64	0.00507	0.0507	0.628	0.650	-0.2378	-	340×16
7	1.4029(9)	32	64	0.00507	0.0507	0.628	0.650	-0.2378	1000×8	220×16
8	1.4029(9)	40	64	0.00507	0.0507	0.628	0.650	-0.2378	-	220×16
12	1.4149(6)	48	64	0.00184	0.0507	0.628	0.643	-0.2336	1000×8	-
13	1.9006(20)	32	96	0.0074	0.037	0.440	0.450	-0.1250	300×8	-
14	1.9330(20)	48	96	0.00363	0.0363	0.430	0.439	-0.1197	300×8	371×16
15	1.9518(7)	64	96	0.00120	0.0363	0.432	0.433	-0.1167	565×8	-
16	2.8960(60)	48	144	0.00480	0.0240	0.286	0.274	-0.0491	1019×8	265×16
17	3.0170(23)	96	192	0.0008	0.022	0.260	0.260	-0.0443	100×8	-
18	3.892(12)	64	192	0.00316	0.0158	0.188	0.194	-0.0250	200×8	-
19	5.243(16)	96	288	0.00223	0.01115	0.1316	0.138	-0.0127	100×4	-

For the pseudoscalar the $\eta(x)$ is always 1 and for the vector in the μ direction $\eta(x) = (-1)^{x_\mu}$. The vector correlator is constructed by averaging over all spatial polarisations μ , i.e. $\mu = 1, 2, 3$.

For the J/ψ decay constant, vector current correlator time moments and the charm connected contribution to the anomalous magnetic moment of the muon that we present here we use the local vector current $(\bar{\psi}\gamma_\mu\psi)$. This lattice vector current is not conserved and requires renormalisation. For this purpose we use the RI-SMOM momentum subtraction scheme implemented on the lattice as discussed in [2] and Section 3.3. In [2] it was shown that these renormalisation factors do not suffer any nonperturbative contamination (at least at the high level of precision explored) and can therefore be safely used in calculations such as those presented here. The QED correction to the RI-SMOM vector current renormalisation was also given in [2] and shown to be tiny ($\sim 0.01\%$). We use the Z_V values from [2] at a scale μ of 2 GeV which are given in Table 3.7.

It is necessary to discuss in some detail the tuning of the charm quark mass. In order to tune the mass of the valence charm quark we would like to use bare charm mass values on each lattice that produce a J/ψ mass equal to the experimental average, once QED effects are included in the calculation. Here we choose the J/ψ rather than the η_c because the relatively large width of the η_c leads to problems related to the annihilation of the η_c to gluons, which is prohibited in the lattice calculation as we only calculate connected correlation functions. However, our valence masses have not been tuned in this way (they in fact used a modified η_c mass [27]). We measure our valence mass mistunings as the difference between our lattice J/ψ mass and the experimental average. The upper panel of Fig. 4.2, where the horizontal line is the experimental average, shows that these mistunings are all comfortably below the 1% level.

4.3.1 Two-point correlator fitting

Here we are largely interested in the ground state properties of charmonium mesons. We therefore need to extract information, specifically the energies and amplitudes, of these ground states from lattice QCD two-point correlators. We do this by fitting the correlators to sums of exponentials associated with each energy eigenvalue of the system and then taking the ground state values returned by the fit. We do this by using Bayesian priors to constrain the excited states in the standard way [51]. The pseudoscalar correlators are fit to

$$C_P(t) = \sum_i A_i^P \left(e^{-E_i^P t} + e^{-E_i^P (t-Lt)} \right), \quad (4.4)$$

while the vector correlators require a more complicated form due to mixing with the opposite parity states as a result of the use of staggered quarks:

$$C_V(t) = \sum_i \left(A_i^V \left(e^{-E_i^V t} + e^{-E_i^P(t-Lt)} \right) + (-1)^t A_i^{V,o} \left(e^{-E_i^{V,o} t} + e^{-E_i^{V,o}(t-Lt)} \right) \right). \quad (4.5)$$

In these fits it is often necessary to remove the data at low values of t , below some value t_{\min} where excited state contamination is most pronounced. It is also often necessary, following the discussion in Appendix D of [53], to modify the eigenvalues of the correlation matrix to avoid issues related to the poor estimation of the lowest lying eigenvalues of the correlation matrix from the available data. This is done by replacing all eigenvalues below a value of $c\lambda_{\max}$, where λ_{\max} is the largest eigenvalue, with $c\lambda_{\max}$. Our fitting procedure adjusts both t_{\min} and c until a good fit is achieved, using χ^2 as a measure of goodness of fit. As the application of svd cut leads to an alteration of the effective number of degrees of freedom in the fit we apply noise to the procedure for applying the svd cut, following Section 2.8, and require that the χ^2/dof be below 1. Once this is achieved that t_{\min} and c are used in a final fit without svd-noise from which fit results are obtained. The fit without svd-noise has a lower χ^2/dof .

4.3.2 Including quenched QED

We also perform calculations in lattice QCD + quenched QED. By quenched QED it is meant that effects due to the nonzero electromagnetic charge of the sea quarks are neglected, but those of the valence quarks are not. For each configuration on which we perform QCD+QED calculations we generate a momentum space photon field $A_\mu(k)$ in Feynman gauge. This choice of gauge simplifies the generation of the photon field as the QED path integral weight takes the form of a Gaussian with variance $1/\hat{k}^2$ where $\hat{k} = 2\sin(k_\mu/2)$. The results presented here do not depend on this gauge choice. Once the momentum space field is generated it is Fourier transformed into position space. We have checked that these Feynman gauge A_μ fields produce the plaquette and average link obtained from leading order perturbation theory, $\mathcal{O}(\alpha_{\text{QED}})$. These gauge fields are then exponentiated as $\exp(i e Q A_\mu)$ to give a U(1) field which is then multiplied into the QCD gauge links before HISQ smearing. Q is the quark electric charge in units of the proton charge e .

When discussing QCD+QED and pure QCD calculations of some quantity X we will use the notation $X[\text{QCD} + \text{QED}]$ and $X[\text{QCD}]$ respectively. We will often consider the ratio of the two

$X[\text{QCD} + \text{QED}]/X[\text{QCD}] \equiv X[(\text{QCD} + \text{QED})/\text{QCD}]$ for which we will also use the shortened notation $R_{\text{QED}}^{(0)}[X]$. The superscript indicates that the ratio is taken at fixed valence mass. In cases where the mass retuning required by the inclusion of QED effects is taken into account this superscript will be dropped.

While there may in principle be a QED effect on the lattice spacing we use the same lattice spacing for both QCD and QCD+QED calculations. The value of f_π extracted from experimental measurements of the pion leptonic decay rate and V_{ud} which is used to calculate w_0 [46] is a pure QCD quantity. This indicates that QED effects in this scale setting scheme will be very small. There may be a difference introduced by the fact that [46] used light quarks tuned to the neutral pion mass which differs from the charged pion mass by corrections quadratic in the $u - d$ mass difference, in the absence of QED. An uncertainty for this was included on the neutral pion mass used in [46] based on an estimate from chiral perturbation theory. A recent calculation of the QED effects on w_0 using the Ω baryon mass by the BMW collaboration [107] showed that the effect was small and obtained a w_0 value in agreement with the one used here (which was obtained in [46]).

An estimate of the size of QED corrections in charmonium systems can be obtained by studying the QED effect on the J/ψ mass. (This depends on the precise tuning scheme used and the form of the photon propagator used but it is still useful to see the sizes of the shifts we will be dealing with.) The bottom panel of Fig. 4.2 shows the J/ψ mass for both QCD+QED and pure QCD calculations using the am_c valence mass (tuned using the η_c mass) on sets 2, 7, 14 and 16. The vast majority of the uncertainties shown comes from the uncertainty in the lattice spacing. The QCD+QED and QCD results at the same lattice spacing are separated on the x -axis for clarity. All points share a correlated uncertainty from w_0 . The uncorrelated error is shown by the smaller error bar, with the full error bar including the uncertainty from w_0 . Note that the points at the same lattice spacing are also correlated through their w_0/a value. The greatest shift is on set 16 at $\sim 0.4\%$.

The top panel of Fig. 4.2 shows the pure QCD results for $M_{J/\psi}$ using am_c . The error bars are displayed in the same way as for the bottom panel. This shows that, although the bare charm masses were not tuned to the J/ψ there is still not much deviation from the physical J/ψ mass across the ensembles. This means that we can safely use the discrepancy from the experimental J/ψ mass as a mistuning parameter (rather than using the η_c mass). The largest mistuning is clearly on set 19, the finest ensemble.

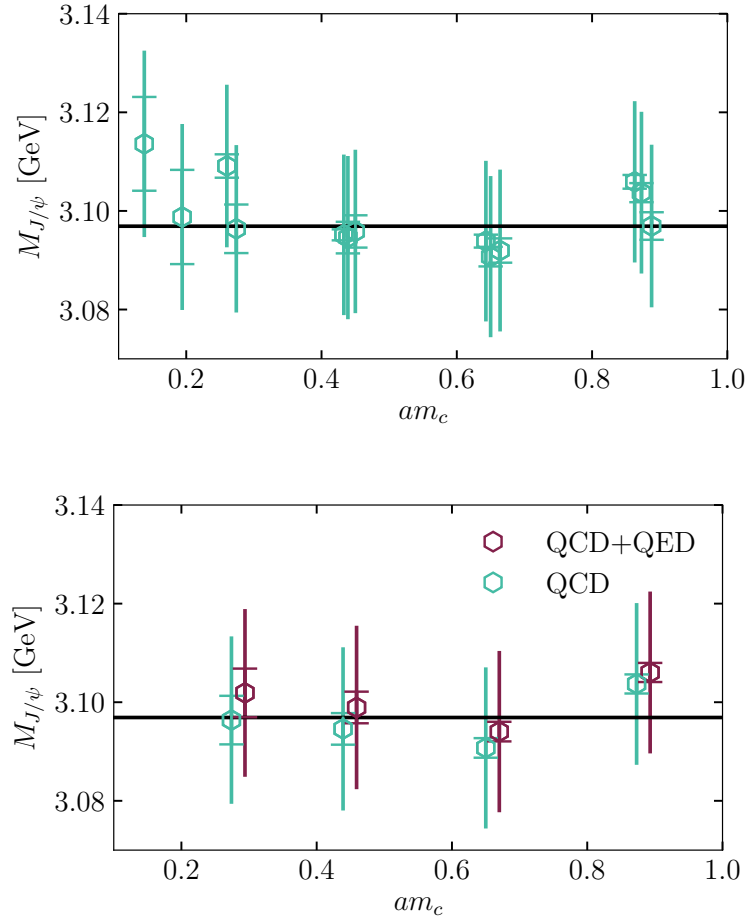


Figure 4.2: Top panel: Pure QCD J/ψ masses on all 15 sets from Table 4.1 using the valence masses in that Table. Two error bars are shown. The error can be broken into parts that are uncorrelated between different sets and the contribution from w_0 which is correlated. The outer error bar shows the full uncertainty and the inner bar the uncertainty without the contribution from w_0 . Bottom panel: The J/ψ masses on sets 2, 7, 10 and 14 with and without the inclusion of quenched QED. On each set the same valence mass was used for both pure QCD and QCD+QED but the points have been separated on the x -axis for clarity. The error bars are the same as for the top panel, but note that here there is a correlation of the uncertainty from w_0/a for the QCD and QCD+QED results on each set.

4.3.3 Fitting strategy for inclusion of QED effects

Our data sets consist of a large amount of pure QCD data on the sets in Table 4.1 with QCD+QED data on a subset of ensembles. To be able to simultaneously account for the effects of valence mass mistuning and QED, which may be similarly sized, we choose to fit all of this data in a single fit for each quantity we consider. The generic form of the fit we use for a quantity X is

$$\begin{aligned}
X(a^2, Q) = x & \left[1 + \sum_{i=1}^5 c_a^{(i)} (am_c)^{2i} + c_m \delta_m^{\text{sea},uds} (1 + c_{a^2,\text{sea}} (a\Lambda)^2 + c_{a^4,\text{sea}} (a\Lambda)^4) + \right. \\
& + c_{m,c} \delta_m^{\text{sea},c} + c_{\text{val},c} \delta_m^{\text{val},c} \times \\
& (1 + c_{\text{val},a} (am_c)^2) + \alpha_{\text{QED}} Q^2 \left\{ c_{\text{QED}} + \sum_{p=1}^3 c_{aQ}^{(p)} (am_c)^{2p} \right. \\
& \left. \left. + c_{\text{val},Q} \delta_{m,\text{val}} \right\} \right]. \tag{4.6}
\end{aligned}$$

Here Λ is chosen to be 1 GeV. Here Q^2 is the valence quark charge used in the calculation and is therefore 0 in pure QCD. The pure QCD value of this fit is x while the value including QED corrections is $x[1 + \alpha_{\text{QED}} Q^2 c_{\text{QED}}]$.

We also include the effect of mistuning of the charm mass in the sea through

$$\delta_m^{\text{sea},c} = \frac{m_c^{\text{sea}} - m_c^{\text{phys}}}{m_c^{\text{phys}}}. \tag{4.7}$$

The values of m_c^{phys} are taken to be the tuned valence mass values divided by the appropriate a . The mistunings in the light and strange quark masses in the sea is accounted for through the mistuning measure:

$$\delta_m^{\text{sea},uds} = \frac{2(m_l^{\text{sea}} - m_l^{\text{phys}}) + m_s^{\text{sea}} - m_s^{\text{phys}}}{10m_s^{\text{phys}}}. \tag{4.8}$$

m_s^{phys} is taken from [27] or, where not available, calculated from the m_c/m_s ratio given in

[27].

Mistuning in the valence mass is measured through $\delta_m^{\text{val},c}$ which we choose to be the difference between the J/ψ mass calculated on each lattice from the PDG experimental average [23] divided by the PDG average:

$$\delta_m^{\text{val},c} = \frac{M_{J/\psi} - M_{J/\psi}^{\text{expt}}}{M_{J/\psi}^{\text{expt}}}. \quad (4.9)$$

All other terms are discretisation effects.

The factor of α_{QED} multiplying the QED part of the fit function is there so that the fit parameters are order 1; this is not a perturbative expansion in α_{QED} . All orders of α_{QED} are included along with $\alpha_{\text{QED}}\alpha_s$ terms. There are some $\alpha_{\text{QED}}\alpha_s$ that are present in full QCD+QED but are not in our full QCD + quenched QED calculation.

In order to make proper use of the correlations between our QCD+QED and pure QCD data we calculate $R_{\text{QED}}^{(0)}[X]$ for each case using the exact same configurations and time sources on both the pure QCD and QCD+QED runs. We then perform simultaneous fits that capture the correlations and appropriately propagate them to the fit outputs from which we calculate $R_{\text{QED}}^{(0)}[X]$. These $R_{\text{QED}}^{(0)}[X]$ values are then multiplied by the full datasets for pure QCD to feed into the fit form of Eq. 4.6. The fit form has been constructed such that the coefficients (apart from x) are expected to be of order 1. We therefore use priors of 0(1) for all fit parameters except x which changes depending on the quantity X and $c_{m,c}$ for which we use a prior of 0 ± 0.1 .

4.4 Hyperfine splitting

The hyperfine splitting, ΔM_{hyp} , is simply calculated on each ensemble as the difference of the vector and pseudoscalar ground state masses, in lattice units, divided by the lattice spacing. The results for aM_{η_c} and $aM_{J/\psi}$ in pure QCD are given in Table 4.2 along with the hyperfine splitting. On Set 7 a purposefully mistuned valence mass of 0.643 was also used to help understand valence mass mistuning effects. Similarly, on Set 18 another mass of 0.188 was also used. Although the pseudoscalar and vector correlators on each configuration are correlated the fit outputs of the vector correlator dominate uncertainties and the correlations have very little effect as a result. We therefore neglect these correlations.

Table 4.2: The η_c and J/ψ masses and their difference ($a\Delta M_{\text{hyp}}$) in pure QCD on each set in lattice units. The pseudoscalar and vector correlator fits have been performed separately and the correlations between aM_{η_c} and $aM_{J/\psi}$ have therefore been ignored because they have little impact.

Set	aM_{η_c}	$aM_{J/\psi}$	$a\Delta M_{\text{hyp}}$
1	2.331899(72)	2.42072(19)	0.08883(20)
2	2.305364(39)	2.39308(14)	0.08772(14)
3	2.287707(26)	2.37476(21)	0.08705(21)
5	1.876536(48)	1.94364(10)	0.06710(11)
7	1.848041(35)	1.914749(67)	0.066708(76)
7*	1.834454(34)	1.901479(66)	0.067025(74)
12	1.833950(18)	1.900441(39)	0.066491(43)
13	1.366839(72)	1.41568(16)	0.04884(17)
14	1.342455(21)	1.391390(43)	0.048935(48)
15	1.329313(18)	1.378237(51)	0.048924(54)
16	0.896675(24)	0.929860(54)	0.033185(59)
17	0.862689(22)	0.895650(37)	0.032961(43)
18	0.666818(39)	0.691981(54)	0.025163(67)
18 [†]	0.652439(56)	0.67798(14)	0.02554(15)
19	0.496991(47)	0.516126(68)	0.019135(82)

Our aim here is to provide a precise enough calculation of the hyperfine splitting to assess the sign and magnitude of the effect of the partial width of the η_c to gluons, which is the largest effect missing from the lattice calculation.

The data, presented in Table 4.2 and Fig. 4.3 (along with a modified version of the fit form Eq. 4.6), show a relatively strong dependence on the light sea quark mass on the finest lattices. This dependence is heavily lattice spacing dependent. We allow for terms in the fit Eq. 4.6 that account for this. The significant lattice spacing dependence of the light sea quark mass mistuning may be due to the masses of the various staggered pions in the sea varying with the lattice spacing.

The effect of quenched QED for the η_c and J/ψ masses and the hyperfine splitting are given in Table 4.3. The inclusion of quenched QED shifts both the η_c and J/ψ masses up by $\mathcal{O}(0.1\%)$. Although these mass shifts are small they can have a more substantial impact on the hyperfine splitting, which is itself less than 10% of the J/ψ mass. The values of $R_{\text{QED}}^{(0)}[\Delta M_{\text{hyp}}]$ are shown against $(am_c)^2$ in Fig. 4.5 where it can be seen that discretisation effects are very small. This is

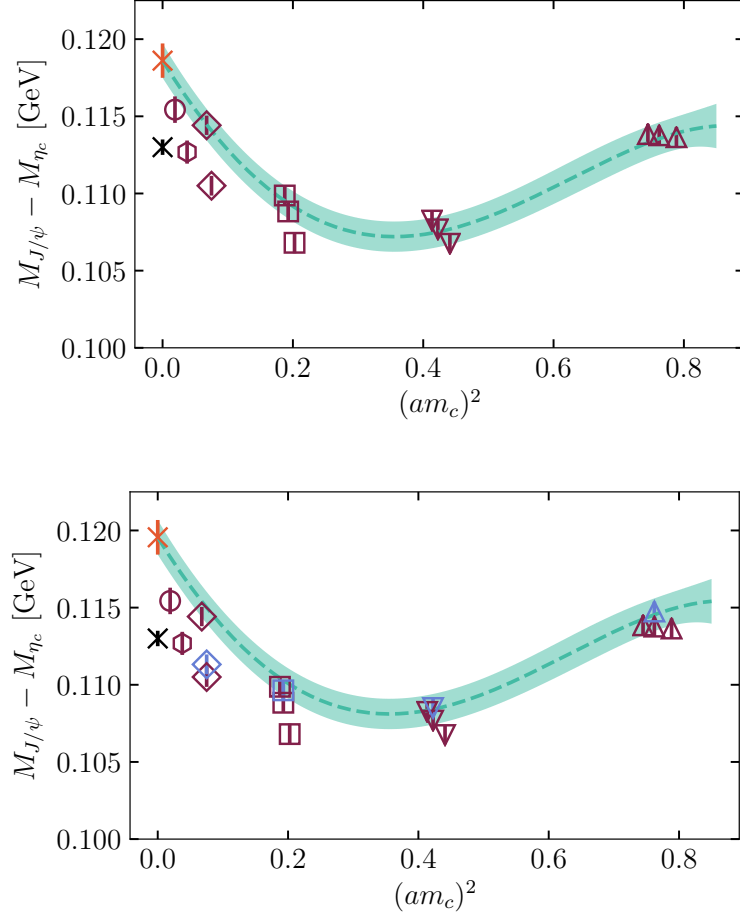


Figure 4.3: The hyperfine splitting against $(am_c)^2$ with the fit of Eq. 4.6. The top plot shows the pure QCD part of the fit while the bottom gives the full fit as well as showing the QCD+QED data points in violet. The two points at purposefully mistuned valence mass are not shown. The black cross is the experimental average and the orange cross is the continuum extrapolation. There is a clear difference between the continuum lattice value and the experimental value which could be explained by the annihilation of the η_c to two gluons.

not true of the individual masses but the effect largely cancels in the difference.

All of our data are shown in Fig. 4.3 against $(am_c)^2$ along with the fit of Eq. 4.6. The fit has a χ^2/dof of 0.59 and the QCD+QED result in the continuum is 0.1196(11) GeV. It is expected that this result will differ from the experimental value of 0.1130(5) GeV due to the missing annihilation

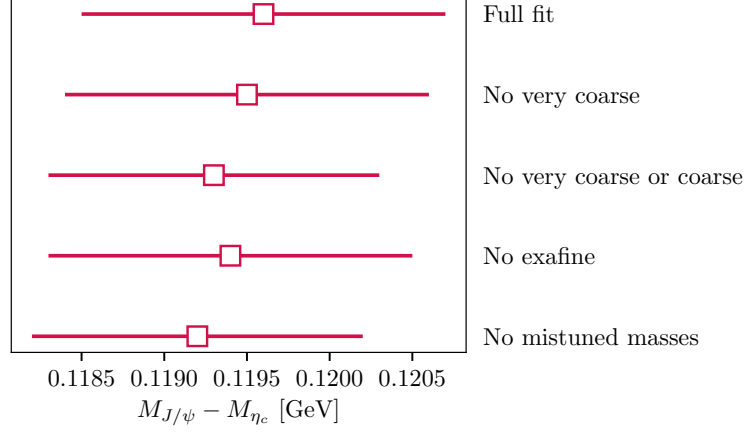


Figure 4.4: Fit results for the hyperfine splitting in QCD+QED (excluding the contribution from the J/ψ annihilation to a photon) with various pieces of data removed. By mistuned masses it is meant the data on sets 7 and 18 that have deliberately mistuned valence masses.

effects discussed above. Taking the (correlated) difference between the continuum value and the x parameter of Eq. 4.6, which corresponds to the pure QCD value, we get 0.948(48) MeV. The continuum value of $R_{\text{QED}}[\Delta M_{\text{hyp}}]$ is 1.00804(43). This fit was tested by removing various pieces of data the results of which are shown in Fig. 4.4. All the results are consistent.

There is an additional, pure QED, contribution to the J/ψ mass from a diagram in which the charm quarks annihilate into a photon which decays back into a charm and anticharm. The contribution of this diagram is

$$\frac{8\pi\alpha_{\text{QED}}Q^2}{M_{J/\psi}^2} |\psi(0)|^2, \quad (4.10)$$

where $\psi(0)$ is the nonrelativistic J/ψ wavefunction equal to (with this normalisation) $f_{J/\psi}\sqrt{M_{J/\psi}}/\sqrt{6}$ [108]. The contribution evaluates to 0.07 MeV. This is added onto our hyperfine splitting result with a 30% uncertainty. This gives a final result of:

$$\Delta M_{\text{hyp}} = 0.1203(11) \text{ GeV}. \quad (4.11)$$

The finite volume effects present in electromagnetic corrections to meson masses have been the

Table 4.3: QCD+QED η_c and J/ψ masses in lattice units and the QED correction to the hyperfine splitting, presented as the ratio of the QCD+QED result to the pure QCD one. Here only the configurations used in the QCD+QED calculation are used for the pure QCD result in the ratio so that correlations in the data can be used.

Set	$R_{\text{QED}}^{(0)}[M_{\eta_c}]$	$R_{\text{QED}}^{(0)}[M_{J/\psi}]$	$R_{\text{QED}}^{(0)}[\Delta M_{\text{hyp}}]$
2	1.000450(26)	1.000750(27)	1.0086(10)
7	1.0008335(59)	1.0010742(81)	1.00774(28)
14	1.0011861(54)	1.0014044(76)	1.00739(26)
16	1.0015755(48)	1.001787(11)	1.00750(33)

subject of extensive study through several different effective field theory approaches. These finite volume effects are organised into a power series in $1/L_s$ as the temporal extent is typically taken to be infinite. To this end [109] uses scalar and spinor QED and then argues for the universality of the leading terms ($\mathcal{O}(1/L_s)$ and $\mathcal{O}(1/L_s^2)$), both between the scalar and spinor case and for point and composite particles. The authors of [110] use scalar NRQED and obtain the same leading terms as [109]. These terms are proportional to the meson electric charge and are therefore not relevant for charmonium. In [110] it is shown that the finite volume expansion for neutral mesons starts at $\mathcal{O}(1/L_s^4)$. We therefore expect finite volume effects to be negligible for the hyperfine splitting calculation we present here. We do, in fact, find that the results for QED mass shifts on Sets 6, 7 and 8 which have spatial extents ranging from 24 to 40 are completely consistent as shown in Fig. 4.6.

4.4.1 Discussion

The experimental average of the hyperfine splitting from the PDG [23] is calculated as the difference of the separate averages for the J/ψ and η_c masses. The different experimental results contributing to the PDG average of the two masses are shown in Fig. 4.7. For the J/ψ mass the average is dominated by the most recent result from KEDR [111]. There are only three experimental results used in these analyses that can independently produce values for the hyperfine splitting. These are the KEDR [111, 112] experiment and two LHCb analyses in different channels [113, 114]. The LHCb result in [114] used the $\eta_c(2S) \rightarrow p\bar{p}$ decay while the analysis of [113] used $\eta_c(1S) \rightarrow p\bar{p}$. In the comparison plot of Fig. 4.8 [113] is referred to as LHCb15 and [114] as LHCb17.

Fig. 4.8 shows a comparison of lattice QCD results for the hyperfine splitting along with the

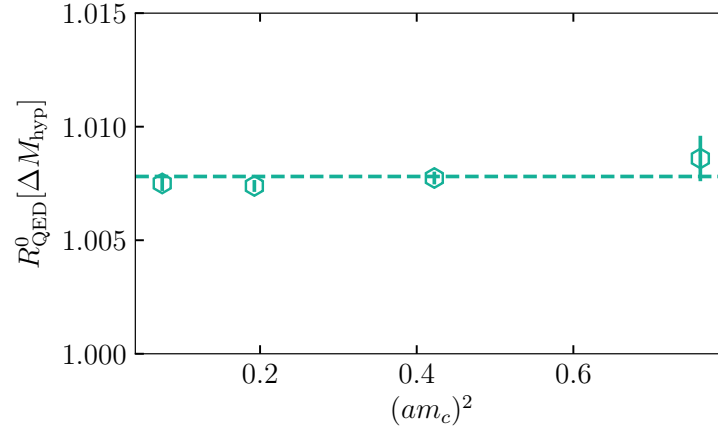


Figure 4.5: The QED effect on the hyperfine splitting against $(am_c)^2$. This shows the smallness of discretisation effects as well as the precision that can be obtained by capitalising on the correlations between QCD+QED and pure QCD correlators. The dashed line shows the average of the points.

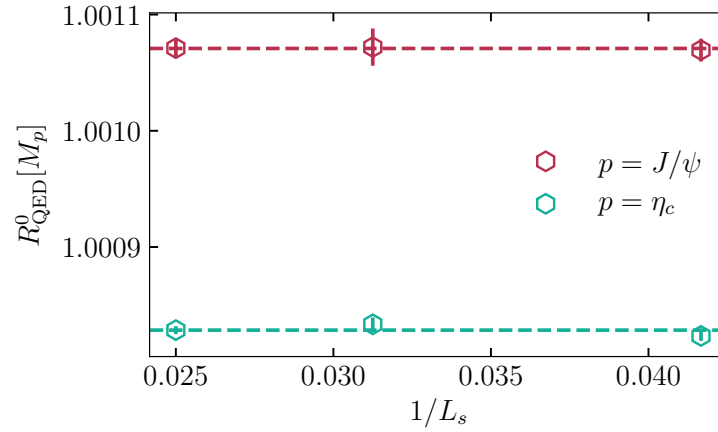


Figure 4.6: The J/ψ and η_c mass shifts from the inclusion of quenched QED presented as the ratio of the QCD+QED value to the pure QCD value. These lines are flat indicating an absence of visible finite volume effects.

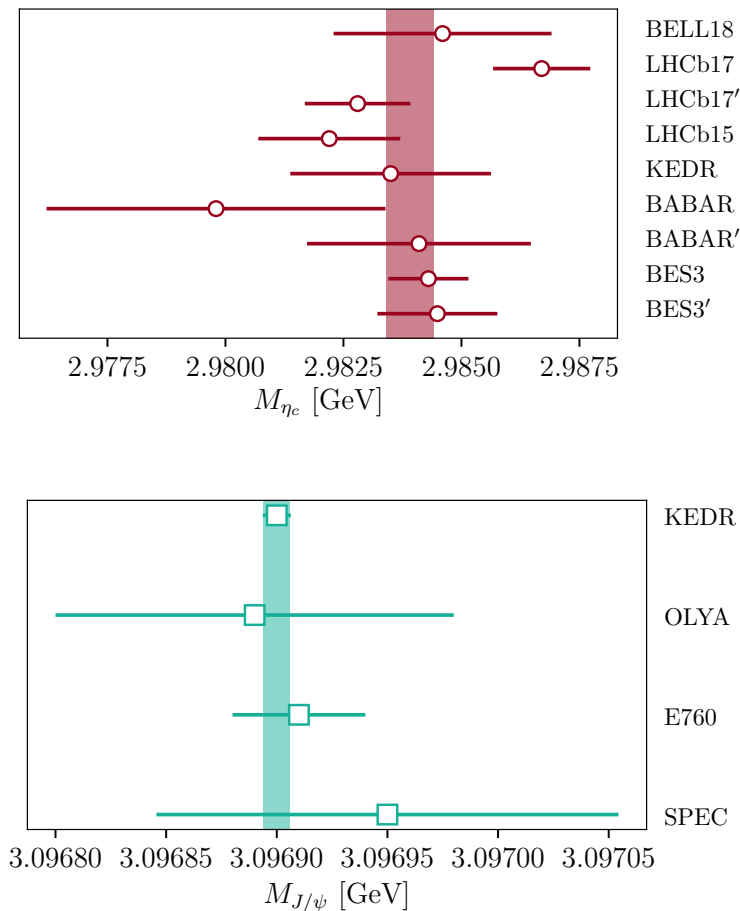


Figure 4.7: Comparison of different experimental results for the charmonium hyperfine splitting as well as the PDG average. The PDG average is obtained from taking the differences of the PDG J/ψ and η_c masses rather than from experiments that directly measure the splitting. The η_c results represent a recent subset of those used in the PDG average. The most recent result is from BELLE [115]. There are three different determinations from LHCb [113, 114, 116], two of which also measured the hyperfine splitting. We include a KEDR measurement [112], two from different BaBar analyses [117] and two from BESIII [118, 119].

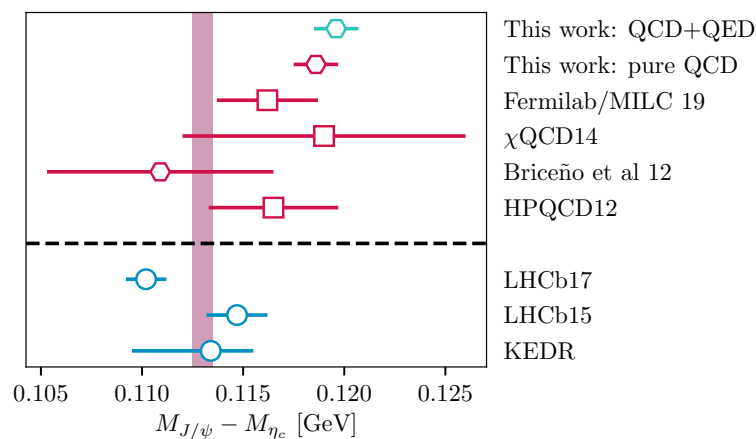


Figure 4.8: Comparison of different lattice results for the charmonium hyperfine splitting and separate experimental results as well as the PDG average. The squares represent 2+1 lattice results and the hexagon this 2+1+1 result. All lattice results have had uncertainties from neglecting η_c annihilation results removed so that we expect some difference between them and experiment. The Fermilab/MILC result using asqtad ensembles and Fermilab charm quarks was presented in [120]. The χ QCD result is from [121] and Briceño et al. is from [122].

Table 4.4: Error budget for our final result for the charmonium hyperfine splitting including quenched QED corrections. The uncertainties shown are given as a percentage of the final result. The largest uncertainties are clearly due to the determination of the lattice spacing.

	ΔM_{hyp}
$a^2 \rightarrow 0$	0.13
Pure QCD statistics	0.24
QCD+QED statistics	0.08
w_0/a	0.24
w_0	0.87
Valence mistuning	0.02
Sea mistuning	0.06
Total	0.96

PDG average and separate experimental values. Both the Fermilab/MILC lattice result and the previous HPQCD result lie above the experimental result although only by just over one standard deviation. The result we present here is substantially more precise than those studies and for the first time displays a nearly 5σ difference from the experimental average, clearly showing that the lattice result lies above the experimental one. We interpret this as the effect of ignoring annihilation to gluons in the calculation of the η_c mass.

The error budget for our hyperfine splitting results is given in Table 4.4. The precise meaning of our error budgets is discussed in Section 2.7. The majority of the uncertainty is associated with the lattice spacing determination, either from the correlated w_0 uncertainty or the individual w_0/a uncertainties. We have separated out the uncertainty arising from the pure QCD data and the $R_{\text{QED}}^{(0)}[\Delta M_{\text{hyp}}]$ values from Table 4.3 which we label “Pure QCD Statistics” and “QCD+QED Statistics” in Table 4.4. The sea mistuning uncertainty comes from the c_m coefficients in Eq. 4.6 and the valence mistuning uncertainty from the c_{val} and $c_{\text{val},Q}$ coefficients. The $a^2 \rightarrow 0$ uncertainty is from the c_a and c_{aQ} coefficients.

Given the precision of our hyperfine splitting result we can give an indication of the size of the η_c annihilation impact on the η_c mass:

$$\Delta M_{\eta_c}^{\text{annihln}} = +7.3(1.2) \text{ MeV.} \quad (4.12)$$

4.5 J/ψ and η_c decay constants

4.5.1 J/ψ decay constant

The decay constant of the J/ψ ($f_{J/\psi}$) is defined such that

$$\langle 0 | \bar{\psi} \gamma_\mu \psi | J/\psi \rangle = f_{J/\psi} M_{J/\psi} \epsilon_\mu, \quad (4.13)$$

where ϵ_μ is the polarisation of the J/ψ . The J/ψ is at rest and has the same polarisation as the current. In terms of the ground state amplitude and mass obtained from the vector correlator it is (in lattice units)

$$f_{J/\psi} = Z_V \sqrt{\frac{2A_{J/\psi}}{M_{J/\psi}}}. \quad (4.14)$$

Here $A_{J/\psi}$ is from Eq. 4.5. Although this cannot be directly measured experimentally it can be related to the partial decay width of the J/ψ to an e^+e^- pair. The relation we use is (correct up to $(m_e/M_{J/\psi})^4$ correction terms from interference between initial and final state radiation [123])

$$\Gamma(J/\psi \rightarrow e^+e^-) = \frac{4\pi}{3} \alpha_{\text{QED}}^2 Q_c^2 \frac{f_{J/\psi}^2}{M_{J/\psi}}, \quad (4.15)$$

where Q_c is the charge of the charm quark in units of the charge of the proton.

Here we give a brief summary of the experimental measurement of the J/ψ decay width to leptons. The spread introduced by imperfect experimental resolution is typically broader than the narrow J/ψ width. If the initial state of the experiment is e^+e^- then $\Gamma(J/\psi \rightarrow e^+e^-)$ can be extracted, in principle, from the cross-section to any final state. The experimental measurement will typically be of the cross-section for the process $e^+e^- \rightarrow e^+e^-$ or $e^+e^- \rightarrow$ hadrons, which will display a resonant contribution on top of a nonresonant background. This measured cross-section is then fitted and resonance parameters extracted. The cross-section can be written in the form [124, 125]

$$\sigma(s) = \int dx \frac{\sigma_0((1-x)s)}{|1 - \Pi((1-x)s)|^2} \mathcal{F}(s), \quad (4.16)$$

where σ_0 is the tree-level cross-section for the relevant process, \mathcal{F} is a function that contains the effects of initial state radiation [126] and Π is the vacuum polarisation function. The vacuum polarisation may be used to separate out nonresonance, resonance and interference terms to the cross-section. To do this the vacuum polarisation may be written as

$$\Pi = \tilde{\Pi} + \Pi_R. \quad (4.17)$$

The resonance contribution to Π may be written as

$$\Pi_R(s) = \frac{3\Gamma_0(J/\psi \rightarrow e^+e^-)}{\alpha_{\text{QED}}} \frac{s}{M_0} \frac{1}{s - M_0^2 + iM_0\Gamma_0}. \quad (4.18)$$

Here the scale independent partial width Γ_0 and mass M_0 (the “bare” parameters of [124]) have been introduced. These are related to the experimentally determined widths by $\Gamma = \Gamma_0/|1 - \tilde{\Pi}|^2$. This amounts to running α_{QED} in Eq. 4.15 to the scale of the charm mass. We take $\alpha_{\text{QED}}(m_c) = 1/133.6$ [127]. While the running of α_{QED} is small it is not negligible and has a 2.5% effect on $\Gamma(J/\psi \rightarrow e^+e^-)$ (compared to taking $\alpha_{\text{QED}} = 1/137$). The expression Eq. 4.15 is clearly tree-level in QED which is the correct form for comparison with experimental measurements inclusive of radiation in the final state. In principle there are corrections from interference between initial and final state radiation but these are heavily suppressed for heavy mesons [123].

The first column of Table 4.5 gives the values of $af_{J/\psi}/Z_V$ in pure QCD on 13 of the sets from Table 4.1. There are clearly reasonably large discretisation effects. In column three we give $R_{\text{QED}}^{(0)}[f_{J/\psi}/Z_V]$ on a subset of these ensembles. These values are shown in Fig. 4.9. Again these effects are comfortably subpercent. We use the values of Z_V from [2] along with a new value for set 18. We collect these values in Table 4.6.

Our results for $f_{J/\psi}$ are shown in Fig. 4.10. The χ^2/dof of the fit from Eq. 4.6 is 0.43. The agreement with experiment can clearly be seen. The sea quark mass dependence is much less than for the hyperfine splitting. We obtain a pure QCD $f_{J/\psi}$ value of 0.4096(16) GeV which becomes 0.4104(17) GeV when including quenched QED. The result for J/ψ derived from experiment using Eq. 4.15 is 0.4064(37) GeV. Our result (both the QCD and QCD+QED results) agree with

Table 4.5: Lattice data and electromagnetic corrections for the J/ψ and η_c decay constants. The electromagnetic corrections for $f_{J/\psi}$ do not include the corrections to Z_V . We take these from [2], using the $\mu = 2$ GeV values except on sets 1-3 which we have calculated for this work as 0.999544(14).

Set	$af_{J/\psi}/Z_V$	af_{η_c}	$R_{\text{QED}}^{(0)}[f_{J/\psi}/Z_V]$	$R_{\text{QED}}^{(0)}[f_{\eta_c}]$
1	0.43370(55)	0.37659(18)	-	-
2	0.42346(48)	0.370332(91)	1.00410(64)	1.00294(50)
3	0.4163(11)	0.366127(57)	-	-
5	0.29411(21)	0.268331(61)	-	-
7	0.28835(15)	0.263727(60)	1.00341(37)	1.00326(13)
7*	0.28671(15)	0.262077(48)	-	-
12	0.285592(88)	0.261676(26)	-	-
13	0.19406(30)	0.18191(12)	-	-
14	0.191341(79)	0.179362(26)	1.00295(12)	1.002951(54)
15	0.18961(15)	0.178039(24)	-	-
16	0.12334(10)	0.117535(28)	1.00283(33)	1.00311(47)
17	0.119606(63)	0.114151(26)	-	-
18	0.091380(85)	0.087772(39)	-	-
18 [†]	0.09069(29)	0.086774(59)	-	-
19	0.06837(11)	0.065876(49)	-	-

Table 4.6: Vector renormalisation constants in the RI-SMOM scheme at both 2 and 3 GeV along with the QED correction at 2 GeV. Most of these values are taken from [2].

β	$Z_V(2 \text{ GeV})$	$Z_V(3 \text{ GeV})$	$R_{\text{QED}}[Z_V](2 \text{ GeV})$
5.80	0.95932(18)	-	0.999544(14)
6.00	0.97255(22)	0.964328(75)	0.999631(24)
6.30	0.98445(11)	0.977214(35)	0.999756(32)
6.72	0.99090(36)	0.98702(11)	0.999831(43)
7.00	0.99203(108)	0.99023(56)	-

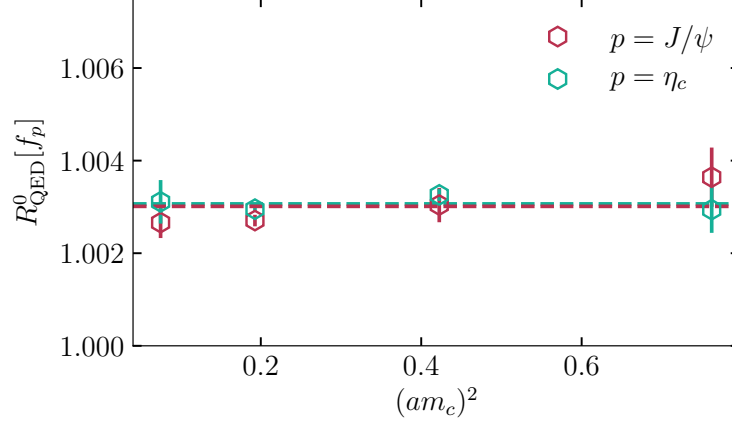


Figure 4.9: The electromagnetic correction to the J/ψ decay constant on lattices with different lattice spacings.

the value obtained using twisted mass fermions and vector current renormalisation (at 2 GeV) in the RI'-MOM scheme¹ [60, 62] in [128]: 0.418(9) GeV.

We studied the volume dependence of the (QCD+QED)/QED ratio of $f_{J/\psi}$ (at fixed valence mass), again, on sets 6-8 and find that the effect is negligible (Fig. 4.11). The value of $R_{\text{QED}}[f_{J/\psi}]$ that we extract from our fit is 1.00188(36).

We have used vector current renormalisations in the RI-SMOM scheme at a scale of 2 GeV. The μ dependence of Z_V should just be the result of discretisation effects and results using different renormalisation scales should agree in the continuum. Here we verify that this is the case using the 2 and 3 GeV results from [2]. There is no 3 GeV result on the very coarse lattices as the discretisation effects are too large. We just use the pure QCD results for $af_{J/\psi}/Z_V$ in the comparison of 2 and 3 GeV, shown in Fig. 4.12. There is clearly agreement between the two results in the continuum limit (the 3 GeV result is 0.4087(18) GeV).

4.5.2 f_{η_c}

We may also calculate the decay constant of the pseudoscalar η_c . While there is not a corresponding experimental measure to compare to directly, it still acts as a test of systematics in different

¹This scheme was shown to suffer from $\mathcal{O}(1\%)$ condensate contamination in the vector current renormalisation in [2] and Section 3.3.

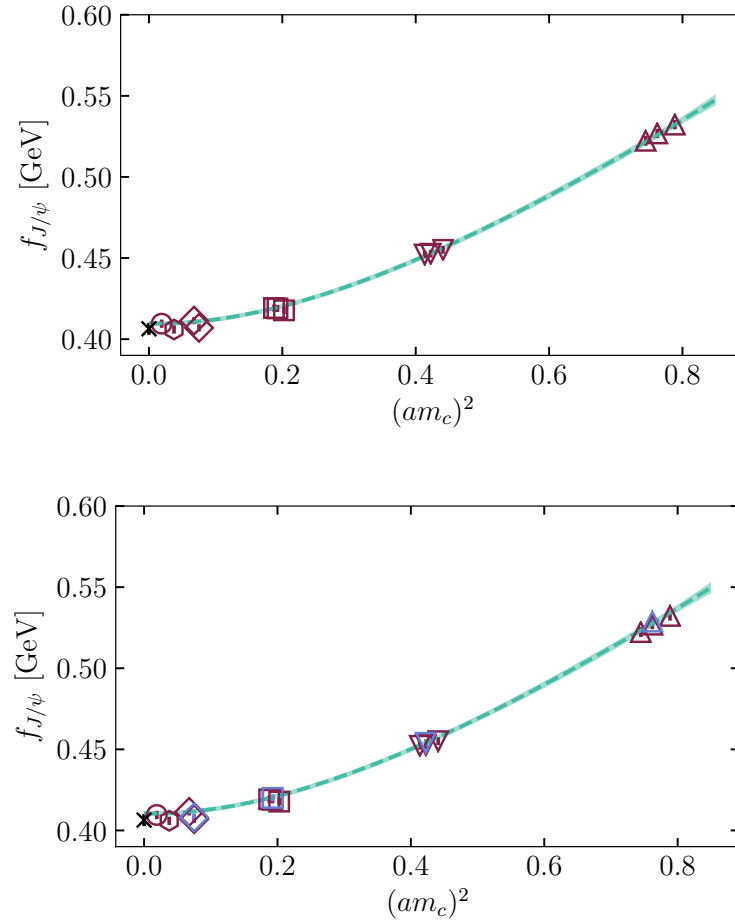


Figure 4.10: The J/ψ decay constant calculated on the ensembles of Table 4.1. The upper plot only gives the pure QCD data points and fit, while the lower plot includes the QCD+QED points in blue which are also included in the fit shown there. There is quite a significant lattice spacing dependence but the sea quark mass dependence is less visible than for the hyperfine splitting. The vector current renormalisation factors determined in the RI-SMOM scheme contribute little to the uncertainties. They also contribute relatively little to the discretisation effects.

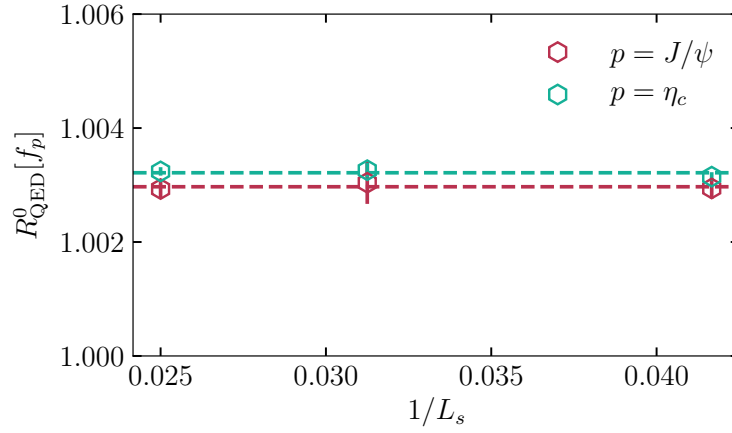


Figure 4.11: The volume dependence of the electromagnetic effect on the J/ψ and η_c decay constants measured on sets 6-8. All results are perfectly consistent with each other indicating that there is no observable finite volume effect.

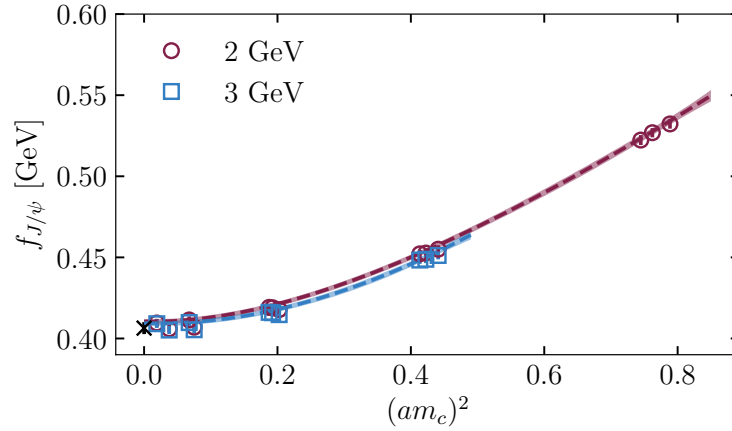


Figure 4.12: The continuum extrapolation of $f_{J/\psi}$ using Z_V at reference scales of 2 and 3 GeV. The points at am_c values of ~ 0.8 are not present for the 3 GeV case as the discretisation errors in Z_V become too large. There is a clear agreement between the two continuum results.

lattice calculations. Here we compare to the result of [106] which also used the HISQ action for valence quarks but on the older $n_f = 2 + 1$ ensembles including asqtad sea quarks.

The pseudoscalar decay constant is extracted from the ground state fit parameters in Eq. 4.4 through:

$$f_{\eta_c} = 2m_c \sqrt{\frac{2A_{\eta_c}}{M_{\eta_c}^3}}. \quad (4.19)$$

We again use data at different valence masses to constrain the fit, as we did with the J/ψ decay constant.

Our results, along with the continuum and mass mistuning fit, are shown in Fig. 4.13. The χ^2/dof of the fit is 0.88. The final result is $f_{\eta_c} = 0.3981(10)$ GeV. Our pure QCD result is $0.3975(10)$ which is in good agreement with the pure QCD result of [106]². The value of $R_{\text{QED}}[f_{\eta_c}]$ we extract is $1.00166(25)$. This lies within a standard deviation of our value for $R_{\text{QED}}[f_{J/\psi}]$.

The volume dependence of the QED effect on f_{η_c} is, again, negligible as shown in Fig. 4.11.

4.5.3 Discussion

We now give the error budget for our final values of $f_{J/\psi}$ and f_{η_c} in Table 4.7. It is clear from this that the dominant sources of error are related to the determination of the lattice spacing.

The error budget presented here for the J/ψ decay constant is markedly different from that of [76]. There the dominant contribution to the error was from the vector renormalisation constant obtained using a matching between lattice time moments and high order perturbative QCD [129]. Here that error is substantially reduced by using the vector current renormalisations of [2]. Again, the largest contributions come from w_0 and the w_0/a values.

Due to a cancellation of w_0 and discretisation effects, the ratio of the vector and pseudoscalar decay constants can be determined to very high precision. This ratio is plotted in Fig. 4.14 with a fit of the form Eq. 4.6 which gives a χ^2/dof of 0.62 and a continuum value of $f_{J/\psi}/f_{\eta_c} = 1.0284(19)$. There is also a significant cancellation of QED effects. The shape of the curve reflects that the discretisation effects are not dominated by $\mathcal{O}(a^2)$.

²In [106] the effects from neglecting the charm quark in the sea are estimated to be $\mathcal{O}(0.01\%)$ which is negligible.

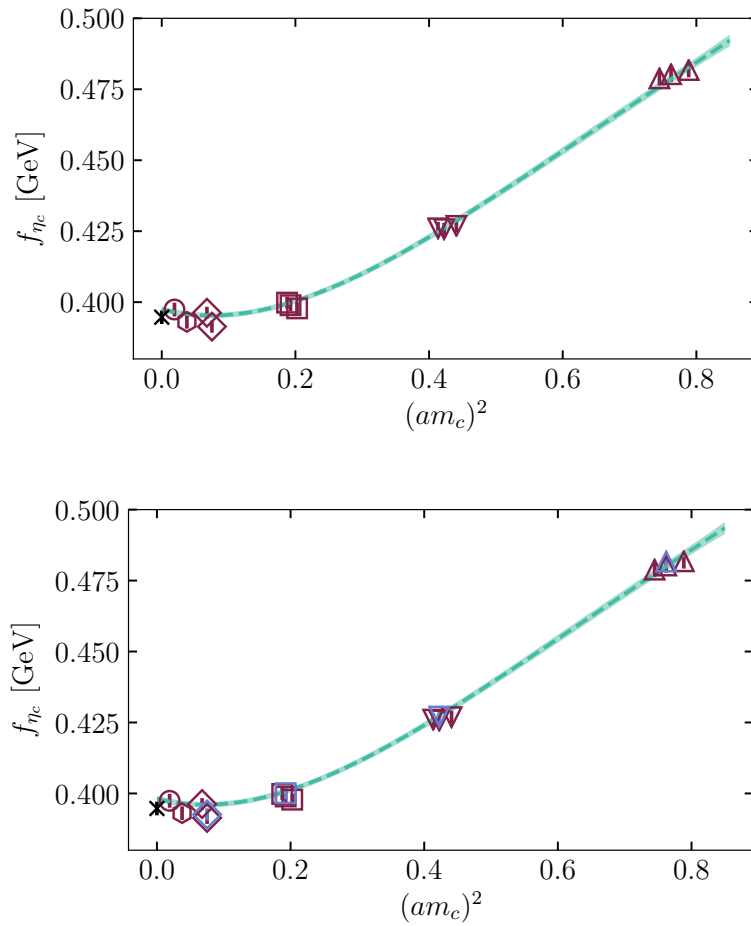


Figure 4.13: The decay constant of the η_c in pure QCD (upper) and QCD+QED (lower). The fit form is the same as was used for $f_{J/\psi}$. The discretisation effects are noticeably smaller than in the J/ψ case.

Table 4.7: Error budget of the J/ψ and η_c decay constants. In both cases the largest uncertainty is contributed by the uncertainty on the value of w_0 , as has also been seen to be the case for the hyperfine splitting. The contributions from different sources are very similar between the two decay constants. The most significant difference between the error budgets is the presence of Z_V in the J/ψ case. This uncertainty has been greatly reduced from the work of [76] by using the RI-SMOM results of [2].

	$f_{J/\psi}$	f_{η_c}
$a^2 \rightarrow 0$	0.09	0.03
Z_V	0.05	-
Pure QCD Statistics	0.12	0.05
QCD+QED Statistics	0.05	0.02
w_0/a	0.11	0.08
w_0	0.34	0.24
Valence mistuning	0.05	0.01
Sea mistuning	0.01	0.00
Total	0.40	0.26

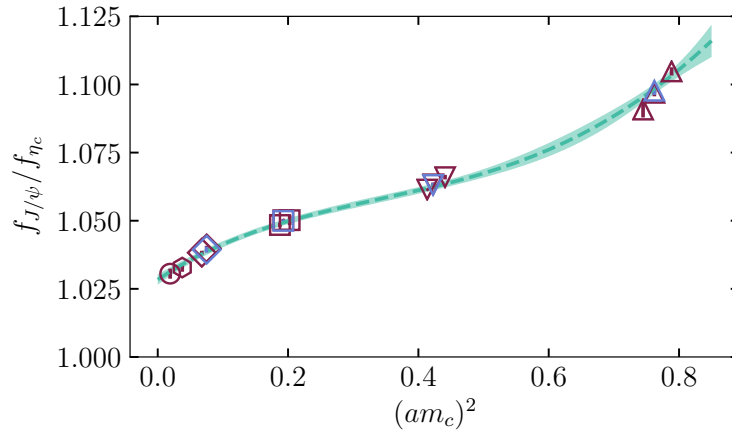


Figure 4.14: Ratio of the vector and pseudoscalar decay constants with continuum extrapolation fit.

4.6 J/ψ tensor decay constant

The J/ψ tensor decay constant is defined analogously to $f_{J/\psi}$. It involves the matrix element of a tensor current in the following way:

$$\langle 0 | \bar{\psi} \sigma_{\mu\nu} \psi | J/\psi \rangle = i f_{J/\psi}^T(\mu) (\epsilon_\mu p_\nu - \epsilon_\nu p_\mu). \quad (4.20)$$

ϵ_μ is the polarisation vector of the J/ψ . Here the decay constant is μ dependent, unlike the vector decay constant. We can therefore extract $f_{J/\psi}^T$ from the two-point tensor correlation function constructed as

$$C_T(t) = \frac{1}{4} \sum_x \langle (-1)^{\eta_T(x)} \text{Tr}(S(x, 0) S^\dagger(x, 0)) \rangle, \quad (4.21)$$

where $\eta_T(x)$ is a position dependent phase remnant of $\sigma_{\mu\nu}$ resulting from the use of staggered quarks. This is the same phase as that appearing in Eq. 3.55. We take ν to be in the temporal direction and average μ over spatial directions. We compute this on a set of ensembles overlapping with those in Table 3.10 summarised in Table 4.8.

There is no standard model observable that can be related to the J/ψ tensor decay constant. A sum rules calculation of $f_{J/\psi}^T$ as well as of the ratio $f_{J/\psi}^T/f_{J/\psi}$ was presented in [128] along with a lattice calculation, and we will compare to their results here. $f_{J/\psi}^T$ is required for the calculation of certain beyond the standard model lepton flavour violating vector meson decay rates [130]. The tensor current requires renormalisation so that $f_{J/\psi}^T$ can be calculated.

The values of $a f_{J/\psi}^T$ extracted from our two point correlator fits on the ensembles in Table 4.8 are given in Table 4.9.

A major goal of the analysis we present here is to investigate the size of nonperturbative effects arising from Z_T and if possible propose a way to remove, or account for, them. We do this by fitting a physical quantity: the tensor decay constant at a scale of 2 GeV. This is obtained by taking the product of the renormalised J/ψ tensor decay constant $f_{J/\psi}^T$ (calculated by multiplying lattice results by $Z_T^{\text{SMOM}}(\mu)$ from Table 3.12 or Table 3.13), the perturbative $\overline{\text{MS}}$ matching discussed in Section 3.4 and the running to 2 GeV in the $\overline{\text{MS}}$ scheme. The fit form used is:

Table 4.8: Parameters of the ensembles on which we calculate the J/ψ tensor decay constant. Some of these ensembles are the same as those in Table 3.10, but here we use a different definition of the lattice spacing that depends on the sea quark masses.

Set	w_0/a	L_s	L_t	am_l^{sea}	am_s^{sea}	am_c^{sea}	am_c^{val}
2	1.1272(7)	24	48	0.0064	0.064	0.828	0.873
5	1.3826(11)	24	64	0.0102	0.0509	0.635	0.664
7	1.4029(9)	32	64	0.00507	0.0507	0.628	0.650
12	1.4149(6)	48	64	0.00184	0.0507	0.628	0.643
14	1.9330(20)	48	96	0.00363	0.0363	0.430	0.439
15	1.9518(7)	64	96	0.00120	0.0363	0.432	0.433
16	2.8960(60)	48	144	0.0048	0.024	0.286	0.274
18	3.892(12)	64	192	0.00316	0.0158	0.188	0.194

Table 4.9: Data for the J/ψ tensor decay constant on each of the ensembles in Table 4.8 in lattice units before multiplication by the tensor renormalisation factor and the ratio of the tensor and vector J/ψ decay constants (again, before renormalisation). The vector decay constant numbers can be found in Table 4.5 in Section 4.5.

Set	$af_{J/\psi}^T/Z_T$	$(Z_V f_{J/\psi}^T)/(Z_T f_{J/\psi})$
2	0.3741(12)	0.8837(30)
5	0.25754(15)	0.87548(81)
7	0.25212(35)	0.8743(13)
12	0.24977(36)	0.8747(13)
14	0.165404(96)	0.86433(62)
15	0.16396(13)	0.86386(78)
16	0.105293(93)	0.8535(10)
18	0.07685(19)	0.8410(22)

$$\begin{aligned}
f_{J/\psi}^T(\mu_{\text{ref}}, \mu, a) &= f_{J/\psi}^T(\mu_{\text{ref}}) \times \left[1 + \sum_n c_{am_c}^{(n)} (am_c)^{2n} + \right. \\
&\quad \left. h_l^{\text{sea}} \frac{\delta_{m_l}^{\text{sea}}}{m_s^{\text{phys}}} + h_c^{\text{sea}} \frac{\delta_{m_c}^{\text{sea}}}{m_c^{\text{phys}}} \right] \times \\
&\quad \left[1 + \sum_i c_{a\mu}^{(i)} (\tilde{a}\mu/\pi)^{2i} + c_\alpha \alpha_{\overline{\text{MS}}}^3(\mu) \right. \\
&\quad \left. + \sum_j c_{\text{cond}}^{(j)} \alpha_{\overline{\text{MS}}}(\mu) \frac{(1 \text{ GeV})^{2j}}{\mu^{2j}} \right].
\end{aligned} \tag{4.22}$$

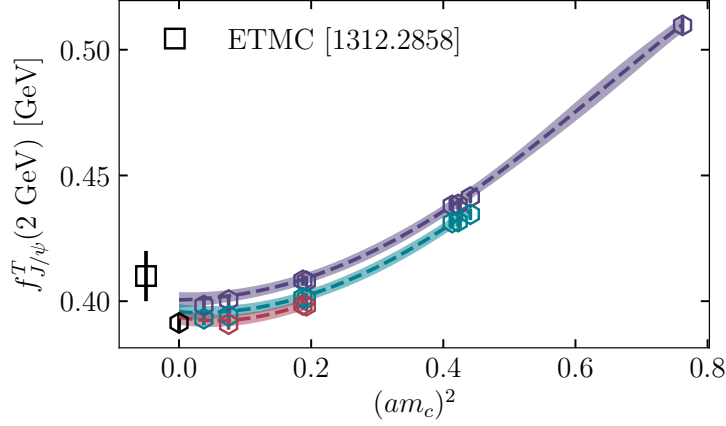


Figure 4.15: Continuum extrapolation of the J/ψ tensor decay constant in the $\overline{\text{MS}}$ scheme at a scale of 2 GeV using tensor current renormalisation in the RI-SMOM scheme. Three different values of the renormalisation scale μ , all converted to $\overline{\text{MS}}$ and run to a reference scale of 2 GeV, are used to allow nonperturbative μ dependence to be fit. These three different μ values are shown as different coloured lines. The purple line is 2 GeV, the blue 3 GeV and the red 4 GeV. The black hexagon at $am_c = 0$ is the physical result for $f_{J/\psi}^T(2 \text{ GeV})$ obtained from the fit (with the condensate pieces removed). The square shows the ETMC result [128] for the J/ψ tensor decay constant.

\tilde{a} refers to the lattice spacing for a given β with physical sea quark masses. The first bracketed term captures the lattice spacing and sea mass dependence of $f_{J/\psi}^T/Z_T$. The second term contains discretisation effects, condensate terms and a term to account for the next term in the perturbative matching to $\overline{\text{MS}}$. This is designed to capture the lattice spacing and μ dependence of Z_T . This is similar to the fit used in Chapter 6 to determine quark masses.

Our data using the RI-SMOM Z_T from Section 3.4 with the fit of Eq. 4.22 are shown in Fig. 4.15. The χ^2/dof is 0.19 giving a continuum value with condensate contributions removed of $0.3912(37)$ GeV. The black hexagon shows the result for the $f_{J/\psi}^T$ fit parameter in Eq. 4.22. This has both the discretisation effects and condensate contributions removed. This is clearly lower than the value you obtain from simply taking the continuum limit of the 2 GeV (purple) line. This indicates the necessity of performing the calculation at multiple values of μ in the RI-SMOM scheme before running all of the results to a reference scale, in this case 2 GeV. The difference between the black hexagon and the lines for the different μ values is then a correction that needs to be applied to

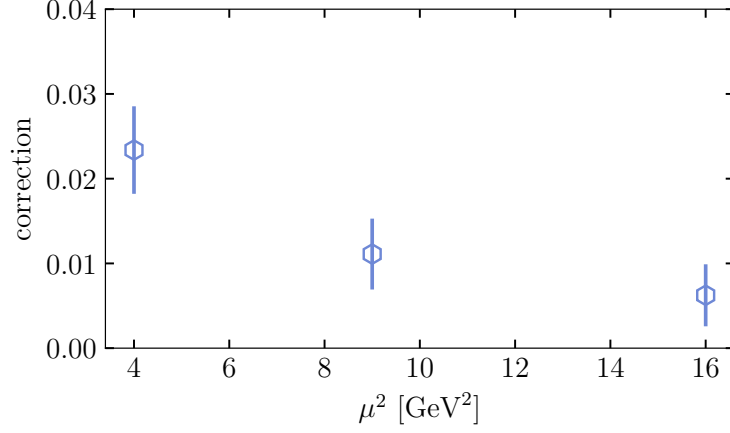


Figure 4.16: The “correction” to the tensor current renormalisation designed to account for nonperturbative effects that must be removed defined in terms of a subset of the fit posteriors of the fit shown in Fig. 4.15. This is the absolute correction. If the corrected value of Z_T is denoted Z_T^{true} and the uncorrected value Z_T^{raw} then $Z_T^{\text{true}} = Z_T^{\text{raw}} - \text{“correction”}$.

the Z_T values to remove the condensate contamination. We define a μ dependent subtraction to apply to the values of Z_T which acts to remove the remaining μ dependence once all Z_T values have been run to the same reference scale μ_{ref} . This is parameterised in Eq. 4.22 by c_α and $c_{\text{cond}}^{(j)}$. It is difficult for the fit to separate these different contributions and as a result the individual coefficients are not well determined. However, if all the terms are combined, taking account of the correlations between the fit parameter outputs, then significant values can be seen across the μ range. These additive corrections are shown in Fig. 4.16 against μ^2 . It can be seen that the corrections are at the 2-3% level for $\mu = 2$ GeV.

We also examine $f_{J/\psi}^T$ using a tensor current renormalisation obtained in the RI'-MOM scheme. In this case we use the conversion to $\overline{\text{MS}}$ in Eq. 3.58 and change the α_s^3 term in Eq. 4.22 to α_s^4 as in this case we use an $\overline{\text{MS}}$ matching accurate through $\mathcal{O}(\alpha_s^3)$. This fit is shown in Fig. 4.17 and the final continuum result agrees with that given by RI-SMOM renormalisation factors. The χ^2/dof of this fit is 0.36 giving a final result for $f_{J/\psi}^T(2 \text{ GeV})$ of 0.3864(38) GeV. This indicates that allowing an α_s^3 term in the continuum extrapolation is sufficient to absorb the potential problems of unknown higher order terms in the perturbative matching to $\overline{\text{MS}}$ in the RI-SMOM case. It can be seen in Fig. 4.17 that the 2 and 3 GeV values are significantly further from each other than the 3 and 4 GeV points. This is reflected in a large coefficient for the $1/\mu^4$ condensate

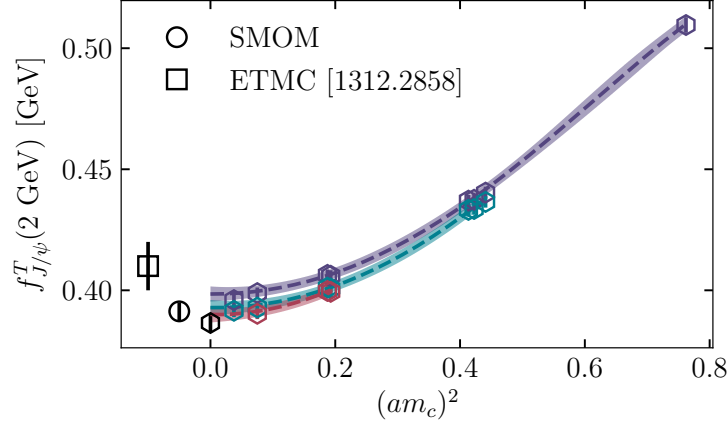


Figure 4.17: Continuum extrapolation of the J/ψ decay constant using a nonperturbative renormalisation of the tensor current in the RI'-MOM scheme. Multiple values of the renormalisation scale μ have been used so that μ dependent nonperturbative effects can be removed in the fit. The result is in agreement with that using RI-SMOM renormalisation (see Fig. 4.15). The colours and shapes denote the same things as in Fig. 4.15.

term in the fit of -1.33(26). The size of the corrections needed for the RI'-MOM scheme is shown in Fig. 4.18 where it can be seen that the correction for 2 GeV is similar to, although more uncertain, than for the RI-SMOM case.

As the discretisation effects in $f_{J/\psi}^T$ are similar to those in $f_{J/\psi}$ on the same set of ensembles, as presented in Section 4.5, we may be able to extract the ratio of the two to a higher precision than can be obtained from the individual fits. (We neglect any correlations between the decay constants on each lattice ensemble.) We may also be able to see a clearer indication of the size of nonperturbative effects in the ratio. This ratio is also presented in [128] using both lattice and sum rules methods.

We show this ratio in Fig. 4.19 using Z_T in the RI-SMOM scheme. We use the fit of Eq. 4.22 and obtain a result for the ratio in the continuum and absent of nonperturbative effects of 0.9627(62). This displays a 2σ with the lattice QCD result of [128], although both are below 1, i.e. the tensor decay constant is lower than the vector decay constant. In Fig. 4.19 two fit lines are shown for each value of μ . This is to display the $\tilde{a}\mu$ dependence of the data. The dashed lines indicate the value of the fit function when $\tilde{a}\mu = 0$. This figure more clearly shows the presence of nonperturbative effects that depend on μ . As discussed in [2] the RI-SMOM Z_V contains no

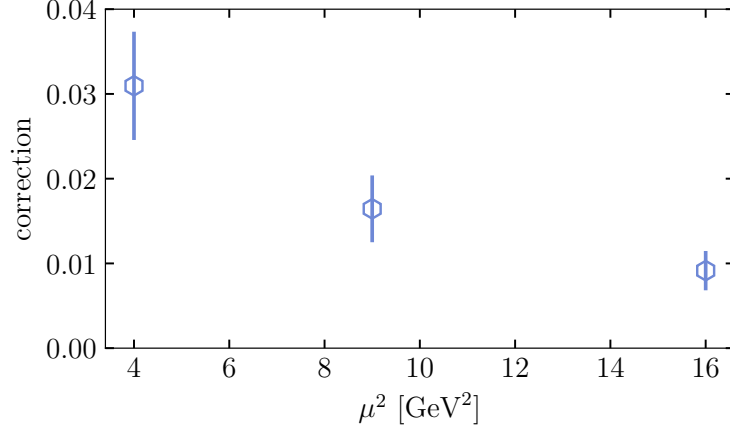


Figure 4.18: The same as Fig. 4.16 but using a tensor current renormalisation in the RI'-MOM scheme.

(at least visible) nonperturbative contamination due to the protection of the Ward-Takahashi identity. Therefore the condensate and α_s^3 terms returned by the fit to the ratio of the vector and tensor J/ψ decay constants should agree with those from the fit to just the tensor decay constant. We find that this is the case for each coefficient individually and for the Z_T correction factor obtained from their combination which we show for the ratio fit in Fig. 4.20.

We give an error budget for our result for the decay constant ratio $f_{J/\psi}^T/f_{J/\psi}$ in Table 4.10. The largest source of uncertainty, other than statistical precision of the lattice decay constant data, comes from the α_s^3 term that allows for the effects of truncating the perturbative matching from RI-SMOM to $\overline{\text{MS}}$.

4.6.1 Final Z_T values

Following the discussion presented above we run all of our results, after converting to $\overline{\text{MS}}$, to a common scale of 2 GeV and then subtract a correction that depends on μ to be applied to the Z_T values of Section 3.4. The scale of 2 GeV allows us to compare directly to the results of [128]. However, another scale is useful when computing form factors for semileptonic B decays. In order to extract phenomenological observables, for example the angular distribution of the differential decay rate of a B to some final state, a weak Hamiltonian in which the W boson degrees of freedom are integrated out is utilised [91]. Observables are then calculated as

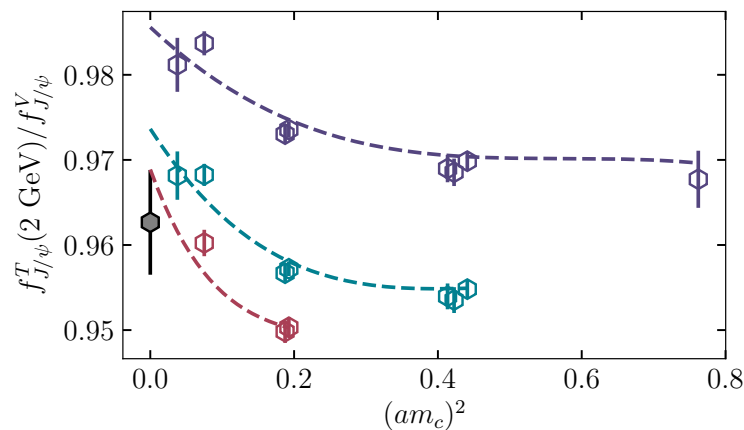


Figure 4.19: Continuum extrapolation of the ratio of the tensor and vector J/ψ decay constants using renormalisation factors in the RI-SMOM scheme. Again, purple points and lines show $\mu = 2$ GeV data and fit lines, blue are 3 GeV and red 4 GeV. The bold dashed lines are continuum extrapolations at each μ value with the condensate terms left in. The black hexagon is the continuum extrapolation with condensates removed.

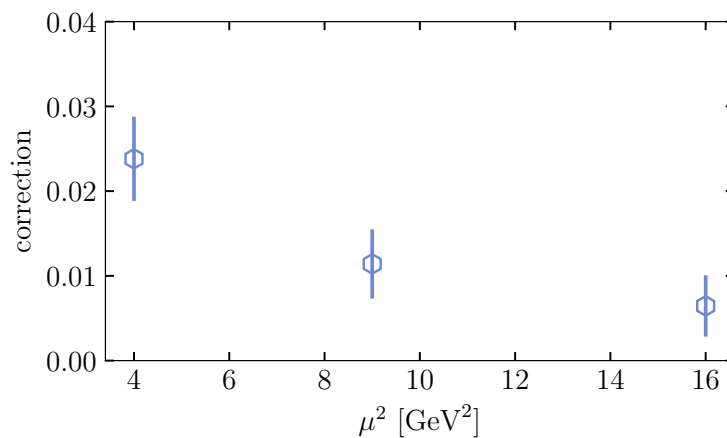


Figure 4.20: Nonperturbative “correction” calculated from a fit to the ratio of the J/ψ vector and tensor decay constants using renormalisation factors from the RI-SMOM scheme. This agrees with Fig. 4.16 as expected from the lack of condensate contributions to the RI-SMOM vector current renormalisation.

Table 4.10: Error budget for the ratio of the J/ψ vector and tensor decay constants. The “Missing α_s^3 ” and “Condensates” error contributions come from the terms in the fit that the Z_T “correction” discussed in the text. Combined, these give the largest contribution to the total uncertainty.

	$f_{J/\psi}^T/f_{J/\psi}$
$(am_c)^2 \rightarrow 0$	0.11
$(\tilde{a}\mu)^2 \rightarrow 0$	0.28
Z_T	0.13
Z_V	0.14
Missing α_s^3 term	0.33
Statistics	0.41
Sea mistuning	0.04
Condensates	0.05
Total	0.64

functions of products of the form factors and the Wilson coefficients of the weak Hamiltonian. These Wilson coefficients are scale dependent and have been calculated at a scale equal to the b mass in the $\overline{\text{MS}}$ scheme $\overline{m}_b(\overline{m}_b)$ in [131].

In Table 4.11 we give both uncorrected and corrected results for Z_T in the $\overline{\text{MS}}$ scheme at a scale equal to the b quark running mass calculated from fully nonperturbative values of Z_T in the RI-SMOM scheme at 2 and 3 GeV. We use a notation $Z_T(\mu_{\text{SMOM}} | \mu_{\overline{\text{MS}}})$ where μ_{SMOM} is the scale at which the RI-SMOM calculation was performed and $\mu_{\overline{\text{MS}}}$ is the final scale at which the $\overline{\text{MS}}$ result is presented. We also give the correlations between these numbers for the corrected case where the source of these correlations is complicated by the addition of terms from a fit to the data.

Table 4.11: Z_T values in the RI-SMOM scheme run to a renormalisation scale of the b quark running mass in the $\overline{\text{MS}}$ scheme. The notation $Z_T(\mu_1|\mu_2)$ indicates that Z_T has been calculated in the RI-SMOM scheme at a scale of μ_1 and then converted to the $\overline{\text{MS}}$ scheme and run to a scale of μ_2 . The first set of results are given without any correction for nonperturbative effects. The second set have a correction applied calculated from continuum fits to the J/ψ vector to tensor decay constant ratio. The superscript c indicates that these are corrected values, i.e. the correction to remove condensate contamination has been applied.

Set	$Z_T(2 \text{ GeV} \overline{m}_b)$	$Z_T(3 \text{ GeV} \overline{m}_b)$
2	0.9846(20)	-
7	1.0097(21)	0.99408(87)
14	1.0392(21)	1.02178(89)
16	1.0704(22)	1.05353(93)
18	1.0820(27)	1.0703(11)
Set	$Z_T^c(2 \text{ GeV} \overline{m}_b)$	$Z_T^c(3 \text{ GeV} \overline{m}_b)$
2	0.9623(51)	-
7	0.9874(51)	0.9834(39)
14	1.0169(51)	1.0111(39)
16	1.0480(51)	1.0428(39)
18	1.0624(49)	1.0596(39)

Table 4.12: Correlation matrix of the corrected Z_T values from Table 4.11. These correlations are large in part due to the correlation of the perturbative matching and running calculations that have been applied.

	(2,2)	(7,2)	(14,2)	(16,2)	(18,2)	(7,3)	(14,3)	(16,3)	(18,3)
(2,2)	1.0	0.99815	0.99895	0.99625	0.95044	0.96298	0.96425	0.96478	0.94788
(7,2)	0.99815	1.0	0.99835	0.99582	0.95032	0.96148	0.96186	0.96247	0.94578
(14,2)	0.99895	0.99835	1.0	0.99702	0.95174	0.95941	0.96099	0.96149	0.94410
(16,2)	0.99625	0.99582	0.99702	1.0	0.94886	0.95649	0.95798	0.96050	0.94215
(18,2)	0.95044	0.95032	0.95174	0.94886	1.0	0.92363	0.92517	0.92586	0.95432
(7,3)	0.96298	0.96148	0.95941	0.95649	0.92363	1.0	0.99964	0.99923	0.98721
(14,3)	0.96425	0.96186	0.96099	0.95797	0.92517	0.99964	1.0	0.99945	0.98752
(16,3)	0.96425	0.96186	0.96099	0.95797	0.92517	0.99923	0.99945	1.0	0.98725
(18,3)	0.96478	0.96247	0.96149	0.96050	0.92586	0.98722	0.98752	0.98725	1.0

4.7 a_μ^c and vector time moments

With new results expected from the Fermilab $g - 2$ experiment soon there has been a concerted effort by the lattice community to understand and control systematic effects, in particular, in the calculation of the hadronic vacuum polarisation contribution to the anomalous magnetic moment of the muon. Classically the magnetic moment of the muon is 2, so the anomaly is presented as a difference from this value $a_\mu \equiv g - 2$. The hadronic vacuum polarisation contribution to this value can be separated into different flavour contributions. The charm quark contribution is denoted a_μ^c . The first calculation of a_μ^c is from [77]. Following [77] we can extract a_μ^c from the charmonium vector current correlators by calculating the current-current correlator time moments:

$$G_n = Z_V^2 \sum_t t^n C_V(t). \quad (4.23)$$

The t here runs from $-T/2$ to $T/2$ rather than from 0 to T ³. The charm contribution to the four lowest moments, $n = 4, 6, 8, 10$, can be compared to values extracted from experiment using high order QCD perturbation theory. The perturbation theory is needed to subtract the u, d, s contribution from experimental $e^+e^- \rightarrow$ hadrons cross-section data. In [129] these are defined as

$$\begin{aligned} \mathcal{M}_k &\equiv \int \frac{ds}{s^{k+1}} R(s) \\ &= \frac{12\pi^2}{k!} \left(\frac{\partial}{\partial q^2} \right)^k \Pi(q^2)|_{q^2=0}, \end{aligned} \quad (4.24)$$

where $\Pi(q^2)$ is the vacuum polarisation function. ($R(s)$ is the charm quark contribution only.) These are related to the time moments defined in Eq. 4.23 by

$$G_n^{\text{exp.}} = \frac{(2k+2)! \mathcal{M}_k}{12\pi^2 Q^2}. \quad (4.25)$$

The analysis of [129] uses a dispersion relation derived from the optical theorem to relate deriva-

³The python package <https://github.com/gplepage/g2tools> is used to calculate time moments and a_μ^c .

Table 4.13: Vector current time moment data on the ensembles in Table 4.1. The values given are $(G_n/Z_V^2)^{1/(n-2)}$ in lattice units.

Set	$n = 4$	$n = 6$	$n = 8$	$n = 10$
1	0.389670(40)	0.949791(62)	1.410524(75)	1.815497(88)
2	0.396283(22)	0.961260(35)	1.425498(42)	1.833868(49)
3	0.400779(15)	0.969045(24)	1.435671(28)	1.846369(33)
5	0.511194(12)	1.164351(19)	1.701040(26)	2.184698(34)
7	0.5206344(85)	1.181180(14)	1.724311(19)	2.214708(24)
7*	0.5254224(87)	1.189687(14)	1.736041(19)	2.229780(25)
12	0.5254560(47)	1.1897785(76)	1.736217(10)	2.230069(13)
13	0.70981(13)	1.53941(21)	2.24688(27)	2.90799(32)
14	0.723760(11)	1.566115(20)	2.285959(27)	2.959283(36)
15	0.731489(11)	1.580936(18)	2.307649(25)	2.987715(32)
16	1.070736(33)	2.276543(58)	3.355470(80)	4.37418(10)
17	1.114660(44)	2.366266(78)	3.48827(11)	4.54699(14)
18	1.431378(91)	3.03675(16)	4.49434(22)	5.86769(29)
18 [†]	1.46556(17)	3.10710(31)	4.59734(43)	6.00058(56)
19	1.91475(23)	4.06357(42)	6.02429(55)	7.86806(66)

Table 4.14: (QCD+QED)/QCD values for the time moments on a subset of the ensembles in Table 4.1. The values given are $(G_n/Z_V^2)^{1/(n-2)}$ [(QCD+QED)/QCD].

Set	$R_{\text{QED}}^{(0)}[n = 4]$	$R_{\text{QED}}^{(0)}[n = 6]$	$R_{\text{QED}}^{(0)}[n = 8]$	$R_{\text{QED}}^{(0)}[n = 10]$
2	0.999954(26)	0.999910(17)	0.999858(15)	0.999810(15)
7	0.9998455(15)	0.9997169(11)	0.9995987(10)	0.9994908(11)
14	0.999554(24)	0.999312(20)	0.999124(20)	0.998995(22)
16	0.999096(59)	0.998767(49)	0.998584(48)	0.998489(48)

Table 4.15: The first four time moments calculated from our lattice data in the continuum limit compared with the results extracted from experiment in [129]. Agreement at the level of a single standard deviation is seen for all time moments.

n	$G_n^{1/(n-2)}$	$(G_n^{\text{exp.}})^{1/(n-2)}$	$R_{\text{QED}} \left[G_n^{1/(n-2)} \right]$
4	0.31715(49)	0.3142(22)	1.00106(13)
6	0.67547(84)	0.6727(30)	1.00069(11)
8	1.0041(11)	1.0008(34)	1.000466(99)
10	1.3117(13)	1.3088(35)	1.000370(96)

tives of the vacuum polarisation function to the $e^+e^- \rightarrow$ hadrons cross-section. As the data for $\sigma(e^+e^- \rightarrow \text{hadrons})$ that are used are inclusive of photons in the final state this should include all the internal QED contributions to vacuum polarisation bubbles. Judging by the good agreement between previously calculated pure QCD time moments [76] and those from experiment we expect QED effects to be small.

In order to compare G_n determined from the lattice and from experiment we must take the continuum limit of our results. As before, we use a fit form that includes terms accounting for $(am_c)^{2i}$ discretisation effects, valence mass mistunings and sea quark mass mistunings. The values of $(G_n/Z_V^2)^{1/(n-2)}$ are given in lattice units for all the ensembles we employ in Table 4.14. The $(n-2)^{\text{th}}$ root is taken in order to reduce all moments to the same dimensionality, that of inverse mass. The QED corrections $R_{\text{QED}}^{(0)}[n]$ to the moments are also given there. The QED corrections to Z_V are not included in these values.

As we have reduced all moments to have dimension of inverse mass we can construct dimensionless quantities by multiplying $G_n^{1/(n-2)}$ by $M_{J/\psi}$. These quantities can be extrapolated to the continuum and then divided by the experimental J/ψ mass to recover the time moments. The lattice spacing cancels in the ratio which we find greatly reduces the uncertainty in the continuum.

Fig. 4.21 shows the four moments multiplied by $M_{J/\psi}$ against $(am_c)^2$ with the fit of Eq. 4.6. The crosses are at the positions of the continuum values. The QED corrected points are not shown here for clarity but are included in the fit. The moments are fit simultaneously. This requires an svd cut of 10^{-3} which produces a χ^2/dof of 0.62. The continuum extrapolated results (divided by the experimental J/ψ mass) are given in column 2 of Table 4.15. In all cases we achieve greater precision than the results of [129] which are given in the third column. Agreement within 2σ is seen between our results and those of [129] for all four moments.

For the first two moments we show a comparison between our results and previous results from lattice QCD calculations as well as phenomenological determinations that make use of experimental data in Fig. 4.22.

Error budgets for the four rooted moments are given in Table 4.16. The additional uncertainty incurred from using an svd cut in the simultaneous fit is contained in the contribution labelled ‘‘Pure QCD Statistics’’. While the lattice spacing cancels in the data we fit, contributions from w_0 and w_0/a still arise through their use in the calculation of the valence mass mistunings on the various ensembles.

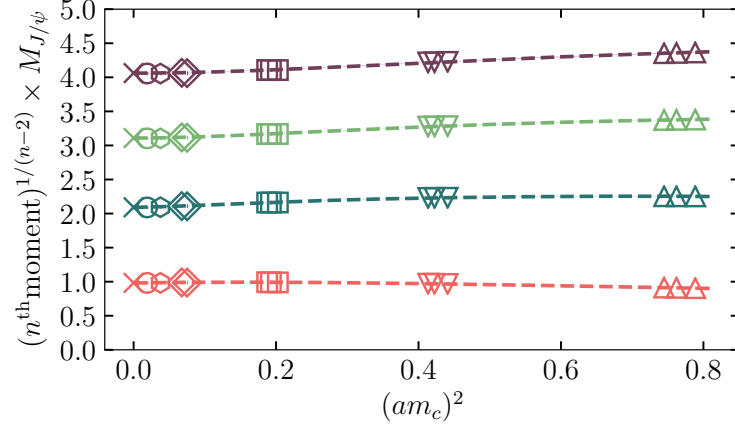


Figure 4.21: The four lowest time moments multiplied by the J/ψ mass and their extrapolation to $a = 0$. The values of the moments increase as the moment number is increased. The extrapolations of the moments shown are performed simultaneously.

The connected charm contribution to the anomalous magnetic moment of the muon, a_μ^c , is related to the vacuum polarisation function $\hat{\Pi}(q^2)$ by an integration over a kinematic kernel. As the time moments are related to derivatives of $\hat{\Pi}(q^2)$ w.r.t q^2 they can be used to construct a Taylor expansion at low q^2 where the kinematic kernel is large. This is done through the relationship

$$\begin{aligned} Q^2 G_{2i} &= (-1)^i \frac{\partial^{2i}}{\partial q^{2i}} q^2 \hat{\Pi}(q^2) |_{q^2=0} \\ &= (-1)^i (2i)! \Pi_{i-1}, \end{aligned} \quad (4.26)$$

where Π_{i-1} is the $(i-1)^{\text{th}}$ Taylor coefficient. In practice the Taylor series is replaced by a Padé approximant to handle the high q^2 behaviour.

To calculate a_μ^c in the continuum we can either use the continuum extrapolated time moments or calculate a_μ^c on each lattice, using the time moments on that lattice, and then take the continuum limit. If a_μ^c were directly calculated from the moments in Table 4.14 on each ensemble then it would contain the uncertainty from the lattice spacing determination. As this has largely been removed from our time moments through multiplication by $aM_{J/\psi}$, using the time moment values

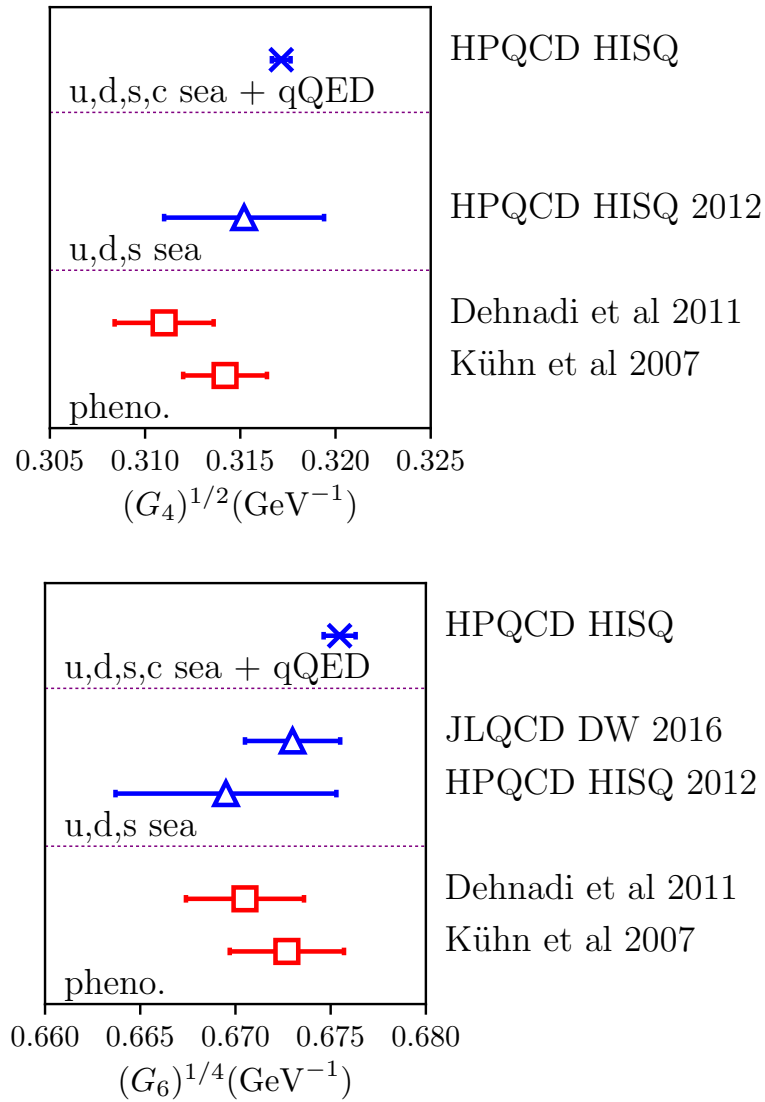


Figure 4.22: Comparisons of various determinations of the first two vector charm moments. Lattice QCD results are shown in blue and phenomenological determinations using $e^+e^- \rightarrow$ hadrons cross-section data are shown in red. The previous HPQCD result is from [76] and the JLQCD result is from [132]. For the latter only the second of the two moments is available due to discretisation effects. The phenomenological results are from [129] and [133]. [Figure courtesy of C. T. H. Davies.]

Table 4.16: Error budget for various time moments as calculated from an extrapolation in the (rooted) moment multiplied by the J/ψ mass.

	$G_4^{1/2}$	$G_6^{1/4}$	$G_8^{1/6}$	$G_{10}^{1/8}$
$a^2 \rightarrow 0$	0.06	0.05	0.04	0.03
Z_V	0.04	0.02	0.02	0.02
Pure QCD Statistics	0.03	0.02	0.02	0.02
QCD+QED Statistics	0.01	0.01	0.01	0.01
w_0/a	0.06	0.05	0.05	0.04
w_0	0.10	0.08	0.06	0.05
Sea mistunings	0.06	0.03	0.03	0.03
Valence mistunings	0.01	0.00	0.00	0.00
$M_{J/\psi}^{\text{exp.}}$	0.02	0.02	0.02	0.02
Total	0.15	0.12	0.11	0.10

calculated in the continuum would be considerably more precise. However, we can calculate a_μ^c on each lattice in a way that removes the relatively large uncertainty contribution from the lattice spacing determination. This is discussed in Section 4.7.1.

By calculating a_μ^c from the continuum values of the time moments given in Table 4.15 we obtain an a_μ^c value of $1.4595(44) \times 10^{-9}$ and an $R_{\text{QED}}[a_\mu^c]$ value of 1.00212(26).

4.7.1 a_μ^c lattice spacing dependence

In order to reduce the uncertainty arising from the lattice spacing determination we multiply the value (in lattice units) of each rooted time moment from Table 4.14 by $aM_{J/\psi}$ and then divide by the experimental value of the J/ψ mass. These values on each ensemble are given in Table 4.17.

The results of calculating a_μ^c on each lattice and then extrapolating are given in Table 4.17 and shown in Fig. 4.23 where the fit has a χ^2/dof of 0.44. This fit obtains

$$\begin{aligned}
 a_\mu^c &= 1.4638(47) \times 10^{-9}, \\
 R_{\text{QED}}[a_\mu^c] &= 1.00214(19).
 \end{aligned}
 \tag{4.27}$$

The final result agrees with that obtained from using the continuum extrapolated moments

(labelled “moments” in Fig. 4.23) as well as the previous HPQCD result and the result obtained by the BMW collaboration using a different staggered quark action [134].

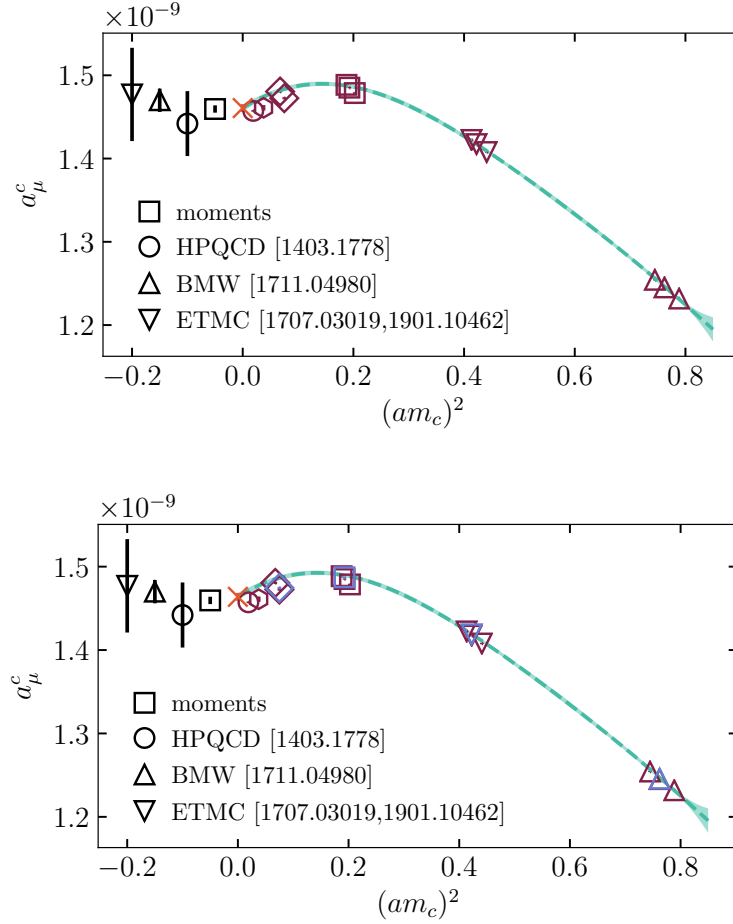


Figure 4.23: Extrapolation of the charm connected HVP contribution to the anomalous magnetic moment of the muon to the continuum. The continuum result is compared to the result obtained by calculating a_μ^c from the individually continuum extrapolated time moments. Agreement is seen, as expected. The result also agrees well with, with a significantly decreased uncertainty, the previous HPQCD result. There is also agreement with the BMW result of [134] and the ETMC result of [135, 136] where we have used the QED correction of [136]. The upper plot displays only pure QCD data with a fit line excluding the QED part of the fit. The lower plot includes the QCD+QED data and the full fit.

In order to demonstrate the reduction in discretisation effects achieved with the HISQ action we

Table 4.17: Values of a_μ^c and the electromagnetic correction $R_{\text{QED}}^{(0)} [a_\mu^c]$ used in the fit shown in Fig. 4.23. The uncertainties quoted are correlated through w_0 across all ensembles and, to a lesser extent, Z_V across those sharing the same β .

Set	$a_\mu^c \times 10^9$	$R_{\text{QED}}^{(0)} [a_\mu^c]$
1	1.23183(78)	-
2	1.24522(75)	1.000478(80)
3	1.25431(77)	-
5	1.40782(91)	-
7	1.41738(91)	1.001080(89)
7*	1.42370(91)	-
12	1.42234(91)	-
13	1.47866(97)	-
14	1.48514(75)	1.001416(83)
15	1.48853(75)	-
16	1.4725(13)	1.00141(15)
17	1.4805(13)	-
18	1.4610(33)	-
18†	1.4702(33)	-
19	1.4572(10)	-

can compare our results to the results of the BMW collaboration who used a different staggered action. We read the BMW a_μ^c values from Fig. S4 of [134]. In Fig. 4.24 we plot these values along with ours against a^2 . The BMW values are shown as green dots. The size of these dots is not indicative of the uncertainty.

An analysis of the QED finite volume effects in the light quark hadronic vacuum polarisation using scalar QED was given in [137]. Scalar QED was used as the dominant finite volume effect should arise from pion loops. There it was shown that the leading finite volume effect for the neutral current goes as $1/L^3$ due to a cancellation of the $1/L^2$ terms. The analysis of that work suggests that the QED finite volume on the light quark HVP contribution is unobservably small so we expect the same to be true of the charm quark contribution. We observe this to be true for both a_μ^c and all the time moments we study as Fig. 4.25 shows.

The quenched QED effect on a_μ^c was studied using a methodology based on an expansion in α_{QED} in [135]. The result was updated in [136] following work on the QED effect to the renormalisation of quark bilinears presented in [138]. The $[(\text{QCD}+\text{QED})/\text{QCD}]$ value obtained in [136] is 1.00123(25). This is in slight disagreement with our result but the two calculations use different

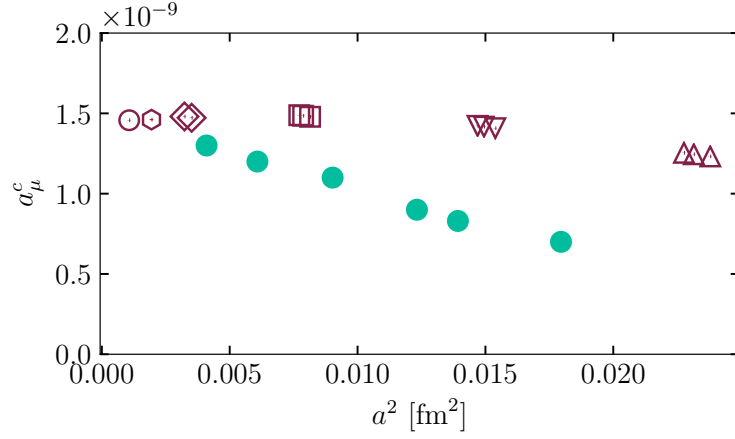


Figure 4.24: Comparison of the discretisation effects in the data of Table 4.17 (red open symbols) and the data from BMW [134] (green circles). The BMW data points are estimates and do not include an uncertainty.

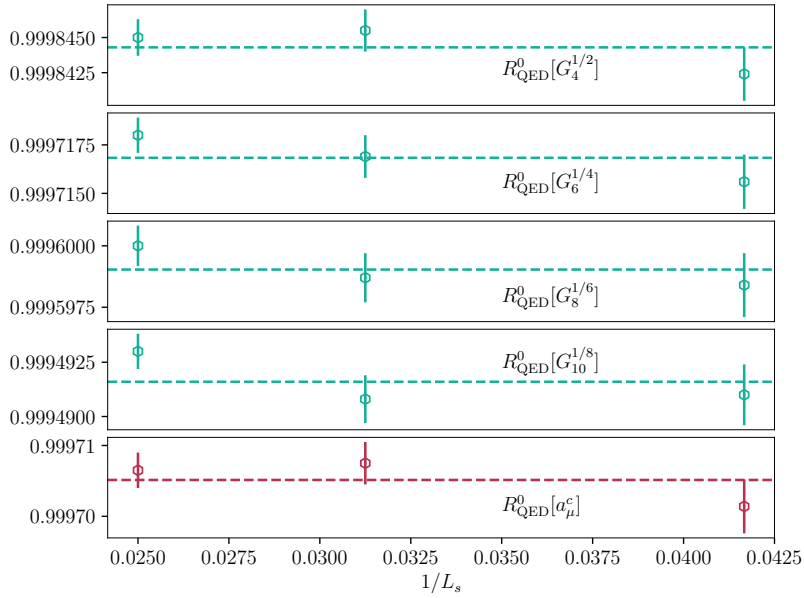


Figure 4.25: Volume dependence of the electromagnetic correction to a_μ^c and the first four vector current correlator time moments on sets 6–8. There is no observable dependence as expected from previous analyses of QED finite volume effects in the hadronic vacuum polarisation.

Table 4.18: Error budget for the direct determination of the charm quark connected HVP contribution to the anomalous magnetic moment of the muon. Factors of the lattice spacing cancel in the raw data we use in the extrapolation but w_0 and w_0/a still contribute to the uncertainty through their use in the calculation of mistuning parameters.

	a_μ^c
$a^2 \rightarrow 0$	0.15
Z_V	0.07
Pure QCD Statistics	0.08
QCD+QED Statistics	0.01
w_0/a	0.16
w_0	0.18
Sea mistunings	0.09
Valence mistunings	0.03
$M_{J/\psi}^{\text{exp.}}$	0.05
Total	0.32

charm mass tuning schemes. The results of [136] also support the conclusion of [137] that finite volume effects are small.

Results for the QED effect on the strange and light connected contributions using domain wall fermions were presented in [89]. While the comparison to our results is not a direct one it is interesting to note that the contribution from the QED correction to Z_V evaluated in [89] forms a significant contribution to the overall QED correction and is in fact considerably larger than the contribution from the correlator in the strange case. Once the correction to the vector current renormalisation is taken into account the correction is $\mathcal{O}(0.1\%)$ which is consistent with our findings for the charm contribution and with the results of [136].

The value of a_μ^c presented here is compared with other results from lattice QCD in Fig. 4.26. The BMWc result is from [134] and the ETMC result from [135]. Agreement is seen between all the lattice results with the result presented here the most precise.

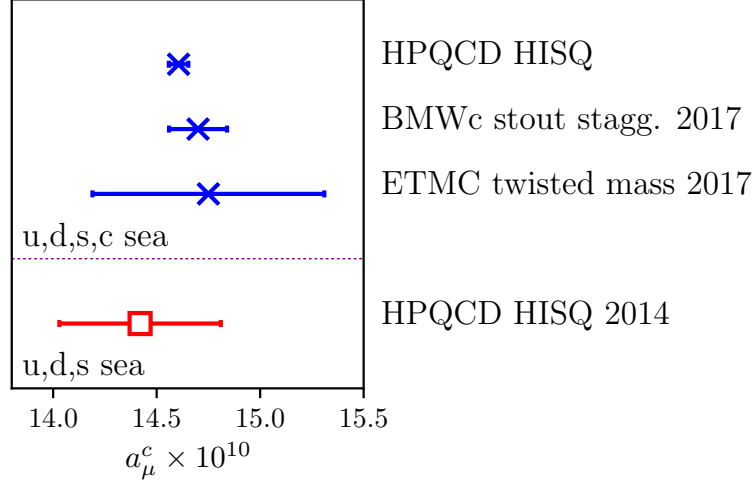


Figure 4.26: Comparison of the charm connected hadronic vacuum polarisation contribution to the anomalous magnetic moment of the muon from different lattice QCD calculations. The BMWc result is from [134]. The ETMC result is from [135]. [Figure courtesy of C. T. H. Davies.]

4.8 Conclusions

We have performed the first $n_f = 2+1+1$ lattice computations of various charmonium properties. We have used a large number of HISQ ensembles to ensure control over both the continuum and chiral extrapolations, improving on previous work by HPQCD. Given the high level of precision this data allows us to achieve we have also performed calculations including quenched QED to assess the impact of and control this remaining source of systematic uncertainty.

Here we collect our final results before discussing each in turn:

$$\begin{aligned}
 M_{J/\psi} - M_{\eta_c} &= 0.1203(11) \text{ GeV} \\
 f_{J/\psi} &= 0.4104(17) \text{ GeV} \\
 f_{\eta_c} &= 0.3981(10) \text{ GeV} \\
 a_\mu^c &= 1.4638(47) \times 10^{-9}.
 \end{aligned}
 \tag{4.28}$$

The precision of our hyperfine splitting result allows us to resolve, for the first time, the sign and

magnitude of the anticipated difference between the lattice and experimental results. We take this to be the effect of the η_c decay to gluons which is prohibited in the lattice calculation and find it to be $+7.3(1.2)$ MeV. The electromagnetic effect on the hyperfine splitting is the largest such effect that we observe here, reaching 1.14% once the pure QED effect from J/ψ annihilation to photons has been included perturbatively.

The J/ψ decay constant is the most precise to date and acts as a subpercent test of QCD. We find agreement with the experimental result of $0.4064(37)$ GeV. The gain in precision from the calculation of [76] is a result of having physical sea mass ensembles and the use of RI-SMOM vector current renormalisation. The importance of the precision of Z_V is further highlighted by our results for f_{η_c} derived from the connected two-point correlator where no such renormalisation is required. In that case we do not see a significant decrease in uncertainty compared to the earlier HPQCD result of [106].

We also updated the HPQCD value for the charm connected contribution to the leading order hadronic vacuum polarisation contribution to the anomalous magnetic moment of the muon. We included electromagnetic effects and charm quarks in the sea, as well as again using RI-SMOM for vector current renormalisation. The electromagnetic effect is very small at about 0.2%.

Chapter 5

Bottomonium Ground State Properties with a Fully Relativistic Action

5.1 Heavyonium physics

The ground state vector $b\bar{b}$ state, the Υ , was discovered at Fermilab in 1977 [139]. It took until 2008 for the discovery of the pseudoscalar η_b by the BaBar experiment [140]. The programs of experiments such as BELLE, BaBar and CLEO have provided a result for the bottomonium hyperfine splitting with a 5% uncertainty. While this is considerably less precise than the charmonium hyperfine splitting it does allow tests of the understanding of systematic uncertainties in lattice hyperfine splitting calculations from the charm mass to the b at the 5% level. In addition measurements of Υ properties are more precise. For example, the partial width of the Υ to an e^+e^- pair is known to 1.4%. We can therefore test lattice QCD in the context of bottomonium to a precision of a few percent.

During the discussion of the previous Chapter the issue of valence mass dependence of various results was raised in the context of accounting for mistuning of the charm mass. However, using purposefully heavy valence masses offers a way of studying $b\bar{b}$ mesons. As, for most available lattice spacings, the b mass cannot be reached while controlling discretisation effects if the HISQ action is to be used for b quarks an extrapolation in mass must be performed. In the case where

the meson consists of a heavy quark and a light quark then the expansion in inverse powers of the meson mass (using the meson mass as a proxy for the heavy quark mass), present in heavy quark effective theory (HQET), suggests that a polynomial in the inverse mass should be appropriate. However, for heavyonium the separation of scales on which HQET relies does not exist and the effective theory justification of the expansion is therefore not valid. However, given sufficiently large masses the polynomial expansion in the inverse mass should still be able to capture the mass dependence as a Taylor expansion. We refer to this method of calculation as the heavy HISQ or all-HISQ method.

The most common lattice methods for studying bottomonium ($b\bar{b}$) use either NRQCD or Fermilab heavy quark [141] actions. The former is explicitly nonrelativistic while the latter is a generalisation of the Wilson action that uses NRQCD to tune its parameters for the heavyonium case [142]. In [94] a different approach was introduced. There, HISQ calculations were performed at a variety of heavy quark masses between m_c and m_b and the heavy mass dependence was fit to allow extrapolation to the physical b mass. In this Chapter this is extended to 2+1+1 ensembles, on the finer of which the b mass can be reached, and to include vector mesons. This method proves to be very precise compared to previous results.

5.2 Lattice calculation

As previously we make use of MILC 2+1+1 HISQ ensembles some parameters of which are given in Table 5.1 along with the valence masses used on each ensemble. Only relatively fine lattices are used as you cannot get far past the charm mass on coarser ensembles.

We use a common fit form for all quantities to perform a simultaneous extrapolation (or interpolation) in both lattice spacing and heavy quark mass. The form accounts for discretisation errors of the form $(am)^{2i}$, the valence mass dependence and sea quark mass mistuning effects. The form is

Table 5.1: Parameters of the ensembles used in this analysis and the heavy valence masses used on each of the ensembles in lattice units.

Set	Label	w_0/a	L_s	L_t	am_l^{sea}	am_h
13	f-5	1.9006(20)	32	96	0.0074	0.6
					0.8	
15	f-phys	1.9518(7)	64	96	0.00120	0.6
					0.8	
16	sf-5	2.8960(60)	48	144	0.0048	0.274
					0.4	
					0.5	
					0.6	
					0.7	
					0.8	
17	sf-phys	3.0170(23)	96	192	0.0008	0.26
					0.4	
					0.6	
					0.8	
18	uf-5	3.892(12)	64	192	0.00316	0.194
					0.4	
					0.6	
					0.8	
					0.9	
19	ef-5	5.243(16)	96	288	0.00223	0.138
					0.45	
					0.55	
					0.65	

$$\begin{aligned}
f(M, a) = A \left(\frac{M}{M_0} \right)^b & \left\{ \sum_{i,j} c_{ij} \left(\frac{M_0}{M} \right)^i (am_h)^j + \right. \\
& \sum_k c_k^\ell \left(\frac{M_0}{M} \right)^k [\delta_\ell (1 + c_{\ell,a^2} (a\Lambda)^2 + c_{\ell,a^4} (a\Lambda)^4) + \\
& \left. c_k^c \delta_c (1 + c_{c,a^2} (a\Lambda)^2) \right\}. \tag{5.1}
\end{aligned}$$

The M here is acting as a proxy for the quark mass. We choose M to be the mass in GeV of the heavyonium vector meson on each ensemble. We take Λ to be 1 GeV. Results for bottomonium are extracted by evaluating the fit function at $M = M_\Upsilon$ using the experimental average value for M_Υ . The δ terms are as follows:

$$\begin{aligned}
\delta_\ell &= \frac{2(m_l^{\text{sea}} - m_l^{\text{phys}}) + (m_s^{\text{sea}} - m_s^{\text{phys}})}{10m_s^{\text{phys}}}, \\
\delta_c &= \frac{m_c^{\text{sea}} - m_c^{\text{phys}}}{m_c^{\text{phys}}}. \tag{5.2}
\end{aligned}$$

We use $M_0 = 2$ GeV throughout. Note that the fit form allows for heavy quark mass dependence in the sea mass mistuning terms. This is found to be crucial to achieve fits with acceptable χ^2/dof given the precision of the data.

5.3 Hyperfine splitting

The experimental average of the bottomonium hyperfine splitting is currently obtained from four experimental measurements with the most precise coming from the Belle Collaboration [143]. These values are shown in Fig. 5.1 along with the PDG average. There is some tension between the different results. The measurement of the Υ mass is an order of magnitude more precise than that of the η_b . The hyperfine splitting results quoted in the PDG correspond to different measurements of the η_b mass which are subtracted from the average Υ mass. The value from [143] lies somewhat lower than the other values that constitute the PDG average.

As for the charmonium case, pseudoscalar and vector connected two-point correlators are com-

Table 5.2: Vector and pseudoscalar heavyonium ground state masses and hyperfine splitting on the ensembles detailed in Table 5.1 with the valence masses given there.

Set	am_{val}	aM_{V_h}	aM_{η_h}	aM_{hyp}
13	0.6	1.717413(70)	1.675594(46)	0.041819(84)
	0.8	2.101519(58)	2.064117(39)	0.037402(70)
15	0.6	1.715445(20)	1.674259(14)	0.041185(25)
	0.8	2.099916(23)	2.063012(12)	0.036903(26)
16	0.274	0.929901(81)	0.896656(32)	0.033245(87)
	0.4	1.202369(82)	1.175551(28)	0.026818(87)
	0.5	1.411146(67)	1.387452(25)	0.023694(72)
	0.6	1.614661(59)	1.593082(23)	0.021579(63)
	0.7	1.813284(52)	1.793112(22)	0.020172(57)
	0.8	2.006815(48)	1.987499(20)	0.019316(52)
17	0.26	0.895692(48)	0.862669(27)	0.033023(55)
	0.4	1.199803(33)	1.173901(23)	0.025902(40)
	0.6	1.612583(25)	1.591667(19)	0.020915(32)
	0.8	2.005042(22)	1.986244(17)	0.018798(28)
18	0.194	0.692016(61)	0.666824(40)	0.025191(73)
	0.4	1.147608(40)	1.130727(30)	0.016882(50)
	0.6	1.562877(32)	1.549105(25)	0.013773(41)
	0.8	1.958249(27)	1.945794(22)	0.012455(35)
19	0.45	1.211599(32)	1.201319(26)	0.010280(42)
	0.65	1.623681(25)	1.614870(21)	0.008811(33)

puted and then a multiexponential fit is used to extract the ground state masses. The vector meson, pseudoscalar and hyperfine splitting results that we extract from these fits are presented in Table 5.2 in lattice units. It can clearly be seen that the hyperfine splitting decreases with increasing quark mass. There are correlations between results on the same ensemble at different masses that we include in our fits.

The fit of Eq. 5.1 gives a χ^2/dof of 1.1 with priors of 0(1) on all parameters except the sea charm mistuning parameters where priors of 0 ± 0.1 were used. A reasonably large effect from light sea quark mass mistuning is seen (as was the case for the charmonium hyperfine splitting, which is effectively included in this fit). The value returned for c_0^c is -1.27(32). The value of $M_\Upsilon - M_{\eta_b}$ extracted from the fit is 0.0583(15) GeV. This is just over 1σ below the experimental average of 0.0623(32) GeV, although it agrees with the BELLE result [143].

Similarly to the case of the η_c the η_b is not allowed to decay to hadrons in this calculation. The

η_b width is approximately a third of that of the η_c which suggests that the effect this has on the hyperfine splitting should be smaller. The perturbative calculation of [39] gives an expected downward shift of approximately 1 MeV. If this perturbative expectation is realised then we would get a result for the hyperfine splitting from the lattice calculation that is approximately 1 MeV lower than the true value.

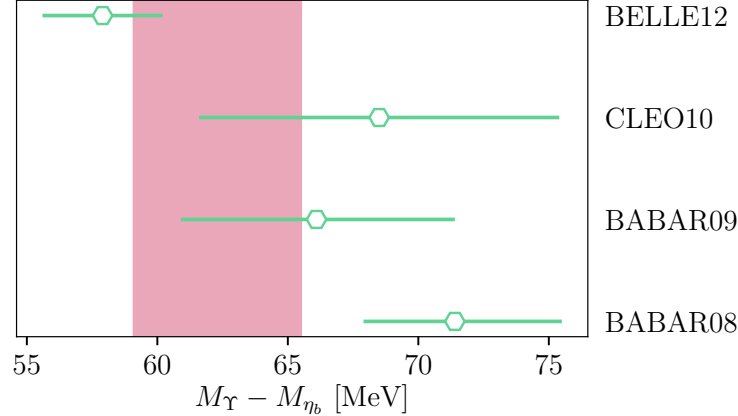


Figure 5.1: Summary of the current status of experimental measurements of the bottomonium hyperfine splitting. The BELLE12 result is from [143], the CLEO12 result is from [144], the BABAR09 result is from [145] and BABAR08 is from [140]. The red band is the PDG average.

The heavy mass dependence of the light sea mass mistuning extracted from the fit is mild as shown in Fig. 5.3. The quantity plotted here is the contribution the fit assigns to the light sea quark mistuning terms in physical units for a given value of the sea mistuning measure δ_ℓ . The curves obtained from using the value on sets 16 (sf-5) and 17 (sf-phys) are shown. This is the “physical” dependence where the lattice spacing has been set to 0.

Previous lattice calculations of the bottomonium hyperfine splitting have used either NRQCD or a variant of the clover action for the b quarks. The result presented here has significantly smaller uncertainties (approximately a factor of 4 better than for the most precise previous result) than these results as shown by the summary plot in Fig. 5.4.

The error budget for the bottomonium hyperfine splitting is given in Table 5.3. The largest single contribution is from the statistical uncertainties in the lattice data. The contribution from statistics is considerably larger than the uncertainties on the data points themselves. This

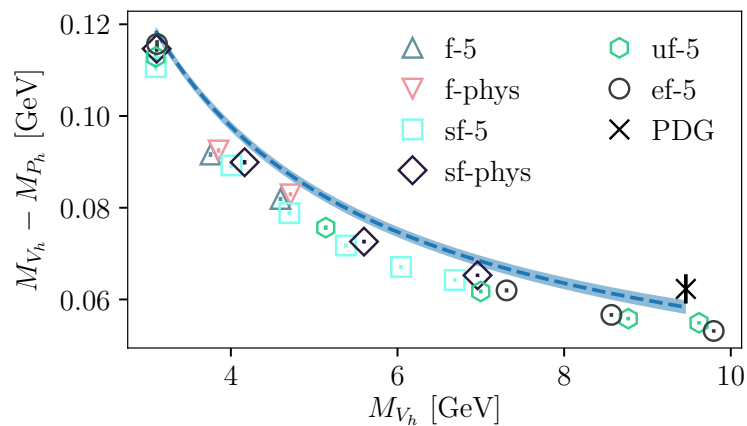


Figure 5.2: Hyperfine splitting of heavyonium including a simultaneous continuum extrapolation and mass interpolation to the b mass, using the vector meson mass as a proxy. The black cross marks the PDG average of the bottomonium hyperfine splitting. The labels in the legend correspond to ensembles according to Table 5.1.

seems to be due to the correlations between the points. If the svdcut of the fit is raised then the uncertainty contribution from statistics decreases but the contribution from the continuum extrapolation rapidly increases. The next largest error is from the continuum extrapolation, even though an ensemble with the very low lattice spacing of 0.03 fm is used.

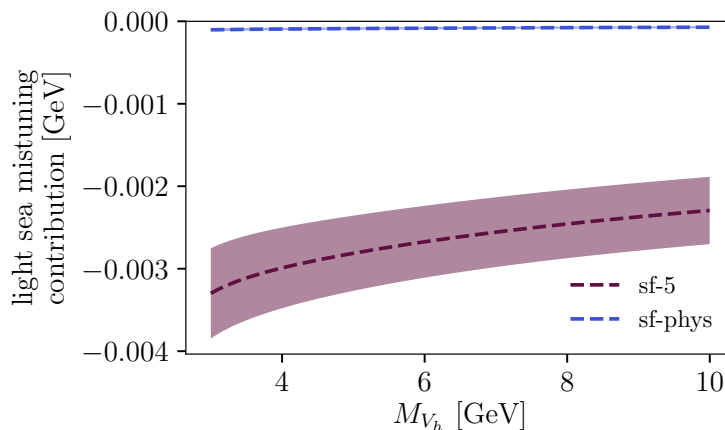


Figure 5.3: Heavy mass dependence of the light sea quark mass mistuning dependence of the hyperfine splitting as calculated from the output of a fit to the from given in Eq. 5.1. The two lines shown are for the δ_ℓ values on sets 16 (purple) and 17 (blue). For the hyperfine splitting this shows little heavy mass dependence with a slight decrease at higher masses.

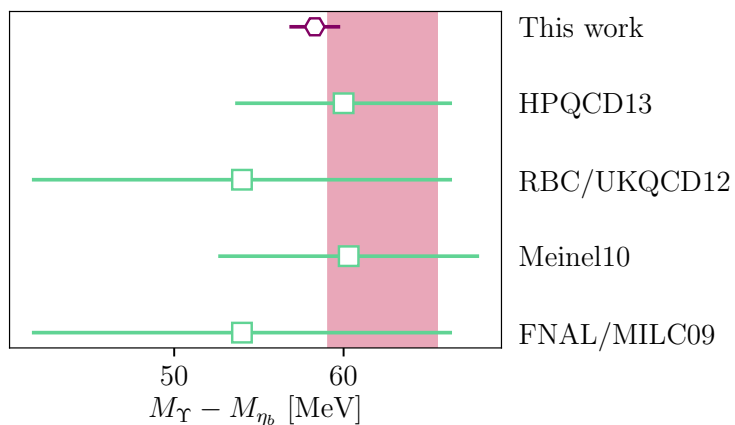


Figure 5.4: Comparison of lattice results for the bottomonium hyperfine splitting. The red band shows the PDG average. The green squares show results that use either NRQCD (HPQCD13 [146] and Meinel10 [147]), Fermilab heavy quarks (FNAL/MILC09 [142]) or the RHQ action (RBC/UKQCD12) [148].

Table 5.3: Error budget for the bottomonium hyperfine splitting. The contributions from the continuum extrapolation are separated into pieces that are independent of the heavy mass and dependent on it (c_{0j} and c_{ij} and $i \neq 0$). There is also an uncertainty contribution from the physical M dependence terms which are not multiplied by a power of am_h .

	$M_\Upsilon - M_{\eta_b}$ [GeV]
$a^2 \rightarrow 0$ M independent	1.08
$a^2 \rightarrow 0$ M dependent	0.92
Physical M extrapolation	0.50
Statistics	1.72
w_0	0.53
w_0/a	0.48
Light sea mass mistuning	0.62
Charm sea mass mistuning	0.58
Total	2.54%

5.4 Vector and pseudoscalar decay constants

Following the precision achieved for the decay constant of the J/ψ using the vector current renormalisation factors in the RI-SMOM scheme an extension of this calculation to the Υ decay constant offers another quantity that could allow comparison between lattice and experiment at high precision. The values of the unrenormalised vector decay constants, af_{V_b}/Z_V , for the various masses and ensembles employed here are given in lattice units in the third column of Table 5.4. These data are then multiplied by the relevant Z_V and divided by the lattice spacing before being fit to Eq. 5.1. The result is shown in Fig. 5.5. The black cross marks the experimental average of the Υ decay constant (calculated from the PDG value of the partial width of the Υ to an e^+e^- pair according to Eq. 4.15 with the appropriate substitutions using a value for $\alpha_{\text{QED}}(m_b)$ of 1/132 from [149]). The red star shows a previous HPQCD determination using an NRQCD quark action [150]. Our result for f_Υ is 0.682(12) GeV compared to the result determined from the experimental average of the leptonic width of the Υ : 0.689(5) GeV.

We can again study the heavy mass dependence of the light sea quark mass mistuning. For the vector decay constant this is shown in Fig. 5.6. While of a smaller magnitude than for the hyperfine splitting (particularly at the charm mass) it displays a steeper heavy mass dependence and increases in size with mass.

This picture is very similar for the pseudoscalar decay constant which was calculated in [94] using the same method as is used here. The calculation presented here improves on that result in a

Table 5.4: Vector and pseudoscalar heavyonium ground state decay constants on the ensembles detailed in Table 5.1 with the valence masses given there.

Set	am_{val}	af_{V_h}/Z_V	af_{η_h}
13	0.6	0.21865(11)	0.208641(60)
	0.8	0.25711(10)	0.249695(64)
15	0.6	0.21690(10)	0.207535(22)
	0.8	0.255249(96)	0.248493(21)
16	0.274	0.12339(15)	0.117554(37)
	0.4	0.13916(21)	0.135692(39)
	0.5	0.15104(20)	0.148936(40)
	0.6	0.16318(19)	0.162314(41)
	0.7	0.17617(19)	0.176638(42)
	0.8	0.19061(19)	0.192680(44)
17	0.26	0.11969(10)	0.114147(34)
	0.4	0.137266(83)	0.134475(37)
	0.6	0.161236(77)	0.161035(39)
	0.8	0.188634(82)	0.191297(41)
18	0.194	0.091442(91)	0.087774(42)
	0.4	0.114918(72)	0.114953(46)
	0.6	0.135412(69)	0.137487(54)
	0.8	0.158238(72)	0.162850(58)
	0.9	0.171745(74)	0.178229(58)
19	0.138	0.06841(10)	0.065916(59)
	0.45	0.100572(70)	0.102989(81)
	0.55	0.109506(67)	0.112668(82)
	0.65	0.118680(64)	0.122639(81)

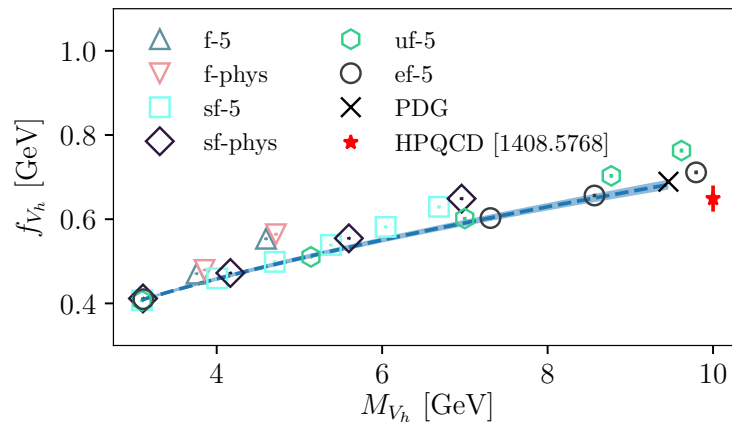


Figure 5.5: Fit of the vector decay constant of heavyonium to Eq. 5.1. The PDG experimental average of the Υ decay constant is shown as a black cross and a previous HPQCD result [150], shown as a red star, using NRQCD b quarks which is set at a point higher than the Υ mass on the x -axis for clarity.

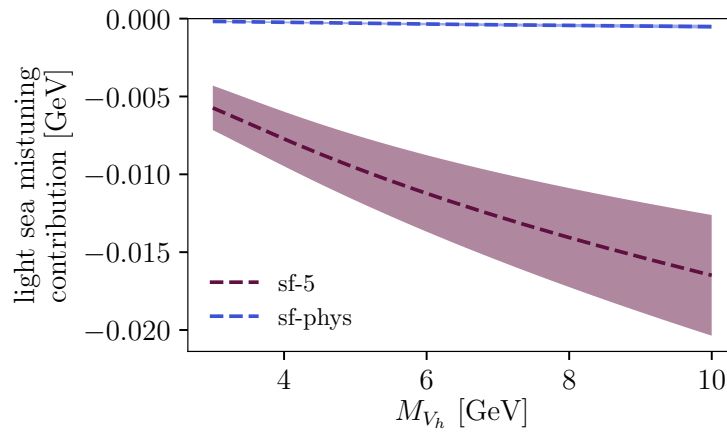


Figure 5.6: Same as Fig. 5.3 but for the vector decay constant. The heavy mass dependence in this case is more significant than for the hyperfine splitting.

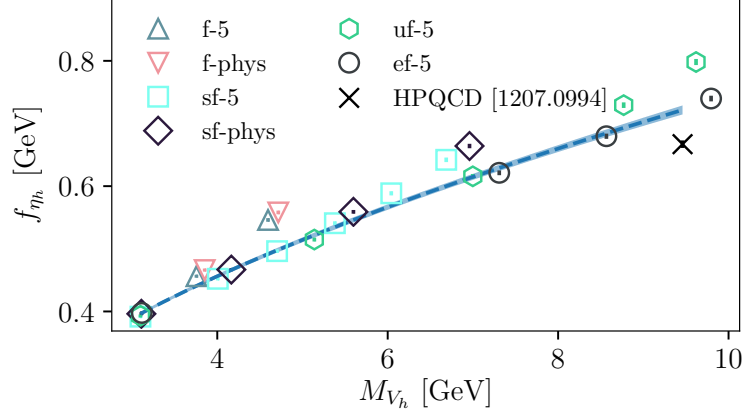


Figure 5.7: The heavyonium pseudoscalar decay constant with the fit of Eq. 5.1. There is no experimental observable that corresponds to this so we compare to a previous HPQCD result [94] (also using the heavy HISQ method) which is shown as a black cross.

few important ways. One change is that [94] used HISQ valence quarks on an asqtad sea while here we use HISQ ensembles (which have a charm quark in the sea not present in the asqtad case). The more important improvements are that we include ensembles with physical sea quark masses at two different lattice spacings and include points on a finer ensemble (set 19) which extend beyond the physical b mass. Our data are given in Table 5.4 and are plotted in Fig. 5.7 along with the fit of Eq. 5.1. The final value for f_{η_b} is 0.7217(72) GeV which is somewhat higher than the value from [94] (0.667(6) GeV). Both studies used data on ensembles with a lattice spacing of approximately 0.045 fm at some of the same valence masses. These data points agree well indicating that the difference arises from the fit. The continuum extrapolation in [94] ends up considerably lower than the data points at high mass which the 0.03 fm data points restrict from happening for our data.

The behaviour of the sea quark mass mistuning dependence on the heavy quark mass is very similar to the vector decay constant case and is shown in Fig. 5.8.

As was done with the charmonium decay constants we can directly examine the ratio of the vector and pseudoscalar decay constants. This is shown in Fig. 5.9. It is quite clear that f_V/f_P is greater than 1 at the charm mass but switches to be below 1 at the b mass. This allows a nearly 0.5% determination of the ratio at the b mass of 0.9577(52).

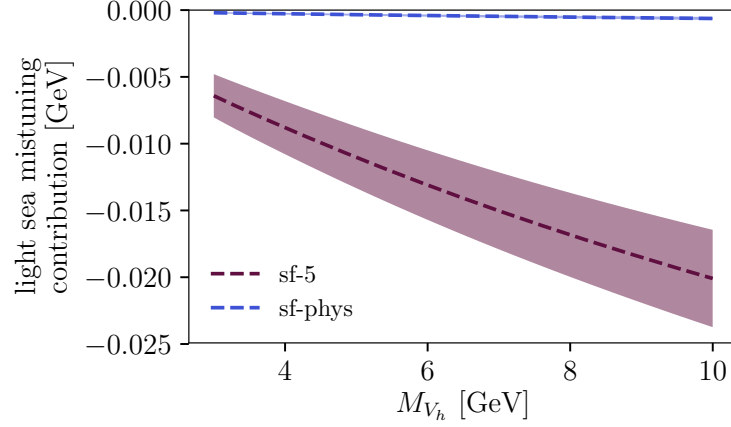


Figure 5.8: Same as Fig. 5.3 but for the heavyonium pseudoscalar decay constant. This is very similar to the vector decay constant case shown in Fig. 5.6.

Table 5.5: Error budgets for the Υ and η_b decay constants.

	f_Υ [GeV]	f_{η_b} [GeV]
$a^2 \rightarrow 0$	0.66	0.10
$a^2 \rightarrow 0$ M dependent	0.73	0.29
Physical M extrapolation	0.26	0.09
Z_V	0.11	-
Statistics	1.14	0.74
w_0	0.52	0.52
w_0/a	0.45	0.16
Light sea mass mistuning	0.34	0.15
Charm sea mass mistuning	0.22	0.11
Total	1.73%	0.99%

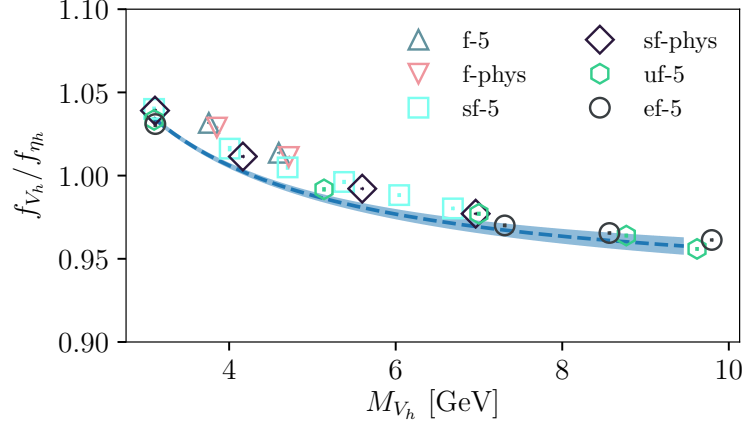


Figure 5.9: Ratio of the heavyonium vector and pseudoscalar decay constants with a fit of the form Eq. 5.1. It is clear that the ratio is above 1 at the charm mass but moves to be below 1 at the b mass.

The error budgets for both the vector and pseudoscalar decay constant at the b mass are given in Table 5.5. All of the contributions, with the exception of that from w_0 , are smaller for the pseudoscalar.

5.5 Bottomonium vector time moments and a_μ^b

As for the charmonium case discussed in Section 4.7 the time moments of the b vector correlator can be used as a precision point of comparison between lattice calculations and experimental data driven determinations. Once the bottomonium time moments are determined in the continuum it is simple to determine the b quark connected HVP contribution to the anomalous magnetic moment of the muon a_μ^b . While this contribution is very small we will see that we can obtain the most precise lattice QCD value to date here.

The appropriately normalised time moments are expected to be inversely proportional to the quark mass (the proportionality being determined by a perturbative expansion) [27]. We therefore constrain b in Eq. 5.1 to be -1.

The time moments for $n = 4, 6, 8, 10$ are shown in Figs. 5.10, 5.11, 5.12 and 5.13.

A comparison of the continuum values extracted at the b mass from the fit and values obtained

Table 5.6: Time moments on the ensembles and valence masses given in Table 5.1. These are $G_n^{1/(n-2)}$ as in Table 4.15.

Set	am_{val}	$n = 4$	$n = 6$	$n = 8$	$n = 10$
13	0.6	0.2533(14)	0.5734(31)	0.8411(45)	1.0871(58)
	0.8	0.1955(10)	0.4681(25)	0.6940(37)	0.8961(48)
15	0.6	0.2467(13)	0.5585(29)	0.8192(43)	1.0588(56)
	0.8	0.1904(10)	0.4558(24)	0.6758(36)	0.8727(46)
16	0.274	0.3184(18)	0.6801(38)	1.0039(57)	1.3097(74)
	0.4	0.2373(13)	0.5161(29)	0.7607(43)	0.9924(56)
	0.5	0.1978(11)	0.4380(25)	0.6448(36)	0.8393(47)
	0.6	0.16924(96)	0.3833(22)	0.5643(32)	0.7325(41)
	0.7	0.14731(83)	0.3423(19)	0.5054(29)	0.6546(37)
	0.8	0.12971(73)	0.3100(17)	0.4602(26)	0.5956(34)
17	0.26	0.3182(17)	0.6785(36)	1.0018(53)	1.3069(69)
	0.4	0.2279(12)	0.4956(26)	0.7306(39)	0.9532(51)
	0.6	0.16247(86)	0.3680(20)	0.5418(29)	0.7034(37)
	0.8	0.12452(66)	0.2976(16)	0.4418(23)	0.5718(30)
18	0.194	0.3171(20)	0.6754(41)	1.0009(61)	1.3077(80)
	0.4	0.1791(11)	0.3909(24)	0.5785(35)	0.7570(46)
	0.6	0.12677(78)	0.2875(18)	0.4243(26)	0.5520(34)
	0.8	0.09685(60)	0.2315(14)	0.3440(21)	0.4459(27)
	0.9	0.08588(53)	0.2115(13)	0.3166(19)	0.4105(25)
19	0.138	0.3153(19)	0.6714(41)	0.9964(61)	1.3021(79)
	0.45	0.12171(74)	0.2683(16)	0.3976(24)	0.5209(32)
	0.55	0.10228(62)	0.2296(14)	0.3396(21)	0.4434(27)
	0.65	0.08798(54)	0.2020(12)	0.2988(18)	0.3888(24)

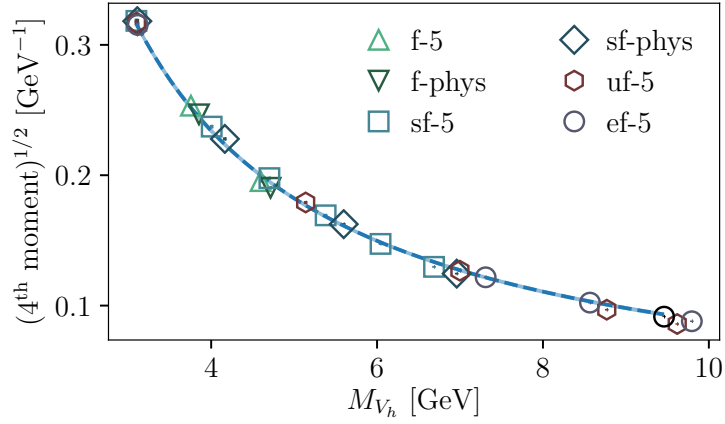


Figure 5.10: Continuum extrapolation and heavy mass interpolation of the 4th vector time moment. The value extracted from experimental data in [151] is shown as the black circle.

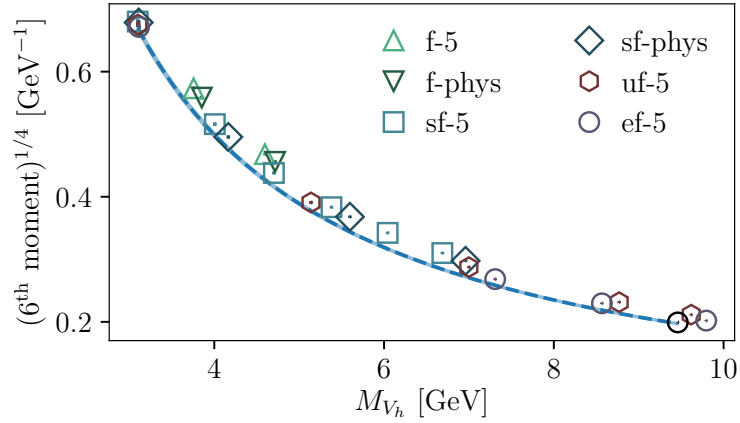


Figure 5.11: Continuum extrapolation and heavy mass interpolation of the 6th vector time moment. The value extracted from experimental data in [151] is shown as the black circle.

from experimental data is given in Table 5.7. Agreement between all values within 2σ is observed. The results we present here are considerably less precise than the corresponding experimental determinations as we have had to determine the dependence of the time moments on the heavy quark mass in order to reach the b mass.

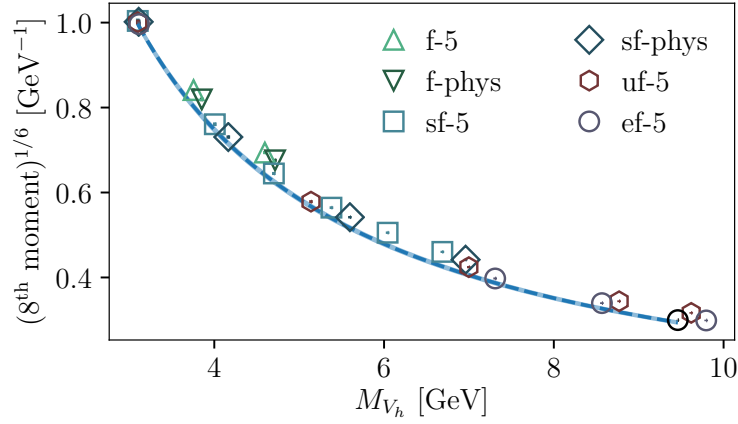


Figure 5.12: Continuum extrapolation and heavy mass interpolation of the 8th vector time moment. The value extracted from experimental data in [151] is shown as the black circle.

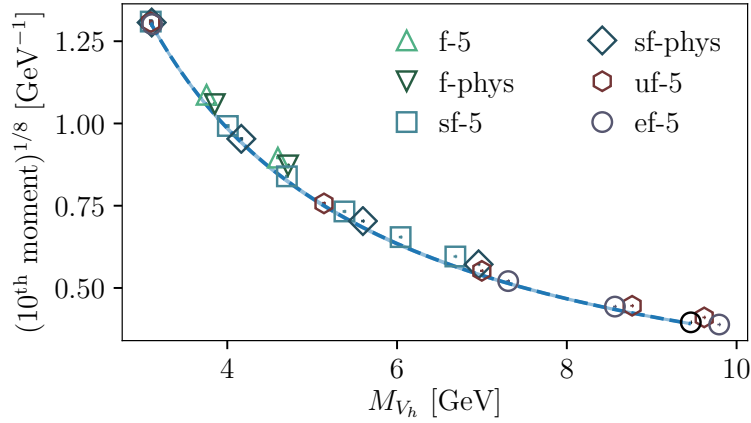


Figure 5.13: Continuum extrapolation and heavy mass interpolation of the 10th vector time moment. The value extracted from experimental data in [151] is shown as the black circle.

Given previous discussions (see Section 4.7) it is nearly trivial to calculate the b quark connected contribution to the HVP contribution to the anomalous magnetic moment of the muon. This contribution is very small and was previously calculated by HPQCD using time moments from lattice NRQCD. Here, we obtain $3.16(12) \times 10^{-11}$ using the time moment values in the continuum

Table 5.7: Comparison of time moments extracted from our fits and those extracted from experiment in [151] for the first four moments.

n	$G_n^{1/(n-2)}$	$(G_n^{\text{exp.}})^{1/(n-2)}$
4	0.0932(16)	0.09151(31)
6	0.1972(27)	0.19910(49)
8	0.2940(51)	0.29964(55)
10	0.3914(47)	0.39548(59)

from the first column of Table 5.5. The result of [150] is $2.71(37) \times 10^{-11}$ which is clearly considerably more uncertain than the all-HISQ result presented here. There is agreement between these two results as well as with the value extracted from the time moments determined from experimental data which is $3.07(2) \times 10^{-11}$.

5.6 Conclusions

In this Chapter we have demonstrated that fully relativistic heavy HISQ data for heavy-heavy mesons can be understood and used to obtain precise results for properties of the η_b and Υ mesons. We collect our results here:

$$\begin{aligned}
 M_\Upsilon - M_{\eta_b} &= 0.583(15) \text{ GeV} \\
 f_\Upsilon &= 0.682(12) \text{ GeV} \\
 f_{\eta_b} &= 0.7217(72) \text{ GeV} \\
 a_\mu^b &= 3.16(12) \times 10^{-11}.
 \end{aligned}
 \tag{5.3}$$

The bottomonium hyperfine splitting obtained is more precise than both previous lattice determinations and the experimental average. We have also used the local vector current renormalisations of Section 3.3 to compute both the Υ decay constant and the first four vector time moments of the b vector correlator. No significant deviations from the experimental value in the former and values extracted from experimental cross-section data in the latter are seen. The uncertainty of our Υ decay constant result is approximately twice that of the experimental average but does improve on previous lattice determinations. We also presented the most precise lattice QCD value for the b quark connected HVP contribution to the hadronic vacuum polarisation to

date.

The case of the η_b decay constant has highlighted the importance of data on an ensemble that can reach the b mass without incurring a large discretisation penalty via am_b . This helps to constrain the discretisation errors that the fit allows for at these higher masses. We have also seen that there can be significant mass dependent effects in quark mass mistuning terms which we are able to account for given the data we have on two physical ensembles at various masses.

Chapter 6

Quark Mass Determinations

A major area in which the precision obtainable through lattice calculations is difficult to match by other means is the determination of the fundamental parameters of QCD. These include the quark masses. Due to the origin of these masses in the SM through the interaction with the Higgs field precise quark masses are needed for precision Higgs studies [65]: a region of great interest to the particle physics community. Part of obtaining precise and robust results is to compare different methodologies with different sources of systematic uncertainty. The HPQCD collaboration performed calculations of the charm mass and the ratio of the strange and charm masses using fits to heavy quark current-current correlator moments [27]. Here we use some of the same gluon field configurations to perform the calculation of charm and strange quark masses using the bare quark masses on a range of lattices in conjunction with the mass renormalisation factor in the RI-SMOM scheme, calculated nonperturbatively on those lattices (see Section 3.2), to be able to perform a continuum extrapolation of the renormalised mass. (A published account of this work can be found in [1].)

The renormalisation of quark masses must be performed within the framework of a renormalisation scheme and then matching calculations may be used to convert between any two schemes, provided the reference scale is sufficiently high. For nonperturbative lattice calculations it is convenient to use the RI-SMOM scheme from which results may be converted to the $\overline{\text{MS}}$ scheme, which is the standard for quoting quark masses. The matching calculation is done perturbatively in the continuum so it is necessary to perform the lattice calculation in a momentum region where such a perturbative calculation is valid, and also to consider nonperturbative ef-

facts that are not present in the perturbative calculation. The lowest momentum value used in this calculation was therefore chosen to be 2 GeV. This lies within the Rome-Southampton window of $\Lambda_{\text{QCD}} \ll \mu \ll \pi/a$ for a large range of lattice spacings and is a commonly chosen scale.

Section 6.1 provides a brief discussion on how we define the lattice spacing in this Chapter to reduce the effect of mistuned sea quark masses. Section 6.2 then presents results for the strange and charm quark masses following the calculation of [1]. The charm quark mass given there is then updated in Section 6.3.

6.1 Tuning to the physical point

In this calculation we deal with energy scales above the charm mass as opposed to most lattice calculations of hadronic properties. The discussion in this Section follows the Appendix of [27].

As the sea quark masses are varied we have to choose what parameters we hold fixed. The bare coupling is fixed at the start of lattice computations so this is kept fixed which leaves a choice of whether to vary the lattice spacing with the sea quark masses, or the physical quantity used to set the lattice spacing which in our case is w_0 (see Section 2.10). Either case will give the same results at the physical point but the trajectories of the approaches will be different. It is typically convenient to vary the lattice spacing as w_0/a depends on the effects of the fermion determinant. By the decoupling theorem low energy physics should be independent of the charm quark mass and therefore of charm mass mistunings. w_0 is a low energy quantity indicating that we may want to keep that fixed. If instead a is held fixed it is possible to see apparent violations of decoupling.

The running of the QCD coupling in the $\overline{\text{MS}}$ scheme is independent of the sea quark masses by definition. However, mass dependence can enter through the chosen starting point of the evolution which is determined by the chosen scale setting procedure on the lattice. This gives

$$\alpha_{\overline{\text{MS}}}(\mu, \delta m^{\text{sea}}) = \alpha_{\overline{\text{MS}}}(\xi_\alpha \mu) \quad (6.1)$$

in the notation of [27]. ξ_α depends on the sea mass mistunings and is studied in the Appendix of [27]. At the charm mass the $n_f = 3$ and $n_f = 4$ coupling constants have to be matched. At

the charm threshold

$$\alpha_s(\mu, n_f = 3) = \alpha_s(\mu, \delta m_c^{\text{sea}}, n_f = 4), \quad (6.2)$$

with $\mu = m_c + \delta m_c^{\text{sea}}$. At leading order

$$\alpha_s(\mu, n_f) = \frac{2\pi}{\beta(n_f) \log(\mu/\Lambda^{(n_f)})}, \quad (6.3)$$

If α is to have dependence on δm_c^{sea} (defined in Eq. 4.7 of Section 4.3.3) this must come from a dependence of Λ on the same quantity. which gives a relationship between the scale Λ for $n_f = 3$ and $n_f = 4$. This approximately evaluates to

$$\Lambda(\delta m_c^{\text{sea}}, n_f) \simeq m_c \left(\frac{\Lambda(n_f = 3)}{m_c} \right)^{\beta(3)/\beta(4)} \left(1 - \frac{2\delta m_c^{\text{sea}}}{25m_c} \right). \quad (6.4)$$

(The factor of $-2/25$ here arises from $1 - \beta(n_f = 3)/\beta(n_f = 4)$.) This implies that $\Lambda(n_f = 4)$ at physical sea quark masses is related to $\Lambda(\delta m_c^{\text{sea}}, n_f = 4)$ via

$$\Lambda(\delta m_c^{\text{sea}}, n_f = 4) \simeq \Lambda(\delta m_c^{\text{sea}} = 0, n_f = 4) \left(1 - \frac{2\delta m_c^{\text{sea}}}{25m_c} \right), \quad (6.5)$$

from which decoupling implies

$$\alpha_s(\mu, \delta m_c^{\text{sea}}, n_f = 4) = \alpha_s(n_f = 4)(\mu(1 + (2\delta m_c^{\text{sea}})/(25m_c))). \quad (6.6)$$

To summarise, we are choosing to keep a fixed as a function of the sea quark mass so that a has the same value on all ensembles with the same β .

An ultraviolet quantity such as Z_m should not display much dependence on sea quark masses (as seen in Section 3.2) in contrast with Eq. 6.6. For a mass calculation where you multiply these Z_m values by bare quark masses you will therefore introduce sea mass dependence by using a lattice spacing definition that varies with sea mass. In this Chapter we therefore prefer to use w_0/a and bare masses at values of the physical sea quark masses. (Above this definition of lattice spacing has been denoted \tilde{a} .)

As quark mass evolution with scale is independent of mass mistunings sea mass dependence of a mass must enter as a rescaling:

$$m_h(\mu, \delta m^{\text{sea}}) = \xi_m m_h(\xi_\alpha \mu). \quad (6.7)$$

Again, ξ_m is studied in [27] and those results are used to compute the bare quark masses at physical sea quark masses that we use here (in conjunction with using \tilde{a}).

6.2 \overline{m}_c and \overline{m}_s using the RI-SMOM intermediate scheme

We have shown that we can reliably determine Z_m^{SMOM} to high precision for a given lattice spacing (β value) in Section 3.2. We must now calculate the renormalised charm quark mass in the $\overline{\text{MS}}$ scheme at a chosen reference scale μ_{ref} . We choose this scale to be 3 GeV.

The tuned bare m_c and m_s values for each spacing for lattices with physical sea quark masses are taken from the analysis of [27]. There, the charm quark mass was tuned using the η_c meson and the strange quark tuned using the η_s meson. We generically denote such a mass $m(a)$. This bare mass must be renormalised and we do this with the renormalisation factors calculated in the RI-SMOM scheme, $Z_m^{\text{SMOM}}(\mu, a)$. Several values of μ are used in this analysis. These are the 2, 2.5, 3, 4 and 5 GeV according to Table 3.2. These values are then multiplied by the matching factor to $\overline{\text{MS}}$ calculated from the coefficients given in Table 6.1, $Z_m^{\overline{\text{MS}}/\text{SMOM}}(\alpha_s(\mu))$. This gives a result for the mass in $\overline{\text{MS}}$ at a scale μ for each lattice:

$$\overline{m}(\mu, a) = Z_m^{\overline{\text{MS}}/\text{SMOM}}(\alpha_s(\mu)) Z_m^{\text{SMOM}}(\mu, a) m(a). \quad (6.8)$$

Now that the mass values are in the $\overline{\text{MS}}$ scheme they can be run to the common reference scale μ_{ref} using the QCD β function. Here we use the four-loop result of [152, 153] using the α_s determination at 5 GeV of [27]. In a perturbative calculation in the continuum this would produce the same value for each initial μ , ignoring the small effects of higher orders in the β function. However, in the lattice case, there is μ dependence coming from discretisation effects, in the form of even powers of $a\mu$, and terms suppressed by powers of μ capturing nonperturbative effects.

6.2.1 Conversion to $\overline{\text{MS}}$ scheme

We now collect some results relevant for the conversion factor between the RI-SMOM and $\overline{\text{MS}}$ schemes, $Z_m^{\overline{\text{MS}}/\text{SMOM}}(\alpha_s(\mu))$. The general form of the conversion factors is a power series in α_s , which for RI-SMOM is known to $\mathcal{O}(\alpha_s^2)$, and which is here denoted

$$Z_m^{\overline{\text{MS}}/\text{SMOM}}(\alpha_s(\mu)) = 1 + c_1 \alpha_{\overline{\text{MS}}}(\mu) + c_2 (\alpha_{\overline{\text{MS}}}(\mu))^2 + c_3 (\alpha_{\overline{\text{MS}}}(\mu))^3 + \dots \quad (6.9)$$

The continuum fit form used allows for various discretisation errors as well as missing α_s^3 terms in the RI-SMOM $\rightarrow \overline{\text{MS}}$ matching, nonperturbative condensate contributions and sea quark mass effects which can split the values obtained for different lattices with the same spacing.

In this calculation the leading effects from using nonzero sea quark masses are also incorporated into the matching to $\overline{\text{MS}}$. It is necessary to use non-zero sea quark masses to properly define the lattice spacing (which is done for a physical sea). These effects first appear at order α_s^2 and so only affect the c_2 coefficient given in Table 6.1. The c_2 corrections from the charm quark mass in the sea Δc_2 were calculated by C. Strum as detailed in [1]. The coefficients are small and indicate a rapidly convergent series expansion so neglecting $\mathcal{O}(\alpha_s^3)$ and higher terms is not expected to have a large impact. This can be contrasted with the case of RI'-MOM where the coefficients are larger and the situation less clear.

Table 6.1: RI-SMOM to $\overline{\text{MS}}$ matching factor coefficients and shifts in the α_s^2 coefficient due to the presence of physical charm quarks in the sea and the appropriate $\alpha_s^{\overline{\text{MS}}}$. The penultimate column contains the $\overline{\text{MS}}$ mass running to 3 GeV. The value given for c_3 was not used in the initial mass calculations presented in [1] and Section 6.2.2 which is indicated by the asterisk. These values were computed recently in [97, 154].

μ (GeV)	c_1	c_2	Δc_2	$\alpha_{\overline{\text{MS}}}(\mu, n_f = 4)$	$R(3 \text{ GeV}, \mu)$	c_3^*
2	-0.0514	-0.0415	-0.015	0.3030(54)	0.9034(20)	-0.1036
2.5	-0.0514	-0.0415	-0.01	0.2741(43)	0.95819(84)	-0.1036
3	-0.0514	-0.0415	-0.007	0.2545(37)	-	-0.1036
4	-0.0514	-0.0415	-0.004	0.2291(29)	1.0616(11)	-0.1036
5	-0.0514	-0.0415	-0.003	0.2128(25)	1.1063(19)	-0.1036

6.2.2 Mass results

The full fit form used to extract the continuum $\overline{\text{MS}}$ mass values is

$$\begin{aligned}
\overline{m}(\mu_{\text{ref}}, \mu, a) &= \overline{m}(\mu_{\text{ref}}) \times \\
&\left(1 + \sum_{i=1}^{N_i} c_{\mu^{2i} a^{2i}} (\mu a / \pi)^{2i} + c_{\alpha} \alpha_{\overline{\text{MS}}}^3(\mu) + \right. \\
&h_{\ell}^{\text{sea}} \frac{\delta_{\ell}^{\text{sea}}}{m_s^{\text{tuned}}} + h_c^{\text{sea}} \frac{\delta_c^{\text{sea}}}{m_c^{\text{tuned}}} + \\
&\sum_{k=1}^{N_k} c_{\text{cond}, 2k} \frac{A}{\mu^{2k}} \alpha_{\overline{\text{MS}}}(\mu) \times [1 + c_{\text{cond}, a^2, 2k} (\Lambda a / \pi)^2] \times \\
&\left. \left[1 + h_{\ell, \mu}^{\text{sea}} \frac{\delta_{\ell}^{\text{sea}}}{m_s^{\text{tuned}}} + h_{c, \mu}^{\text{sea}} \frac{\delta_c^{\text{sea}}}{m_c^{\text{tuned}}} \right] \right) \times \\
&\left(1 + \sum_{j=1}^{N_j} c_{\Lambda^{2j} a^{2j}} (\Lambda a / \pi)^{2j} \right)
\end{aligned} \tag{6.10}$$

$\overline{m}(\mu_{\text{ref}})$ is the $\overline{\text{MS}}$ mass value at the reference scale μ_{ref} , which here is 3 GeV. The mistuning parameters $\delta_{\ell}^{\text{sea}}$ and δ_c^{sea} are defined as

$$\begin{aligned}
\delta_{\ell}^{\text{sea}} &= \sum_{q=u,d,s} (m_q - m_q^{\text{tuned}}), \\
\delta_c^{\text{sea}} &= m_c - m_c^{\text{tuned}}.
\end{aligned} \tag{6.11}$$

The priors on c_{a^2} are taken as 0 ± 1 . The prior on c_{α} is 0.0 ± 0.2 which allows for the coefficient to be four times the size of c_1 or c_2 . The priors on the coefficients for the condensate terms are taken as 0 ± 2 . The c_{cond, a^2} prior is 0 ± 1 and a prior of 0.0 ± 0.2 on mass mistuning terms.

The two factors in parentheses model the a and μ dependence of the Z_m and quark bare mass respectively. There are terms allowing for discretisation effects behaving as $(a\mu)^{2n}$ in Z_m and $(a\Lambda)^{2n}$ in the bare mass, where Λ was taken as 500 MeV for the strange case and 1 GeV (approximately the charm mass) for the charm case as these are the relevant scales.

The fit also allows for condensate terms beginning at μ^{-2} arising from the expected presence of the $\langle A^2 \rangle$ condensate. Sea mass dependence of Z_m is allowed for as well as sea mass dependence of the condensate contributions. An $(a\Lambda)^2$ dependence is also allowed for in the condensates

with $\Lambda = 500$ MeV in both cases.

The one-loop coefficient of $\langle A^2 \rangle$ in the operator product expansion of Z_m can be calculated by considering low-energy gluon scattering and takes the value $(\pi\alpha_s C_F \langle A^2 \rangle)/(2\mu^2)$. This therefore suggests that a $1/\mu^2$ condensate term could be visible and must be allowed for. If just this condensate is allowed then the coefficient produced by the fit is not consistent between the charm and strange cases. The addition of a $1/\mu^4$ term results in consistent fits with a positive $1/\mu^2$ and a negative $1/\mu^4$. These coefficients are reasonably large.

Figure 6.1 shows the continuum extrapolation of the charm and strange quark masses in the $\overline{\text{MS}}$ scheme at a scale $\mu = 3$ GeV. Also shown are the results obtained from matching current-current correlators from lattice calculations to high order perturbation theory [27] and good agreement can be seen between the two.

The uncertainty in w_0 and w_0/a means that there is some uncertainty in the value of μ which we account for as a systematic uncertainty. There is an uncertainty in the values of μ used on each ensemble arising from the uncertainty in the lattice spacing. We therefore include a correlated (for each β value) uncertainty of 0.0003 on the coarse lattices, 0.0002 on the fine lattices and 0.0008 on the superfine lattices to account for uncertainty in the μ values calculated on each ensemble as they depend on $w_0\tilde{a}$. Another 0.1% correlated uncertainty was added to all points to account for the effect from w_0 .

The final results from these fits are

$$\begin{aligned}\overline{m}_c(3 \text{ GeV}) &= 0.9897(60) \\ \overline{m}_s(3 \text{ GeV}) &= 0.08538(84),\end{aligned}\tag{6.12}$$

and the robustness of the fit is demonstrated in Figure 6.2 where the mass values from various altered fits are shown. These alterations involve the removal of certain parts of the data set from the fit, doubling various prior widths and including more terms. The error budgets for the two fits are given in Table 6.2. This gives contributions arising from the extrapolation in lattice spacing, the term accounting for missing α_s^3 terms in the matching, terms accounting for condensates and sea mistuning effects. There are also contributions from the uncertainty in the mass running and matching factors which come from the uncertainty on α_s .

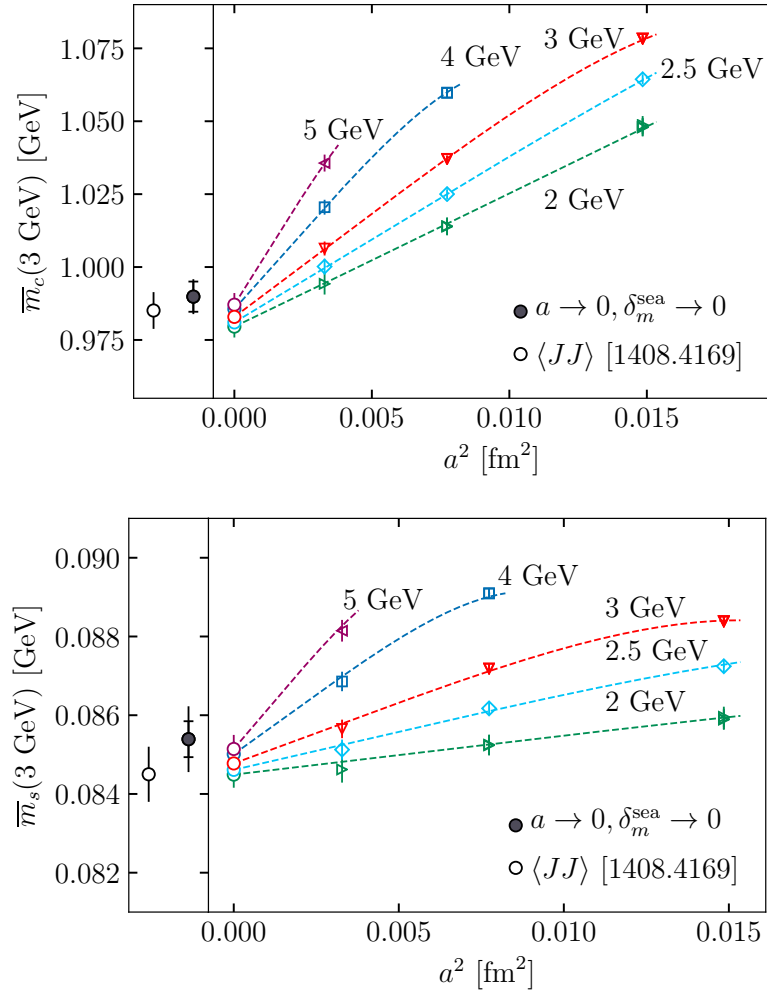


Figure 6.1: Final mass continuum extrapolations. The dashed lines have the sea quark mass mistunings set to 0. The shaded point on the left gives the final value at $a = 0$ with the condensate contributions removed. The empty black circle is the value from the current-current correlator method of [27].

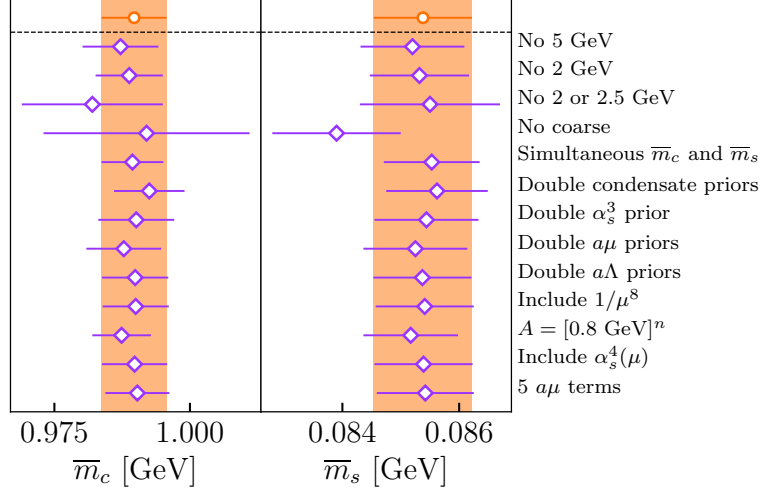


Figure 6.2: Robustness checks of the final mass fits. The 5 $a\mu$ points mark only uses 5 different powers of $a\mu$ in the fit as opposed to 10, which was used in the fit presented in Figure 6.1.

Table 6.2: Error budget, giving a breakdown of the uncertainties in the c and s quark masses in the $\overline{\text{MS}}$ scheme at a scale of 3 GeV obtained from the fits described in the text. All the uncertainties are given as a percentage of the final answer. The condensate uncertainties include all the uncertainties from that term in the fit function, which also allows for discretisation and m_{sea} effects.

	$\overline{m}_c(3 \text{ GeV})$	$\overline{m}_s(3 \text{ GeV})$
$a^2 \rightarrow 0$	0.28	0.28
Missing α_s^3 term	0.22	0.22
Condensate	0.22	0.13
m_{sea} effects	0.00	0.00
$Z_m^{\overline{\text{MS}}/\text{SMOM}}$ and R	0.04	0.04
Z_m^{SMOM}	0.13	0.13
Uncorrelated m^{tuned}	0.19	0.23
Correlated m^{tuned}	0.30	0.82
Gauge fixing	0.11	0.09
Total:	0.61%	0.98%

6.3 Charm tuning with the J/ψ

The masses given above in Section 6.2.2 are the results published in [1]. Here a small update to that calculation of the charm mass is provided by including data from the finer $\beta = 7$ ensemble and applying a correction such that the bare masses are now tuned using the J/ψ for the reasons discussed in Chapter 4. We also use the recent three-loop calculation of the Z_m matching to the $\overline{\text{MS}}$ scheme which allows us to change the α_s^3 in Eq. 6.10 to α_s^4 and reduce the uncertainty arising from that term. For the charmonium calculations presented here we have tuned the charm quark mass on set 18. For the calculation of [1] it is not the tuned bare charm mass on set 18 that we need but the tuned bare mass on an ensemble with the same β but physical sea quarks. To get this result, and the w_0/a value on such an ensemble, we make use of the results of Appendix A of [27]. We obtain $w_0/\tilde{a} = 3.970(15)$ and $m_c^{\text{tuned}} = 0.859(3)$ GeV where the correlated uncertainty from w_0 has been removed (it will be added back in at the end of the calculation as was done in [1]). [Note that the results presented here differ slightly from those in [3] as the latter uses newer w_0/a determinations, using tuning to the J/ψ mass for the sea charm quarks.]

The $Z_m(\mu)$ and $Z_V(\mu)$ that we have calculated on set 18 are at slightly mistuned values of μ compared to the results previously gathered on the other ensembles. This can be accounted for by changing the scale μ at which the $\overline{\text{MS}}$ and QCD running are evaluated. The Z factors on set 18 were evaluated at μ values of 2.04 and 2.98 GeV. We allow for the uncertainty on these values arising from the lattice spacing determination by including a correlated error across the two μ values of 0.001 on the $\overline{\text{MS}}$ conversion factor.

In Section 6.2 and [1] the bare masses were taken from [27] where they were tuned using an adjusted value of the η_c mass. The adjustment was composed of an estimate of the effect of QED on the mass using a Coulomb potential model and a perturbative adjustment for gluon annihilation taking a 100% uncertainty on the adjustment. Because the contribution from annihilation to gluons is much smaller in the case of the J/ψ it is preferable to use the J/ψ mass for this tuning. The value of the charmonium hyperfine splitting from Chapter 4 can be used to adjust the bare masses so that they are tuned to the J/ψ mass instead. As there is little lattice spacing dependence in the hyperfine splitting we adjust all bare masses by the same percentage. The hyperfine splitting gives a fractional discrepancy between η_c and J/ψ mass tuning of 0.25%. The deliberately mistuned data used in the analyses of Chapter 4 indicate that the fractional change in quark mass is 1.5 times the change in the J/ψ mass. We therefore apply a 0.38% shift to all bare masses.

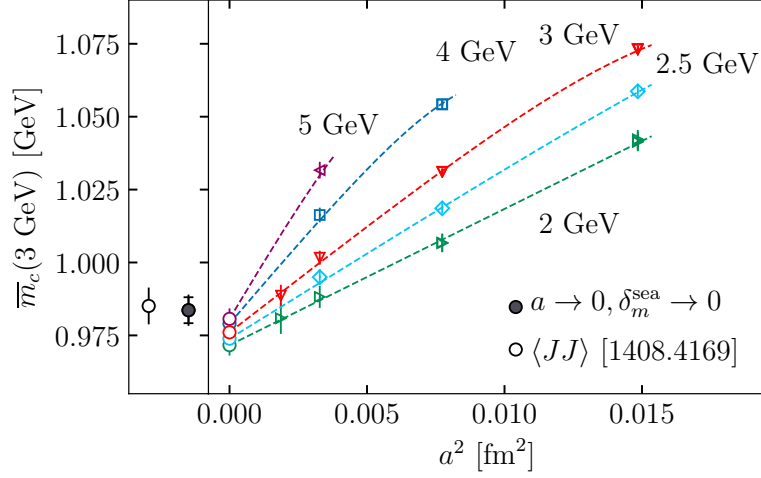


Figure 6.3: $\overline{m}_c(3 \text{ GeV})$ extrapolated to the continuum with a fit form that allows for condensate terms that behave like inverse powers of the renormalisation scale μ . This plot is the same as the upper section of Fig. 6.1 but with added data at a finer lattice spacing (ultrafine). The ultrafine points deviate from the μ values of the corresponding lines by 1-2% because the μ values on these points are slightly mistuned. We are also here using tuning to the J/ψ mass rather than the η_c mass as was done in [1].

The continuum extrapolation and μ fit is shown in Fig. 6.3 including the ultrafine points. This fit has a χ^2/dof of 0.81. The error budget for this calculation is shown in Table 6.4. Most of the entries are very similar to those in [1]. The contribution due to the continuum extrapolation has, unsurprisingly, dropped a little. The fit returns a result of 0.9836(54) GeV for $\overline{m}_c(3 \text{ GeV})$.

6.4 QED impact on the determination of m_c in the $\overline{\text{MS}}$ scheme

To assess the QED impact on the bare masses we use the QCD+QED J/ψ masses shown in Fig. 4.2. As we have corrected the result of [1] as if it were tuned to the experimental J/ψ mass this is the tuning we need to use for the QCD+QED case as well. The shift in am_c required to obtain the correct J/ψ mass after QED has been included (which we denote $R_{\text{QED}}[am_c]$) can be evaluated as the J/ψ mass should vary as $2am_c$ plus some binding energy to a first approximation. We therefore expect that, to a first approximation, $R_{\text{QED}}[am_c] = R_{\text{QED}}[M_{J/\psi}]$. The deliberately mistuned am_c values in Table 4.2 show that the fractional change in the value of am_c is 1.5 times larger than the change in $aM_{J/\psi}$. Using this factor of 1.5 we calculate $R_{\text{QED}}[am_c]$ to be

Table 6.3: The electromagnetic correction to Z_m for different values of μ and different lattice spacings are shown in the third column, The fourth column is the QED component of the RI-SMOM to $\overline{\text{MS}}$ matching for each μ and the fifth is the QED mass running to a reference scale of 3 GeV.

Set	μ [GeV]	$R_{\text{QED}}[Z_m^{\text{SMOM}}]$	$Z_m^{\overline{\text{MS}}/\text{SMOM}}[\text{QED}]$	$R(3 \text{ GeV}, \mu)[\text{QED}]$
6	2	1.001200(83)	0.999872	0.999372
14	2	1.001516(35)	0.999872	0.999372
16	2	1.001853(83)	0.999872	0.999372
6	2.5	1.000827(31)	0.999873	0.999718
6	3	1.000540(15)	0.999873	-
14	3	1.000851(11)	0.999873	-
16	3	1.001308(18)	0.999873	-
14	4	1.0005001(21)	0.999873	1.000446
16	4	1.0009331(34)	0.999873	1.000446

0.99840(8), 0.99790(4) and 0.99734(9) on sets 6, 14 and 16 respectively. The uncertainty on these values has been increased by a factor of 5 to account for uncertainty in the factor of 1.5.

As was done in [1] we perform calculations of Z_m ($R_{\text{QED}}[Z_m]$) at multiple values of the renormalisation scale μ , convert to $\overline{\text{MS}}$, and run all values to 3 GeV using the QCD four loop $\overline{\text{MS}}$ mass anomalous dimension. This allows us to account for nonperturbative contaminations which are generically suppressed by powers of μ . (In this case these would be QED corrections to QCD condensates.)

It is necessary to include QED effects on the matching to $\overline{\text{MS}}$ and the running of the mass renormalisation in the $\overline{\text{MS}}$ scheme to the reference scale of 3 GeV. The values needed to do this are given in Table 6.3. In that Table $R_{\text{QED}}[X]$ is a shorthand for $X[(\text{QCD}+\text{QED})/\text{QCD}]$. The values for $R_{\text{QED}}[Z_m]$ from Table 3.3 are also included.

For consistency we should also include QED effects to the mass anomalous dimension. Again, the α_{QED} coefficient can be obtained from the α_s term as before. Higher order terms in α_{QED} are known but their high suppression renders them negligible. The $\alpha_s\alpha_{\text{QED}}$ term could, in principle, have some impact. This term is calculated in [155]. The coefficient is very small and we therefore ignore it.

We fit the product of $R_{\text{QED}}[am_c]$, $R_{\text{QED}}[Z_m]$, the QED $\overline{\text{MS}}$ conversion and QED mass running. This gives the (QCD+QED)/QCD renormalised charm mass run to a reference scale of 3 GeV.

Z_m is in the RI-SMOM scheme and therefore needs to be converted to $\overline{\text{MS}}$ before we run to 3 GeV. We use the following fit form:

$$\begin{aligned}
R_{\text{QED}}[\overline{m}_c(3 \text{ GeV}, \mu, a)] &= R_{\text{QED}}[\overline{m}_c(3 \text{ GeV})] \times \\
&\left[1 + \alpha_{\text{QED}} Q^2 \sum_{i=1} c_{a^2}^{(i)} (a(1 \text{ GeV}))^{2i} \right] \times \\
&\left[1 + \alpha_{\text{QED}} Q^2 \left(\sum_{j=1} c_{\mu^2 a^2}^{(j)} (a\mu)^{2j} \right. \right. \\
&\left. \left. + \sum_{n=1} \alpha_s(\mu) c_{\text{cond}}^{(n)} \frac{(1 \text{ GeV})^{2n}}{\mu^{2n}} \right) \right]. \tag{6.13}
\end{aligned}$$

Here the first term on the second line accounts for discretisation effects in $R_{\text{QED}}[am_c]$; a scale of 1 GeV is chosen as this is close to the charm mass. The term multiplying this models the a and μ dependence of the QED correction to Z_m . This includes discretisation effects of the form $(a\mu)^{2i}$. There are, in addition, terms to model condensate contributions, starting at $1/\mu^2$. The condensate coefficients are not resolved by the fit. The fit result, with a χ^2/dof of 0.87, for $R_{\text{QED}}[\overline{m}_c(3 \text{ GeV})]$ is 0.99823(17), which we multiply the pure QCD result by to obtain a final answer for the charm quark mass in the $\overline{\text{MS}}$ scheme at a reference scale of 3 GeV: 0:9819(54) GeV. The error budget for this final value is given in Table 6.4.

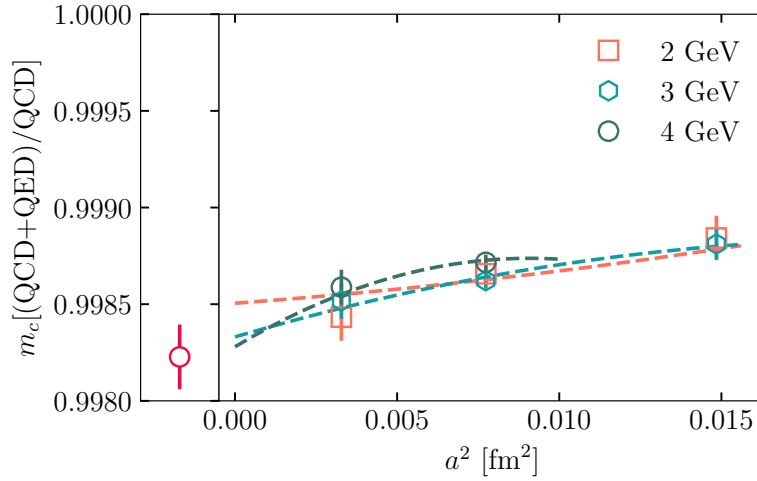


Figure 6.4: Electromagnetic correction to the charm quark mass in the $\overline{\text{MS}}$ scheme at a scale of 3 GeV. The final, continuum extrapolated, result is shown as the red circle to the left. The different μ values, shown as different colours and shapes, have all been run to 3 GeV and only differ by discretisation and condensate effects. In fact, there is no visible difference. The vast majority of the discretisation effect here is due to discretisation effects in the ratio of the charm bare mass tuned to give the experimental J/ψ mass with and without the inclusion of QED effects. These appear as even powers of am_c .

Table 6.4: Error budget for the calculation of the charm quark mass in the $\overline{\text{MS}}$ scheme at a scale of 3 GeV using RI-SMOM as an intermediate scheme. The listed contributions have the same meaning as those in [1] except for the “QED effect” which comes from the continuum extrapolation shown in Fig. 6.4.

	$\overline{m}_c(3 \text{ GeV})$
$a^2 \rightarrow 0$	0.25
Missing α_s^3 term	0.10
Condensate	0.21
m_{sea} effects	0.00
$Z_m^{\overline{\text{MS}}/\text{SMOM}}$ and R	0.05
Z_m^{SMOM}	0.12
Uncorrelated m^{tuned}	0.13
Correlated m^{tuned}	0.30
Gauge fixing	0.09
μ error from w_0	0.12
QED effect	0.02
Total	0.51%

6.5 Cross-check with determination from time moments

The previous HPQCD determination of m_c [27] used fits to (pseudoscalar) time moment data utilising the available three-loop QCD perturbation theory evaluations of those moments in terms of the quark mass. The fit used was sophisticated and involved division of the moments by their tree level values to reduce discretisation effects. Here we perform a similar but simpler procedure to provide another cross-check of our m_c value.

For each vector time moment whose continuum value was calculated in Section 4.7 we may calculate the charm quark mass by dividing by the perturbative expressions given in Section 1.5.1. The α_s in the perturbative expression can be chosen to be evaluated at m_c to avoid logarithmic terms in the series. However, a scale of ~ 1 GeV poses potential problems for the convergence of the perturbative expansion. We therefore also evaluate the series, including log terms, at a scale of 3 GeV. This gives a charm mass in the $\overline{\text{MS}}$ scheme at a scale of 3 GeV. The perturbative expansion becomes less convergent as the n value of the moment increases and we therefore only use the first three moments. The m_c values at both the charm mass itself and 3 GeV for the first three moments are given in Table 6.5. The numbers there are very precise, with the uncertainty being dominated by α_s . Given the level of precision and the simplicity of the analysis no claim is made that the final uncertainties are reliable given that the perturbation theory used is truncated and performed at reasonably low scales.

The values in Table 6.5 are fit to a constant and a different α_s^4 term for each moment to allow for the next unknown term in the perturbative expansion. A prior of 0 ± 0.5 was used for each of these terms. We obtain the values:

$$\begin{aligned}\overline{m}_c(\overline{m}_c) &= 1.2653(86), \\ \overline{m}_c(3 \text{ GeV}) &= 0.9790(84).\end{aligned}\tag{6.14}$$

Table 6.5: The charm quark mass determined from various vector time moments at scales of the charm mass itself and 3 GeV.

	$n = 4$	$n = 6$	$n = 8$
$\mu = \overline{m}_c$	1.2653(41)	1.2689(28)	1.2677(19)
$\mu = 3 \text{ GeV}$	0.9789(35)	0.9787(49)	0.9842(51)

According to the discussion of [133] an uncertainty of ± 0.02 GeV on $\overline{m}_c(\overline{m}_c)$ should cover the systematic uncertainty of unknown higher order perturbation theory, so the results of Eq. 6.14 may not fully capture this. There are also gluon condensate ($\langle G_{\mu\nu}G^{\mu\nu} \rangle$) effects that are being ignored which are expected to be small but grow with n . However, even given these considerations Eq. 6.14 still agree well with our RI-SMOM results.

6.6 Summary

The current status of lattice determinations of the charm quark mass is displayed in Fig. 6.6. This only includes lattice QCD results with 4 active flavours of quark in the sea. There are three lattice determinations using independent methods (with different systematic uncertainties) that have subpercent uncertainties. The FNAL/MILC/TUMQCD result [156] uses HQET to parameterise the heavy quark mass dependence of heavy-light meson masses calculated on the lattice. The quark mass from this expansion is then perturbatively matched to the $\overline{\text{MS}}$ scheme. (There is a subtlety in the definition of the quark mass that is made well defined through the use of the minimal renormalon-subtracted (MRS) scheme [157].) The HPQCD HISQ JJc result is from [27] and uses fits to pseudoscalar time moments (divided by their tree level values) to a fit including the perturbative expansion. These three all use the MILC HISQ ensembles with HISQ valence quarks. The ETMC result from [158] uses mass renormalisation performed in the RI'-MOM scheme with a twisted mass action.

There is very good (well within 1σ) agreement between the different HISQ determinations (which are the most precise) indicating that the separate methods have well controlled systematic uncertainties. All these determinations are considerably more precise than the PDG average.

Our final results for the strange and charm quark masses are:

$$\begin{aligned}\overline{m}_c(3 \text{ GeV}) &= 0.9819(54), \\ \overline{m}_s(3 \text{ GeV}) &= 0.08538(84).\end{aligned}\tag{6.15}$$

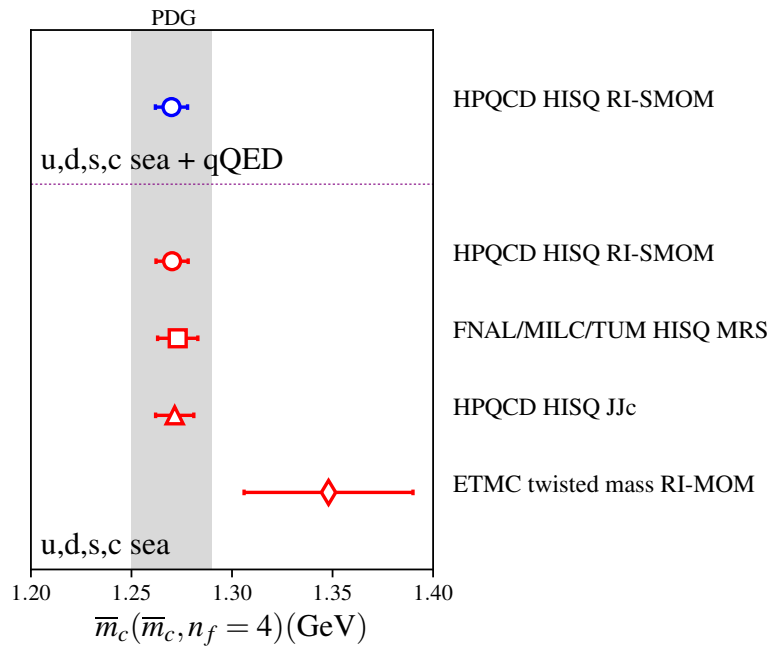


Figure 6.5: Comparison plot of lattice determinations of the charm quark running mass in the $\overline{\text{MS}}$ scheme with four flavours in the sea. The grey band corresponds to the PDG average. [Figure courtesy of C. T. H. Davies.]

Chapter 7

Conclusions

This work has consisted of two main streams. The first is the computation of renormalisation factors for various currents using largely nonperturbative methods. This has allowed for very precise results for these factors and we have demonstrated that the systematics associated with these nonperturbative calculations can be understood and controlled. This included a detailed examination of the nonperturbative renormalisation of lattice vector currents. The conclusion of this study was that the RI-SMOM momentum subtraction scheme provides a method for the calculation of vector current renormalisation factors (Z_V) devoid of nonperturbative contamination. This was shown to not be the case for the RI'-MOM scheme through analysis of the conserved and local lattice vector current renormalisations, due to the lack of protection given to the RI'-MOM scheme by the Ward-Takahashi identity. It was also shown that nonperturbative contributions to the mass renormalisation factors obtained using momentum subtraction schemes on the lattice need to be accounted for in order to achieve percent level precision in determinations of quark masses that use such renormalisation factors.

The second stream involves applications of these renormalisation factors in the calculations of charmonium and bottomonium meson properties and the determination of quark masses. This has resulted in high precision results for ground state charmonium properties. We have provided the first calculation of the charmonium hyperfine splitting that is precise enough to show separation from the experimental average which is expected due to the contribution to the η_c mass from annihilation to gluons. We have made efforts to control all the systematics of this calculation by using lattice ensembles that cover a very wide range of lattice spacings, going

down to ~ 0.03 fm, as well as including electromagnetic effects. We therefore take the difference between our hyperfine splitting result of $0.1203(11)$ GeV and the experimental average of $0.1130(5)$ GeV to be the contribution of η_c annihilation which is missing from the lattice calculation. (Properly including this contribution would require the calculation of disconnected correlators and a complicated analysis of the results. At present this is too difficult.) We also calculated the J/ψ decay constant, making use of RI-SMOM vector current renormalisation factors, and achieved better precision (0.4%) than both any previous lattice calculation and the experimental average. The agreement between our result and the experimental average shows that our systematic uncertainties are controlled at a level below 1% precision. These results are summarised in Eq. 4.28.

We have extended these results to higher masses with the aim of reaching the b mass. Using both the bottomonium hyperfine splitting and Υ decay constant we have demonstrated that we can parameterise the heavy mass dependence of heavyonium quantities provided that we have data at small lattice spacings where the b mass can be reached. We have been able to provide bottomonium results at the 5% level which is comparable to experiment and more precise than previous lattice results using NRQCD or Fermilab quarks. Bottomonium results are summarised in Eq. 5.3.

Finally, we presented determinations of the strange and charm quark masses using mass renormalisation factors calculated nonperturbatively in the RI-SMOM scheme and then perturbatively matched to the $\overline{\text{MS}}$ scheme achieving precision below 1% for both. For the charm quark mass we also included the effects of QED given that we have reached subpercent precision. Our final values in the $\overline{\text{MS}}$ scheme at a renormalisation scale of 3 GeV are given in Eq. 6.15.

There are several further applications of the renormalisation factors presented here that are currently underway. Tensor form factors which require the tensor current renormalisation factors discussed in Section 3.4 are currently being calculated for a study of $B \rightarrow K$ decays using an all-HISQ approach, as discussed in Chapter 5. There are also plans to study the QED correction to the light quark contribution to the HVP which will require the use of the QED corrections to the local vector current renormalisation given in Section 3.3.7.

Bibliography

- [1] A. T. Lytle, C. T. H. Davies, D. Hatton, G. P. Lepage, and C. Sturm (HPQCD), “Determination of quark masses from $\mathbf{n}_f = 4$ lattice QCD and the RI-SMOM intermediate scheme,” *Phys. Rev.* **D98**, 014513 (2018), [arXiv:1805.06225 \[hep-lat\]](#) .
- [2] D. Hatton, C.T.H. Davies, G.P. Lepage, and A.T. Lytle (HPQCD), “Renormalizing vector currents in lattice QCD using momentum-subtraction schemes,” *Phys. Rev. D* **100**, 114513 (2019), [arXiv:1909.00756 \[hep-lat\]](#) .
- [3] D. Hatton, C.T.H. Davies, B. Galloway, J. Koponen, G.P. Lepage, and A.T. Lytle (HPQCD), “Charmonium properties from lattice QCD + QED: hyperfine splitting, J/ψ leptonic width, charm quark mass and a_μ^c ,” (2020), [arXiv:2005.01845 \[hep-lat\]](#) .
- [4] Roel Aaij *et al.* (LHCb), “Angular analysis of the $B^0 \rightarrow K^{*0} \mu^+ \mu^-$ decay using 3 fb^{-1} of integrated luminosity,” *JHEP* **02**, 104 (2016), [arXiv:1512.04442 \[hep-ex\]](#) .
- [5] R. Aaij *et al.* (LHCb), “Measurement of the ratio of branching fractions $\mathcal{B}(B_c^+ \rightarrow J/\psi \tau^+ \nu_\tau) / \mathcal{B}(B_c^+ \rightarrow J/\psi \mu^+ \nu_\mu)$,” *Phys. Rev. Lett.* **120**, 121801 (2018), [arXiv:1711.05623 \[hep-ex\]](#) .
- [6] Roel Aaij *et al.* (LHCb), “Measurement of the ratio of branching fractions $\mathcal{B}(\bar{B}^0 \rightarrow D^{*+} \tau^- \bar{\nu}_\tau) / \mathcal{B}(\bar{B}^0 \rightarrow D^{*+} \mu^- \bar{\nu}_\mu)$,” *Phys. Rev. Lett.* **115**, 111803 (2015), [Erratum: *Phys.Rev.Lett.* 115, 159901 (2015)], [arXiv:1506.08614 \[hep-ex\]](#) .
- [7] R. Aaij *et al.* (LHCb), “Measurement of the ratio of the $B^0 \rightarrow D^{*-} \tau^+ \nu_\tau$ and $B^0 \rightarrow D^{*-} \mu^+ \nu_\mu$ branching fractions using three-prong τ -lepton decays,” *Phys. Rev. Lett.* **120**, 171802 (2018), [arXiv:1708.08856 \[hep-ex\]](#) .
- [8] Andrew Lytle, “Lattice $B \rightarrow D^{(*)}$ form factors, $R(D^{(*)})$, and $|V_{cb}|$,” PoS **LATTICE2019**, 228 (2020), [arXiv:2004.01132 \[hep-lat\]](#) .

- [9] G. W. Bennett *et al.* (Muon g-2), “Measurement of the negative muon anomalous magnetic moment to 0.7 ppm,” *Phys. Rev. Lett.* **92**, 161802 (2004), [arXiv:hep-ex/0401008 \[hep-ex\]](#) .
- [10] Georges Aad *et al.* (ATLAS), “Observation of a new particle in the search for the Standard Model Higgs boson with the ATLAS detector at the LHC,” *Phys. Lett.* **B716**, 1–29 (2012), [arXiv:1207.7214 \[hep-ex\]](#) .
- [11] Serguei Chatrchyan *et al.* (CMS), “Observation of a New Boson at a Mass of 125 GeV with the CMS Experiment at the LHC,” *Phys. Lett.* **B716**, 30–61 (2012), [arXiv:1207.7235 \[hep-ex\]](#) .
- [12] Matthew D. Schwartz, *Quantum Field Theory and the Standard Model* (Cambridge University Press, 2014).
- [13] Steven Weinberg, *The Quantum theory of fields. Vol. 1: Foundations* (Cambridge University Press, 2005).
- [14] Steven Weinberg, *The quantum theory of fields. Vol. 2: Modern applications* (Cambridge University Press, 2013).
- [15] M. Srednicki, *Quantum field theory* (Cambridge University Press, 2007).
- [16] Steven Weinberg, “A Model of Leptons,” *Phys. Rev. Lett.* **19**, 1264–1266 (1967).
- [17] Sheldon L. Glashow, “The renormalizability of vector meson interactions,” *Nucl. Phys.* **10**, 107–117 (1959).
- [18] Abdus Salam and John Clive Ward, “Weak and electromagnetic interactions,” *Nuovo Cim.* **11**, 568–577 (1959).
- [19] Peter W. Higgs, “Broken Symmetries and the Masses of Gauge Bosons,” *Phys. Rev. Lett.* **13**, 508–509 (1964), [[160\(1964\)](#)].
- [20] F. Englert and R. Brout, “Broken Symmetry and the Mass of Gauge Vector Mesons,” *Phys. Rev. Lett.* **13**, 321–323 (1964), [[157\(1964\)](#)].
- [21] G. S. Guralnik, C. R. Hagen, and T. W. B. Kibble, “Global Conservation Laws and Massless Particles,” *Phys. Rev. Lett.* **13**, 585–587 (1964), [[162\(1964\)](#)].
- [22] C. S. Wu, E. Ambler, R. W. Hayward, D. D. Hoppes, and R. P. Hudson, “Experimental Test of Parity Conservation in Beta Decay,” *Phys. Rev.* **105**, 1413–1414 (1957).

- [23] M. Tanabashi *et al.* (Particle Data Group), “Review of Particle Physics,” *Phys. Rev.* **D98**, 030001 (2018).
- [24] H. David Politzer, “Reliable Perturbative Results for Strong Interactions?” *Phys. Rev. Lett.* **30**, 1346–1349 (1973), [,274(1973)].
- [25] D. J. Gross and Frank Wilczek, “Asymptotically Free Gauge Theories - I,” *Phys. Rev.* **D8**, 3633–3652 (1973).
- [26] F. Herzog, B. Ruijl, T. Ueda, J. A. M. Vermaseren, and A. Vogt, “The five-loop beta function of Yang-Mills theory with fermions,” *JHEP* **02**, 090 (2017), arXiv:1701.01404 [hep-ph] .
- [27] Bipasha Chakraborty, C. T. H. Davies, B. Galloway, P. Knecht, J. Koponen, G. C. Donald, R. J. Dowdall, G. P. Lepage, and C. McNeile, “High-precision quark masses and QCD coupling from $n_f = 4$ lattice QCD,” *Phys. Rev.* **D91**, 054508 (2015), arXiv:1408.4169 [hep-lat] .
- [28] A. Maier, P. Maierhofer, P. Marquard, and A. V. Smirnov, “Low energy moments of heavy quark current correlators at four loops,” *Nucl. Phys.* **B824**, 1–18 (2010), arXiv:0907.2117 [hep-ph] .
- [29] Y. Kiyo, A. Maier, P. Maierhofer, and P. Marquard, “Reconstruction of heavy quark current correlators at $O(\alpha(s)^3)$,” *Nucl. Phys.* **B823**, 269–287 (2009), arXiv:0907.2120 [hep-ph] .
- [30] Kenneth G. Wilson, “Nonlagrangian models of current algebra,” *Phys. Rev.* **179**, 1499–1512 (1969).
- [31] K. G. Chetyrkin and A. Maier, “Wilson Expansion of QCD Propagators at Three Loops: Operators of Dimension Two and Three,” *JHEP* **01**, 092 (2010), arXiv:0911.0594 [hep-ph] .
- [32] Thomas DeGrand and Carleton E. Detar, *Lattice methods for quantum chromodynamics* (2006).
- [33] Kenneth G. Wilson, “Confinement of Quarks,” *Phys. Rev.* **D10**, 2445–2459 (1974), [,45(1974); ,319(1974)].
- [34] Holger Bech Nielsen and M. Ninomiya, “Absence of Neutrinos on a Lattice. 1. Proof by

- Homotopy Theory,” *Nucl. Phys.* **B185**, 20 (1981), [Erratum: *Nucl. Phys.*B195,541(1982); ,533(1980)].
- [35] Holger Bech Nielsen and M. Ninomiya, “Absence of Neutrinos on a Lattice. 2. Intuitive Topological Proof,” *Nucl. Phys.* **B193**, 173–194 (1981).
- [36] Maarten F.L. Golterman and Jan Smit, “Selfenergy and Flavor Interpretation of Staggered Fermions,” *Nucl. Phys. B* **245**, 61–88 (1984).
- [37] Satchidananda Naik, “On-shell Improved Lattice Action for QCD With Susskind Fermions and Asymptotic Freedom Scale,” *Nucl. Phys.* **B316**, 238–268 (1989).
- [38] G. Peter Lepage, “Flavor symmetry restoration and Symanzik improvement for staggered quarks,” *Phys. Rev.* **D59**, 074502 (1999), [arXiv:hep-lat/9809157 \[hep-lat\]](#) .
- [39] E. Follana, Q. Mason, C. Davies, K. Hornbostel, G. P. Lepage, J. Shigemitsu, H. Trottier, and K. Wong (HPQCD, UKQCD), “Highly improved staggered quarks on the lattice, with applications to charm physics,” *Phys. Rev.* **D75**, 054502 (2007), [arXiv:hep-lat/0610092 \[hep-lat\]](#) .
- [40] Martin Luscher, Stefan Sint, Rainer Sommer, and Peter Weisz, “Chiral symmetry and $O(a)$ improvement in lattice QCD,” *Nucl. Phys.* **B478**, 365–400 (1996), [arXiv:hep-lat/9605038 \[hep-lat\]](#) .
- [41] M. R. Hestenes and E. Stiefel, “Methods of conjugate gradients for solving linear systems,” *Journal of research of the National Bureau of Standards* **49**, 409–436 (1952).
- [42] A. Bazavov *et al.* (MILC), “Lattice QCD ensembles with four flavors of highly improved staggered quarks,” *Phys. Rev.* **D87**, 054505 (2013), [arXiv:1212.4768 \[hep-lat\]](#) .
- [43] Michael Betancourt, “A conceptual introduction to hamiltonian monte carlo,” (2017), [arXiv:1701.02434 \[stat.ME\]](#) .
- [44] Gordon C. Donald, Christine T. H. Davies, Eduardo Follana, and Andreas S. Kronfeld, “Staggered fermions, zero modes, and flavor-singlet mesons,” *Phys. Rev.* **D84**, 054504 (2011), [arXiv:1106.2412 \[hep-lat\]](#) .
- [45] A. Hart, G. M. von Hippel, and R. R. Horgan (HPQCD), “Radiative corrections to the lattice gluon action for HISQ improved staggered quarks and the effect of such corrections on the static potential,” *Phys. Rev.* **D79**, 074008 (2009), [arXiv:0812.0503 \[hep-lat\]](#) .

- [46] R. J. Dowdall, C. T. H. Davies, G. P. Lepage, and C. McNeile, “Vus from pi and K decay constants in full lattice QCD with physical u, d, s and c quarks,” *Phys. Rev.* **D88**, 074504 (2013), [arXiv:1303.1670 \[hep-lat\]](#) .
- [47] Paulo F. Bedaque, “Aharonov-Bohm effect and nucleon nucleon phase shifts on the lattice,” *Phys. Lett.* **B593**, 82–88 (2004), [arXiv:nucl-th/0402051 \[nucl-th\]](#) .
- [48] G. M. de Divitiis, R. Petronzio, and N. Tantalo, “On the discretization of physical momenta in lattice QCD,” *Phys. Lett.* **B595**, 408–413 (2004), [arXiv:hep-lat/0405002 \[hep-lat\]](#) .
- [49] D. Guadagnoli, F. Mescia, and S. Simula, “Lattice study of semileptonic form-factors with twisted boundary conditions,” *Phys. Rev.* **D73**, 114504 (2006), [arXiv:hep-lat/0512020 \[hep-lat\]](#) .
- [50] M. A. Clark, R. Babich, K. Barros, R. C. Brower, and C. Rebbi, “Solving Lattice QCD systems of equations using mixed precision solvers on GPUs,” *Comput. Phys. Commun.* **181**, 1517–1528 (2010), [arXiv:0911.3191 \[hep-lat\]](#) .
- [51] G. P. Lepage, B. Clark, C. T. H. Davies, K. Hornbostel, P. B. Mackenzie, C. Morningstar, and H. Trottier, “Constrained curve fitting,” *Lattice field theory. Proceedings, 19th International Symposium, Lattice 2001, Berlin, Germany, August 19-24, 2001*, *Nucl. Phys. Proc. Suppl.* **106**, 12–20 (2002), [arXiv:hep-lat/0110175 \[hep-lat\]](#) .
- [52] C. M. Bouchard, G. Peter Lepage, Christopher Monahan, Heechang Na, and Junko Shigemitsu, “ $B_s \rightarrow K\ell\nu$ form factors from lattice QCD,” *Phys. Rev.* **D90**, 054506 (2014), [arXiv:1406.2279 \[hep-lat\]](#) .
- [53] R. J. Dowdall, C. T. H. Davies, R. R. Horgan, G. P. Lepage, C. J. Monahan, J. Shigemitsu, and M. Wingate, “Neutral B-meson mixing from full lattice QCD at the physical point,” (2019), [arXiv:1907.01025 \[hep-lat\]](#) .
- [54] A. Portelli *et al.* (Budapest-Marseille-Wuppertal), “Electromagnetic corrections to light hadron masses,” *Proceedings, 28th International Symposium on Lattice field theory (Lattice 2010): Villasimius, Italy, June 14-19, 2010*, *PoS LATTICE2010*, 121 (2010), [arXiv:1011.4189 \[hep-lat\]](#) .
- [55] A. Hart, R. R. Horgan, and L. C. Storoni, “Perturbation theory versus simulation for tadpole improvement factors in pure gauge theories,” *Phys. Rev.* **D70**, 034501 (2004), [arXiv:hep-lat/0402033 \[hep-lat\]](#) .

- [56] R. J. Dowdall *et al.* (HPQCD), “The Upsilon spectrum and the determination of the lattice spacing from lattice QCD including charm quarks in the sea,” *Phys. Rev.* **D85**, 054509 (2012), [arXiv:1110.6887 \[hep-lat\]](#) .
- [57] Martin Lüscher, “Properties and uses of the Wilson flow in lattice QCD,” *JHEP* **08**, 071 (2010), [Erratum: *JHEP*03,092(2014)], [arXiv:1006.4518 \[hep-lat\]](#) .
- [58] Szabolcs Borsanyi *et al.*, “High-precision scale setting in lattice QCD,” *JHEP* **09**, 010 (2012), [arXiv:1203.4469 \[hep-lat\]](#) .
- [59] A. Bazavov *et al.* (MILC), “Gradient flow and scale setting on MILC HISQ ensembles,” *Phys. Rev.* **D93**, 094510 (2016), [arXiv:1503.02769 \[hep-lat\]](#) .
- [60] G. Martinelli, C. Pittori, Christopher T. Sachrajda, M. Testa, and A. Vladikas, “A General method for nonperturbative renormalization of lattice operators,” *Nucl. Phys.* **B445**, 81–108 (1995), [arXiv:hep-lat/9411010 \[hep-lat\]](#) .
- [61] C. Sturm, Y. Aoki, N. H. Christ, T. Izubuchi, C. T. C. Sachrajda, and A. Soni, “Renormalization of quark bilinear operators in a momentum-subtraction scheme with a nonexceptional subtraction point,” *Phys. Rev.* **D80**, 014501 (2009), [arXiv:0901.2599 \[hep-ph\]](#) .
- [62] K. G. Chetyrkin and A. Retey, “Renormalization and running of quark mass and field in the regularization invariant and MS-bar schemes at three loops and four loops,” *Nucl. Phys.* **B583**, 3–34 (2000), [arXiv:hep-ph/9910332 \[hep-ph\]](#) .
- [63] R. Arthur and P. A. Boyle (RBC, UKQCD), “Step Scaling with off-shell renormalisation,” *Phys. Rev.* **D83**, 114511 (2011), [arXiv:1006.0422 \[hep-lat\]](#) .
- [64] Andrew T. Lytle and Stephen R. Sharpe, “Nonperturbative renormalization for improved staggered bilinears,” *Phys. Rev.* **D88**, 054506 (2013), [arXiv:1306.3881 \[hep-lat\]](#) .
- [65] G. Peter Lepage, Paul B. Mackenzie, and Michael E. Peskin, “Expected Precision of Higgs Boson Partial Widths within the Standard Model,” (2014), [arXiv:1404.0319 \[hep-ph\]](#) .
- [66] Jeffrey E. Mandula and Michael Ogilvie, “Efficient gauge fixing via overrelaxation,” *Phys. Lett.* **B248**, 156–158 (1990).
- [67] C. T. H. Davies, G. G. Batrouni, G. R. Katz, Andreas S. Kronfeld, G. P. Lepage, K. G.

- Wilson, P. Rossi, and B. Svetitsky, “Fourier Acceleration in Lattice Gauge Theories. 1. Landau Gauge Fixing,” *Phys. Rev.* **D37**, 1581 (1988).
- [68] V.N. Gribov, “Quantization of Nonabelian Gauge Theories,” *Nucl. Phys. B* **139**, 1 (1978).
- [69] Christof Gatttringer, M. Gockeler, Philipp Huber, and C. B. Lang, “Renormalization of bilinear quark operators for the chirally improved lattice Dirac operator,” *Nucl. Phys.* **B694**, 170–186 (2004), [arXiv:hep-lat/0404006 \[hep-lat\]](#) .
- [70] Y. Aoki *et al.*, “Non-perturbative renormalization of quark bilinear operators and B(K) using domain wall fermions,” *Phys. Rev.* **D78**, 054510 (2008), [arXiv:0712.1061 \[hep-lat\]](#) .
- [71] Masashi Hayakawa and Shunpei Uno, “QED in finite volume and finite size scaling effect on electromagnetic properties of hadrons,” *Prog. Theor. Phys.* **120**, 413–441 (2008), [arXiv:0804.2044 \[hep-ph\]](#) .
- [72] Christine Davies, “Standard Model Heavy Flavor physics on the Lattice,” *Proceedings, 29th International Symposium on Lattice field theory (Lattice 2011): Squaw Valley, Lake Tahoe, USA, July 10-16, 2011*, **PoS LATTICE2011**, 019 (2011), [arXiv:1203.3862 \[hep-lat\]](#) .
- [73] Jack Laiho, Enrico Lunghi, and Ruth Van de Water, “Flavor Physics in the LHC era: The Role of the lattice,” *Proceedings, 29th International Symposium on Lattice field theory (Lattice 2011): Squaw Valley, Lake Tahoe, USA, July 10-16, 2011*, **PoS LATTICE2011**, 018 (2011), [arXiv:1204.0791 \[hep-ph\]](#) .
- [74] Harvey B. Meyer and Hartmut Wittig, “Lattice QCD and the anomalous magnetic moment of the muon,” *Prog. Part. Nucl. Phys.* **104**, 46–96 (2019), [arXiv:1807.09370 \[hep-lat\]](#) .
- [75] Bipasha Chakraborty, C. T. H. Davies, G. C. Donald, J. Koponen, and G. P. Lepage (HPQCD), “Nonperturbative comparison of clover and highly improved staggered quarks in lattice QCD and the properties of the ϕ meson,” *Phys. Rev.* **D96**, 074502 (2017), [arXiv:1703.05552 \[hep-lat\]](#) .
- [76] G. C. Donald, C. T. H. Davies, R. J. Dowdall, E. Follana, K. Hornbostel, J. Koponen, G. P. Lepage, and C. McNeile, “Precision tests of the J/ψ from full lattice QCD: mass, leptonic width and radiative decay rate to η_c ,” *Phys. Rev.* **D86**, 094501 (2012), [arXiv:1208.2855 \[hep-lat\]](#) .
- [77] Bipasha Chakraborty, C. T. H. Davies, G. C. Donald, R. J. Dowdall, J. Koponen, G. P. Lep-

- age, and T. Teubner (HPQCD), “Strange and charm quark contributions to the anomalous magnetic moment of the muon,” *Phys. Rev.* **D89**, 114501 (2014), [arXiv:1403.1778 \[hep-lat\]](#) .
- [78] Bipasha Chakraborty, C. T. H. Davies, P. G. de Oliveira, J. Koponen, G. P. Lepage, and R. S. Van de Water, “The hadronic vacuum polarization contribution to a_μ from full lattice QCD,” *Phys. Rev.* **D96**, 034516 (2017), [arXiv:1601.03071 \[hep-lat\]](#) .
- [79] Shuhei Yamamoto, Carleton DeTar, Aida X. El-Khadra, Craig McNeile, Ruth S. Van de Water, and Alejandro Vaquero, “Disconnected hadronic vacuum polarization contribution to the muon $g-2$ with HISQ,” in *36th International Symposium on Lattice Field Theory (Lattice 2018) East Lansing, MI, United States, July 22-28, 2018* (2018) [arXiv:1811.06058 \[hep-lat\]](#) .
- [80] Luuk H. Karsten and Jan Smit, “Lattice Fermions: Species Doubling, Chiral Invariance, and the Triangle Anomaly,” *Nucl. Phys.* **B183**, 103 (1981), [495(1980)].
- [81] Marco Bochicchio, Luciano Maiani, Guido Martinelli, Gian Carlo Rossi, and Massimo Testa, “Chiral Symmetry on the Lattice with Wilson Fermions,” *Asia Pacific Conf.1987:439, Trieste Electroweak 1985:25*, *Nucl. Phys.* **B262**, 331 (1985).
- [82] Philipp Huber, “Renormalization factors of quark bilinears using the DCI operator with dynamical quarks,” *JHEP* **11**, 107 (2010), [arXiv:1003.3496 \[hep-lat\]](#) .
- [83] Apoorva Patel and Stephen R. Sharpe, “Perturbative corrections for staggered fermion bilinears,” *Nucl. Phys.* **B395**, 701–732 (1993), [arXiv:hep-lat/9210039 \[hep-lat\]](#) .
- [84] David Daniel and Stephen N. Sheard, “PERTURBATIVE CORRECTIONS TO STAGGERED FERMION LATTICE OPERATORS,” *Nucl. Phys.* **B302**, 471–498 (1988).
- [85] A. Bazavov *et al.* (MILC), “Scaling studies of QCD with the dynamical HISQ action,” *Phys. Rev.* **D82**, 074501 (2010), [arXiv:1004.0342 \[hep-lat\]](#) .
- [86] G. Peter Lepage and Paul B. Mackenzie, “On the viability of lattice perturbation theory,” *Phys. Rev.* **D48**, 2250–2264 (1993), [arXiv:hep-lat/9209022 \[hep-lat\]](#) .
- [87] J. Koponen, F. Bursa, C. T. H. Davies, R. J. Dowdall, and G. P. Lepage, “Size of the pion from full lattice QCD with physical u , d , s and c quarks,” *Phys. Rev.* **D93**, 054503 (2016), [arXiv:1511.07382 \[hep-lat\]](#) .

- [88] Zohreh Davoudi, James Harrison, Andreas Jüttner, Antonin Portelli, and Martin J. Savage, “Theoretical aspects of quantum electrodynamics in a finite volume with periodic boundary conditions,” (2018), [arXiv:1810.05923 \[hep-lat\]](#) .
- [89] P. Boyle, V. Gülpers, J. Harrison, A. Jüttner, C. Lehner, A. Portelli, and C. T. Sachrajda, “Isospin breaking corrections to meson masses and the hadronic vacuum polarization: a comparative study,” *JHEP* **09**, 153 (2017), [arXiv:1706.05293 \[hep-lat\]](#) .
- [90] A. Bazavov *et al.*, “ B - and D -meson leptonic decay constants from four-flavor lattice QCD,” *Phys. Rev.* **D98**, 074512 (2018), [arXiv:1712.09262 \[hep-lat\]](#) .
- [91] Chris Bouchard, G. Peter Lepage, Christopher Monahan, Heechang Na, and Junko Shigemitsu (HPQCD), “Rare decay $B \rightarrow K\ell^+\ell^-$ form factors from lattice QCD,” *Phys. Rev.* **D88**, 054509 (2013), [Erratum: *Phys. Rev.*D88,no.7,079901(2013)], [arXiv:1306.2384 \[hep-lat\]](#) .
- [92] Jon A. Bailey *et al.*, “ $B \rightarrow K\ell^+\ell^-$ Decay Form Factors from Three-Flavor Lattice QCD,” *Phys. Rev.* **D93**, 025026 (2016), [arXiv:1509.06235 \[hep-lat\]](#) .
- [93] C. McNeile, C. T. H. Davies, E. Follana, K. Hornbostel, and G. P. Lepage, “High-Precision f_{B_s} and HQET from Relativistic Lattice QCD,” *Phys. Rev.* **D85**, 031503 (2012), [arXiv:1110.4510 \[hep-lat\]](#) .
- [94] C. McNeile, C. T. H. Davies, E. Follana, K. Hornbostel, and G. P. Lepage, “Heavy meson masses and decay constants from relativistic heavy quarks in full lattice QCD,” *Phys. Rev.* **D86**, 074503 (2012), [arXiv:1207.0994 \[hep-lat\]](#) .
- [95] E. McLean, C. T. H. Davies, A. T. Lytle, and J. Koponen, “Lattice QCD form factor for $B_s \rightarrow D_s^*\ell\nu$ at zero recoil with non-perturbative current renormalisation,” *Phys. Rev.* **D99**, 114512 (2019), [arXiv:1904.02046 \[hep-lat\]](#) .
- [96] E. McLean, C. T. H. Davies, J. Koponen, and A. T. Lytle, “ $B_s \rightarrow D_s\ell\nu$ Form Factors for the full q^2 range from Lattice QCD with non-perturbatively normalized currents,” (2019), [arXiv:1906.00701 \[hep-lat\]](#) .
- [97] Bernd A. Kniehl and Oleg L. Veretin, “Bilinear quark operators in the RI/SMOM scheme at three loops,” (2020), [arXiv:2002.10894 \[hep-ph\]](#) .
- [98] M. Constantinou, M. Hadjiantonis, H. Panagopoulos, and G. Spanoudes, “Singlet versus

- nonsinglet perturbative renormalization of fermion bilinears,” *Phys. Rev.* **D94**, 114513 (2016), [arXiv:1610.06744 \[hep-lat\]](#) .
- [99] Leandro G. Almeida and Christian Sturm, “Two-loop matching factors for light quark masses and three-loop mass anomalous dimensions in the RI/SMOM schemes,” *Phys. Rev.* **D82**, 054017 (2010), [arXiv:1004.4613 \[hep-ph\]](#) .
- [100] J. A. Gracey, “Three loop anomalous dimension of nonsinglet quark currents in the RI-prime scheme,” *Nucl. Phys.* **B662**, 247–278 (2003), [arXiv:hep-ph/0304113 \[hep-ph\]](#) .
- [101] C. Davies, “The Heavy hadron spectrum,” *Computing particle properties. Proceedings, 36. Internationale Universitätswochen für Kern- und Teilchenphysik: Schladming, Austria, March 1-8, 1997*, *Lect. Notes Phys.* **512**, 1–64 (1998), [arXiv:hep-ph/9710394 \[hep-ph\]](#) .
- [102] L. Levkova and C. DeTar, “Charm annihilation effects on the hyperfine splitting in charmonium,” *Phys. Rev.* **D83**, 074504 (2011), [arXiv:1012.1837 \[hep-lat\]](#) .
- [103] Geoffrey T. Bodwin, Eric Braaten, and G. Peter Lepage, “Rigorous QCD analysis of inclusive annihilation and production of heavy quarkonium,” *Phys. Rev.* **D51**, 1125–1171 (1995), [Erratum: *Phys. Rev.*D55,5853(1997)], [arXiv:hep-ph/9407339 \[hep-ph\]](#) .
- [104] Gavin K.C. Cheung, Cian O’Hara, Graham Moir, Michael Peardon, Sinéad M. Ryan, Christopher E. Thomas, and David Tims (Hadron Spectrum), “Excited and exotic charmonium, D_s and D meson spectra for two light quark masses from lattice QCD,” *JHEP* **12**, 089 (2016), [arXiv:1610.01073 \[hep-lat\]](#) .
- [105] J. Grange *et al.* (Muon g-2), “Muon (g-2) Technical Design Report,” (2015), [arXiv:1501.06858 \[physics.ins-det\]](#) .
- [106] C. T. H. Davies, C. McNeile, E. Follana, G. P. Lepage, H. Na, and J. Shigemitsu, “Update: Precision D_s decay constant from full lattice QCD using very fine lattices,” *Phys. Rev.* **D82**, 114504 (2010), [arXiv:1008.4018 \[hep-lat\]](#) .
- [107] Sz. Borsanyi *et al.*, “Leading-order hadronic vacuum polarization contribution to the muon magnetic moment from lattice QCD,” (2020), [arXiv:2002.12347 \[hep-lat\]](#) .
- [108] A. Gray, I. Allison, C. T. H. Davies, Emel Dalgic, G. P. Lepage, J. Shigemitsu, and M. Wingate, “The Upsilon spectrum and $m(b)$ from full lattice QCD,” *Phys. Rev.* **D72**, 094507 (2005), [arXiv:hep-lat/0507013 \[hep-lat\]](#) .

- [109] Sz. Borsanyi *et al.*, “Ab initio calculation of the neutron-proton mass difference,” *Science* **347**, 1452–1455 (2015), [arXiv:1406.4088 \[hep-lat\]](#) .
- [110] Zohreh Davoudi and Martin J. Savage, “Finite-Volume Electromagnetic Corrections to the Masses of Mesons, Baryons and Nuclei,” *Phys. Rev.* **D90**, 054503 (2014), [arXiv:1402.6741 \[hep-lat\]](#) .
- [111] V. V. Anashin *et al.*, “Final analysis of KEDR data on J/ψ and $\psi(2S)$ masses,” *Phys. Lett.* **B749**, 50–56 (2015).
- [112] V. V. Anashin *et al.*, “Measurement of $J/\psi \rightarrow \gamma\eta_c$ decay rate and η_c parameters at KEDR,” *Phys. Lett.* **B738**, 391–396 (2014), [arXiv:1406.7644 \[hep-ex\]](#) .
- [113] Roel Aaij *et al.* (LHCb), “Measurement of the $\eta_c(1S)$ production cross-section in proton-proton collisions via the decay $\eta_c(1S) \rightarrow p\bar{p}$,” *Eur. Phys. J.* **C75**, 311 (2015), [arXiv:1409.3612 \[hep-ex\]](#) .
- [114] Roel Aaij *et al.* (LHCb), “Observation of $\eta_c(2S) \rightarrow p\bar{p}$ and search for $X(3872) \rightarrow p\bar{p}$ decays,” *Phys. Lett.* **B769**, 305–313 (2017), [arXiv:1607.06446 \[hep-ex\]](#) .
- [115] Q. N. Xu *et al.* (Belle), “Measurement of $\eta_c(1S)$, $\eta_c(2S)$ and non-resonant $\eta' \pi^+ \pi^-$ production via two-photon collisions,” *Phys. Rev.* **D98**, 072001 (2018), [arXiv:1805.03044 \[hep-ex\]](#) .
- [116] R. Aaij *et al.* (LHCb), “Study of charmonium production in b -hadron decays and first evidence for the decay $B_s^0 \rightarrow \phi\phi\phi$,” *Eur. Phys. J.* **C77**, 609 (2017), [arXiv:1706.07013 \[hep-ex\]](#) .
- [117] J. P. Lees *et al.* (BaBar), “Dalitz plot analysis of $\eta_c \rightarrow K^+K^-\eta$ and $\eta_c \rightarrow K^+K^-\pi^0$ in two-photon interactions,” *Phys. Rev.* **D89**, 112004 (2014), [arXiv:1403.7051 \[hep-ex\]](#) .
- [118] M. Ablikim *et al.* (BESIII), “Measurements of the mass and width of the η_c using $\psi' \rightarrow \gamma\eta_c$,” *Phys. Rev. Lett.* **108**, 222002 (2012), [arXiv:1111.0398 \[hep-ex\]](#) .
- [119] M. Ablikim *et al.* (BESIII), “Study of $\psi(3686) \rightarrow \pi^0 h_c, h_c \rightarrow \gamma\eta_c$ via η_c exclusive decays,” *Phys. Rev.* **D86**, 092009 (2012), [arXiv:1209.4963 \[hep-ex\]](#) .
- [120] Carleton DeTar, Andreas S. Kronfeld, Song-haeng Lee, Daniel Mohler, and James N. Simone (Fermilab Lattice, MILC), “Splittings of low-lying charmonium masses at the physical point,” *Phys. Rev.* **D99**, 034509 (2019), [arXiv:1810.09983 \[hep-lat\]](#) .

- [121] Yi-Bo Yang *et al.*, “Charm and strange quark masses and f_{D_s} from overlap fermions,” *Phys. Rev.* **D92**, 034517 (2015), [arXiv:1410.3343 \[hep-lat\]](#) .
- [122] Raul A. Briceño, Huey-Wen Lin, and Daniel R. Bolton, “Charmed-Baryon Spectroscopy from Lattice QCD with $N_f=2+1+1$ Flavors,” *Phys. Rev.* **D86**, 094504 (2012), [arXiv:1207.3536 \[hep-lat\]](#) .
- [123] Victor S. Fadin, Valery A. Khoze, and Alan D. Martin, “How suppressed are the radiative interference effects in heavy unstable particle production?” *Phys. Lett.* **B320**, 141–144 (1994), [arXiv:hep-ph/9309234 \[hep-ph\]](#) .
- [124] V. V. Anashin *et al.*, “Measurement of main parameters of the $\psi(2S)$ resonance,” *Phys. Lett.* **B711**, 280–291 (2012), [arXiv:1109.4215 \[hep-ex\]](#) .
- [125] V. V. Anashin *et al.*, “Measurement of J/psi leptonic width with the KEDR detector,” *Proceedings, 6th International Workshop on e+e- Collisions from Phi to Psi (PHIPSI09): Beijing, China, October 13-16, 2009*, *Chin. Phys.* **C34**, 836–841 (2010), [arXiv:1110.0328 \[hep-ex\]](#) .
- [126] E. A. Kuraev and Victor S. Fadin, “On Radiative Corrections to e+ e- Single Photon Annihilation at High-Energy,” *Sov. J. Nucl. Phys.* **41**, 466–472 (1985), [*Yad. Fiz.*41,733(1985)].
- [127] Jens Erler, “Calculation of the QED coupling $\alpha(M(Z))$ in the modified minimal subtraction scheme,” *Phys. Rev.* **D59**, 054008 (1999), [arXiv:hep-ph/9803453 \[hep-ph\]](#) .
- [128] Damir Bečirević, Goran Duplanić, Bruno Klajn, Blaženka Melić, and Francesco Sanfilippo, “Lattice QCD and QCD sum rule determination of the decay constants of η_c , J/ ψ and h_c states,” *Nucl. Phys.* **B883**, 306–327 (2014), [arXiv:1312.2858 \[hep-ph\]](#) .
- [129] Johann H. Kuhn, Matthias Steinhauser, and Christian Sturm, “Heavy Quark Masses from Sum Rules in Four-Loop Approximation,” *Nucl. Phys.* **B778**, 192–215 (2007), [arXiv:hep-ph/0702103 \[HEP-PH\]](#) .
- [130] Derek E. Hazard and Alexey A. Petrov, “Lepton flavor violating quarkonium decays,” *Phys. Rev.* **D94**, 074023 (2016), [arXiv:1607.00815 \[hep-ph\]](#) .
- [131] Wolfgang Altmannshofer, Patricia Ball, Aoife Bharucha, Andrzej J. Buras, David M. Straub, and Michael Wick, “Symmetries and Asymmetries of $B \rightarrow K^* \mu^+ \mu^-$ Decays in the Standard Model and Beyond,” *JHEP* **01**, 019 (2009), [arXiv:0811.1214 \[hep-ph\]](#) .

- [132] Katsumasa Nakayama, Brendan Fahy, and Shoji Hashimoto, “Short-distance charmonium correlator on the lattice with Möbius domain-wall fermion and a determination of charm quark mass,” *Phys. Rev.* **D94**, 054507 (2016), [arXiv:1606.01002 \[hep-lat\]](#) .
- [133] Bahman Dehnadi, Andre H. Hoang, Vicent Mateu, and S. Mohammad Zebarjad, “Charm Mass Determination from QCD Charmonium Sum Rules at Order α_s^3 ,” *JHEP* **09**, 103 (2013), [arXiv:1102.2264 \[hep-ph\]](#) .
- [134] Sz. Borsanyi *et al.* (Budapest-Marseille-Wuppertal), “Hadronic vacuum polarization contribution to the anomalous magnetic moments of leptons from first principles,” *Phys. Rev. Lett.* **121**, 022002 (2018), [arXiv:1711.04980 \[hep-lat\]](#) .
- [135] D. Giusti, V. Lubicz, G. Martinelli, F. Sanfilippo, and S. Simula, “Strange and charm HVP contributions to the muon ($g - 2$) including QED corrections with twisted-mass fermions,” *JHEP* **10**, 157 (2017), [arXiv:1707.03019 \[hep-lat\]](#) .
- [136] D. Giusti, V. Lubicz, G. Martinelli, F. Sanfilippo, and S. Simula, “Electromagnetic and strong isospin-breaking corrections to the muon $g - 2$ from Lattice QCD+QED,” *Phys. Rev.* **D99**, 114502 (2019), [arXiv:1901.10462 \[hep-lat\]](#) .
- [137] J. Bijnens, J. Harrison, N. Hermansson-Truedsson, T. Janowski, A. Jüttner, and A. Portelli, “Electromagnetic finite-size effects to the hadronic vacuum polarization,” *Phys. Rev.* **D100**, 014508 (2019), [arXiv:1903.10591 \[hep-lat\]](#) .
- [138] M. Di Carlo, D. Giusti, V. Lubicz, G. Martinelli, C. T. Sachrajda, F. Sanfilippo, S. Simula, and N. Tantalo, “Light-meson leptonic decay rates in lattice QCD+QED,” *Phys. Rev.* **D100**, 034514 (2019), [arXiv:1904.08731 \[hep-lat\]](#) .
- [139] S. W. Herb *et al.*, “Observation of a Dimuon Resonance at 9.5-GeV in 400-GeV Proton-Nucleus Collisions,” *Phys. Rev. Lett.* **39**, 252–255 (1977).
- [140] Bernard Aubert *et al.* (BaBar), “Observation of the bottomonium ground state in the decay $v_{3S} \rightarrow \gamma eta_b$,” *Phys. Rev. Lett.* **101**, 071801 (2008), [Erratum: *Phys. Rev. Lett.*102,029901(2009)], [arXiv:0807.1086 \[hep-ex\]](#) .
- [141] Aida X. El-Khadra, Andreas S. Kronfeld, and Paul B. Mackenzie, “Massive fermions in lattice gauge theory,” *Phys. Rev.* **D55**, 3933–3957 (1997), [arXiv:hep-lat/9604004 \[hep-lat\]](#) .

- [142] T. Burch, C. DeTar, M. Di Pierro, A. X. El-Khadra, E. D. Freeland, Steven Gottlieb, A. S. Kronfeld, L. Levkova, P. B. Mackenzie, and J. N. Simone, “Quarkonium mass splittings in three-flavor lattice QCD,” *Phys. Rev.* **D81**, 034508 (2010), [arXiv:0912.2701 \[hep-lat\]](#) .
- [143] R. Mizuk *et al.* (Belle), “Evidence for the $\eta_b(2S)$ and observation of $h_b(1P) \rightarrow \eta_b(1S)\gamma$ and $h_b(2P) \rightarrow \eta_b(1S)\gamma$,” *Phys. Rev. Lett.* **109**, 232002 (2012), [arXiv:1205.6351 \[hep-ex\]](#) .
- [144] G. Bonvicini *et al.* (CLEO), “Measurement of the eta(b)(1S) mass and the branching fraction for Upsilon(3S) \rightarrow gamma eta(b)(1S),” *Phys. Rev.* **D81**, 031104 (2010), [arXiv:0909.5474 \[hep-ex\]](#) .
- [145] Bernard Aubert *et al.* (BaBar), “Evidence for the eta(b)(1S) Meson in Radiative Upsilon(2S) Decay,” *Phys. Rev. Lett.* **103**, 161801 (2009), [arXiv:0903.1124 \[hep-ex\]](#) .
- [146] R. J. Dowdall, C. T. H. Davies, T. Hammant, R. R. Horgan, and C. Hughes (HPQCD), “Bottomonium hyperfine splittings from lattice nonrelativistic QCD including radiative and relativistic corrections,” *Phys. Rev.* **D89**, 031502 (2014), [Erratum: *Phys. Rev.* **D92**, 039904(2015)], [arXiv:1309.5797 \[hep-lat\]](#) .
- [147] Stefan Meinel, “Bottomonium spectrum at order v^6 from domain-wall lattice QCD: Precise results for hyperfine splittings,” *Phys. Rev.* **D82**, 114502 (2010), [arXiv:1007.3966 \[hep-lat\]](#) .
- [148] Yasumichi Aoki, Norman H. Christ, Jonathan M. Flynn, Taku Izubuchi, Christoph Lehner, Min Li, Hao Peng, Amarjit Soni, Ruth S. Van de Water, and Oliver Witzel (RBC, UKQCD), “Nonperturbative tuning of an improved relativistic heavy-quark action with application to bottom spectroscopy,” *Phys. Rev.* **D86**, 116003 (2012), [arXiv:1206.2554 \[hep-lat\]](#) .
- [149] A. A. Pivovarov, “Running electromagnetic coupling constant: Low-energy normalization and the value at $M(Z)$,” *Phys. Atom. Nucl.* **65**, 1319–1340 (2002), [*Yad. Fiz.* **65**, 1352(2002)], [arXiv:hep-ph/0011135 \[hep-ph\]](#) .
- [150] B. Colquhoun, R. J. Dowdall, C. T. H. Davies, K. Hornbostel, and G. P. Lepage, “ Υ and Υ' Leptonic Widths, a_μ^b and m_b from full lattice QCD,” *Phys. Rev.* **D91**, 074514 (2015), [arXiv:1408.5768 \[hep-lat\]](#) .
- [151] K. G. Chetyrkin, J. H. Kuhn, A. Maier, P. Maierhofer, P. Marquard, M. Steinhauser, and

- C. Sturm, “Charm and Bottom Quark Masses: An Update,” *Phys. Rev.* **D80**, 074010 (2009), [arXiv:0907.2110 \[hep-ph\]](#) .
- [152] K. G. Chetyrkin, “Quark mass anomalous dimension to $O(\alpha_s^4)$,” *Phys. Lett.* **B404**, 161–165 (1997), [arXiv:hep-ph/9703278 \[hep-ph\]](#) .
- [153] J. A. M. Vermaseren, S. A. Larin, and T. van Ritbergen, “The four loop quark mass anomalous dimension and the invariant quark mass,” *Phys. Lett.* **B405**, 327–333 (1997), [arXiv:hep-ph/9703284 \[hep-ph\]](#) .
- [154] Alexander Bednyakov and Andrey Pikelner, “Quark masses: NNLO bridge from RI/SMOM to \overline{MS} scheme,” (2020), [arXiv:2002.12758 \[hep-ph\]](#) .
- [155] A. V. Bednyakov, B. A. Kniehl, A. F. Pikelner, and O. L. Veretin, “On the b -quark running mass in QCD and the SM,” *Nucl. Phys.* **B916**, 463–483 (2017), [arXiv:1612.00660 \[hep-ph\]](#) .
- [156] A. Bazavov *et al.* (Fermilab Lattice, MILC, TUMQCD), “Up-, down-, strange-, charm-, and bottom-quark masses from four-flavor lattice QCD,” *Phys. Rev.* **D98**, 054517 (2018), [arXiv:1802.04248 \[hep-lat\]](#) .
- [157] N. Brambilla, J. Komijani, A. S. Kronfeld, and A. Vairo (TUMQCD), “Relations between Heavy-light Meson and Quark Masses,” *Phys. Rev.* **D97**, 034503 (2018), [arXiv:1712.04983 \[hep-ph\]](#) .
- [158] N. Carrasco *et al.* (European Twisted Mass), “Up, down, strange and charm quark masses with $N_f = 2+1+1$ twisted mass lattice QCD,” *Nucl. Phys.* **B887**, 19–68 (2014), [arXiv:1403.4504 \[hep-lat\]](#) .